

# High frequency parametric amplification based on the non-linear dynamics of superconductors

A THESIS SUBMITTED TO THE UNIVERSITY OF MANCHESTER  
FOR THE DEGREE OF DOCTOR OF PHILOSOPHY  
IN THE FACULTY OF SCIENCE AND ENGINEERING

August 2022

By

Danielius Banys

Jodrell Bank Centre for Astrophysics  
Department of Physics and Astronomy  
School of Natural Sciences



# Contents

<b>List of Tables</b>	<b>7</b>
<b>List of Figures</b>	<b>8</b>
<b>Abstract</b>	<b>36</b>
<b>Declaration</b>	<b>38</b>
<b>Copyright</b>	<b>39</b>
<b>Acknowledgements</b>	<b>40</b>
<b>Supporting Publications</b>	<b>42</b>
<b>1 Introduction</b>	<b>43</b>
1.1 Science Case . . . . .	43
1.2 Project Objectives and Thesis Outline . . . . .	51
<b>2 Superconductivity and Parametric Amplification</b>	<b>55</b>
2.1 Introduction . . . . .	55
2.2 Superconductivity . . . . .	58
2.2.1 Mattis-Bardeen Conductivity . . . . .	62
2.2.2 Zimmermann Conductivity . . . . .	66
2.2.3 Surface Impedance . . . . .	70
2.3 Superconducting Nonlinearities . . . . .	75

## CONTENTS

2.3.1	Josephson Inductance . . . . .	75
2.3.2	Kinetic Inductance . . . . .	77
2.4	Parametric Amplification . . . . .	79
2.4.1	Parallels to Optics . . . . .	79
2.4.2	Parametric Amplifier Overview . . . . .	82
2.4.3	Resonant Parametric Amplifiers . . . . .	84
2.4.4	Travelling-Wave Parametric Amplifiers . . . . .	96
<b>3</b>	<b>Cryogenic Measurement System</b>	<b>107</b>
3.1	Introduction . . . . .	107
3.2	Cryostat Consideration . . . . .	108
3.2.1	Reaching Base Temperature . . . . .	111
3.2.2	Cryogenic Device Testing . . . . .	115
3.2.3	Microwave Testing Equipment . . . . .	118
3.3	Circular Waveguide Resonator . . . . .	119
3.3.1	The Pillbox Cavity Resonator . . . . .	119
3.4	Design Of Modular Test Cryostat . . . . .	125
<b>4</b>	<b>Ka band Ridge Gap Waveguide KI RPA</b>	<b>129</b>
4.1	Introduction . . . . .	129
4.1.1	Chapter Outline . . . . .	132
4.2	Design and Simulation . . . . .	133
4.2.1	Ridge Gap Waveguide . . . . .	133
4.2.2	Ridge Gap Waveguide Resonator . . . . .	141
4.2.3	Nonlinear Circuit Simulations . . . . .	160
4.3	Mechanical Design and Fabrication . . . . .	168
4.3.1	Mechanical Design . . . . .	168
4.3.2	Surface Polishing . . . . .	173
4.3.3	Superconducting Coating . . . . .	179
4.4	Resonator Measurements . . . . .	191



4.4.1	Copper RGWG Resonator . . . . .	193
4.4.2	Superconducting RGWG Resonators . . . . .	195
4.5	Summary and Outlook . . . . .	213
4.5.1	Summary . . . . .	213
4.5.2	Future Work . . . . .	215
<b>5</b>	<b>W band Ridge Gap Waveguide KI TWPA</b>	<b>219</b>
5.1	Introduction . . . . .	219
5.1.1	Motivation and Applications . . . . .	221
5.1.2	Chapter Outline . . . . .	222
5.2	Ridge Gap Waveguide Design . . . . .	223
5.2.1	RGWG HFSS Simulations . . . . .	223
5.2.2	Kinetic Inductance Participation . . . . .	230
5.2.3	Scaling Current Estimate . . . . .	232
5.3	Ridge Gap Waveguide TWPA . . . . .	235
5.3.1	Periodic Loading Structure . . . . .	236
5.3.2	Nonlinear S-parameters . . . . .	238
5.3.3	TWPA gain . . . . .	242
5.4	Summary and Outlook . . . . .	246
5.4.1	Summary . . . . .	246
5.4.2	First Prototype . . . . .	247
5.4.3	Future Work . . . . .	248
<b>A</b>	<b>Ka Band RGWG Resonator</b>	<b>251</b>
A.1	ADS Simulation Circuits . . . . .	251
A.2	Technical Drawings . . . . .	258
<b>B</b>	<b>W Band KI RGWG TWPA</b>	<b>263</b>
B.1	ADS Simulation Circuit . . . . .	263

## *CONTENTS*

<b>Bibliography</b>	<b>271</b>
<b>Word count: ~50,000</b>	

# List of Tables

- 4.1 The calculated linear kinetic inductance contribution of each resonance in the simulated superconducting pin-coupled RGWG resonator with two different coatings and ridge-lid spacings. The values were found by comparison to the equivalent PEC simulation. 151

## *LIST OF TABLES*

# List of Figures

- 1.1 A figure showing the dynamic range of an amplifier with a gain  $G$  [1]. The minimum signal power that can be amplified is defined by the noise floor of amplifier and the highest power is defined by the compression point at which the gain of the amplifier stops scaling linearly with input power. . . . . 44
- 1.2 Schematics of two common amplification schemes used in radio or mm-wave receivers [2]. The scheme presented in the upper panel is most common for signals below 100 GHz where radiation captured by the feedhorn is amplified directly by an LNA which has a sufficiently high gain and low noise. Following this, the signal is down converted by a mixer to an intermediate frequency (IF) of  $< 10$  GHz and amplified by the IF amplifier. The lower panel shows a scheme used for signal over 100 GHz and up to around 1000 GHz, where LNAs with sufficient gain and low enough noise are not available. Here, a superconducting mixing is used instead to first down convert the signal from the feedhorn to then be amplified by a LNA at a considerably lower frequency followed by the same amplification by the IF amplifier. . . . . 46

## LIST OF FIGURES

1.3	A labelled CAD model and photograph of an ALMA band 5 receiver covering a frequency range of 163-211 GHz [3]. This receiver uses a superconducting mixer scheme like the one described in the lower panel of Fig. 1.2. . . . .	47
1.4	The receiver noise temperature of ALMA bands 3 to 10 where the black dashed lines represent 4 and 10 times the quantum noise limit [22, 2]. . . . .	49
2.1	The reduced superconducting gap parameter as a function of reduced temperature found using a script adapted from “Supermix” [51]. Values for $T/T_c < 0.18$ were found using Eq. 2.16. . . . .	64
2.2	The real and imaginary part of the normalised Mattis-Bardeen conductivity in the local limit. Niobium is used as example with $T_c = 9.2$ K and $\Delta_0/kT_c = 1.83$ . . . . .	65
2.3	The real and imaginary part of the normalised Zimmermann conductivity for dirty niobium with $T_c = 9.2$ K, $\Delta_0/kT_c = 1.83$ , $\xi_0 = 39$ nm and $l = 5.7$ nm. . . . .	67
2.4	A comparison of the complex conductivities of three grades of niobium calculated with the Zimmermann conductivity vs the Mattis-Bardeen conductivity of niobium in the local limit. A temperature of 1 K is chosen as an example but other temperatures demonstrate similar behaviour. The parameters used are the following: ‘clean’[54], $\Delta_0/kT_c = 1.97$ , $\xi_0 = 39$ nm, $l = 100$ nm; ‘mid-range’[38], $\Delta_0/kT_c = 1.76$ , $\xi_0 = 39$ nm, $l = 20$ nm; ‘dirty’[51], $\Delta_0/kT_c = 1.83$ , $\xi_0 = 39$ nm, $l = 5.7$ nm. $T_c = 9.2$ K for all 4. . . .	68
2.5	A comparison of the complex conductivities of NbTiN found via M-B and Zimmermann methods. The temperature is set to 1 K and the parameters used for NbTiN are [55]: $T_c = 14.1$ K, $\Delta_0/kT_c = 1.86$ , $\xi_0 = 170$ nm, $l = 0.57$ nm . . . . .	70

2.6	A diagram used for the derivation of the surface impedance of a thick conductor. Top: A diagram of a plane wave at normal incidence to a conductor of surface impedance $Z_s$ . Bottom: A lumped element model representation of the case above where the impedance at the surface is given by $Z_{in}$ which is equal to $Z_s$ when looking in the direction of the conductor, the infinitesimally small thickness of conductor $dz$ is represented by a lumped element transmission line model. The inductance and conductance of the this sheet is given by $dL$ and $dG$ , respectively. The capacitance is zero since the sheet is at the same potential and resistance is neglected due the infinitesimally thin sheet thickness. . . . .	72
2.7	The complex surface impedance of dirty Nb ( $\sigma_n = 2 \times 10^7 \text{ S m}^{-1}$ ) and NbTiN ( $\sigma_n = 0.55 \times 10^6 \text{ S m}^{-1}$ ) at 1 K. The other material properties are the same as in Fig. 2.4. . . . .	74
2.8	A simplified output spectrum of two types of mixing processes with input tones at $\omega_s$ and $\omega_p$ . The 4WM amplifier (left) shows the signal response centered around $\omega_p$ , with a generated idler at $2\omega_p = \omega_s + \omega_i$ and the 3WM amplifier (right) shows the signal response around $\omega_p/2$ with an idler at $\omega_p = \omega_s + \omega_i$ . In each case the amplifiers are in phase-preserving operation. The black arrows indicate the energy flow fo the system. . . . .	83
2.9	A cartoon showing two configurations of an RPA: <i>Top</i> shows the non-linear resonator (NLR) operated in reflection mode with a circulator isolating the three ports from one another. <i>Bottom</i> shows the NLR resonator with 2 ports operated in transmission mode with isolators on each port to prevent back reflections leaking to a device that may be under test. The NLR is coupled to the ports by a coupling strength $g$ . . . . .	85

## LIST OF FIGURES

2.10	A schematic showing the input-output model used for deriving the response of a signal when coupled to a parametric amplifier with a loss reservoir. . . . .	87
2.11	The signal gain of a resonant parametric amplifier with a resonant pump ( $\Omega = 0$ ) as a function signal-pump detuning $\bar{\omega}$ normalised by the bare resonance width $\kappa$ . This is plotted at a number of different pump amplitudes $\lambda$ inside the resonator normalised by the critical drive $\lambda_{crit}^2 = \kappa^2/4$ . . . . .	91
2.12	The normalised mean photon occupancy number inside the non-linear resonant cavity excited by a single input tone at a range of different drive strengths that are normalised by the critical pump drive of $\xi_{crit} = -1/\sqrt{27}$ . . . . .	93
2.13	RPA signal gain for $\delta = 0$ as function of the normalised pump detuning at different dimensionless pump strengths. . . . .	96
2.14	A cartoon showing exponential parametric amplification within a nonlinear medium of a weak signal in the presence of a strong pump. Here the pump, signal and idler complex magnitudes are represented by $A_p$ , $A_s$ and $A_i$ , respectively. The idler is assumed to be instantaneously generated at $t = 0$ . . . . .	98
3.1	The left panel shows a photograph of a cryostat on a mobile frame. The middle panel shows the the 4 K stage of the cryostat with a 1 K sorption cooler and a heat switch mounted. The right panel shows a schematic drawing of the cryostat which includes the free standing $\mu$ metal magnetic shield as well as the radiation shields that get secured to the 40 K and 4 K stages via screws. . . . .	111



- 3.2 The left panel shows the 1 K helium-4 sorption cooler, which can also be seen mounted in the cryostat in Fig. 3.1. The upper right panel shows a picture with the convective heatswitch and copper brackets used to thermally connect the top of the switch to the 4 K plate as seen in Fig. 3.1. The lower right panel shows a schematic of the sorption cooler. The chamber which contains the charcoal is referred to as the cryopump while the chamber with liquid He is the evaporator pot. This 1 K system was developed by May *et al.* [107]. . . . . 112
- 3.3 The left panel shows the heat load characteristics of the Sumitomo RDK-415D GM cryocooler (see footnote). The vertical lines represent heat loads on the 1st stage, while the horizontal line on the 2nd stage. The crossing points between these two lines shows the temperature of each stage with the set heat loads. The right panel shows the evaporation pot temperature for different heat loads of the 1 K helium-4 sorption cooler. The hold time for a heat load of 0.7 mW at a temperature of  $\sim 820$  mK was 22 hours [107]. The lines labelled the continuum and molecular model refer to the theoretical modelling of the expected pot temperature under different pressures and hence different flow regimes. These regimes are dictated by the Knudsen number  $K_n = l/L$  with  $l$  being the mean free path and  $L$  the characteristic length scale. At the lowest temperatures  $K_n$  is above the upper limit for the continuum regime while still below the minimum limit for the molecular flow regime i.e. in an intermediate regime in which the measured data falls (see [107] for full details). . . . . 114
- 3.4 The saturated vapour pressure curves of helium-4 and helium 3. Showing the minimum temperature that can be reached by pumping on the saturated vapour above the liquid helium. . . . . 115

## LIST OF FIGURES

- 3.5 The left panel shows a niobium pillbox cavity mounted in the cryostat demonstrating the use of waveguide thermal breaks (see Section 3.3 for more information about the mounted device). The DUT in this case is directly connected to the 4 K stage via a copper braid but it can be connected to the 1 K sorption cooler behind it instead. The upper right panel shows a screenshot of an underside of a CAD model of a hermetic Ka band feedthrough that is used at the top of the cryostat (see right panel of Fig. 3.6 and right panel of Fig. 3.8 for a schematic drawing). The feedthrough is made of two parts between which a thin mylar film that is transparent to microwave radiation is compressed with an o-ring to create a vacuum seal. The lower right panel shows a close up of the Ka band thermal break that was developed by Melhuish *et al.* [110]. . 116
- 3.6 The left panel shows a photograph of the Keysight N5245A PNA-X which could operate in the range of 10 MHz to 50 GHz and had 2.4mm coaxial connections. The right panel shows one of the VNA coaxial lines connected to the rectangular waveguide hermetic feedthrough via a transition from 2.4 mm coaxial to Ka band waveguide. The lower panel shows the internal path configuration of the VNA. In the image it is configured for the routing of the outputs from the two internal synthesisers through a single port that is needed for mixing measurements. . . . . 117

3.7	Circular WG cavities of inner diameter 11.9 mm and length 15.7 mm made from annealed niobium rod (99.9% purity). The cavities had multiple covers with circular apertures that were different in diameter and thickness in order to investigate different coupling regimes. After machining, the cavities were cleaned in sonicated chemical baths consisting of Decon 90 detergent, acetone and isopropyl alcohol. The left panel shows the two port cavity with two parts containing the aperture couplings next to it. These attached via screws passing through a rectangular waveguide feed as shown in the left panel of Fig. 3.5, while the right panel shows a single port cavity with a copper lid containing a coupling aperture. . . . .	120
3.8	Schematic view of the signal flow from the generation of the two tones by separate sources within a Keysight N5245A PNA-X, through to the cryostat via Ka band copper rectangular waveguide and into the niobium resonator to be received at the internal receiver of the PNA-X. Due to the limitation of both tones being attenuated by a single attenuator bank, the maximum power difference between the tones was 30 dB. The IF bandwidth of the PNA-X was kept at 100 Hz for the measurements . . . . .	121

## LIST OF FIGURES

3.9	Investigation of a SC circular waveguide cavity $TM_{110}$ resonance. The plots are centred at the resonance frequency of 30.64 GHz, which is referred to as the relative frequency here. <i>Top left</i> : Single tone transmission at various input power. Equivalent pump power (total power – signal power) is used for a more direct visual comparison with the gain data. Two dotted lines are included to draw attention to the positions of kinks in transmission. The waveguide feedline losses were not calibrated out. <i>Top right</i> : The gain in signal power relative to the transmission spectrum that is traced out by the pump tone. The signal was kept at a constant –60 dBm and 10 kHz below the pump tone as the two tones were swept through the profile of the resonance. <i>Bottom left</i> : The power of the idler at $f_{i,1} = 2f_p - f_s$ . The receiver noise floor was at –110 dBm. <i>Bottom right</i> : The power of the idler at $f_{i,2} = 2f_s - f_p$ . . . . .	122
3.10	Images of the CAD model of a new modular test cryostat that can accept a cartridge which would contain the necessary rectangular waveguide feeds and the DUT at bottom. The right image shows the structure inside the cryostat as well as an inserted cartridge. .	126
3.11	An image of the CAD model of a W band cartridge designed for the testing of multiple LNAs at the same time. The thermal breaking between cold stages was done with thin wall stainless steel waveguide pieces that are drawn in grey. There was space for a 55 pin hermetic DC connector for the connection of all the necessary DC biasing lines. . . . .	127

- 4.1 A RGWG model showing the central ridge of width  $w$  and height  $d$ , in a groove of width  $a$  and height  $b$  with 3 rows of pins either side of the ridge with width  $w_{\text{pin}}$ , height  $d$ , and period  $p$ . These dimensions are typically on a similar scale to the dimensions of rectangular waveguide at a similar frequency. The gap labelled  $h$  is exaggerated to demonstrate how the 2 parts of the structure are joined together. . . . . 130
- 4.2 A model of a bed of nails array with a lid that is separated by a small gap  $h$ . The inset shows the repeating unit cell that is used to simulate the dispersion diagram of the full structure. Here,  $d$  is the nail length,  $w_{\text{pin}}$  is the nail width,  $h$  is the gap between the top of the nail and the PEC lid, and  $p$  is the nail period. In the simulation master and slave (coupled lattice) boundaries are set on the 2 pairs of horizontally opposing faces of the unit cell shown in the top right of the figure. . . . . 134
- 4.3 *Left:* The full dispersion diagram of a bed of nails periodic structure for the first 2 propagating modes, one below and one above the desired stopband of the structure. The black lines show the useable structure bandwidth that are positioned on the orange dots, which show the highest and lowest propagating frequency on the lower and upper modes, respectively. Note that the dispersion diagram is relatively flat due to the small gap that is used in this simulation. *Right:* The Brillouin zone showing the high symmetry points for a bed of nails cell of size  $p$ . The colours indicate the regions that cover the full dispersion diagram of the periodic structure. The dimensions of the simulated unit cell are:  $d = 3.55$  mm,  $h = 10$   $\mu\text{m}$ ,  $w_{\text{pin}} = 1.5$  mm, and  $p = 1.5$ mm. . . . . 135

## LIST OF FIGURES

4.4	The bandwidth of the bed of nails as a function the structure dimensions. The bandwidth is the stopband over which no modes propagate within an infinite array of nails and the PEC top. The final chosen nail dimensions were $d = 3.55$ mm, $h = 10$ $\mu$ m, $p = 3$ mm, and $w_{pin} = 1.5$ mm. . . . .	138
4.5	A diagram showing the unit cell used to simulate groove gap waveguide in HFSS and the resulting eigenmode dispersion diagram. The unit cell had a single set of lattice boundaries set on the faces along the direction of propagation of the confined wave (in/out of page). The width of the groove was set $a = 7.11$ mm, matching the long wall of Ka band rectangular waveguide. The modes shown in the dispersion diagram are the solutions of an eigenmode simulation for a sweep of the phase difference between the lattice boundary faces. Modes below the light line ( $\beta = 2\pi f/c$ ) are allowed to propagate, which shows that mode 8 is the groove gap waveguide mode. . . .	140
4.6	The magnitude of the complex electric field in a cross section of part of a GGWG. The field from the edge of the central groove decays by $\sim 30$ dB per row of nails. . . . .	141
4.7	A diagram showing the unit cell used to simulate ridge gap waveguide in HFSS and the resulting eigenmode dispersion diagram. . .	142
4.8	<i>Top:</i> a model of a ridge gap waveguide series resonator with a ridge of length 4.2 mm, width of 3.3 mm and height of 3.56 mm. The nail dimensions can be found in Fig. 4.4. The flat lid that sits on a $h = 10$ $\mu$ m spacer is omitted to show the internal structure of the resonator. <i>Bottom:</i> the simulated S-parameter spectrum of the model with PEC boundaries showing a resonance at $\sim 35$ GHz with $Q \sim 300$ . . . . .	143

4.9	<i>Top</i> : a model of a groove gap series resonator formed between two pins that act as impedance boundaries. The two square pins have a centre-centre separation of 6.5 mm, a height of 3 mm and a width of 1.5 mm. The flat lid is omitted. <i>Bottom</i> : the simulated S-parameter spectrum of the model with PEC boundaries showing a resonance at $\sim 34$ GHz with $Q \sim 400$ . . . . .	144
4.10	<i>Top</i> : a model of the three resonator structure combining GGWG and RGWG resonators. The two square pins have a centre-centre separation of 16.775 mm, a height of 3 mm and a width of 1.5 mm. The ridge is 4.2 mm long and 3.3 wide. <i>Bottom</i> : the simulated S-parameter spectrum of the model showing three resonances at $\sim 32.9$ , $\sim 33.8$ , and $\sim 34.2$ GHz with $Q \sim 2000$ , 700, and 1100, respectively. The field distributions of these modes are shown in Fig. 4.11. . . . .	145
4.11	The electric field vector plots and magnitude of the complex surface current of the modes that exist in the three resonator device shown in Fig. 4.10. The surface current of mode 1 shows that this mode is dominated by the dimensions and surface dynamics of the ridge and the complementary area of the flat lid above it (the lid is made transparent to show fields within). . . . .	146
4.12	The calculated resistance and reactance of the surface impedance as a function of frequency of a 20 nm thick NbTiN coating and bulk NbTiN at 1 K. The parameters used in the calculation are [55]: $\sigma_n = 0.55 \times 10^6$ , $T_c = 14.1$ K, $\Delta_0/kT_c = 1.86$ , $\xi_0 = 170$ nm, $l = 0.57$ nm. The London penetration depth with these parameters is calculated to be $\lambda_L \approx 250$ nm. . . . .	148

## LIST OF FIGURES

- 4.13 The simulated S-parameters of the pin-coupled RGWG resonator shown in Fig. 4.10 with two different NbTiN coatings: a coating of 1  $\mu\text{m}$ , which acts as bulk NbTiN, and a 20 nm thick NbTiN coating. For the latter case, an additional simulation is shown where the ridge-lid spacing has been increased to 20 nm which possesses a lower linear kinetic inductance fraction. The total quality factor,  $\omega_r/\kappa$ , of mode 1 is  $\sim 5,000$ , 43,000 and 13,000 moving from the upper to the lower plots. The other modes are have a Q of around 1,000. The KI fraction of each resonance is shown in Table 4.1. . . . . 150
- 4.14 The linear kinetic inductance fraction as a function of ridge-lid separation  $h$  for a 20 nm NbTiN ( $\lambda_L = 250$  nm) film and a 1  $\mu\text{m}$  NbTiN coating. The thick coating produces the same result as bulk NbTiN. The black crosses are the kinetic inductance fraction values of mode 1 from Tab. 4.1. . . . . 153
- 4.15 The theoretical critical current of a 3.3 mm wide and 20 nm thick NbTiN film against temperature. The following characteristics of NbTiN were used in the calculation  $T_c = 14.1$  K,  $\lambda_{\perp} = 3.13 \mu\text{m}$ ,  $\xi(0) = 8.4$  nm. The latter two were calculated using values from Hong *et al.* [55]. . . . . 156
- 4.16 The expected circulating current in the resonator as a function of input power at different coupling quality factors. The impedance of the resonator was set to  $Z_0 = 2 \Omega$  for simplification purposes, since the impedances was calculated to be in the range of 1.2 to 2.6  $\Omega$  for all the variations with the bulk and 20 nm NbTiN coatings as well as the 10  $\mu\text{m}$  and 20  $\mu\text{m}$  ridge-lid spacings. . . . . 158



4.17	The equivalent circuit model of a series $\lambda/2$ resonator coupled to input(output) port with impedance $Z_{\text{in}}(Z_{\text{out}})$ via a coupling capacitance $C_c$ . The total inductance and capacitance of the resonator is split up into an LC ladder that is $N$ cells (orange box) long where $N > 10$ per wavelength of the RGWG. The resonator is split into a geometric $L_g$ , and kinetic $L_k$ inductances as well as resonator capacitance $C_{\text{res}}$ . . . . .	162
4.18	The simulated nonlinear insertion loss at a number of input powers leading up to the point where the resonator bifurcates. This point presents itself when the resonance profile bends to produce a near discontinuous jump in transmission, which is around -38.5 dBm in this case. A scaling current of 1.3 A was set for this simulation. .	164
4.19	The parametric gain of a weak signal in the presence of a pump of different input power for a series pin-coupled RGWG resonator simulated with the HB simulation mode in ADS. The signal power is set to -110 dBm to ensure operation well below the compression point. A constant pump detuning of $f_p - f_s = 10$ kHz is used. The scaling current was set to 1.3 A. . . . .	165
4.20	The simulated signal gain for three different peak gain conditions and the dynamic range at each of these points. . . . .	167

## LIST OF FIGURES

- 4.21 The mechanical model of the Ka band RGWG resonator. The top shows the full resonator assembly including rectangular waveguide feeds and fasteners. It should be noted that the fasteners are all brass to avoid stray magnetic fields due to impurities in some grades of stainless steel. The bottom left part is referred to as the resonator body while the bottom right is resonator lid. Both of these part show the inner features of the resonator. The resonator was designed such that the ridge and top of the nails were flush with the outer rim to allow these to be polished prior to thin film coating. The footprint of both resonator parts is 65x40x10 mm. . 169
- 4.22 A photograph of one of five identical RGWG resonators that were machined from OFHC copper. Machining marks are visible along all of the surfaces. . . . . 171
- 4.23 An AFM 3D profile of a 30 by 30  $\mu\text{m}$  square in the middle of the ridge of the RGWG resonator. The post-processing on the raw data included levelling using mean plane subtraction and alignment of row. . . . . 173
- 4.24 An illustration of the Logitech PM5 polishing and lapping system. An abrasive slurry is drip-fed onto the rotating lapping pad during the polishing process. The lapping jig to which the sample is affixed is held in place by a motorised arm that sweeps across the radius of the lapping plate. The lapping jig is allowed to freely rotate via the bearing on the jig arm and the contact with the lapping plate [123]. . . . . 174

4.25	An illustration showing the two key mechanism in surface polishing. The first polishing stages are done via abrasive action using a slurry containing particulates such as alumina ( $\text{Al}_2\text{O}_3$ ) in multiple stages with particulates of decreasing size. The final polishing stage uses a suspension like colloidal silica ( $\text{SiO}_2$ ) via a CMP mechanism involving both mechanical polishing and chemical etching simultaneously [123]. . . . .	175
4.26	Photographs showing the progression of the polishing of the RGWG resonator using a two step process. From left to right: unpolished, post 6 $\mu\text{m}$ polish, post Col-K polish. . . . .	178
4.27	AFM images of the worst (left) and best (right) polished surface, where the surface roughnesses are 0.03 and 0.007 Ra, respectively.	178
4.28	A labelled photograph of the magnetron sputtering system at STFC Daresbury. Shown is the ultra high vacuum deposition chamber, which contains a heated and rotating sample jig. A separate loading chamber is separated by a pneumatic gate valve, which separates the two chambers during a deposition. Both chambers have separate turbo molecular pumps that use scroll pumps for backing. Multiple gas supplies are connected to gas flow meters and controllers which are operated via a set of panels below the deposition chamber. Three water cooled magnetrons are connected to the deposition chamber, which are powered by a pulsed DC sources and controlled via a separate control panel. . . . .	181

## LIST OF FIGURES

- 4.29 A labelled photograph of the loading chamber of the sputtering system. The chamber is opened by removing the chamber window after which vertical magnetic sample selection arm can be used to move the sample holder in order for a separate magnetic sample loading arm to move below a chosen sample plate. The plate is lowered onto the arm after which it can be moved into the deposition chamber. . . . . 182
- 4.30 Photographs showing the deposition of the Nb spacer layers. The deposition rate of this was  $\sim 1\mu\text{m}/\text{hour}$ . The top left panel shows the three bodies on sample plates that had their internal structure masked off using stainless steel sheet masks that were cut and bent into place such that they were secured in place. Small pieces of sapphire substrate were also mounted on the sample plates to be used for film property characterisation. The top right panel shows the one of the bodies during the deposition as seen through a window with a shutter where the blue hue is the due to the krypton plasma. Bottom left shows the sputtering result on one of the bodies that was had some unintentional residue left over from the cleaning and drying process. Bottom right panel shows a coating with a visibly smoother finish, where the outer edges appear darker due to smoother Nb coating that resulted from a better polish on the edges of the body. . . . . 186

4.31	Photographs showing the deposition of the 1 $\mu\text{m}$ NbTiN layer on one device or a mutli-layer film structure composed of 2 $\mu\text{m}$ NbTi layer, 30 nm of AlN insulator and a 20 nm coating of NbTiN. The deposition rate of AlN was $\sim 90$ nm/hour, while NbTiN had a rate of 180 nm/hour. The top left panel shows the lid and body placed on a single deposition plate to deposit the same film(s) on both bodies simultaneously. The outer perimeter is masked off using a stainless steel mask to protect prevent the spacer layer from any further coating. The top right panel shows the deposition taking place where the pink hue is the due to the Kr and N <sub>2</sub> plasma. Bottom left two panels show the sputtering result on one of the the thick NbTiN layer and the multi-layers. The golden hue is characteristic of a NbTiN coating while the darker grey is the Nb coating. . . . .	188
4.32	Cryogenic 4 point probe measurements that show the resistance against temperature of the films that were deposited on sapphire samples simultaneously to those shown in Fig. 4.30 and 4.31 In the multi-layer measurement 3 separate critical temperature were present while cycling up and down in temperature. . . . .	190
4.33	The surface resistance as a function of frequency for a 20 nm thick NbTiN film at 1 and 4 K. The material properties can be found by following the caption of Fig. 2.7. . . . .	192
4.34	The preparation of a polished RGWG resonator for room temperature measurement with an aluminium foil spacer. The standard supermarket foil which was measured to have a micrometer screw gauge to have a consistent thickness of 13 $\mu\text{m}$ and was cut around a copper stencil that is shown in the lower left panel. The coaxial to rectangular waveguide transition were used to connect the resonator to the VNA. . . . .	194

## LIST OF FIGURES

4.35	Comparison of the room temperature S-parameters of the polished copper resonator with a $13\text{ }\mu\text{m}$ aluminium foil spacer to an equivalent HFSS simulation. The HFSS simulation used an imported CAD model that is shown in Appendix A.2 with the same $13\text{ }\mu\text{m}$ spacer. The bandwidth shown covers all 3 structure resonances. . . . .	195
4.36	Room temperature measurement of $1\text{ }\mu\text{m}$ NbTiN coated RGWG resonator with a design spacer layer of $h = 6\text{ }\mu\text{m}$ . The spacer layer has some build up which is likely to affect the actual ridge to lid separation and the parallelism of the two surfaces. . . . .	196
4.37	Photographs of the thick film device measurement in the cryostat at 4 K. Left panel shows the disassembled resonators while the right panel shows the resonator mounted to the rectangular waveguide feeds. The resonator was connected to the 4 K stage via a copper braid which provided a medium thermal link and allowed the temperature of the resonator to be changed with a single $330\text{ }\Omega$ heater. The feeds were thermally isolated at each temperature stage using thermal breaks that incorporate a hollow gap between waveguide flanges and are supported with carbon fibre tubes which have a low thermal conductivity (see Section 3.2.2)) . . . . .	197
4.38	Cryogenic low power S-parameters at 4 K base temperature of the RGWG resonator shown in Fig. 4.37 with a $1\text{ }\mu\text{m}$ coating of NbTiN on the inner surfaces. The spacing between the ridge and lid is set by the deposited Nb spacer layer on the outer area of the body of the resonator (the grey metallic finish), which resulted in a spacing of $6\text{ }\mu\text{m}$ . Overlaid are the simulations performed in HFSS with surface impedance of NbTiN at 4 K, which was calculated using the Zimmermann conductivity (see Fig. 4.12). . . . .	198

4.39	Left panel shows a close up of the build up on the spacer layer of the thick film device. The right panel shows the spacer after a rotary tool was used to remove the affected areas. In the process some nails at the edges of the device were damaged. The lower panel shows a microscope image of the surface of the ridge taken prior to the use of rotary tool, indicating that some coating is missing, which could have occurred during transport of the device.	200
4.40	Cryogenic low power S-parameters at 4 K base temperature of the thick film RGWG resonator after a part of the deposited spacer layer was removed as shown in Fig. 4.39. The HFSS simulation is the same as in Fig. 4.38. . . . .	201
4.41	A demonstration of the resonance finding routine for a spectrum of three resonances. The final weaker resonance is found in a subset of the data that has been manually trimmed to ensure better detection at temperatures closer to $T_c$ where this resonance gets even less shallow. Each resonance was fitted with a general Lorentzian function to extract the resonance frequency. . . . .	202
4.42	The fits of the fractional resonance shift with temperature of Eq. 4.15 of the three resonances present in the RGWG resonator with a $1\text{ }\mu\text{m}$ coating of NbTiN. Note that resonance 3 disappear is very poorly detected near the critical temperature due the onset of higher dissipation. . . . .	203
4.43	A photograph of the thin film device with a $20\text{ nm}$ NbTiN film, as well as a microscope image of the top of the ridge showing the quality of the surface. The ridge to gap spacing was set using a spacer deposition as well as an aluminium foil which produced a $5 + 13\text{ }\mu\text{m}$ ridge to lid spacing. . . . .	205

## LIST OF FIGURES

4.44	The measured and simulated S-parameters at 4 K of the thin film device with a total ridge to lid spacing of 18 $\mu\text{m}$ . The undulations in the measured insertion loss ( $S_{21}$ ) are likely due to a calibration issue. The resonance frequencies of the measured data should not be affected by the calibration. . . . .	205
4.45	The received power spectrum when two tones at 0 dBm (measured at the output of the VNA cables) were inserted with a 10 kHz spacing in the middle of resonance 3 of the thin film device shown in Fig. 4.44. . . . .	207
4.46	The measured S-parameters at 4 K of the RGWG resonator with the body of the thick film and the lid of the thin film device. The spacing was set by the deposited spacer layer only resulting in a ridge to lid spacing of 6 $\mu\text{m}$ . This can be compared to Fig. 4.40 since the same body and ridge to lid spacing was used. . . . .	208
4.47	The fractional frequency shift as a function of temperature of the mixed resonator being composed of the thick film body and thin film lid. The two resonances refer to those shown in Fig. 4.46. . .	208
4.48	The received power spectrum when two tones at 0 dBm were inserted with a 10 kHz spacing in the middle of resonance 1 of the mixed film device. Visible is a cascade of evenly spaced harmonics indicating non linear behaviour. . . . .	210



4.49	The fractional frequency shift against circulating current of resonance 1 of the mixed film device shown in Fig. 4.46. The input power which was measured at the input of the cryostat was converted to a circulating current using Eq. 4.10. This relied on the assumptions that the total $Q$ measured as the $-3\text{ dB}$ point of the resonance was limited by the coupling $Q$ such that $Q_c \sim Q_t$ , which was measured to be $\sim 1000$ . The impedance was calculated using Eq. 4.18 which was calculated to be near $1\ \Omega$ . $I_2$ was used to signify the second order scaling current which is identical to $I_*$ . . . . .	211
5.1	A RGWG model showing the central ridge of width $w = 0.5\text{ mm}$ in a groove of width $a = 2.54\text{ mm}$ and height $b = 1.27\text{ mm}$ , with 3 rows of pins with width of $0.5\text{ mm}$ and pin period of $1\text{ mm}$ . The pins and ridge are of the same height $d$ . The gap labelled $h$ is exaggerated to demonstrate how the 2 parts of the waveguide are joined together. In actuality, this gap is set to $5\ \mu\text{m}$ to provide a large kinetic inductance fraction. . . . .	224
5.2	Unit cells used in the HFSS eigenmode analysis to identify allowed propagation modes. The unit cell used to simulate the pin surface employed master and slave (coupled lattice) boundaries on the 2 pairs of horizontally opposing faces. The unit cells of the groove gap and ridge gap waveguide unit cells had 1 set lattice boundaries on the faces along the direction of propagation of the confined wave (in/out of page). Here, $d$ , $w_{\text{pin}}$ , $p$ are the pin length, width and period; $h$ is the hollow gap between the top of the pin and the opposing conducting sheet; $b$ is the separation between the two parallel surfaces of the structure and $a$ is the width of the groove in groove gap waveguide. $b$ and $a$ correspond to the short and long wall of Ka band rectangular waveguide, respectively. . . . .	226

## LIST OF FIGURES

- 5.3 The dispersion of the first 8 propagation modes of the eigenmode simulation of RGWG in HFSS with PEC boundaries using the model from Fig. 5.2c. The structure dimensions are outlined in Fig. 5.1. Mode 7 is the quasi-TEM mode possessing near linear dispersion across a 20 to 115 GHz band. Therefore, the phase constant,  $\beta$ , can be used interchangeably with the angular wavenumber  $\beta \equiv k = 2\pi/\lambda$ . . . . . 227
- 5.4 Real and imaginary components of the Zimmermann conductivity relative to the normal state conductivity of NbTiN at 4 and 1 K. The inset shows  $Re\{\sigma_{\text{zimm}}\}/\sigma_n$  at 1 K which varies on a much smaller scale. The parameters used for the calculation were adapted from [55, 132]:  $T_c = 15$  K,  $\Delta_0/k_bT_c = 1.86$ , BCS coherence length  $\xi_0 = 170$  nm, mean free path  $l = 0.57$  nm. . . . . 228
- 5.5 Surface impedance components of a 30nm NbTiN film with a typical normal state conductivity  $\sigma_n = 0.55 \times 10^6$  S m at 4 and 1 K. The inset shows the surface resistance at 1 K, which varies on a much smaller scale. The reactance curves at both temperatures are near identical showing that the reactance does not vary with temperature on this scale unlike the surface resistance. The common calculation parameters were identical to those used to produce Fig. 5.4. . . . . 229
- 5.6 A model of a 10 mm long RGWG in HFSS used for a driven modal analysis with frequency dependent surface impedance boundaries. The light blue regions show the defined waveports of the structure. PEC boundaries are automatically applied to all outer surfaces. It was found that the impedance of the RGWG mode with  $w = 500$   $\mu\text{m}$  was approximately  $6\Omega$ . . . . . 229

5.7	The transmission coefficient of the first 3 propagating modes in a simulation of the model in Fig. 5.6 with the surface impedance of a superconducting 30 nm NbTiN film from Fig.5.5 applied to all inner surfaces. Mode 1 (solid line) is the TEM RGWG mode of interest while the other two modes (dashed lines) are the modes propagating in the groove and nail regions. . . . .	230
5.8	The surface reactance of 30 nm NbTiN film found via the Zimmermann conductivity from Fig. 5.5 against the surface reactance calculated using the kinetic inductance Eq. 2.34 with $\lambda_L = 365$ nm. . . . .	231
5.9	The kinetic inductance fraction scaling with the size of gap, $h$ , at different film thickness. The thin film coating is present on both the top and bottom surfaces meaning that the kinetic inductance of both of these is included in the calculation. At the design values of $t = 30$ nm and $h = 5$ $\mu$ m, $\alpha_k \approx 0.64$ . . . . .	233
5.10	The critical current of a 30 nm thick NbTiN strip as a function of width, $w$ , at 3 selected temperatures. Assumptions include pristine film edges and a width $w > \lambda_{\perp}$ . The values used for this calculation were $\lambda_L(0) = 365$ nm, $\xi(0) = 9$ nm, and $T_c = 15$ K. Three possible operating temperatures are shown with 1 K being a likely candidate for W band operation due the significantly better dissipation than at 4 K (see Fig. 5.5) and more accessible cooling capability than 20 mK. . . . .	234
5.11	A schematic of a section of the ridge in a dispersion engineered RGWG using design principle from [61]. The physical width of the main line is 500 $\mu$ m, while the repeating perturbations are 650 $\mu$ m wide, and $\lambda_{per}/20 = 25$ $\mu$ m long. The separation of loading mid-points is $\lambda_{per}/2 = 250$ $\mu$ m. . . . .	237

## LIST OF FIGURES

- 5.12 An equivalent circuit model of  $\lambda_{\text{per}}/2$  cell showing an unperturbed and perturbed section of the RGWG. The impedances of the main line and perturbed sections were chosen to be  $Z_0 \sim 6 \Omega$  and  $Z_1 \sim 4.75 \Omega$ , respectively. The kinetic inductance contribution of two surfaces coated with 30 nm of NbTiN ( $\lambda_L \sim 365 \text{ nm}$ ) was included in the impedance calculation. A conductor spacing of  $h = 5 \mu\text{m}$  was chosen, which resulted in  $\alpha \sim 60 \%$ . This impedance were confirmed in HFSS simulations. The corresponding equivalent circuit parameters were  $L_{m,0} \sim 12.5 \text{ nH m}^{-1}$ ,  $L_{g,1} \sim 9.5 \text{ nH m}^{-1}$ ,  $L_{k,0} \sim 22 \text{ nH m}^{-1}$ ,  $L_{k,1} \sim 17 \text{ nH m}^{-1}$ ,  $C_0 \sim 0.9 \text{ nF m}^{-1}$ ,  $C_1 \sim 1.1 \text{ nF m}^{-1}$ . The scaling current was chosen to be 50 mA as discussed in Section 5.2.3. . . . . 239
- 5.13 Transmission coefficient and effective dispersion from a simulation of 900  $\lambda/2$  dispersion engineered RGWG cells in ADS, corresponding to a physical propagation length of 25 cm. The first 2 stopbands at  $f_{\text{per}} \sim 95 \text{ GHz}$  and  $2f_{\text{per}} \sim 190 \text{ GHz}$  are shown. The second stopband would be outside of the single-mode bandwidth of the RGWG but appears in the lumped element representation since these transmission line effects are not accounted for in the equivalent circuit model. The unperturbed dispersion,  $k_0$ , was found by fitting a second order polynomial to the perturbed dispersion,  $k$ . . 240

5.14	The simulated signal gain using the ADS method (solid) and solutions of the CMEs (dashed). The pump power in ADS was set to -9 dBm and was positioned at 93 GHz, while the signal was at -80 dBm to avoid significant depletion of the pump tone as a result of the mixing. The CME solution [92] uses the dispersion properties extracted from the 900 cell LSSP simulation to calculate the phase mismatch between the 3 involved tones. Here, the calculated CME gain that fits the ADS gain corresponds to a $I/I_* \sim 0.075$ compared to $I/I_* \sim 0.09$ in ADS. . . . .	241
5.15	A plot showing the effect of dispersion engineering on the total phase mismatch $\Delta k$ . The linear phase mismatch, $\Delta k_L$ , represents the anomalous dispersion introduced via dispersion engineering and is calculated using the simulated dispersion of the $450\lambda$ dispersion engineered RGWG. The pump is at the same frequency and power as in Fig. 5.14. $\Delta\theta_{NL}$ shows the phase shift that needs to be compensated by the anomalous dispersion in order to achieve total phase matching, $\Delta k \approx 0$ and exponentially scaling gain. . . .	245
5.16	Examples of patterned traces that would reduce the phase velocity of a propagating tone within a transmission line. Metallised parts are shown in black. These patterns would be etched into the thin superconducting coating on a flat silicon chip of the silicon micro-machined variant of the RGWG TWPA. Milling this structure in a metal machined variant would not achieve the desired effect on the reduced phase velocity due to the continuity of the superconducting coating. (a): a fishbone pattern that has increased capacitance due to the proximity of the trace fingers to those of the ground plane. (b): a meandered trace that would increase the inductance via the self inductance of the trace. . . . .	248

## LIST OF FIGURES

A.1	The equivalent circuits of the pin-coupled RGWG resonator used in the S-parameter, LSSP, and HB simulations. The HB simulation used a multi-tone source for input and 377 Ohm termination for the output. . . . .	252
A.2	The LSSP simulation setup applied to the circuits shown in Fig. A.1 and example result screen. . . . .	253
A.3	The HB simulation applied to the circuits shown in Fig. A.1 as well as the example output for at a single pump power and frequency.	254
A.4	A figure explaining the use of the <i>Mix()</i> function and an example gain curve that makes use of this to identify the signal tone. . . .	256
A.5	The amplifier compression point analysis using the HB simulation mode and a parameter sweep to sweep the signal input power. The parameters in the top panel are used to produce the dynamic range plot in the lower panel. . . . .	257
A.6	Pages 1 and 2 of the technical drawings submitted for the manufacture of the Ka band pin-coupled RGWG resonator. . . . .	259
A.7	Pages 3 and 4 of the technical drawings submitted for the manufacture of the Ka band pin-coupled RGWG resonator. . . . .	260
A.8	Page 5 of the technical drawings submitted for the manufacture of the Ka band pin-coupled RGWG resonator. . . . .	261
B.1	The procedure for nesting elements of an LC ladder into unit cells.	264
B.2	A further nesting of cells into groups of 10 cells. A symbol is defined to represent 10 cells. . . . .	265
B.3	The circuit used to simulate the $450\lambda_{\text{per}}$ RGWG TWPA described in Section 5.3. . . . .	266
B.4	The large signal s-parameter simulation setup that was used to simulate the linear and nonlinear S-parameters of the periodically loaded RGWG. . . . .	267

B.5	The linear S-parameters that are simulated using the circuit shown in Fig. B.4. . . . .	268
B.6	The harmonic balance simulation setup used to simulate the gain of the W-band RGWG TWPA. . . . .	269

# The University of Manchester

ABSTRACT OF THESIS submitted by Danielius Banys

for the Degree of Doctor of Philosophy and entitled

“High frequency parametric amplification based on the non-linear dynamics of superconductors”

August 2022

Low noise amplifiers (LNAs) are critical components of the receivers that are used for radio and microwave astronomy. In a typical direct amplification system, the radiation that is collected by an antenna and focussed by a series of mirrors must be amplified by a chain of amplifiers within the receiver prior to any further processing. The noise and gain performance of the first LNA in this amplifier chain has the most significant impact on the total signal to noise ratio of the output signal, which can greatly influence the quality and speed at which the observatory can collect its data. Typically, high electron mobility transistor (HEMT) based LNAs have been used for this purpose but these are only suitable for applications below around 100 GHz since their gain and noise performance becomes inadequate at frequencies above this mark. For higher frequency applications, a receiver comprised of a superconducting mixer as the first component is employed to down convert the signal to a lower frequency at which an LNA with a significantly better gain and noise performance can be used. The best of these transistor based LNAs have gains of 20 dB and noise at around 5 to 10 times the quantum noise limit over up to an octave of bandwidth up to 20 GHz.

In the last decade, significant development has been carried out on parametric amplifiers (paramps) that make use of nonlinear inductance of Josephson junctions or the kinetic inductance of thin superconducting films. These types of amplifiers have been demonstrated to show high gain over multiple octaves of bandwidth when engineered into travelling wave structures with noise performance nearing the quantum limit. Resonant paramps operate over a narrow bandwidth and routinely reach gains of over 20 dB with noise performance at the quantum limit. Most of this paramp development has been focussed on frequencies below 30 GHz where the dielectric loss of the substrate, and the losses of the necessary interconnects and transitions can be managed. However, if such paramps could be realised at frequencies of over 100 GHz with a gain of over 20 dB and noise performance near the quantum level over a similar bandwidth of operation as the best mixer and HEMT LNA pair (which are predominantly limited by the performance of the LNA) then these paramps could significantly improve the overall performance of the receiver. In addition when considering



operation at 4 K there is potential of reducing power dissipated by these paramp at the coldest temperature stages of the receiver which may allow for an increase in the overall available cryogenic budget.

This project aims to demonstrate parametric amplification using transmission lines that can be scaled to hundreds of GHz while maintaining low losses. Structures such as circular waveguide and ridge gap waveguide are used to demonstrate Josephson and kinetic inductance type paramps, respectively. Initially narrow-band resonant amplifier at 30 GHz are demonstrated, followed by a description of the design of a wide band kinetic inductance variant with ridge gap waveguide operating at a bandwidth of 75 to 110 GHz. An additional goal of this project and thesis is to provide a practical guide for future paramp designers that includes the fundamental theory of superconductivity and parametric amplification, simulation methods of superconducting devices in 3D electromagnetic and 2D circuit solvers, as well as paramp fabrication and cryogenic testing techniques.

# Declaration

No portion of the work referred to in this thesis has been submitted in support of an application for another degree or qualification of this or any other university or other institution of learning.

# Copyright

The author of this thesis (including any appendices and/or schedules to this thesis) owns certain copyright or related rights in it (the “Copyright”) and he has given The University of Manchester certain rights to use such Copyright, including for administrative purposes.

Copies of this thesis, either in full or in extracts and whether in hard or electronic copy, may be made **only** in accordance with the Copyright, Designs and Patents Act 1988 (as amended) and regulations issued under it or, where appropriate, in accordance with licensing agreements which the University has from time to time. This page must form part of any such copies made.

The ownership of certain Copyright, patents, designs, trademarks and other intellectual property (the “Intellectual Property”) and any reproductions of copyright works in the thesis, for example graphs and tables (“Reproductions”), which may be described in this thesis, may not be owned by the author and may be owned by third parties. Such Intellectual Property and Reproductions cannot and must not be made available for use without the prior written permission of the owner(s) of the relevant Intellectual Property and/or Reproductions.

Further information on the conditions under which disclosure, publication and commercialisation of this thesis, the Copyright and any Intellectual Property and/or Reproductions described in it may take place is available in the University IP Policy (see <http://documents.manchester.ac.uk/DocuInfo.aspx?DocID=24420>), in any relevant Thesis restriction declarations deposited in the University Library, the University Library’s regulations (see <http://www.library.manchester.ac.uk/about/regulations/>) and in the University’s policy on Presentation of Theses.

# Acknowledgements

This PhD project could not have developed in the way that it has without the input and assistance of the many colleagues, collaborators, and friends that all deserve their own individual acknowledgement. I would like to provide at least a short word on most of the people that have influenced me and/or my project during these 4 exciting years of research.

I will begin by acknowledging my core research group. Mark McCulloch has provided completely invaluable support for the whole duration of my PhD - being there for every brain storming session, as well as every success and failure. Simon Melhuish has answered so many of my questions on cryogenics and ensured I knew how to keep our cryo hardware running. Vic Haynes has started me with the necessary mindset for experimental research in the amazing 2 months that we worked together setting up his laboratory. Andrew May has provided continued support and ideas in the lab while also aiding in the relationships with key external collaborators. Thomas Sweetnam and Valerio Gilles were fantastic lab mates that have helped reduce my workload by taking over some of my project that will hopefully lead to even more new and exciting ideas. My main supervisor Lucio Piccirillo has had an immense influence in my development as an independent researcher, providing me with opportunities to take the lead while keeping me on track when I veered off target.

I want to thank my co-supervisory teams led by Danielle George (ARIG) and Thomas Thomson (NEST) who have both provided invaluable discussions, opportunities and monetary support for my project. In the ARIG group I received

continuous support from Gary Fuller, William McGenn and Claudio Jarufe. In the NEST group, I must thank Alex Lincoln, Charley Bull, William Griggs and Harry Waring for the help over the years with training and measurements in clean rooms.

I cannot thank enough the staff at the Schuster machining workshop of the University of Manchester who did not turn me away when I would come to them with last minute part manufacturing requests. The work that they have done for me has been the foundation to nearly every project I undertook during my PhD. In addition, the help of the amazing people at STFC Daresbury laboratories cannot be overstated. Andrew May who made sure I gained access to the facilities, and Reza Valizadeh with his support staff who not only took me in during their tight work schedules but also spent time to prepare, modify the equipment that I needed and helped me throughout the whole thin film coating procedure.

The years spent working on my PhD would not have been anywhere near as precious and memorable without the amazing friendships that I have had the opportunity to build. The office was such an incredible environment thanks to Nialh, Shankar, Eunseong, Valerio, Tom S, Luke, Tom H, Dom, Susanna, Jakob, and Edoardo. Having made it through a world pandemic and being locked up at home with Eunseong, Adrian and Harry left nothing but great memories who made home feel like a true sanctuary. I would not have managed to keep my sanity during the pandemic without my closest friends Nialh, Adrian, Eunseong, Harry, Shankar, Guuske, Valerio, Tom S and Manish. I am truly thankful to you all for having had the opportunity to build these friendships that will hopefully last a whole life time.

The one constant in life was the full support of my mum, dad and sister who have been there for me every step of the way. They have done everything in their power so that I could get the education that I wanted and I cannot thank them enough for guiding me to become the person that I am today.

# Supporting Publications

## **Parametric Amplification at Ka Band via Nonlinear Dynamics in Superconducting 3D Cavities**

**Banys, D.**, McCulloch, M. A., Azzoni, S., Cooper, B., May, A.J., Melhuish, S. J., Piccirillo, L., Wenninger, J., 2020, Journal of Low Temperature Physics. Vol 200. doi: 10.1007/s10909-020-02439-w

## **Development of a sorption-cooled continuous miniature dilution refrigerator for 100 mK detector testing**

May, A. J., **Banys, D.**, Coppi, G., Haynes, V., McCulloch, M. A., Melhuish, S. J., Piccirillo, L., Wenninger J., 2019 IOP Conference Series: Materials Science and Engineering. Vol 502. doi: 10.1088/1757-899x/502/1/012135

## **Millimetre Wave Kinetic Inductance Parametric Amplification using Ridge Gap Waveguide**

**Banys, D.**, McCulloch, M. A., Gilles, V., Piccirillo, L., Sweetnam, T., 2022, Journal of Low Temperature Physics. Vol 209. doi: 10.1007/s10909-022-02859-w

## **Simulating the behaviour of travelling wave superconducting parametric amplifiers using a commercial circuit simulator**

Sweetnam, T., **Banys, D.**, Gilles, V., McCulloch, M. A., Piccirillo, L., 2022, IOP Superconductor Science and Technology. Vol 35  
doi: 10.1088/1361-6668/ac850b

## **Parametric amplification via superconducting contacts in a Ka band bulk pillbox cavity**

Gilles, V., **Banys, D.**, McCulloch, M. A., Piccirillo, L., Sweetnam, T., 2022, Journal of Low Temperature Physics. doi: 10.1007/s10909-022-02891-w

# Chapter 1

## Introduction

### 1.1 Science Case

The science that can be achieved by a given astrophysics instrument is fundamentally limited by the performance of the components that make up its receiver. More specifically, many such instruments require low noise amplification of weak signals, usually in a chain of amplifiers, in order to increase their overall signal to noise ratio (SNR), which allows for the signals to be interpreted by room temperature electronics in preparation for further analysis. This is particularly important in radio and millimetre wave observatories, where cryogenic amplifier chains are used in their receivers. These receivers are positioned at a specific focal point of a satellite dish or large antenna that are pointed at a particular target to maximise the collected radiation. The performance of the first amplifier in this amplification chain is the most critical in determining the overall signal-to-noise ratio of the output signal. Often, the noise of an amplifier is given in terms of noise temperature,  $T_N$ . Considering an ideal amplifier with gain  $G$  and bandwidth  $B$ , the equivalent noise temperature can be calculated from the output noise power  $N_o$  using the relation given [1] by

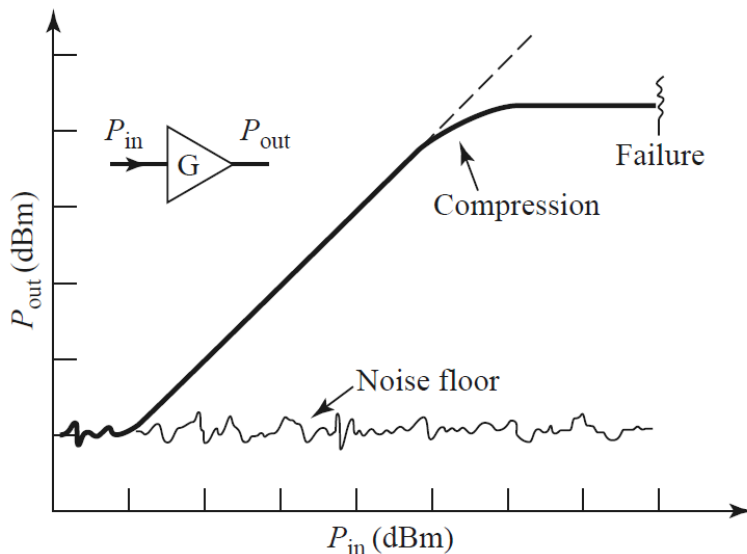


Figure 1.1: A figure showing the dynamic range of an amplifier with a gain  $G$  [1]. The minimum signal power that can be amplified is defined by the noise floor of amplifier and the highest power is defined by the compression point at which the gain of the amplifier stops scaling linearly with input power.

$$T_N = \frac{N_o}{GkB} \quad (1.1)$$

where  $k$  is the Boltzmann constant. The nature of  $N_o$  varies significantly with different amplifier architectures, materials and operating temperatures. In an amplifier chain the contribution of each amplifier to the total system noise temperature,  $T_{\text{sys}}$ , can be expressed by the Friis formula for noise

$$T_{\text{sys}} = T_1 + \frac{1}{G_1}T_2 + \frac{1}{G_1G_2}T_3 + \dots + \frac{1}{G_1G_2\dots G_{n-1}}T_n, \quad (1.2)$$

where  $T_n$  and  $G_n$  with  $n = \{1, 2, \dots, n\}$  is the noise temperature and gain of each amplifier in the chain. Eq. 1.2 shows that total noise of the chain is linearly proportional to the noise of the first amplifier and the gain of this amplifier suppresses the noise contributions of any subsequent amplifiers.

A low noise amplifier possesses other figures of merit in addition to the gain and noise that must be considered, which are the bandwidth, dynamic range and



operating temperature. The bandwidth of a conventional LNA is usually limited by the characteristics of the transmission lines upon which the amplifier is based as well as the quality of the impedance matching of the elements within the amplifier and the transitions to the in/output lines. Fig. 1.1 shows an illustration of the scaling of an output power of a signal with input power for an amplifier with a gain  $G$  up the point of compression. At this point the gain of the amplifier begins to drop and is defined as the power at which the gain drops by 1 decibel. The dynamic range is defined as the power range from the lowest signal power that can be amplified, being of a higher power than the added noise of the amplifier, to the 1 dB compression point where the amplifier is no longer able to amplify the signal due to a number of possible effects such as the onset of higher dissipation. The operating temperature is often set by considering a trade-off between the noise requirements of the instrument and the total cooling power available. In cases where superconducting amplifiers are used the operating temperature is usually some fraction of the critical temperature of the superconductor to manage dissipative losses.

Receivers in radio and mm-wave astronomy commonly use high electron mobility transistor (HEMT) based LNAs amplifiers [2]. Depending on the desired frequency of amplification the receiver has two typical arrangements, which are shown in Fig. 1.2. At frequencies under  $\sim 100$  GHz a direct amplification of the signal from the feedhorn can be used which is then down-converted by a mixer to some intermediate frequency (IF) (usually below 10 GHz) after which the signal is amplified further by an IF amplifier at a higher temperature. At frequencies higher than this, the gain and noise of these LNAs becomes inadequate to maintain a certain total receiver noise temperature target, in which case a superconducting mixer is used to initially down-convert the signal to a frequency in the range of 10 to 20 GHz. At this frequency the signal amplified by an LNA with appropriate gain and noise characteristics. The typical coldest stage on these higher frequency receivers is 4 K which is needed for the superconducting mixers

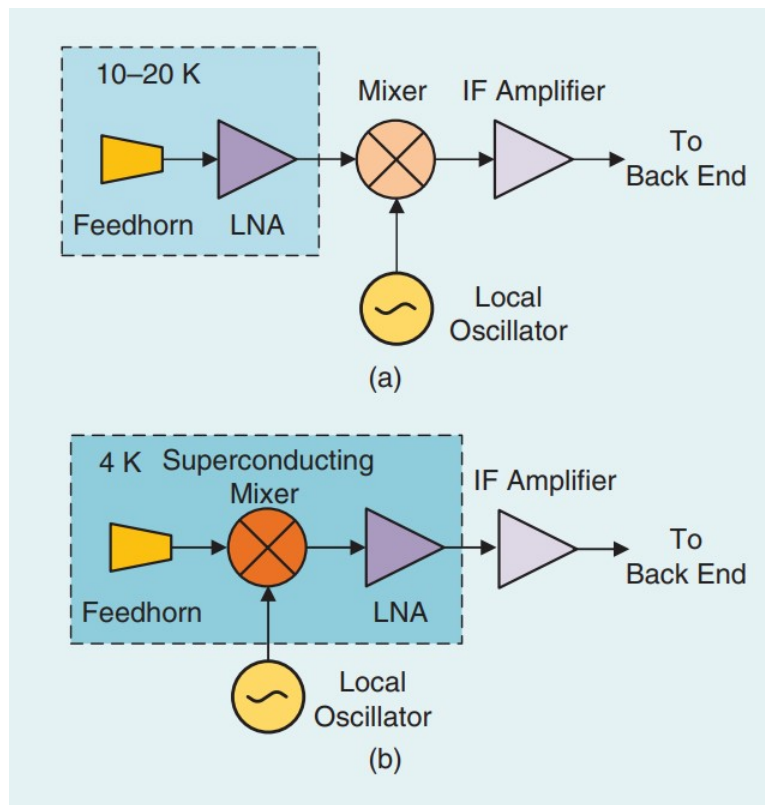


Figure 1.2: Schematics of two common amplification schemes used in radio or mm-wave receivers [2]. The scheme presented in the upper panel is most common for signals below 100 GHz where radiation captured by the feedhorn is amplified directly by an LNA which has a sufficiently high gain and low noise. Following this, the signal is down converted by a mixer to an intermediate frequency (IF) of  $< 10$  GHz and amplified by the IF amplifier. The lower panel shows a scheme used for signal over 100 GHz and up to around 1000 GHz, where LNAs with sufficient gain and low enough noise are not available. Here, a superconducting mixing is used instead to first down convert the signal from the feedhorn to then be amplified by a LNA at a considerably lower frequency followed by the same amplification by the IF amplifier.

to operate and for the LNAs to have adequate gain and noise, an example of such a receiver is shown in Fig. 1.3.

The minimum noise that is necessarily added by a linear amplifier is dictated by the Heisenberg uncertainty principle,  $\Delta n \Delta \phi \geq 1/2$ , which is rewritten here in terms of the uncertainty on the photon number  $\Delta n$ , and the phase  $\Delta \phi$ . For this condition to be satisfied at the amplifier's input and output, the amplifier must add some amount of noise itself. The minimum bound on this noise is

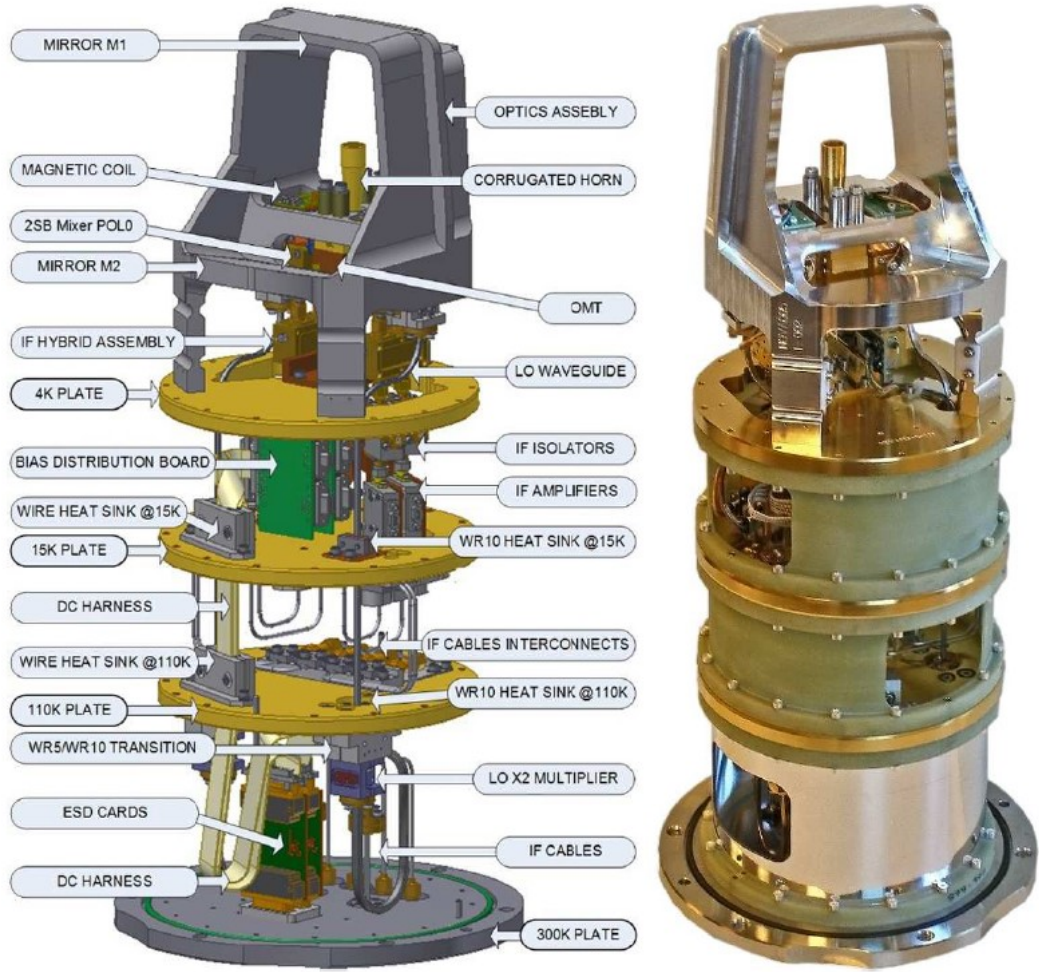


Figure 1.3: A labelled CAD model and photograph of an ALMA band 5 receiver covering a frequency range of 163-211 GHz [3]. This receiver uses a superconducting mixer scheme like the one described in the lower panel of Fig. 1.2.

known as quantum noise limit (QNL), which can be found [4] by comparing the minimum added noise power of a linear amplifier to an equivalent black body at temperature  $T_{n,\min}$ , resulting in the following expression

$$T_{n,\min} = \ln \left[ \frac{2 - 1/G}{1 - 1/G} \right]^{-1} \frac{hf}{k}, \quad (1.3)$$

where  $h$  is the Planck constant,  $f$  is the frequency of the signal, and  $G$  is the gain of the amplifier. In the high gain limit such that  $G \gg 1$ , Eq. 1.1 simplifies to

## 1: INTRODUCTION

$T_{n,\min} \approx hf/(k \ln 2)$ . It should be noted that the discussion of quantum noise has been simplified here, a more detailed discussions can be found in [5, 6]. Eq. 1.1 allows for the noise temperature of an amplifier to be compared to this fundamental limit. Indeed, the added noise level of the lowest noise HEMT LNAs is usually around 5 to 10 times the QNL [2] at a frequency of up to 100 GHz, with little improvement as the LNAs get cooled down closer to 1 K temperatures [7]. The noise performance of these HEMT LNAs seems to have reached their capability limit. However, development of these types of LNAs is continuing in their other characteristics such as a reduction in their dissipated power [8], improvements to their overall bandwidth [9], and improvements on the upper bound of their operating frequencies to reach hundreds of GHz [10].

In order to pursue further total receiver noise improvements alternative amplifier technologies began being investigated. The superconducting parametric amplifier is one such technology that promises high gain and quantum limited noise with a potential for broad bandwidth operation. Narrowband superconducting resonant parametric amplifiers (RPAs) often engineered from a nonlinear resonator have been routinely shown to achieve noise performance at the quantum level or even below with noise squeezing [11]. However, for broadband operation a travelling wave structure is required which is known as the travelling wave parametric amplifier (TWPA) where achieving quantum limited performance is more challenging. These challenges [12] arise due the the length of the structures involved which manifest themselves as difficulties in the form of impedance matching, harmonic management, transmission line and film uniformity (see Section 2.4.2). A TWPA based on the nonlinear kinetic inductance (KI) of superconducting thin films was first demonstrated in 2012 by Eom et al. [13] with over 10 dB of gain over a 4 GHz band centred around  $\sim 11.5$  GHz with an added noise as low as 2.3 photons, which is at 4.6 times the QNL. This noise performance is a result of the mechanism through which the amplification occurs, which is a photon mixing process in a transmission line with very low dissipation. Such low

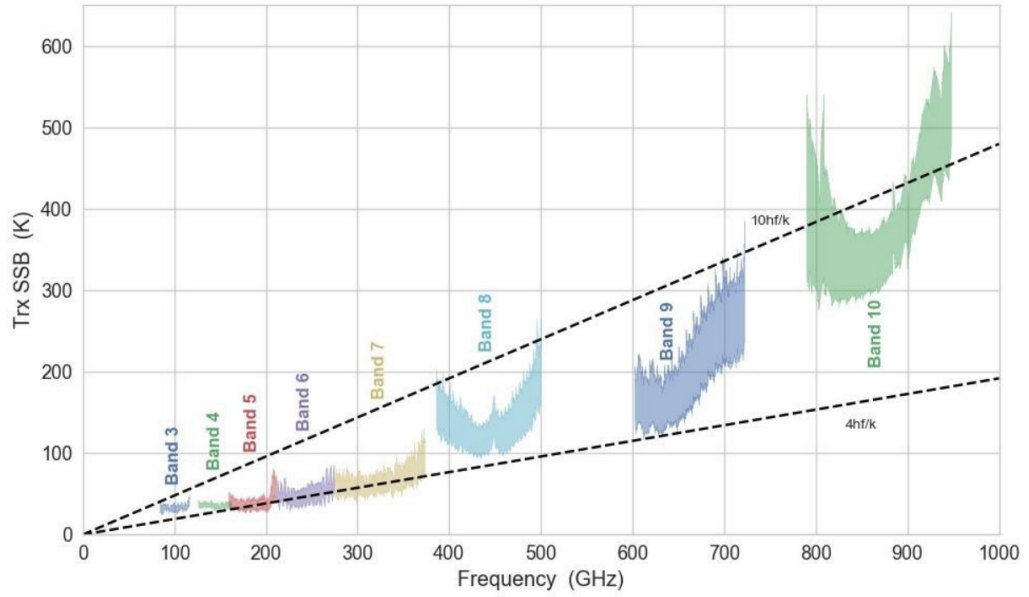


Figure 1.4: The receiver noise temperature of ALMA bands 3 to 10 where the black dashed lines represent 4 and 10 times the quantum noise limit [22, 2].

added noise values opened up a host of new applications in areas such as mm-wave astronomy for readout amplifiers of MKIDs[14]; electron spin resonance [15]; quantum computing – in the form of readout for spin qubits [16] or the readout of superconducting qubits [17]. Since then significant advancements have been made with the bandwidth and frequency operation of these KI amplifiers such as ultra broad band operation with a bandwidth of 3 to 30 GHz [18], as well as high frequency RPAs operating at 95 GHz [19]. It was also shown [20] that KI-TWPAs can be competitive to HEMT LNAs at 4 K in terms of gain and noise while outputting only a small fraction of heat compared to the transistor based LNA. This is an incredibly promising result for KI-TWPAs to replace the first amplifier in most applications that required operation at 4 K and below. A more detailed overview of parametric amplifiers will be provided in Section 2.4.2, which can also be supplemented with general reviews in literature [21, 12].

For mm-wave astronomy applications, the largest improvements in receiver noise performance would be accomplished at frequencies over 100 GHz for ob-

## 1: INTRODUCTION

servatories such as the Atacama Large Millimeter/submillimeter Array (ALMA) which has operational observational bands from 67 to 950 GHz as shown by 1.4 with additional planned bands (1 and 2) down to a 35 GHz [22]. Bands 3 to 10 are currently operational and are using receivers with SIS mixers as shown in the lower panel of Fig. 1.2. As can be seen by Fig. 1.4 the system noise at each band is targetted to be within the 4 to 10 times the quantum noise limit ( $\sim hf/k$ ). There is interest in the astrophysics community to improve these noise levels especially near the band 3 (100 GHz) and above band 7 (400 GHz) since the improved noise levels could allow for detection of weaker spectral lines through the improved SNR and allow for a reduced integration time which could improve the quality and/or reduce the time of a given observation survey. Indeed, KI-TWPAs have been investigated for an ALMA upgrade study [23], funded by the ALMA collaboration, as a replacement front end amplifier. The study concluded in 2013 with a design and simulation of a 55 – 175 GHz KI-TWPA which could cover ALMA bands 2 to 4, while a band 3 prototype was in the process of fabrication. However, it was decided that even though these types of amplifiers could be “ground breaking” for the observatory, the technology was not yet ready for adoption on a large scale due to the lower required operating temperature of 1 K, which would warrant significant changes to the cryogenic design of the receiver and uncertainties with device yield and gain ripples (see Section 2.4.4 for TWPA limitations). However, work on this subject had considerable promise even at that time which justified their further development, which is continuing to this day.

Instead, it was decided in ALMA to use a direct amplification system with ultra-wideband HEMT LNAs [9] for a combined band 2 + 3 specification which is planned for the frequency range of 67 to 116 GHz [24]. The current LNA specification [24] for this band includes a gain requirement of  $> 40$  dB and a noise temperature of  $< 23$  K at an operating temperature of 15 K and a compression point of  $-10$  dBm. For this specific application a replacement parametric am-

plifier would have to improve on some or all of these metrics in some meaningful way such as covering a larger bandwidth, lower noise levels, reduced heat output or a higher compression point while operating at least 1 – 4 K. This operating temperature requirement is there to minimise the changes needed in the cryogenic design of current receivers for such an experiment like ALMA.

Considering other astrophysics applications, these low noise KI-TWPAs can be critical where operation at the quantum noise level is necessary such as in the detection of axionic dark matter experiments [25, 26, 27, 28]. In addition these kinetic inductance structures are paving the way for new technologies such as compact on-chip Fourier transform spectrometers [29, 30, 31].

## 1.2 Project Objectives and Thesis Outline

The main mission of this PhD project is to push the upper boundaries of the operational frequency of superconducting parametric amplifiers with a particular interest in frequencies of 100 GHz and above. The reasoning for this mission is to improve the total system noise temperature of receivers in astrophysical observatories like ALMA without requiring significant change of the operating temperature capability of the current 4 K SIS mixer receivers. In addition, there should be limited change on the amplifier’s bandwidth, gain and dynamic range, with exceptions in the case of for significant improvement in one characteristic while slightly compromising on another such as much lower noise level but slightly reduced gain.

A paramp that would demonstrate the proof of principle for high frequency operation should amplify a signal with at least 10 dB of gain to overcome the noise contributions of the subsequent amplifier chain (see Eq. 1.2), which could improve the overall system noise temperature. This gain can be over a narrow band in an RPA which is more straightforward to design and fabricate compared to an electrically long TWPA, but the narrowband variant should be based on

## 1: INTRODUCTION

the same transmission line structure. The compression point of these paramps should be maximised by choosing a transmission line with dimensions that gives the largest critical current. The RPA has a compression point that is inherently smaller by orders of magnitude than the one of a TWPA based on a transmission line with equivalent dimensions. The RPA compression point decreases as the linewidth of the resonance increases, which means that the RPA is unlikely to be able to reach the dynamic range specification for an observatory like ALMA. However, the TWPA may be able to reach this specification which should be targetted for  $-10$  dBm [24].

During the course of this project two types of transmission lines were explored, namely circular waveguide which employed a Josephson nonlinearity that arises from the contact of two superconducting parts; and ridge gap waveguide (RGWG) which made use of the kinetic inductance nonlinearity of a thin NbTiN coating. These transmission lines were engineered into nonlinear resonators at 30 GHz as a step towards 100 GHz since these resonators are simpler structures to design, fabricate and test while being important demonstrators of narrowband parametric gain and allows for characterisation of the structure nonlinearity. The resonator work acted as a foundation for the design and simulation of a wideband TWPA based on the kinetic inductance of a thin film coated RGWG, with a bandwidth of 75 to 110 GHz (W-band). A design and simulation pipeline of such W-band KI-TWPAs with a periodically impedance loaded design is proposed with a discussion on the possible fabrication methods that can be used to realise this structure. Importantly, the techniques developed in the design, simulation, fabrication and testing of these parametric amplifiers aims to prepare future parametric amplifier designers with the theoretical understanding and toolkit needed to design their own high frequency variants based on the same transmission lines or other alternatives.

Following the introduction, this thesis is split into four main chapters. Chapter 2 will cover the foundations of superconductivity, including how Mattis-



Bardeen and Zimmermann conductivities of superconductors can be calculated, the Josephson and kinetic inductance nonlinearities that may be created with superconductors. This chapter will also contain the foundations of parametric amplification including the theory of RPAs and TWPAs. Chapter 3 will cover the cryogenic testing system that was used throughout this project, as well as description of a shorter piece of work on a resonant parametric amplifier based on the contact junction nonlinearities in circular waveguide resonators that resulted in one first author [32] and another co-authored publication [33]. Chapter 4 which is the largest chapter in the thesis which will cover the design, simulation, fabrication and testing of a kinetic inductance based RGWG resonator at  $\sim 30$  GHz which was designed to be used as an RPA. Chapter 5 will describe a design study that was published [34] of a TWPA based on a dispersion engineered RGWG structure. This work was developed in parallel with a publication by Sweetnam et al. [35] on the simulation of kinetic inductance TWPAs using a commercial circuit simulator.



## Chapter 2

# Superconductivity and Parametric Amplification

### 2.1 Introduction

Superconducting materials characteristically possess zero DC and a small AC resistance which makes them foundational to many low temperature and low noise electronics. Superconducting mixers and amplifiers rely on nonlinear elements within them to allow for the power transfer of the incident propagating wave to generated harmonics and mixing products. Superconductors can exhibit nonlinear behaviour in a number of ways including extrinsic nonlinearities via the introduction of structures such as Josephson junctions [36] or intrinsic nonlinearities in the form of the kinetic inductance of thin films [37]. Both types of nonlinearities possess an inductance that can be expressed nonlinearly with current (see Section 2.3). These reactive nonlinearities are very attractive since they do not inherently add any dissipation into the circuits in question.

These nonlinear elements can be used to create a nonlinear medium, which permits the transfer of energy between a strong pump tone to a much weaker signal, leading to parametric amplification. In order for significant power transfer

## *2: SUPERCONDUCTIVITY AND PARAMETRIC AMPLIFICATION*

to occur, sufficient interaction time is needed between these two tones and the nonlinear medium. There are two methods for increasing this interaction time: embedding the nonlinear medium within a resonant cavity or creating an electrically long nonlinear medium. The former leads to a resonant parametric amplifier (RPA) while the latter to a travelling wave parametric amplifier (TWPA). The interaction time of RPAs is proportional to the inverse of the linewidth of the resonant cavity upon which they are based but this comes at a cost of a limited bandwidth and low saturation power. In general, RPAs in their simplest form are the most straightforward implementations of superconducting parametric amplifiers since they are simple to fabricate due to their relatively short length without the need for any impedance engineering. TWPAs overcome the aforementioned bandwidth limitations since the nonlinear interaction is no longer constrained to a resonant cavity and the operational bandwidth is instead limited to the frequency range over which a phase-matching condition between the pump and signal tones can be maintained. However, TWPAs come with their own challenges such as more complex design, often needing dispersion engineering, and more complex fabrication of such electrically long structures as well as impedance matching difficulties to the feedline.

The superconducting resonators and transmission lines that these parametric amplifiers are based on require careful design and simulation prior to fabrication. Full 3D electromagnetic (EM) simulators can be used to simulate the linear structure properties such as the eigenmode frequencies, scattering matrices, couplings and quality factors. 2D circuit simulations can be used to simulate the nonlinear properties such as power dependent frequency shifts, harmonic generation, and parametric gain processes. In general the low surface dissipation of superconductors in 3D EM simulations can be approximated with perfect electrical conductor (PEC) boundaries. However, in structures where the surface inductance of the superconductor has a large contribution to the overall structure inductance the PEC approximated surface can provide inaccurate resonance

frequencies, impedances and couplings. This is because the PEC surface does include the contribution of this inductance to the overall surface reactance. Superconducting surfaces are not built-in by default to 3D EM simulators such as Ansys HFSS <sup>1</sup>. However, it will be shown in this chapter that a superconducting surface can be implemented via user-defined surface impedance boundaries that require the calculation of the complex conductivity of superconductors. The nonlinear parametric processes of these nonlinear structures cannot be simulated in 3D due to the lack of harmonic balance functionality.

A harmonic balance simulator is able to account for intermodulation (generation of harmonics as well as sum and difference tones) between different input tones due to nonlinear elements. This means that not only are circuit harmonics included in the simulation but also the harmonics or small-signal sidebands of each signal source (excitation). 2D circuit simulators such as Keysight's ADS <sup>2</sup> include harmonic balance functionality which allows for the nonlinear behaviour of a circuit to be simulated through an equivalent lumped element model of the structure with user-defined nonlinear components. As mentioned previously such circuit simulators can be used to simulate nonlinear parametric processes in resonators containing a few elements (see Chapter 4) but also electrically long nonlinear circuits containing hundreds of elements (see Chapter 5).

This chapter is split into 3 parts: superconductivity; superconducting nonlinearities; and parametric amplification. The first part of the chapter aims to cover the foundational topics needed to understand and simulate superconducting surfaces including a short history of the development of the theories behind superconductivity, which will be summarised using the work by Tinkham [36]. Using the methods set out Gao [38] and Aude [39], the complex conductivity of superconductors will be described from the Mattis-Bardeen theory [40] and then more generally using the Zimmermann theory [41]. These two complex

---

<sup>1</sup><https://www.ansys.com/products/electronics/ansys-hfss>

<sup>2</sup><https://www.keysight.com/us/en/products/software/pathwave-design-software.html>

conductivities will be compared, after which it will be shown how the complex conductivity can be used to calculate the surface impedance of superconducting surface. The second part of the chapter will be covering the nonlinearities that can be engineered from these superconductors including those based on Josephson junctions and the kinetic inductance of superconducting thin films. The third part of the chapter will focus on the theory behind resonant and travelling-wave parametric amplifiers, which makes use of the work done by Planat [42] as a guide.

## 2.2 Superconductivity

In order to understand the conductivity of superconductors and to derive the surface impedance it is instructive to cover a few historical developments of the leading theories in superconductivity [36]. The first hallmark of superconductors discovered by Kamerlingh Onnes [43] in 1911 was the complete disappearance of electrical resistance below a certain critical temperature  $T_c$ , i.e. the discovery of perfect conductivity. The second hallmark discovered was the Meissner effect in 1933 [44, 45] by Meissner and Ochsenfeld which presented itself as a complete expulsion of external fields from the superconducting material i.e. perfect diamagnetism.

The two hallmarks of superconductivity were described in 1935 by the London brothers [46] using two equations. The first of these equations was conceived by considering the electrons within a superconductor to be free and flowing without experiencing resistance while still being influenced by a standard Lorentz force  $F = m\partial\vec{v}/\partial t = e(\vec{E} + \vec{v} \times \vec{B})$ . Here,  $m$ ,  $e$ , and  $v$  are the electron mass, charge and velocity, while  $\vec{E}$  and  $\vec{B}$  are the electric and magnetic field, respectively. As a result of this force the electrons accelerate within the conductor. Assuming that the electrons are driven by only an electric field and using supercurrent density in the form  $J_s = -n_s e \vec{v}$ , the first of the London equations can be derived to become

$$\frac{\partial}{\partial t} \vec{J}_s = \frac{n_s e^2 \vec{E}}{m} = \frac{\vec{E}}{\mu_0 \lambda_L^2}, \quad (2.1)$$

where  $n_s$  is the phenomenological constant associated with the number density of electrons,  $\mu_0$  is the permeability of free space, and  $\lambda_L$  is the London penetration depth. The second London equation can be found by taking the curl of the first equation and applying Faraday's law,  $\vec{\nabla} \times \vec{E} = -\partial \vec{B} / \partial t$ , to obtain the following relation

$$\frac{\partial}{\partial t} \left( \vec{\nabla} \times \vec{J}_s + \frac{n_s e^2}{m} \vec{B} \right) = 0. \quad (2.2)$$

The London brothers recognised that due the Meissner effect constant nonzero solutions of this expression were not physical and so it was not only the derivative of Eq. 2.2 that must be zero but also the expression within the parentheses. This resulted in the second London equation which is given by

$$\vec{\nabla} \times \vec{J}_s = -\frac{n_s e^2}{m} \vec{B} = -\frac{1}{\mu_0 \lambda_L^2} \vec{B}. \quad (2.3)$$

The London penetration depth in Eq. 2.1 and 2.3 shows that an electromagnetic field actually penetrates into a superconductor by some distance  $\lambda_L$  – which is analogous to the skin depth of a normal conductor. The penetration depth at zero temperature is given by

$$\lambda_{L0} = \sqrt{\frac{m}{\mu_0 n_s e^2}}. \quad (2.4)$$

This penetration depth is an important scaling parameter for the kinetic inductance of thin films (see Section 2.3.2). The London equations are only valid where the local condition is satisfied, that is, that the electric field varies little within a radius of the mean free path,  $l$ .

In 1953 Pippard [47] introduced a coherence length,  $\xi$ , while proposing a non-local generalisation of the the London equations. This emperical non-local

equation is

$$\vec{J}_s(\vec{r}) = -\frac{3}{4\pi\xi_0\lambda_L^2} \int_V \frac{\vec{R}\vec{R} \cdot \vec{A}(\vec{r}')e^{-R/\xi}}{R^4} d\vec{r}', \quad (2.5)$$

where  $\vec{A}$  is the gauge invariant vector potential such that  $\nabla \cdot \vec{A} = 0$ ,  $\vec{R} = \vec{r}' - \vec{r}$ , and  $\xi$  is given by

$$\frac{1}{\xi} = \frac{1}{\xi_0} + \frac{1}{\alpha_p l}, \quad (2.6)$$

where  $\xi$  is the coherence length in the presence of scattering,  $\xi_0$  is the BCS coherence length of a pure metal with very little scattering, and  $\alpha_p$  is an empirical constant. The coherence length  $\xi_0$  is related [48] to the Fermi velocity  $v_0$  and the superconducting gap parameter at zero kelvin,  $\Delta_0$ , by

$$\xi_0 = \frac{\hbar v_0}{\pi \Delta_0}. \quad (2.7)$$

This coherence length can be considered as the minimum size of a Cooper pair as dictated by the Heisenberg uncertain principle. The coherence length of Eq. 2.7 was one of many results of the ground-breaking pairing theory of superconductivity that was produced by Bardeen, Cooper, and Schrieffer [48] in 1957. This BCS theory showed that even a weak attractive interaction between electrons, such as the one caused by second order electron-phonon interactions, causes an instability of the Fermi-sea ground state of the electron gas with respect to the formation of bound pairs of electrons occupying states with equal and opposite momentum and spin. These electrons were referred to as the famous Cooper pairs, which occupied a volume of radius  $\xi_0$ , and were the charge carriers that the supercurrent was composed of. One of the key results of this theory was that the minimum energy needed to break one of these Cooper pairs and create two quasi-particle excitations was given by  $E_g = 2\Delta(T)$ . The zero kelvin value of this energy was given by



$$E_g(0) = 2\Delta_0 = 3.528kT_c, \quad (2.8)$$

where  $k$  is the Boltzmann constant.

In 1950, seven years before the BCS theory, Ginzburg and Landau [49] introduced a complex pseudo wavefunction  $\psi$  as an order parameter in Landau's general theory of second-order phase transitions. This  $\psi$  describes the superconducting electrons, where their local density is described by  $n_s = |\psi(x)|^2$ . They also derived the following differential equation for  $\psi$  and using a series of expansion of the free energy in powers of  $\psi$  and  $\nabla\psi$  with expansion coefficients  $\alpha$  and  $\beta$  for  $\psi$  being small near  $T_c$ ,

$$\frac{1}{4m} \left( \frac{\hbar}{i} \nabla - \frac{2e}{c} A \right)^2 \psi + \beta |\psi|^2 \psi = -\alpha(T) \psi, \quad (2.9)$$

where  $m$  and  $e$  are the electronic mass and charge. The corresponding equation for the supercurrent was

$$\vec{J}_s = \frac{e\hbar}{i2m} (\psi^* \nabla \psi - \psi \nabla \psi^*) - \frac{2e^2}{mc} |\psi|^2 \vec{A}. \quad (2.10)$$

With this formalism the GL theory was able to address two features that were beyond the scope of the London theory: (1) non-linear effects of fields strong enough to change  $n_s$  and (2) the spatial variation of  $n_s$ . This allowed the handling of intermediate state of superconductors at a field  $H$  close to the critical field  $H_c$ , where superconducting and normal domains could coexist. In 1959 Gor'kov [50] showed that the GL theory was a limiting form of the microscopic theory of BCS, valid near  $T_c$ , in which  $\psi$  was directly proportional to the gap parameter  $\Delta$ . In physical terms,  $\psi$  can be thought of as the wavefunction of the centre-of-mass motion of the Cooper pairs.

The GL theory introduced a characteristic length, which is now usually called the GL coherence length

$$\xi(T) = \sqrt{\frac{\hbar^2}{4m\alpha(T)}}, \quad (2.11)$$

which characterises the minimal distance over which the wavefunction  $\psi(\vec{r})$  can vary. In a pure metal far below  $T_c$ ,  $\xi(T) \approx \xi_0$  but near  $T_c$  this coherence length diverges from  $\xi_0$  (which does not vary with temperature). The temperature dependence of  $\xi(T)$  can be related [36] to the BCS coherence length with

$$\xi(T) = 0.74 \frac{\xi_0}{\sqrt{1 - T/T_c}}, \quad \text{pure} \quad (2.12a)$$

$$\xi(T) = 0.855 \sqrt{\frac{\xi_0 l}{1 - T/T_c}}. \quad \text{dirty} \quad (2.12b)$$

where a superconductor is considered “dirty” when  $l \ll \xi_0$  and “pure” when  $l \gg \xi_0$ . This GL coherence length will be important when estimating the critical current in superconducting traces with non-uniform current distributions such as the ridge gap waveguide structures discussed in Chapters 4 and 5.

The discussed developments in superconductivity outline the relevant characteristics and length scales needed to understand the validity of the expressions for the complex conductivity of superconductors. This conductivity can be used to compute the bulk and thin film surface impedance of the superconductor which allows for the resistance and reactance of these coatings to be included in 3D EM simulations. In the following sections two types of complex conductivity of superconductors will be discussed and compared, after which the surface impedance will be calculated.

### 2.2.1 Mattis-Bardeen Conductivity

From the BCS theory, Mattis and Bardeen [40] have derived a non-local equation between the total current density  $\vec{J} = \vec{J}_n + \vec{J}_s$  and the vector potential  $\vec{A}$

$$\vec{J}(\vec{r}) = -\frac{3}{4\pi^2 v_0 \hbar \lambda_L^2} \int_V \frac{\vec{R} \vec{R} \cdot \vec{A}(\vec{r}') I(\omega, R, T) e^{-R/\xi}}{R^4} d\vec{r}', \quad (2.13)$$

where  $\xi$  is given by Eq. 2.6 with

$$\begin{aligned} I(\omega, R, T) = & -j\pi \int_{\Delta - \hbar\omega}^{\Delta} [1 - 2f(E + \hbar\omega)][g(E) \cos \alpha \Delta_2 - j \sin \alpha \Delta_2] e^{j\alpha \Delta_1} dE \\ & - j\pi \int_{\Delta}^{\infty} [1 - 2f(E + \hbar\omega)][g(E) \cos \alpha \Delta_2 - j \sin \alpha \Delta_2] e^{j\alpha \Delta_1} dE \\ & + j\pi \int_{\Delta}^{\infty} [1 - 2f(E)][g(E) \cos \alpha \Delta_1 + j \sin \alpha \Delta_1] e^{-j\alpha \Delta_2} dE \end{aligned}$$

and

$$\begin{aligned} \Delta_1 = & \begin{cases} \sqrt{E^2 - \Delta^2}, & \text{for } |E| > \Delta \\ j\sqrt{\Delta^2 - E^2}, & \text{for } |E| < \Delta \end{cases}, \Delta_2 = \sqrt{(E + \hbar\omega)^2 - \Delta^2}, \\ g(E) = & \frac{E^2 + \Delta^2 + \hbar\omega E}{\Delta_1 \Delta_2}, \alpha = \frac{R}{\hbar v_0}, \end{aligned}$$

where  $f(E)$  is the Fermi-Dirac distribution given by

$$f(E) = \frac{1}{1 + \exp(E/kT)}. \quad (2.14)$$

The function  $I(\omega, R, T)$  decays on a characteristic length scale  $R \sim \xi_0$ , which arises as a consequence of the superconducting electron density not being able to change considerably within distance of the coherence length [38].

The full Mattis-Bardeen expression in Eq. 2.13 can be simplified in the local regime where the local Ohm's law holds  $\vec{J} = \sigma \vec{E}$ . Here  $\sigma$  is the complex conductivity in the form  $\sigma = \sigma_1 - j\sigma_2$  that was first proposed by Glover and Tinkhman [52] to represent the superconducting state. The Mattis-Bardeen conductivity

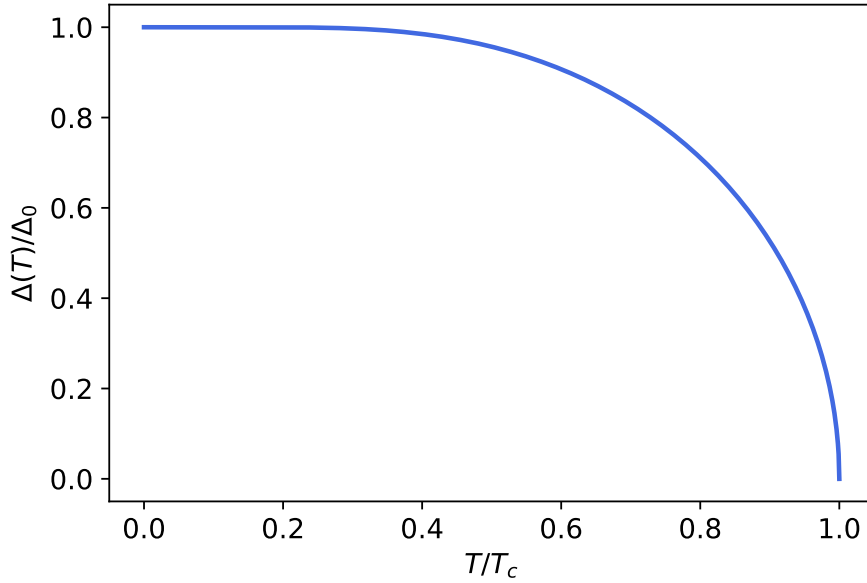


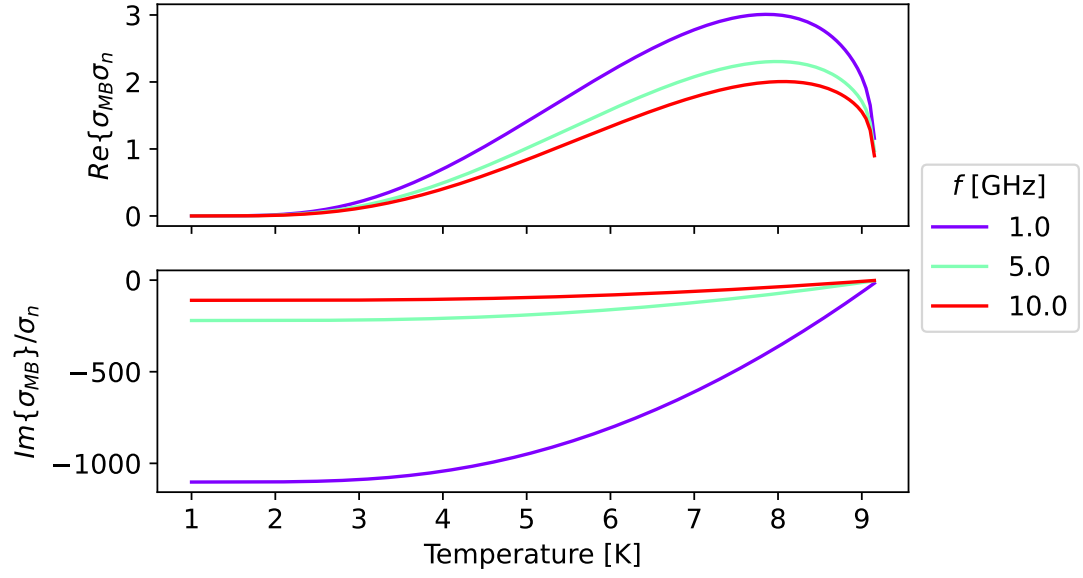
Figure 2.1: The reduced superconducting gap parameter as a function of reduced temperature found using a script adapted from “Supermix” [51]. Values for  $T/T_c < 0.18$  were found using Eq. 2.16.

can be expressed [40] in this form with the following

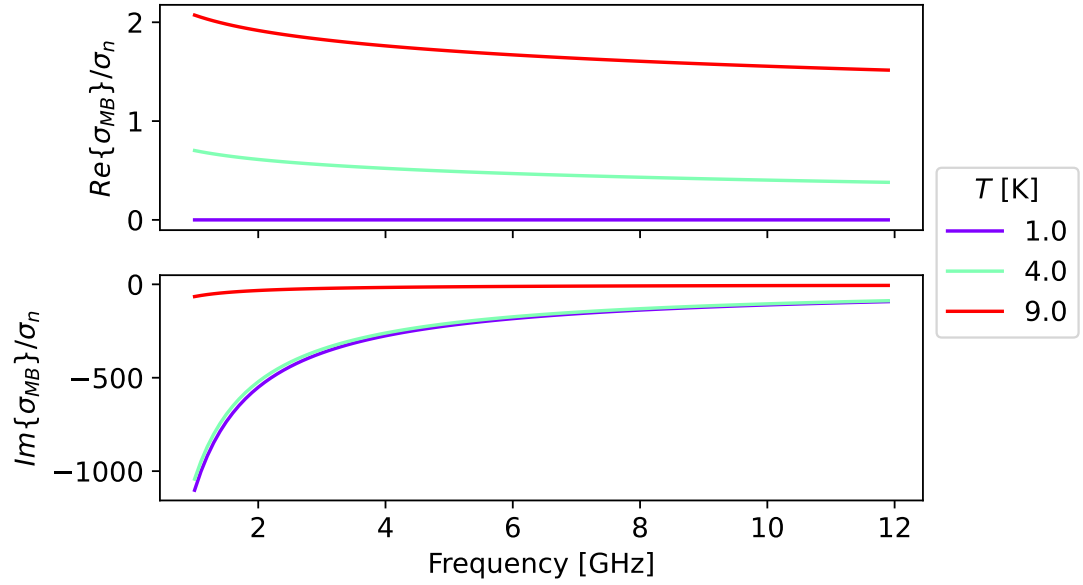
$$\begin{aligned} \frac{\sigma_1}{\sigma_n} = & \frac{2}{\hbar\omega} \int_{\Delta}^{\infty} dE \frac{E^2 + \Delta^2 + \hbar\omega E}{\sqrt{E^2 - \Delta^2} \sqrt{(E + \hbar\omega)^2 - \Delta^2}} [f(E) - f(E + \hbar\omega)] \\ & + \frac{1}{\hbar\omega} \int_{\Delta - \hbar\omega}^{-\Delta} dE \frac{E^2 + \Delta^2 + \hbar\omega E}{\sqrt{E^2 - \Delta^2} \sqrt{(E + \hbar\omega)^2 - \Delta^2}} [1 - 2f(E + \hbar\omega)], \end{aligned} \quad (2.15a)$$

$$\frac{\sigma_2}{\sigma_n} = \frac{1}{\hbar\omega} \int_{\max\{\Delta - \hbar\omega, -\Delta\}}^{\Delta} dE \frac{E^2 + \Delta^2 + \hbar\omega E}{\sqrt{\Delta^2 - E^2} \sqrt{(E + \hbar\omega)^2 - \Delta^2}} [1 - 2f(E + \hbar\omega)]. \quad (2.15b)$$

In order to find solutions to Eq. 2.15, an expression for  $\Delta(T)$  is required, which was calculated using a script borrowed from a subroutine of a package called “SuperMix” [51] – originally developed for SIS mixer design. This script



(a) Temperature variation



(b) Frequency variation

Figure 2.2: The real and imaginary part of the normalised Mattis-Bardeen conductivity in the local limit. Niobium is used as example with  $T_c = 9.2$  K and  $\Delta_0/kT_c = 1.83$ .

computes the reduced superconducting gap parameter  $\Delta(T)/\Delta_0$  as a function of  $T/T_c$ . It uses a table of experimentally measured values by Muhlschlegel [53] for  $T/T_c > 0.18$  to interpolate the reduced gap parameter. Values below that range are found [38] by using the following equation

$$\frac{\Delta(T)}{\Delta_0} \approx \exp \left[ -\sqrt{\frac{2\pi kT}{\Delta_0}} \exp \left( -\frac{\Delta_0}{kT} \right) \right] \approx \exp \left[ -\sqrt{3.562 \frac{T}{T_c}} \exp \left( -1.764 \frac{T_c}{T} \right) \right] \quad (2.16)$$

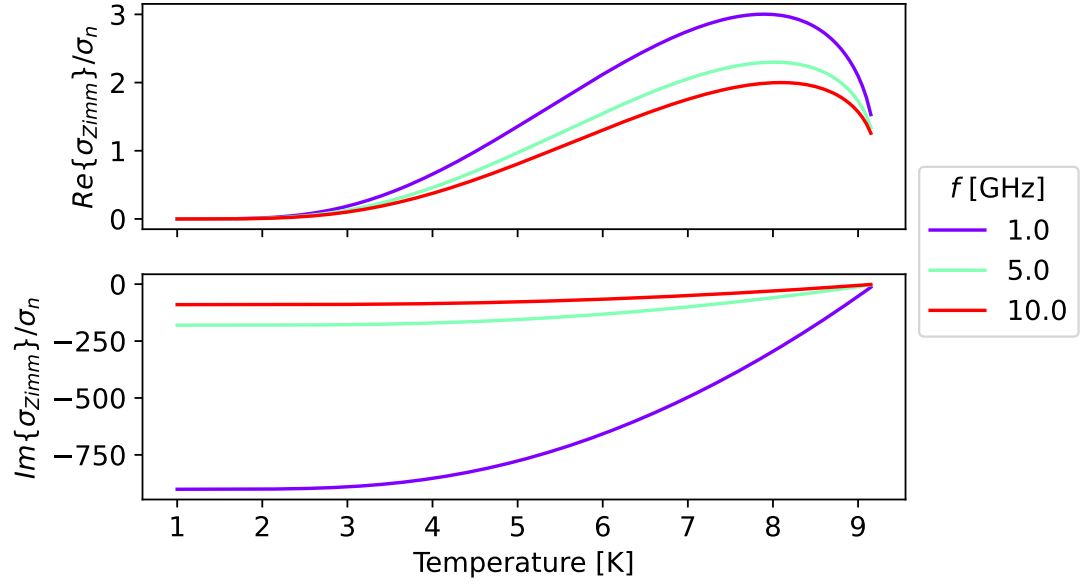
where Eq. 2.8 was used to get the expression on the left of Eq. 2.16. Fig. 2.1 shows this reduced gap parameter, which decreases as  $T \rightarrow T_c$ . This decrease is a result of the increase of quasiparticle density, which in turn suppresses the gap parameter [37]. This reduced gap parameter script is used in the calculation of the proceeding Mattis-Bardeen and Zimmermann conductivities. The Mattis-Bardeen conductivity is calculated numerically and shown in Fig. 2.2.

The M-B conductivity presented in Eq. 2.15 is limited to the local limit theory that is valid for dirty superconductors only unless the full non-local integral is computed. These limits can be removed to compute the conductivity of clean,  $l \gg \xi_0$ , and mid-range,  $l \sim \xi_0$ , superconductors by considering a different theory for the conductivity of superconductors.

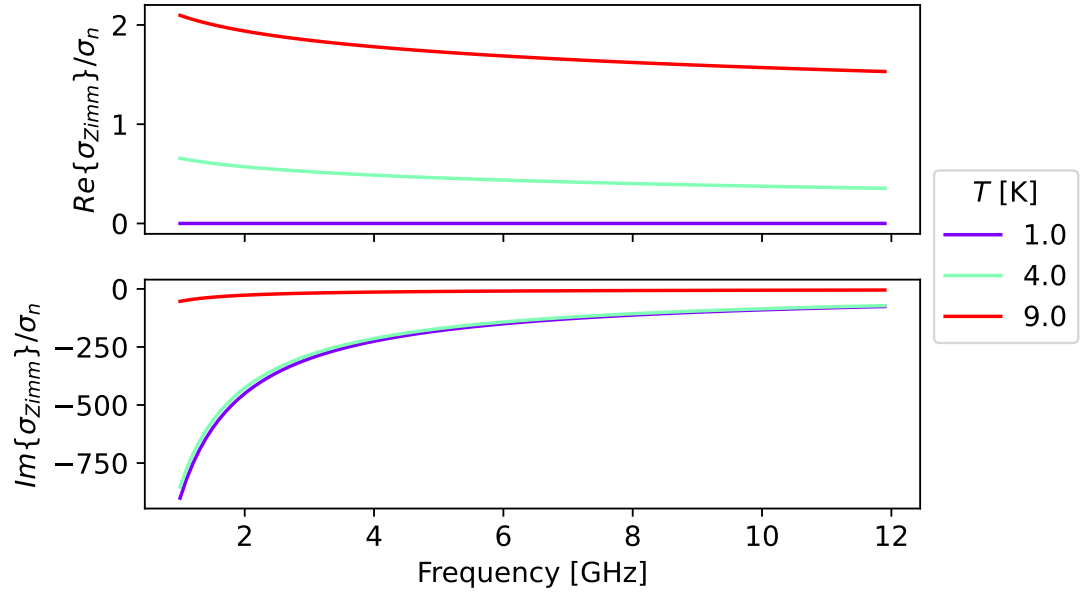
## 2.2.2 Zimmermann Conductivity

In 1991, Zimmermann [41] derived equations of the complex conductivity for homogeneous isotropic BCS superconductors with arbitrary electron mean free path using the quasi-classical formalism of the energy-integrated Green functions. This allowed for the complex conductivity of arbitrary purity superconductors to be computed with two extra parameters  $\xi_0$  and  $l$  in addition to the  $T_c$  and  $\Delta_0/kT_c$  that were needed for the M-B conductivity.

The explicit expressions for  $\sigma_{\text{Zimm}}(\omega)$  are the following



(a) Temperature variation



(b) Frequency variation

Figure 2.3: The real and imaginary part of the normalised Zimmernann conductivity for dirty niobium with  $T_c = 9.2$  K,  $\Delta_0/kT_c = 1.83$ ,  $\xi_0 = 39$  nm and  $l = 5.7$  nm.

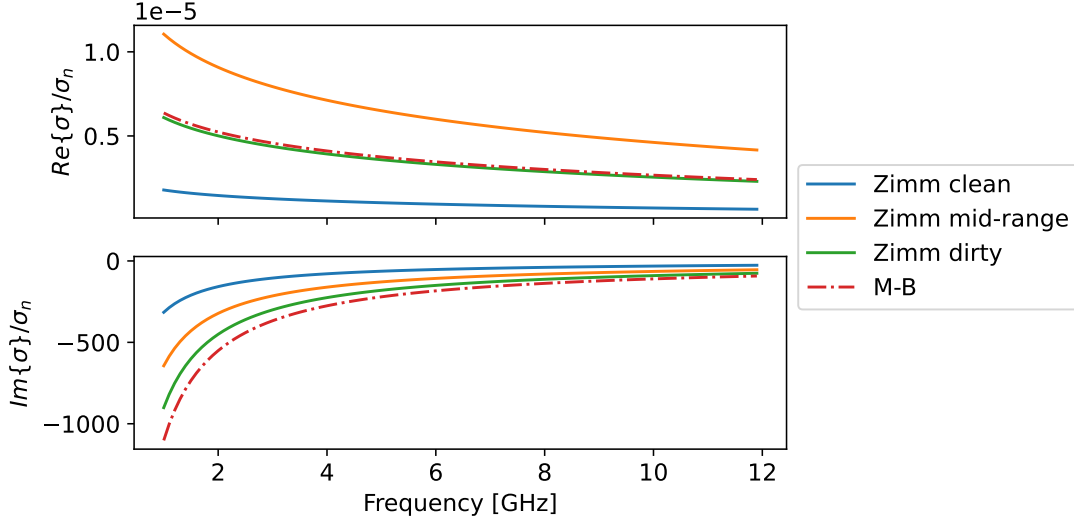


Figure 2.4: A comparison of the complex conductivities of three grades of niobium calculated with the Zimmermann conductivity vs the Mattis-Bardeen conductivity of niobium in the local limit. A temperature of 1 K is chosen as an example but other temperatures demonstrate similar behaviour. The parameters used are the following: 'clean'[54],  $\Delta_0/kT_c = 1.97$ ,  $\xi_0 = 39$  nm,  $l = 100$  nm; 'mid-range'[38],  $\Delta_0/kT_c = 1.76$ ,  $\xi_0 = 39$  nm,  $l = 20$  nm; 'dirty'[51],  $\Delta_0/kT_c = 1.83$ ,  $\xi_0 = 39$  nm,  $l = 5.7$  nm.  $T_c = 9.2$  K for all 4.

$$\frac{\sigma_{\text{Zimm}}(\omega)}{\sigma_n} = \frac{j}{2\omega\tau} \left( J + \int_{\Delta}^{\infty} I_2 dE \right) \quad (2.17a)$$

with

$$J(\omega \leq 2\Delta) = \int_{\Delta}^{\omega+\Delta} I_1 dE, \quad (2.17b)$$

$$J(\omega \geq 2\Delta) = \int_{\Delta}^{\omega-\Delta} I_3 dE + \int_{\omega-\Delta}^{\omega+\Delta} I_1 dE, \quad (2.17c)$$

where the time constant is given by  $\tau = l/v_0$  and the expressions of the integrands are given by



$$I_1 = \tanh \frac{E}{2kT} \left[ \left( 1 - \frac{\Delta^2 + E(E - \omega)}{P_4 P_2} \right) \frac{1}{P_4 + P_2 + j/\tau} - \left( 1 + \frac{\Delta^2 + E(E - \omega)}{P_4 P_2} \right) \frac{1}{P_4 - P_2 + j/\tau} \right], \quad (2.18a)$$

$$I_2 = \tanh \frac{E + \omega}{2kT} \left[ \left( 1 + \frac{\Delta^2 + E(E + \omega)}{P_1 P_2} \right) \frac{1}{P_1 - P_2 + j/\tau} - \left( 1 - \frac{\Delta^2 + E(E + \omega)}{P_1 P_2} \right) \frac{1}{-P_1 - P_2 + j/\tau} \right] \\ + \tanh \frac{E}{2kT} \left[ \left( 1 + \frac{\Delta^2 + E(E + \omega)}{P_1 P_2} \right) \frac{1}{P_1 + P_2 + j/\tau} - \left( 1 + \frac{\Delta^2 + E(E + \omega)}{P_1 P_2} \right) \frac{1}{P_1 - P_2 + j/\tau} \right], \quad (2.18b)$$

$$I_3 = \tanh \frac{E}{2kT} \left[ \left( 1 - \frac{\Delta^2 + E(E - \omega)}{P_3 P_2} \right) \frac{1}{P_3 + P_2 + j/\tau} - \left( 1 + \frac{\Delta^2 + E(E - \omega)}{P_3 P_2} \right) \frac{1}{P_3 - P_2 + j/\tau} \right], \quad (2.18c)$$

with

$$P_1 = \sqrt{(E + \omega)^2 - \Delta^2}, \quad P_2 = \sqrt{E^2 - \Delta^2}, \\ P_3 = \sqrt{(E - \omega)^2 - \Delta^2}, \quad P_4 = j\sqrt{\Delta^2 - (E - \omega)^2}.$$

The computed Zimmermann conductivity tend towards the Mattis-Bardeen conductivity for dirty superconductors  $l \ll \xi_0$ . This relationship can be demonstrated by computing the Zimmermann conductivity for niobium of different purities and comparing this to the result of the M-B conductivity as shown in Fig. 2.4. For superconductors that are in the deep dirty limit such as NbTiN, the two types of conductivities agree very closely with one another, which is shown in

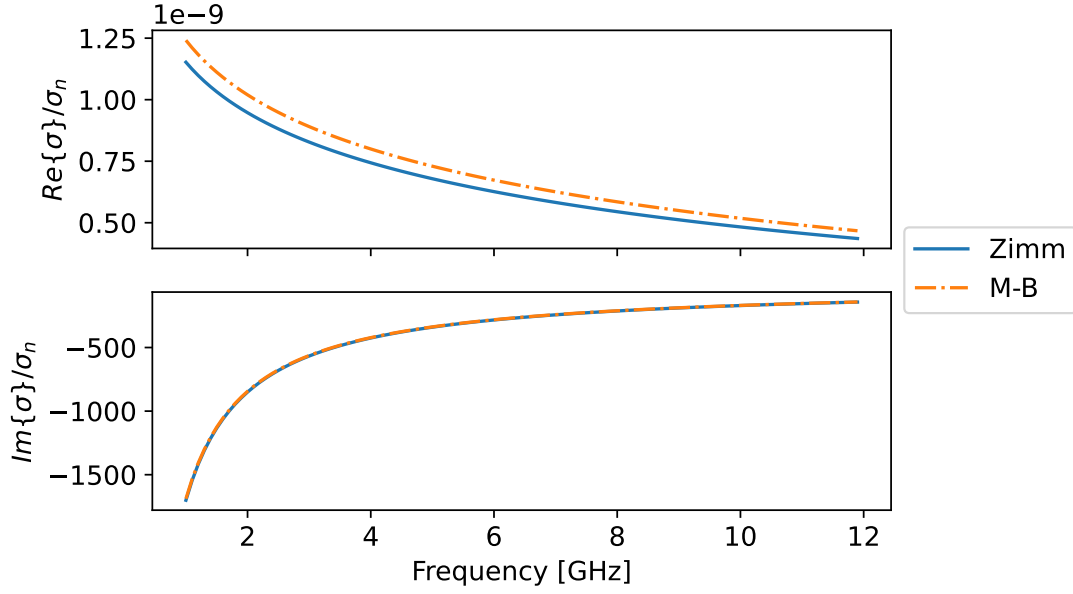


Figure 2.5: A comparison of the complex conductivities of NbTiN found via M-B and Zimmermann methods. The temperature is set to 1 K and the parameters used for NbTiN are [55]:  $T_c = 14.1$  K,  $\Delta_0/kT_c = 1.86$ ,  $\xi_0 = 170$  nm,  $l = 0.57$  nm

Fig. 2.5. Since the Zimmermann conductivity is not restricted to the local limit and can be used more universally for isotropic BCS superconductors it will be used in the proceeding analyses.

### 2.2.3 Surface Impedance

The complex surface impedance, in units of  $\Omega/\square$ , characterises the absorption and reflection of an electromagnetic wave at the surface of a conductor. In the case of a superconductor this surface impedance takes the following general form

$$Z_s = R + jX = R_s + j\omega L_s = R_s + j\omega\mu_0\lambda_{\text{eff}} \quad (2.19)$$

where  $R$  and  $X$  are the sheet resistance and reactance,  $R_s$  and  $L_s$  are the surface resistance and inductance, and  $\lambda_{\text{eff}}$  is referred to as the effective London penetration depth. Calculation of the surface impedance in the general case is not simple and often requires numerical techniques to compute [37, 38]. However, it can be

very insightful to consider a few limiting cases that simplify the problem.

One of these cases is the local (or dirty) limit in which  $l \ll \xi_0$  and  $l \ll \lambda_{\text{eff}}$ , and the local version of Ohm's law is valid  $\vec{J} = \sigma \vec{E}$ . Here, the effective penetration depth is given by

$$\lambda_{\text{local}} = \sqrt{\frac{\hbar}{\pi \Delta_0 \mu_0 \sigma_n}}, \quad (2.20)$$

where  $\Delta_0$  is the superconducting gap parameter at zero temperature (see Eq. 2.8) and  $\sigma_n$  is the normal state electrical conductivity. This limit is indeed valid for NbTiN and “dirty” niobium which are used in this project.

Another case is the extreme anomalous limit in which  $\xi_0 \gg \lambda_{\text{eff}}$  and  $l \gg \lambda_{\text{eff}}$ , meaning that the response of the charge carriers is non-local due the long mean free path of the electrons compared to the distance over which the fields vary. In this case, the effective penetration depth takes a modified form given by

$$\lambda_{\text{e.a.}} = \lambda_{\text{local}} \left[ \frac{\sqrt{3}l}{2\pi\lambda_{\text{local}}} \right]^{1/3}, \quad (2.21)$$

which is indeed independent of  $l$  since  $\lambda_{\text{local}} \propto l^{-1/2}$  [37]. This limit is less applicable to the superconductors explored in this project and so will not be the main focus of discussion. More information on these limits can be found in [38].

The expressions of the effective penetration depth given in Eq. 2.20 and Eq. 2.21 are valid for thick superconductors such that the thickness  $t \gg l$  and  $t \gg \lambda_{\text{eff}}$ . The reverse of this situation will be explored further in this section. In the case of a thick superconductor in the dirty limit the surface impedance can be related to the conductivities covered in Sections 2.2.1 and 2.2.2 by considering a plane wave at normal incidence to a surface with impedance  $Z_s$ . The incident wave excites voltages and currents in the conductor that vary with the depth from the surface. This scenario is depicted in Fig. 2.6 in which a slice of the conductor

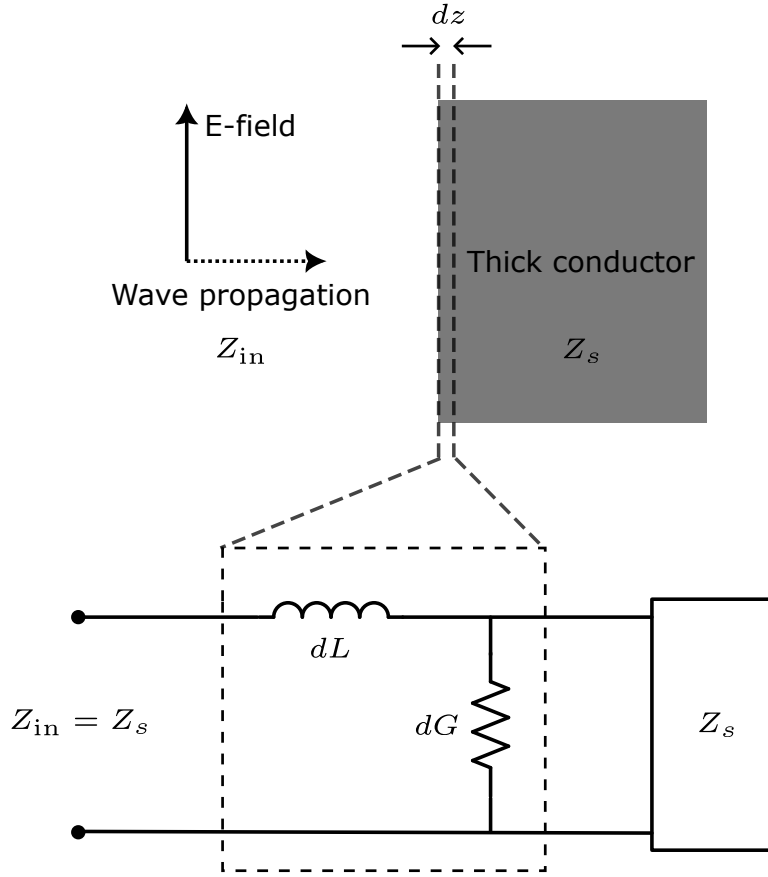


Figure 2.6: A diagram used for the derivation of the surface impedance of a thick conductor. Top: A diagram of a plane wave at normal incidence to a conductor of surface impedance  $Z_s$ . Bottom: A lumped element model representation of the case above where the impedance at the surface is given by  $Z_{in}$  which is equal to  $Z_s$  when looking in the direction of the conductor, the infinitesimally small thickness of conductor  $dz$  is represented by a lumped element transmission line model. The inductance and conductance of this sheet is given by  $dL$  and  $dG$ , respectively. The capacitance is zero since the sheet is at the same potential and resistance is neglected due to the infinitesimally thin sheet thickness.

with thickness  $dz$  over which the magnetic field of the incident wave decays is modelled as an equivalent lumped element transmission line. The capacitance in this model is zero due to the slice being composed of a single piece of metal which is at the same potential and the resistance can be neglected due to the vanishingly small resistance of the infinitesimally thin sheet. The conductance of the model cannot be ignored due to surface current flowing on the surface in the direction of the electric field, with the conductance being given by  $dG = \sigma dz$  in  $S/\square$ . This

sheet also possesses an inductance since the propagating wave experiences a phase delay as it travels to a thickness  $dz$ , which is given by  $dL = \mu_0 dz$ . Hence, the input impedance is given by

$$Z_{\text{in}} = Z_s = j\omega dL + \frac{1}{dG + 1/Z_s} = j\omega\mu_0 dz + \frac{1}{\sigma dz + 1/Z_s}, \quad (2.22)$$

which can be simplified by ignoring terms in  $dz$  since  $dz$  is infinitesimally small to get the following expression for the bulk surface impedance

$$Z_{s,\text{bulk}}(\omega, T) = \sqrt{\frac{j\omega\mu_0}{\sigma(\omega, T)}}, \quad (2.23)$$

which can be used to calculate the surface impedance of a bulk superconductor via a substitution of the computed complex conductivity.

However, when the superconducting layer thickness  $t$  is thinner than the mean free path, then  $l$  will become limited by surface scattering such that  $l \approx d$ . Moreover, if the film thickness  $t \ll \lambda_L$ , then the field penetrates through the entire film and the current distribution becomes almost uniform across the film. Note, that the perpendicular penetration depth,  $\lambda_\perp = \lambda_L^2/t$ , needs to be considered for wide films. If the film width  $w > \lambda_\perp$  then the current density becomes concentrated on the edges of the trace. Reducing the superconductor thickness to below  $\lambda_L$  has the effect of enhancing the reactance since the kinetic inductance of the films increases as  $\coth(t/\lambda_L)$ . An expression for  $\lambda_L$  can be found in Eq. 2.20.

The surface impedance for a film of arbitrary thickness [56] is given by

$$Z_s(\omega, T, t) = \sqrt{\frac{j\omega\mu_0}{\sigma(\omega, T)}} \coth\left(t\sqrt{j\omega\mu_0\sigma(\omega, T)}\right). \quad (2.24)$$

The surface impedance of dirty Nb and NbTiN at different conductor thicknesses is shown in Fig. 2.7. These surface impedance show a few interesting results: the reactance of Nb is smaller reactance since the London penetration

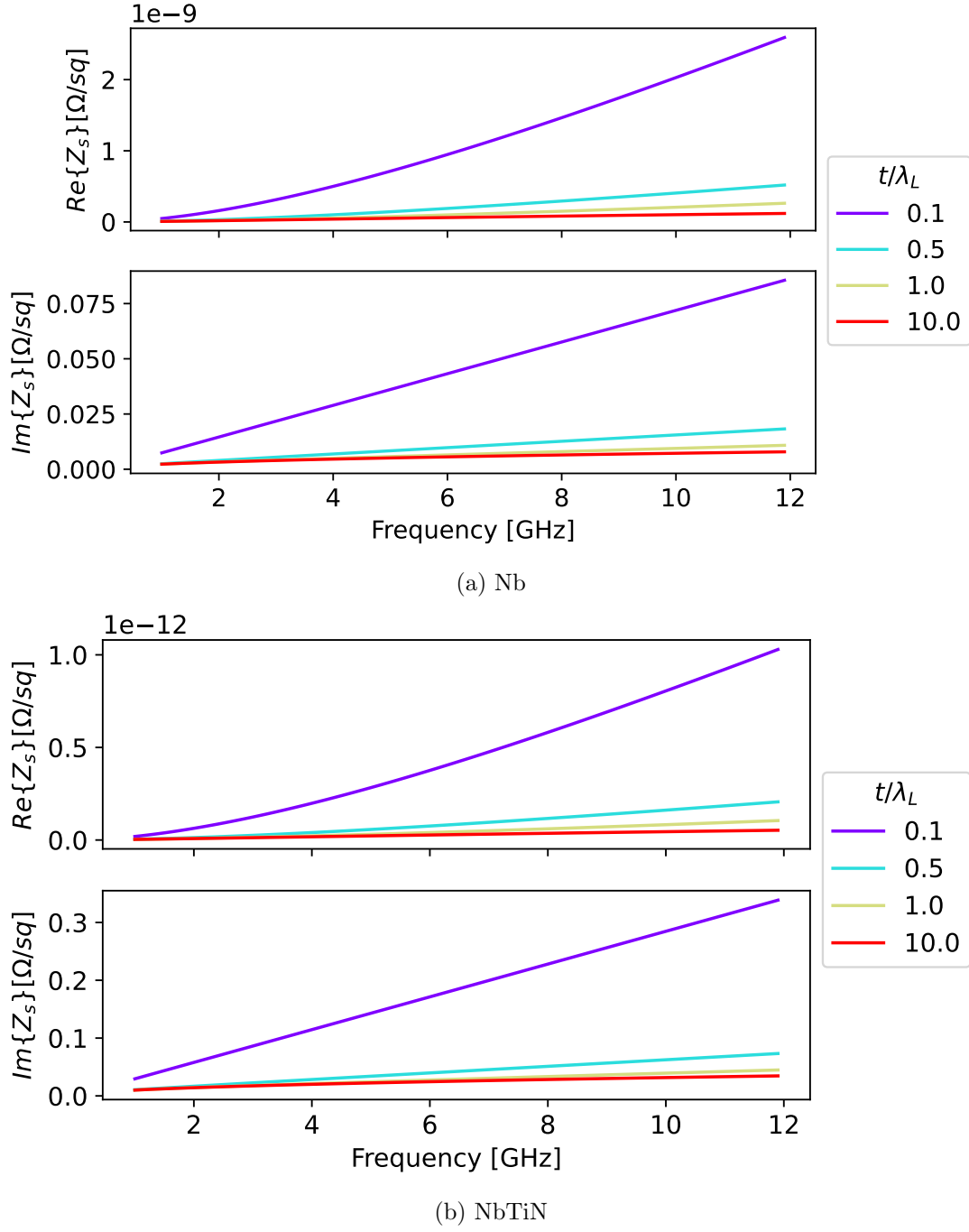


Figure 2.7: The complex surface impedance of dirty Nb ( $\sigma_n = 2 \times 10^7 \text{ S m}^{-1}$ ) and NbTiN ( $\sigma_n = 0.55 \times 10^6 \text{ S m}^{-1}$ ) at 1 K. The other material properties are the same as in Fig. 2.4.

depth of Nb is smaller than that of NbTiN; the sheet resistance of the NbTiN film is smaller than Nb since both films are at temperature of 1 K and the resistance scales as  $\exp(-T_c/T)$ . The analytic form of this surface resistance can be derived [57] by considering the real part of the surface impedance calculated using the M-B conductivity (see Section 2.2.1) for GHz range frequencies and temperatures of below a few K. The resulting expression for the surface resistance is given by

$$R_s = \frac{\mu_0^2 \omega^2 \lambda_L^3 \Delta \sigma_n}{k_b T} \ln \left[ \frac{C_1 k_b T}{\hbar \omega} \right] \exp \left[ -\frac{\Delta}{k_b T} \right] \quad (2.25)$$

where  $C_1 = 4/e^C$  with  $C = 0.577$  being the Euler constant. By substituting for the superconducting gap  $\Delta$  using Eq. 2.16, it can be shown that  $R_s \propto \exp(-T_c/T)$ . This exponential resistance scaling allows for NbTiN based devices with a higher  $T_c$  to have significantly smaller levels of dissipation for a given operating temperature compared to materials like Nb.

Specifying this surface impedance on a surface in a 3D EM solver like HFSS allows for the superconducting reactance to be included in the simulation which can have a large effect on the resonance frequency of a resonator. This is particularly important for structures that have a significant surface inductance contribution to the total structure inductance. These methods will be used in the simulations of superconducting resonators and transmission lines in Chapters 4 and 5.

## 2.3 Superconducting Nonlinearities

### 2.3.1 Josephson Inductance

A Josephson junction [58] consists of two superconducting electrodes with some thin barrier or current constriction between them. This weak connection can be in multiple forms: a thin insulating layer – known as an SIS junction; a constriction in current via a thin normal metal which becomes weakly superconducting due to the proximity effect – referred to as an SNS junction; or a narrow and

thin superconducting constriction, which forms an ScS junction. A Josephson tunnel junction i.e. one with an insulating barrier can be described [36] using the Josephson equations which are given by

$$I = I_c \sin \varphi, \quad (2.26a)$$

$$\frac{\partial \varphi}{\partial t} = \frac{2e}{\hbar} V, \quad (2.26b)$$

where  $I$  is the current flowing across the junction, and the critical current  $I_c$  is the maximum current that the junction can support,  $\varphi$  is the difference in the phase of the Ginzburg-Landau wavefunction in the two electrodes, and  $V$  is the voltage across the junction. The first Josephson equation shows that with no voltage applied a current will flow across the junction dictated by the wavefunction phase difference – this is known as the DC Josephson effect. The second Josephson equation shows that if a voltage difference is maintained across the junction then the phase difference will evolve in such a way as to generate an alternating current with amplitude  $I_c$  and a frequency  $\omega = 2eV/\hbar$ , which is known as the AC Josephson effect. This shows that the quantum energy  $\hbar\omega$  equals to the energy change of a Cooper pair transferred across the junction. By taking the derivative of Eq. 2.26a with respect to  $\varphi$  and using the chain rule for the time derivative of current such that

$$\frac{\partial I}{\partial t} = \frac{\partial I}{\partial \varphi} \frac{\partial \varphi}{\partial t} = \frac{\hbar}{2eI_c \cos \varphi}, \quad (2.27)$$

the voltage–current relationship of an inductor,  $V = LdI/dt$ , can be used to infer the Josephson inductance,  $L_J$ . This is given by

$$L_J(\varphi) = \frac{\Phi_0}{2\pi I_c} \frac{1}{\cos \varphi} = L_{J0} \frac{1}{\cos \varphi}, \quad (2.28)$$



where  $\Phi_0 = h/2e$  is the flux quantum and  $L_{J0}$  is the linear Josephson inductance. Eq. 2.28 can be expressed in terms of current by using Eq. 2.26a and expanding  $1/\cos \varphi$  around  $\varphi = 0$ , yielding the following relation

$$L_J(I) \approx L_{J0} \left( 1 + \frac{I^2}{2I_c^2} + \dots \right). \quad (2.29)$$

The Josephson inductance presented in Eq. 2.28 and 2.29 make the Josephson junction a valuable source of nonlinear behaviour that can be used in various types of parametric amplifiers [59, 60]. In this PhD project the Josephson inductance is key in explaining the nonlinear parametric processes observed in a niobium circular waveguide pillbox cavity, where a junction or distribution of junctions is believed to form at the contact point between two parts of the resonator assembly (see Section 3.3 for more details).

### 2.3.2 Kinetic Inductance

In general kinetic inductance arises as a result of the inertia of mobile charge carriers resisting changes in applied voltage. It is present in all materials but its contribution is only visible in conductors with very high charge carrier mobility or in the presence of high frequency radiation e.g. the optical range.

The kinetic inductance in a superconductor is a result of the inertia of the Cooper pairs resisting the changes in applied voltage. This introduces a phase delay between voltage and resulting current which presents itself as an equivalent series inductance. Compared to a geometric inductance, the kinetic inductance does not involve any energy transfer through magnetic fields, instead the energy transfer is purely through the inertia of the Cooper pairs [37].

The kinetic inductance is nonlinear with applied current which allows it to be used in the design of nonlinear devices. This semi empirical current dependence is generally assumed [13, 61] to be of the following form

$$L_k(I) \approx L_{k0} \left( 1 + \frac{I^2}{I_*^2} + \dots \right), \quad (2.30)$$

where  $L_{k0} = \hbar R_n / \pi \Delta$  is the linear KI with  $R_n$  being the normal state resistance and  $I_*$  is the scaling current that is of the order of the critical current of the superconducting trace. The expression in Eq. 2.30 is valid for low drive currents,  $I/I_* \ll 1$ , at frequencies well below the superconducting gap such that  $\hbar\omega \ll 2\Delta$ , and for a temperature  $T \sim T_c$ . The zero current kinetic inductance and scaling current are usually measured experimentally [62, 18] rather than only being calculated analytically. However, this generally assumed form of the non-linearity has been confirmed via a derivation by Semenov [63]. It is predicted in the Ginzburg-Landau theory that a supercurrent modifies the density of states [64] and lowers the energy gap, resulting in an increase of the kinetic inductance. Semenov [63] demonstrated that the alternating current (ac) excitation modifies the order parameter  $\Delta$ , such that

$$\frac{\delta\Delta}{\Delta} \cong -\pi \frac{\alpha_d}{\Delta} = -\frac{1}{2\pi (\xi\Delta/eR_n)^2} \frac{I^2}{I_c^2}, \quad (2.31)$$

where the normalised ac drive is given by  $\alpha_d = e^2 D L_{k0}^2 I^2 / 2\hbar$  with  $D$  being the diffusion coefficient and the coherence length is given by  $\xi = \sqrt{\hbar D / \Delta}$ . This results in the modification of the kinetic inductance in the form

$$\frac{\delta L_k}{L_{k0}} = \left( \frac{16}{3\pi} + \pi \right) \frac{\alpha_d}{\Delta}. \quad (2.32)$$

Finally, Eq. 2.32 can be rewritten to be in same form as Eq. 2.30 by considering a general perturbation of the kinetic inductance in the form  $L_k = L_{k0} + \delta L_k$  and by substituting an expression for  $\alpha_d/\Delta$  provided in [63]

$$\frac{\alpha_d}{\Delta} = \frac{1}{2\pi^2} \frac{I^2}{(\Delta\xi/eR_n)^2}, \quad (2.33)$$

where the scaling current is given by  $I_* = \sqrt{2}/(16/3\pi + \pi)^{-1/2} \pi \Delta \xi / e R_n \approx 2.69 I_c$ .

Further details of this derivation can be found in [63].

The value of the scaling current depends on the film geometry and the distribution of the current. Specific cases will be discussed in Sections 4.2.2 and 5.2.3. It should be noted that the units of the inductance in Eq. 2.30 are given in per square meaning that this should be divided by the width of the trace to extract the inductance per length. In addition, the linear KI in units of per square can be expressed as

$$L_{K0} = \mu_0 \lambda_L \coth \frac{t}{\lambda_L}, \quad (2.34)$$

where  $\lambda_L$  is the bulk London penetration depth and  $t$  is the thickness of the film. The penetration depth can be approximated [37] using Eq. 2.20.

Eq. 2.34 for the linear KI shown can be used to calculate the kinetic inductance fraction of the structure under investigation. The fraction of the kinetic inductance relative to the total inductance dictates the extent to which the non-linearity will dominate over the device dynamics and is often denoted by  $\alpha_k$ . High kinetic inductance structures with  $\alpha_k \rightarrow 1$  are needed for parametric amplifiers where the KI dominance is achieved by using thin films that have a large  $\lambda_L$  such as NbTiN [13, 65, 18].

In this PhD project the kinetic inductance is engineered to provide the nonlinearity for a Ka band resonant parametric amplifier (see Chapter 4) and a W-band travelling wave parametric amplifier (see Chapter 5).

## 2.4 Parametric Amplification

### 2.4.1 Parallels to Optics

A parametric process can be defined as a process that does not change the quantum state of a medium in which it occurs. Meaning that no net energy or momentum is exchanged between the fields of an interacting mode and the physical

system. In contrast to a non-parametric process which can change any part of the quantum state of the physical system. This distinction can be demonstrated in the field of optics where many examples of such processes exist. In *linear* optics a parametric process can be the refraction or elastic scattering due to a lossless medium, while a linear non-parametric process would be an absorption, emission or inelastic scattering. In *nonlinear* optics parametric processes take the form of various types of harmonic generation, mixing and phase modulation, while nonlinear non-parametric process include types of stimulated scattering and multiphoton absorption. Such processes are not solely constrained to the field of optics but also exist in the microwave frequency regime. Of most interest to this project are the nonlinear parametric process that give rise to parametric amplification. Specifically the analogous counterpart to the optical Kerr effect but in a microwave superconducting circuit giving rise to self-phase (SPM) and cross-phase modulation (XPM); as well as four-wave (4WM) and three-wave mixing (3WM). Covering this Kerr effect that occurs in nonlinear optics can prove very useful in understanding the nonlinear parametric processes in the microwave frequency regime.

The optical Kerr effect [66] presents itself in nonlinear optics as a phase shift of a propagating mode due to an intensity modulated refractive index. This can be understood by considering the polarization of a nonlinear optical medium in a presence of a strong field,  $\vec{E}$ ,

$$\vec{P} = \epsilon_0 \left[ \chi^{(1)} \cdot \vec{E} + \chi^{(2)} : \vec{E}\vec{E} + \chi^{(3)} : \vec{E}\vec{E}\vec{E} + \dots \right], \quad (2.35)$$

where  $\epsilon_0$  is the vacuum permittivity and  $\chi^{(j)}$  is the dielectric susceptibility which is a tensor of rank  $j + 1$  and describes the nonlinearity of the material. These second and third order nonlinearities give rise to their respective order processes. For the former these are 2nd harmonic generation and 3WM while for the latter these are 3rd harmonic generation and 4WM. In a centrosymmetric medium (an

isotropic medium) due to the inversion symmetry the even order nonlinearities vanishes meaning that the first nonlinear term is the 3rd order susceptibility. Considering light polarized in one direction and dropping the tensor indices, the light intensity dependent nonlinear refractive index in its simplest form can be written as

$$\tilde{n} = n_L + n_{NL}|E|^2, \quad (2.36)$$

where  $n_L = \sqrt{\epsilon_r} = \sqrt{1 + \chi^{(1)}}$  and  $n_{NL} = \frac{3}{8n_L}\chi^{(3)}$  are the linear and nonlinear refractive indices, respectively. The derivation for these refractive indices involves solutions of the nonlinear wave equation which can be found in Section 2.3 in [66]. The light propagating in such a medium will experience a phase shift due to the intensity dependent refractive index. If this phase shift is due to the power of the light beam then it is referred to as self-phase modulation (SPM). If the phase-shift is due to another beam then this is referred to as cross-phase modulation (XPM). These same effects are seen in nonlinear superconducting circuits except the power dependent phase shift arise a result of the modulated circuit inductance (see Section 2.3). Additionally, a 2nd order nonlinearity can be engineered in these superconducting circuits to allow for 3WM mixing process to take place. In Josephson junction circuits the 2nd order nonlinearity can be induced via flux-pumped SQUIDS [67, 68, 69] or SNAILs [70, 71, 72, 73], while in kinetic inductance circuits this is done by introducing a DC bias [61, 65, 74]. In the KI case the presence of a DC bias modifies the current in Eq. 2.30 such that is is replaced by contributions of the alternating current,  $I_{AC}$ , and the direct current,  $I_{DC}$ , i.e.  $I \rightarrow I_{AC} + I_{DC}$ . This has the effect of adding a term proportional to  $I_{AC}$ , which lowers the order of kinetic inductance nonlinearity and gives way for lower order mixing processes such as 3WM to take place. These different types of parametric amplifiers will be discussed in the proceeding sections.

### 2.4.2 Parametric Amplifier Overview

Parametric signal gain is achieved when the interaction time between incident modes and the nonlinear medium is maximised. As highlighted in Section 2.3, this nonlinear medium can be realised in a number of different methods such as the introduction of extrinsic nonlinear elements such as Josephson junctions or the engineering of an intrinsic nonlinearity such as the kinetic inductance of thin superconducting traces. The nonlinear medium allows for the exchange of energy between co-propagating modes which can be used to generate gain of a weak signal in the presence of a strong pump with angular frequencies  $\omega_s$  and  $\omega_p$ , respectively. The interaction time between these tones can be increased via two methods: embedding the nonlinear medium within a resonant cavity or distributing the nonlinear medium over a sufficiently long transmission line. The former method gives rise to resonant parametric amplifiers (RPAs) while the latter produces a travelling-wave parametric amplifiers (TWPAs). The main differences in performance between these two types of params is in their bandwidth and saturation power. RPA bandwidth is restricted to a fraction of the resonator linewidth,  $\kappa$ , obeying the constant gain-bandwidth product. On the other hand the TWPA bandwidth is usually much larger and is limited by the frequency range over which a phase matching condition can be maintained.

These parametric amplifiers can operate in 4WM or 3WM mode depending on how the nonlinear medium is engineered and/or biased. These operation modes are shown in Fig. 2.8 and often take place simultaneously since both nonlinearities are stimulated by the strong pump tone. This can degrade the parametric gain and limit the performance of these amplifiers [75]. Unless the nonlinearity is engineered in such a way as to suppress the  $\chi^{(3)}$  term like in SNAILs [70]. One of the key advantages of the 3WM mode is that the pump is spectrally displaced from the gain curve, meaning that it can be filtered out before causing saturation for the rest of the amplification chain. However, additional consideration of the

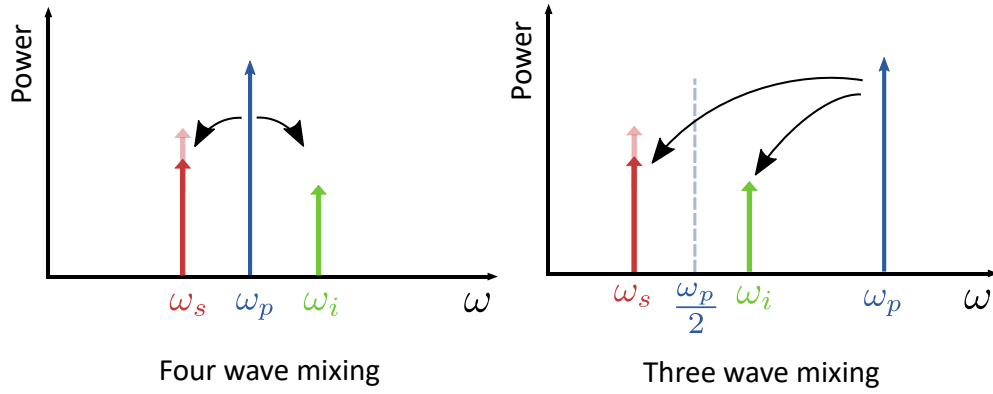


Figure 2.8: A simplified output spectrum of two types of mixing processes with input tones at  $\omega_s$  and  $\omega_p$ . The 4WM amplifier (left) shows the signal response centered around  $\omega_p$ , with a generated idler at  $2\omega_p = \omega_s + \omega_i$  and the 3WM amplifier (right) shows the signal response around  $\omega_p/2$  with an idler at  $\omega_p = \omega_s + \omega_i$ . In each case the amplifiers are in phase-preserving operation. The black arrows indicate the energy flow for the system.

flux or DC bias is needed as well as sufficient feedline bandwidth to allow the pump tone to reach the amplifier. Rectangular waveguide usually has around an octave of bandwidth which may not be sufficient for 3WM operation since the gain would be centered near the lower end of the waveguide range and a part of the gain curve would be lost due to the lower cut-off of the waveguide. Therefore, broadband feedlines such as coaxial cables should be used (lossy at high frequency), or alternatively two separate bands of rectangular waveguide.

The parametric amplifiers explored in this project are all phase-preserving (or phase-insensitive), meaning that they amplify a signal irrespective of the phase of the pump. However, for completeness phase-sensitive amplifiers should be outlined since phase-sensitive operation leads to important field of noise-squeezing.

### Phase-Preserving vs Phase-Sensitive Amplifiers

A electromagnetic field can be decomposed into two quadratures such that  $\hat{X} = \hat{X}_1 \cos \omega t + \hat{X}_2 \sin \omega t$ , which are described by dimensionless field quadrature operators  $\hat{X}_1 = (\hat{a}^\dagger + \hat{a})/2$  and  $\hat{X}_2 = i(\hat{a}^\dagger - \hat{a})/2$ . Here,  $\hat{a}^\dagger$  and  $\hat{a}$  are the bosonic annihilation and creation operators. The processes shown in Fig. 2.8 are phase

preserving meaning that both quadratures of the decomposed signal are amplified equally by a factor  $G$  such that the output field take the form of  $\langle \hat{Y}_1 \rangle = G\langle \hat{X}_1 \rangle$  and  $\langle \hat{Y}_2 \rangle = G\langle \hat{X}_2 \rangle$ . Each quadrature here adds at least  $1/4$  of noise to each field quadrature. A phase-sensitive mode may be induced when the signal and idler modes are degenerate in frequency. In this mode the amplitude of one quadrature is amplified  $\langle \hat{Y}_1 \rangle = G\langle \hat{X}_1 \rangle$  while the other de-amplified  $\langle \hat{Y}_2 \rangle = \langle \hat{X}_2 \rangle / G$ , allowing one quadrature to be amplified without adding any additional noise. This deamplification can allow the noise of one of these quadratures to be squeezed to a level below that of vacuum fluctuations. These fluctuations obey the uncertainty principle  $\delta \hat{X}_1^2 \delta \hat{X}_2^2 \geq 1/16$ , where the  $\delta \hat{X}_1^2$  and  $\delta \hat{X}_2^2$  are the variances of the field quadratures. This squeezing can result in a single quadrature variance lower than would be possible by a quantum limited phase-preserving amplifier [5]. Noise squeezing has been developed the most using JPAs [59, 76, 11, 77], but very recently broadband squeezing was demonstrated in a JTWPA [12] and for the first time with a kinetic inductance in an RPA [74].

The field of phase-sensitive amplifiers is an extensive and active field of study, with the aforementioned recent developments in broadband noise squeezing as well as the first squeezing shown in a kinetic inductance RPA. However, the focus of this project is to first demonstrate the simplest phase-preserving amplification with high frequency structures. The high frequency paramp work could follow the developments for their lower frequency counterparts and also develop in the direction of phase-sensitive operation in the future.

### 2.4.3 Resonant Parametric Amplifiers

RPAs can be operated in a number of different configurations. Operation in 4WM mode is the most straightforward to realise since the pump and signal tones can be brought in through a single input port. For 3WM operation, the bandwidth of the waveguide or the circulator can complicate the addition of a pump at twice the



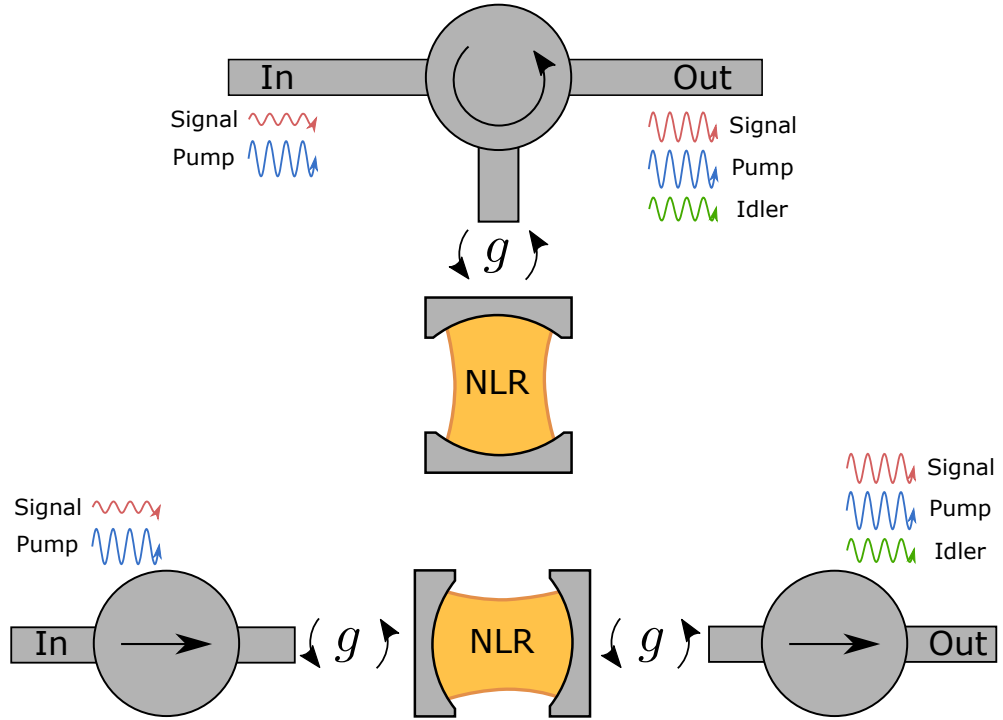


Figure 2.9: A cartoon showing two configurations of an RPA: *Top* shows the non-linear resonator (NLR) operated in reflection mode with a circulator isolating the three ports from one another. *Bottom* shows the NLR resonator with 2 ports operated in transmission mode with isolators on each port to prevent back reflections leaking to a device that may be under test. The NLR is coupled to the ports by a coupling strength  $g$ .

signal frequency. Two scenarios are shown in Fig. 2.9, a reflection amplifier and a transmission amplifier. The reflection amplifier has an inherent advantage in that the gain is usually larger since transmission through the circulator is high outside of resonance unlike the transmission amplifier which only transmits at resonance. However, this filtering nature of the transmission variant may be useful in some applications requiring amplification in a narrowband only. The dynamics of both of these amplifiers are similar and will be covered in this section.

This section will start with a brief development timeline of the field of resonant parametric amplifiers including Josephson junction and kinetic inductance based variants. After this the dynamics of a general degenerate RPA will be covered, including methods to calculate the parametric gain of such a system. We will

concentrate on degenerate RPAs where the maximum signal gain occurs when the pump is positioned on peak resonance and the signal has a small detuning from the pump. The proceeding discussion and solutions can be applied to Josephson or kinetic inductance RPAs where the main difference will be in the definition of the Kerr constant.

### Development History

RPAs can be realised with Josephson junctions (which I will refer to as J-RPAs for consistency with the kinetic inductance variants but conventionally these are called JPAs), or kinetic inductance (KI-RPAs) or even using weak links [78, 79]. The majority of the RPA development consisted of advances with Josephson based devices. In the 1980s, the first J-RPA was demonstrated by Yurke *et al.* [59]. Then in the early 2000s in line with the growing field of circuit quantum electrodynamics, there was a renewed interest in quantum limited microwave amplifiers to obtain high-fidelity single-shot qubit readout, which was achieved using the first Josephson bifurcation amplifiers that exploited the bistable region of an rf-biased junction [80, 81]. A few years later Castellanos-Beltran *et al.* [82] realised the J-RPA scheme that most current RPAs make use of, consisting of an array of junctions in a resonant cavity that is operated through a single port as a reflection amplifier. The noise performance of these J-RPAs has been demonstrated to be at the quantum limit by multiple laboratories around the world.

Following these developments the J-RPAs performance has improved in multiple other ways: the operational bandwidth has been increased as a result of strong coupling to the feedline via impedance tapers [83, 84]; the saturation power has been increased by exploring the effect of a lower Kerr factors [11, 85, 86]; various flux pumping schemes have been investigated to stimulate 3WM [69, 87, 70]; frequency tunability was achieved using arrays of resonant modes [72]. Commercial

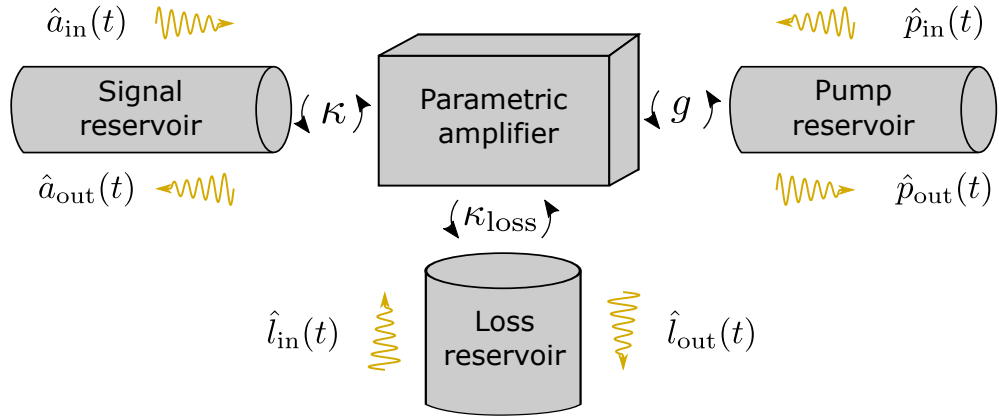


Figure 2.10: A schematic showing the input-output model used for deriving the response of a signal when coupled to a parametric amplifier with a loss reservoir.

JPA<sup>3</sup> have started to be sold that can operate in 4WM or 3WM mode in the same device.

Since the main focus of RPA development has been on JPAs, only a handful of kinetic inductance based RPAs were explored including one based on a NbN ring resonator [88] and more recently Parker et al [74] with the realisation of a low-Kerr 3WM variant that has also demonstrated noise squeezing. Another highlight was the first demonstration [19] of high frequency operation at 90 GHz, which was achieved using high kinetic inductance dipole antennas on a chip in the transverse plane of a rectangular waveguide.

### RPA Dynamics

One approach in understanding the response of the RPA is to analyse an input-output model of a parametric amplifier that is coupled to a number of different reservoirs. This approach was developed by Yurke and Buks [89], and was extended in a number of ways where we will concentrate on the approach outlined by Planat [42]. A schematic of such a model is presented in Fig. 2.10, which shows a signal reservoir with field  $\hat{a}(t)$ , and pump reservoir with field  $\hat{p}(t)$  (these can be thought of as transmission lines) coupled to a the parametric amplifier

<sup>3</sup><https://bbn-jpa.myshopify.com/>

with coupling rates  $\kappa$  and  $g$ , respectively. As well as loss reservoir with its field  $\hat{l}(t)$  with some coupling rate  $\kappa_{\text{loss}}$ . Here the signal and pump reservoirs are shown to be separate but often the signal and pump are brought through the same port and in that case the coupling rate would be  $\kappa = g$ . The signal gain is expressed by comparing  $\hat{a}_{\text{out}}$  with  $\hat{a}_{\text{in}}$ , which can be done by studying the intra-resonator fields which are represented by the annihilation  $\hat{a}$  and creation  $\hat{a}^\dagger$  operators. These intra-resonator field dynamics can be analysed through solutions of the quantum Langevin equations (QLE) [90, 42], which can be solved once the system Hamiltonian  $\hat{H}_{\text{sys}}$  is known. Two approximations are useful for solving the system dynamics: the Markov approximation, which states that the system itself does not affect the reservoirs from which the fields are coming; and the rotating wave approximation stating that only slowly varying fields in the rotating frame of interest are kept and the others are discarded. This QLE [90, 42] for the non linear resonator (NLR) field  $\hat{a}(t)$  is the following

$$\frac{d\hat{a}}{dt} = \frac{i}{\hbar} \left[ \hat{H}_{\text{sys}}, \hat{a} \right] - \frac{\kappa + \kappa_{\text{loss}}}{2} \hat{a} + \sqrt{\kappa} \hat{a}_{\text{in}}(t) + \sqrt{\kappa_{\text{loss}}} \hat{l}_{\text{in}}(t). \quad (2.37)$$

where the terms in the equation are defined in Fig. 2.10. Here, the output signal field can be related to the input signal field and intra-resonator field by assuming the boundary condition

$$\sqrt{\kappa} \hat{a}(t) = \hat{a}_{\text{in}}(t) + \hat{a}_{\text{out}}(t). \quad (2.38)$$

The QLE is solved by considering the full system Hamiltonian  $\hat{H}_{\text{sys}}$ , which is composed of at least three elements. The first being the Hamiltonian of the nonlinear resonator where amplification occurs, denoted by  $\hat{H}_a$ . Then the nonlinear resonator must be driven by a strong pump field in order to modulate the inductance, the pump is modelled as a classical drive of frequency  $\omega_p/2\pi$  with a field amplitude  $p$ , and a Hamiltonian denoted by  $\hat{H}_p$ . The final part is the interaction between the nonlinear resonator and the pump whose Hamiltonian is denoted by

$\hat{H}_{\text{int}}$ . Therefore, the total system Hamiltonian is  $\hat{H}_{\text{sys}} = \hat{H}_a + \hat{H}_p + \hat{H}_{\text{int}}$ .

It can be found [91, 42], that the system Hamiltonian, after several transformations, can take a canonical form based on the degenerate 4WM parametric amplifier model, is in the form given by

$$\frac{\hat{H}_{4\text{WM,DEG}}}{\hbar} = \Omega \hat{a}^\dagger \hat{a} + \frac{\lambda}{2} \hat{a}^{\dagger 2} + \frac{\lambda^*}{2} \hat{a}^2, \quad (2.39a)$$

$$\Omega = \omega_0 - \omega_p + 2K|\alpha|^2, \quad (2.39b)$$

$$\lambda = K\alpha^2. \quad (2.39c)$$

where  $\Omega$  is the frequency of the rotating frame under which the system is studied,  $\lambda$  is the pumping strength,  $\omega_0$  is the bare resonator frequency,  $\omega_p$  is the angular frequency of the pump,  $K$  is the Kerr coefficient (coming from the optical Kerr effect) which quantifies the nonlinearity of the system in units of Hz/photon, and finally  $\alpha$  is the complex amplitude of the pump *inside* the resonator.

Eq. 2.39a shows that a strong pump drive to the nonlinear resonator will shift its resonance frequency  $\omega_0/2\pi$  by  $2K|\alpha|^2/2\pi$  which is a result of the Kerr effect. Another important observation is that the product of the drive power and nonlinearity determines the dynamics of the system but not each quantity itself. Therefore, a small nonlinearity can at least in principle be compensated by increasing the drive power provided that this increased drive. The drawback of using a stronger drive is that it may saturate proceeding amplifiers or affect other sensitive components such as superconducting detectors via backscattering if not filtered appropriately. As will be seen next this means that the gain-bandwidth product is independent of the strength of the nonlinearity.

### RPA Gain

The expression for signal power gain  $G$  can be found by considering the in/output ports as shown in Fig. 2.10. The loss port doesn't need to be considered in the

## 2: SUPERCONDUCTIVITY AND PARAMETRIC AMPLIFICATION

ideal case since the losses within a J-RPA or KI-RPA are very low. The pump and signal reservoirs can be considered to be connected via the same port with a coupling rate  $\kappa$ , which simplifies the notation. We are interested in the signal gain as a function of angular frequency  $\omega$ , therefore the frequency domain operators are needed which involve a Fourier transformation such that

$$\hat{a}[\bar{\omega}] = \int_{-\infty}^{\infty} \hat{a}(t) e^{i\bar{\omega}t} dt, \quad \hat{a}^\dagger[\bar{\omega}] = \int_{-\infty}^{\infty} \hat{a}^\dagger(t) e^{i\bar{\omega}t} dt \quad (2.40)$$

where  $\bar{\omega} = \omega_p - \omega_s$  denotes the detuning between the pump and signal frequencies. Here, it should be noted that the operators  $\hat{a}[\bar{\omega}]$  and  $\hat{a}^\dagger[\bar{\omega}]$  do not commute in the case  $\bar{\omega} \neq 0$ , meaning that these operators describe two independent quantities i.e. photons at frequency  $\bar{\omega}/2\pi$  and  $-\bar{\omega}/2\pi$ , respectively, which represent the signal and idler. In the case  $\bar{\omega} = 0$  we have phase-sensitive operation, which will not be explored here. These frequency domain operators can be used to solve the QLE with Hamiltonian defined in Eq. 2.39a, which generates two coupled equations

$$(i(\Omega - \bar{\omega}) + \kappa/2)\hat{a}[\bar{\omega}] + i\lambda\bar{a}^\dagger[\bar{\omega}] = \sqrt{\kappa}\hat{a}_{\text{in}}[\bar{\omega}], \quad (2.41a)$$

$$(-i(\Omega + \bar{\omega}) + \kappa/2)\hat{a}[\bar{\omega}] - i\lambda^*\bar{a}^\dagger[\bar{\omega}] = \sqrt{\kappa}\hat{a}_{\text{in}}^\dagger[\bar{\omega}], \quad (2.41b)$$

Eq. 2.41 can be used with boundary condition defined in Eq. 2.38 to eliminate the intra-resonator field  $\hat{a}$  to arrive at the output field  $\hat{a}_{\text{out}}[\bar{\omega}]$  as a sum of the incoming signal at detuning  $\bar{\omega}$  and idler at detuning  $-\bar{\omega}$

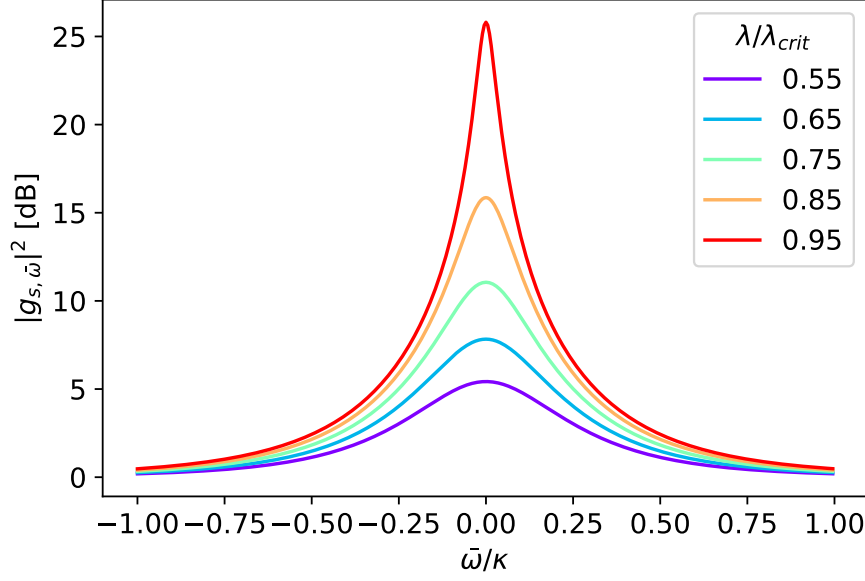


Figure 2.11: The signal gain of a resonant parametric amplifier with a resonant pump ( $\Omega = 0$ ) as a function signal-pump detuning  $\bar{\omega}$  normalised by the bare resonance width  $\kappa$ . This is plotted at a number of different pump amplitudes  $\lambda$  inside the resonator normalised by the critical drive  $\lambda_{crit}^2 = \kappa^2/4$ .

$$\hat{a}_{out}[\bar{\omega}] = g_{s,\bar{\omega}}\hat{a}_{in}[\bar{\omega}] + g_{i,\bar{\omega}}\hat{a}_{in}^\dagger[\bar{\omega}], \quad (2.42a)$$

$$g_{s,\bar{\omega}} = -1 + \frac{\kappa^2/2 - i\kappa(\Omega + \bar{\omega})}{\Omega^2 - \bar{\omega}^2 - |\lambda|^2 + \kappa(\kappa/4 - i\bar{\omega})}, \quad (2.42b)$$

$$g_{i,\bar{\omega}} = \frac{-i\kappa\lambda}{\Omega^2 - \bar{\omega}^2 - |\lambda|^2 + \kappa(\kappa/4 - i\bar{\omega})}, \quad (2.42c)$$

where  $g_{s,\bar{\omega}}$  and  $g_{i,\bar{\omega}}$  are the signal and idler gain, respectively. Finally, the signal power gain is defined as  $G = |g_{s,\bar{\omega}}|^2$ , which results in the following expression

$$|g_{s,\bar{\omega}}|^2 = \frac{(\kappa^2/4 + |\lambda|^2 + \bar{\omega}^2)^2}{(\kappa^2/4 - |\lambda|^2 - \bar{\omega}^2)^2 + (\kappa\bar{\omega})^2}. \quad (2.43)$$

A plot of Eq. 2.43 is presented in Fig. 2.11 which shows a few important results. The signal gain is maximum when the pump is resonant with the resonator frequency ( $\Omega = 0$ ), and the signal gain diverges at a critical pumping of

$|\lambda_{crit}|^2 = \kappa^2/4$ . The bandwidth at the peak gain in Fig. 2.11 is around 10 % of the bare resonator bandwidth  $\kappa$ , which means that the gain bandwidth of the RPA is strongly influenced by the bare resonator bandwidth. The gain-bandwidth product is constant i.e. higher gain means lower bandwidth. This can be interpreted as follows – for higher gain, a longer interaction time between the signal and the nonlinear medium is required and in order to increase this time the instantaneous bandwidth must be reduced.

This analysis also provides insight to the saturation power of these RPAs. For a Kerr based RPA the saturation power occurs when the signal strength is large enough such that it causes the resonator frequency to shift meaning that the pump becomes off-resonant  $\Omega \neq 0$  and the signal gain drops. Since the Kerr shift is proportional  $K|\alpha|^2$ , it shows that in a device with a larger Kerr, less pump drive is needed. However this also means that the Kerr shift due to the signal amplitude will become important at a lower signal power, lowering the overall dynamic range of the device.

### RPA Gain Considering The Resonator Photon Occupancy

The previous analysis considered the pump strength  $\lambda$  related to the pump amplitude *inside* the resonator. However in the laboratory setting we don't have direct access to  $\alpha$  instead having the input pump amplitude  $\alpha_{in}$ . These two quantities can be linked by solving the intra-resonator dynamics for the pump only [90, 42]. We need start with the QLE of the system in the form

$$\frac{dA}{dt} = -i\omega_0 A - iK A^\dagger A A - \frac{\kappa}{2} A + \sqrt{\kappa} A_{in} \quad (2.44)$$

where  $A(t) = (\alpha + a(t))e^{i\omega t}$  is the intra-resonator field decomposed in two components: a strong classical pump  $\alpha e^{i\omega t}$ , and a weak signal with a quantum field  $a(t)e^{i\omega t}$ . To get a relationship between the input pump amplitude and the pump strength inside the resonator we consider only the pump field such that



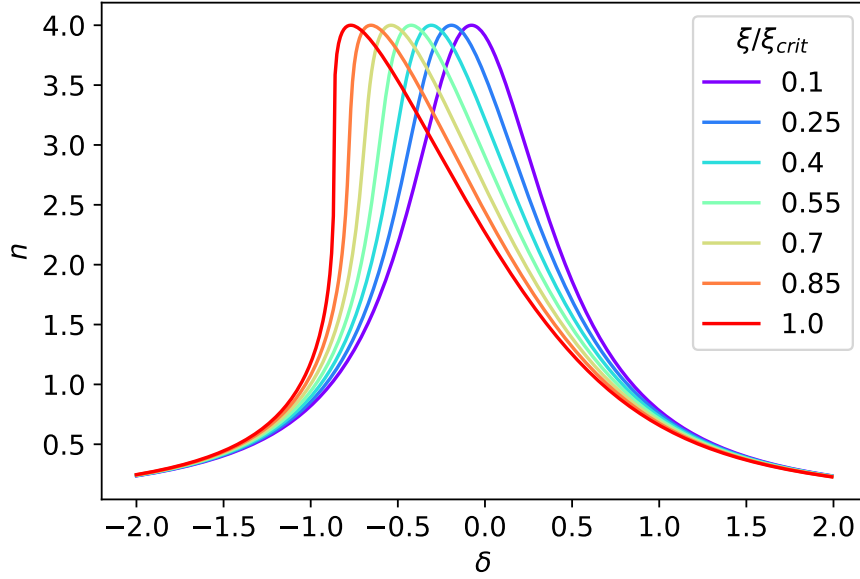


Figure 2.12: The normalised mean photon occupancy number inside the nonlinear resonant cavity excited by a single input tone at a range of different drive strengths that are normalised by the critical pump drive of  $\xi_{crit} = -1/\sqrt{27}$ .

$A(t) = \alpha(t)e^{i\omega t}$ , which can be substituted into Eq. 2.44. Then multiplying each side by their complex conjugate we get the following expression

$$|\alpha_{in}|^2 = \left( \left( \frac{\omega_p - \omega_0}{\kappa} \right)^2 + \frac{1}{4} \right) |\alpha|^2 - \frac{2(\omega_p - \omega_0)}{\kappa^2} |\alpha|^4 + \left( \frac{K}{\kappa} \right)^2 |\alpha|^6, \quad (2.45)$$

This equation can be reduced by converting to the following dimensionless parameters: pump to signal detuning  $\Delta$ , pump to bare resonator frequency detuning  $\delta$  and dimensionless pump strength  $\xi$ , which are given by

$$\Delta = \frac{\omega_p - \omega_s}{\kappa}, \quad \delta = \frac{\omega_p - \omega_0}{\kappa}, \quad \xi = \frac{|\alpha_{in}|^2 K}{\kappa^2}. \quad (2.46)$$

Eq. 2.45 can be rewritten to be a cubic in  $n$  such that

$$1 = \left( \delta^2 + \frac{1}{4} \right) n - 2\delta\xi n^2 + \xi^2 n^3, \quad \text{where } n = \frac{\kappa|\alpha|^2}{|\alpha_{in}|^2}. \quad (2.47)$$

where  $n$  is the mean photon number normalised by the input pump power. Eq. 2.47 can be solved numerically and has been plotted in Fig. 2.12, which shows that the peak occupancy number shifts down in frequency with increasing drive, characteristic to Kerr nonlinear resonators. At a critical power  $\xi_{crit} = -1/\sqrt{27}$  the derivative  $\partial n/\partial \delta$  diverges and thus the response of the RPA becomes extremely sensitive to small changes. This critical drive is negative due to the sign of the Kerr constant. For effective drive powers  $\xi/\xi_{crit} > 1$ , Eq. 2.47 has three real solutions, where the high and low photon number solutions are stable while the intermediate one is unstable [90], which defines the bifurcation regime. The RPAs we are considering operate at a power below this bifurcation regime. Although in this regime we are in the realm of bifurcation amplifiers that have been mentioned in the RPA development history section.

Having solutions for  $n$  means that we can add the signal tone back in such that  $A(t) = \alpha(t) + a(t)$  which can be substituted into Eq. 2.44 and linearised for the weak quantum signal, where only first order terms in  $a(t)$  are kept

$$\frac{da(t)}{dt} = i \left( \omega_0 - \omega_p - 2K|\alpha|^2 + i\frac{\kappa}{2} \right) a(t) - iK\alpha^2 a^\dagger(t) + \sqrt{\kappa}a_{in}. \quad (2.48)$$

This linearised equation can be solved in the same way as previously by decomposing  $a(t)$  into its Fourier components using

$$a(t) = \frac{\kappa}{\sqrt{2\pi}} \int_{-\infty}^{\infty} a_{\Delta} e^{-i\Delta\kappa t} d\Delta. \quad (2.49)$$

Eq. 2.48 can be re-written in terms of the Fourier components of  $a(t)$  using the dimensionless parameters defined in Eq. 2.45, to get the following expression

$$0 = \left( i(\delta - 2\xi n - \Delta) - \frac{1}{2} \right) a_{\Delta} - i\xi n e^{2i\phi} a_{-\Delta}^{\dagger} + \frac{a_{\text{in},\Delta}}{\sqrt{\kappa}}, \quad (2.50)$$

where  $\phi$  is the phase difference between the pump and signal. Eq. 2.48 mixes  $a_{\Delta}$  and its conjugate  $a_{-\Delta}^{\dagger}$ , therefore this equation can be used to account for the signal and idler input amplitudes  $a_{\text{in},\Delta}$  and  $a_{\text{in},\Delta}^{\dagger}$ , which yields a set of two equations linking the input and output fields. These equations can be used in conjunction to the boundary condition

$$a_{\text{out},\Delta} = \sqrt{a_{\Delta}} - a_{\text{in},\Delta}, \quad (2.51)$$

to derive an expression for the output field in the form

$$a(\Delta) = g_{s,\Delta} a_{\text{in}}(\Delta) + g_{i,\Delta} a_{\text{in}}^{\dagger}(-\Delta), \quad (2.52)$$

with  $g_{s,\Delta}$  and  $g_{i,\Delta}$  being the signal and idler gain given by

$$g_{s,\Delta} = -1 + \frac{i(\delta - 2\xi n - \Delta) + \frac{1}{2}}{(i\Delta - \lambda_{-})(i\Delta - \lambda_{+})}, \quad (2.53a)$$

$$g_{i,\Delta} = \frac{-i\xi n e^{2i\phi}}{(i\Delta - \lambda_{-})(i\Delta - \lambda_{+})}, \quad (2.53b)$$

$$\text{where } \lambda_{\pm} = \frac{1}{2} \pm \sqrt{(\xi n)^2 - (\delta - 2\xi n)^2}.$$

Eq. 2.53a can be used to find the signal power gain using  $G_s = |g_{s,\Delta}|^2$ , which can be solved numerically. Maximum signal gain is occurs when the signal to pump detuning is  $\Delta \approx 0$ , this is shown in Fig. 2.13. These gain curves show that with increasing pump drive the resonance shifts in line with the photon occupancy number shown in Fig. 2.12. For a given pump to bare resonator frequency detuning  $\delta$ , the variation of the gain with  $\Delta$  is qualitatively identical to the gain curve shown in Fig. 2.11. Therefore, in 4WM operation the pump

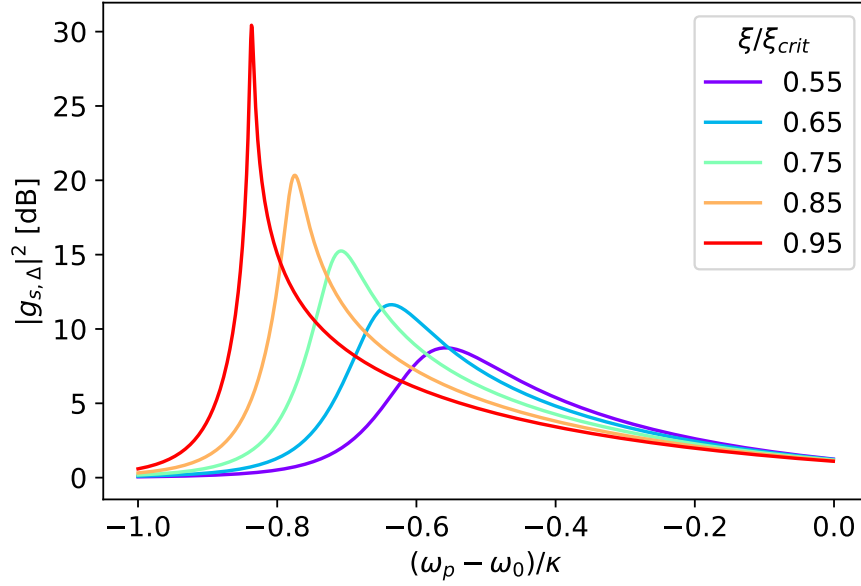


Figure 2.13: RPA signal gain for  $\delta = 0$  as function of the normalised pump detuning at different dimensionless pump strengths.

to signal detuning needs to be chosen wisely such that the signal could still be distinguished from the pump tone.

In this analysis, the signal has been assumed to be weak. However, the signal power can be taken into account by considering it in the calculation for the photon occupancy number. This analysis can be found here [86, 42].

#### 2.4.4 Travelling-Wave Parametric Amplifiers

Compared to RPAs, TWPAs are the second method in ensuring a high interaction time between the pump, signal and nonlinear medium. This is done by extending the nonlinear medium into an electrically long transmission line. As outlined in section 2.4.2, TWPAs can be operated in 4WM or 3WM mixing mode, where the former is a result of  $\chi^{(3)}$  nonlinearity and the latter can be stimulated as a result of a  $\chi^{(2)}$  nonlinearity when a flux or DC biasing is introduced. The operational bandwidth of TWPAs is dependent on the bandwidth over which a

phase matching condition between the pump, signal, and the generated idler can be maintained. The phase mismatch occurs due to the inherent dispersion of the transmission line and a Kerr-induced phase-mismatch due to the SPM and XPM making the pump travel with a higher phase velocity than the signal and the idler. Together these effects produce the total phase mismatch that needs to be compensated for to reach a high gain over a broad bandwidth. An additional consideration to ensure maximum gain is the prevention of the formation of a shock front. This is due to the 3rd order nonlinearity allowing for processes such as 3rd harmonic generation to occur, which generate harmonics of the pump at odd integer multiples of the pump frequency. Ideally, the propagation of these higher order harmonics should be blocked to prevent the generation of a shock front of interfering mixing products [92, 93, 94]. This shock front blocking is often achieved by dispersion engineering [13] or the use of an artificial transmission line [95, 96] with a natural cut-off frequency which blocks the propagation of these higher order modes. It will be shown in this section, when perfect phase matching is achieved the signal gain scales exponentially with the length of the nonlinear transmission medium. This is illustrated in Fig. 2.14 which shows the exponential increase of a weak signal amplitude as it co-propagates within a nonlinear medium in the presence of a strong pump, which is undepleted as a result of the parametric process. Also shown in the figure is that the generated idler grows at the same rate as the signal, hence the idler will be nearly at the same output power as the signal by the end of the amplification process.

This section will cover a brief development history of TWPAs including the exploration of different dispersion engineering and phase-mismatch managing schemes both in Josephson and kinetic inductance based variants. Following this, the theory of TWPAs will be covered, which is heavily based on the results found through nonlinear fibre optics where the first TWPAs have been realised. The formalisms there clearly explain the origin of the key equations needed to describe TWPAs.

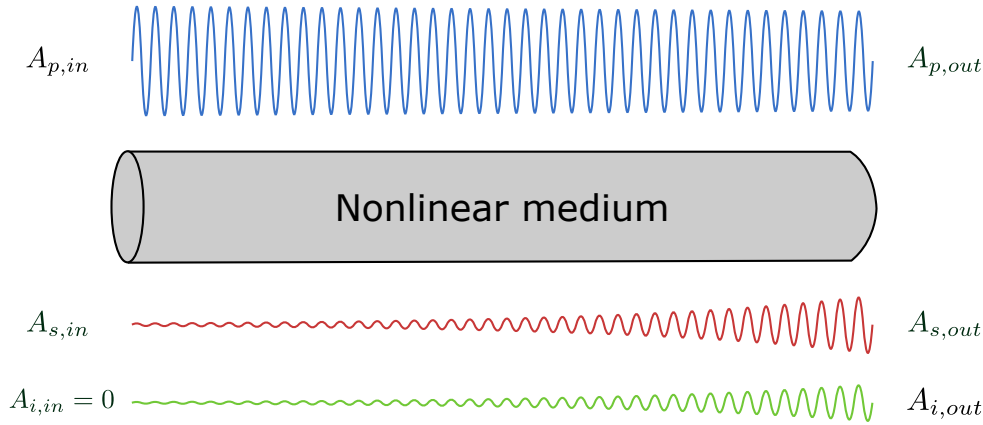


Figure 2.14: A cartoon showing exponential parametric amplification within a nonlinear medium of a weak signal in the presence of a strong pump. Here the pump, signal and idler complex magnitudes are represented by  $A_p$ ,  $A_s$  and  $A_i$ , respectively. The idler is assumed to be instantaneously generated at  $t = 0$ .

### Development History

The first experimental realisation of a superconducting TWPA was achieved by Eom et al. [13] in 2012 using the kinetic inductance nonlinearity of monolithic layer of NbTiN. A few years after in 2015 the first Josephson based TWPA were realised [97, 60] using over 1000 Josephson junctions distributed over the transmission line.

The development of TWPAs initially progressed with different implementations of dispersion engineering schemes in order to attain broadband phase matching. The initial dispersion engineering schemes were in the form of periodic loadings patterns [13] of transmission line or via periodic resonant structures [98] alongside the nonlinear medium, referred to as resonant phase matching. These methods introduced anomalous dispersion to the transmission line at frequency that is positioned in the middle of desired gain band. The pump tone could be positioned near this dispersion feature to bring the pump tone back into phase matching with the signal and idler. Recently, developments have been made in the JTWPA field to achieve phase matching by reversing the sign of Kerr phase mismatch such that it compensates for the mismatch due the dispersion of the

line by engineering the nonlinearity using SNAILs[99], these are referred to as reverse-Kerr JTWPAs [100], other schemes include left-handed JTWPAs [101] which includes changing the sign of the refractive index of the line such that phase matching is autonomously achieved without the need for any dispersion engineering. Additionally, a Floquet-Mode JTWPA [102] scheme has been proposed that introduce true directionality to prevent the propagation of backward travelling waves and mitigate the effect of sideband generation on the amplifier added noise. The other developments have been in the push for 3WM operation. This was first demonstrated experimentally in a KI TWPAs in 2016 [61] using a DC bias to induce a  $\chi^{(2)}$  nonlinearity, while in JTWPAs this was first achieved in 2017 [103] using rf-SQUIDS which are similar to SNAILs.

KI-TWPAs and JTWPAs have been split in their applications, partly due to the difference in the pump power requirements between the two types of devices. In JTWPAs the scaling current is dictated by the critical current of the junctions, which is orders of magnitude lower than the critical current of thin superconducting transmission lines of KI-TWPAs. This difference means that the required pump power is much smaller in JTWPAs, which is a necessary requirement for applications for the readout of superconducting qubits, where a strong pump tone may cause decoherence if not filtered correctly. However, this lower scaling current comes at a cost of reduced saturation power compared to the KI-TWPAs which are being aimed at applications such as the readout of a larger number of MKIDs, where the high current handling capability and high saturation power come in very useful (see review by Esposito *et al.* [12] for a comparison of the saturation powers). Therefore, JTWPAs are being primarily developed for quantum limited operation at frequencies below  $\sim 15$  GHz, with focus on broadband matching and 3WM operation. There is a recent push for commercialisation <sup>45</sup> of JTWPAs also. On the other hand KI-TWPAs are being

---

<sup>4</sup><https://silent-waves.com/>

<sup>5</sup><https://www.quantware.eu/>

aimed more towards higher power applications and higher frequencies needed for astrophysics. It was found recently that KI-TWPAs could be used as a replacements for transistor based amplifiers and operated at 4 K with much lower heat output and similar noise performance [20]. In addition, it was shown that the operational bandwidth with 3WM can be extended to 3-30 GHz [18].

### TWPA Dynamics

The first TWPAs were realised using nonlinear optical fibres where the foundational expressions for the system dynamics were derived [66, 104]. The formalisms from optical parametric amplifiers (OPAs) with isotropic nonlinear media where the second order nonlinearity  $\chi^{(2)}$  vanishes and the third order nonlinearity  $\chi^{(3)}$  dominates are analogous to that of Josephson or kinetic inductance TWPAs operating in four wave mixing mode (see Section 2.4.1). We will therefore cover the methods used in nonlinear optics to show how the TWPA dynamics are derived.

Beginning with an electric field  $\vec{E}(x, z, t)$  polarised along the x-axis while propagating in the z-direction with three continuous waves: the pump ( $\omega_p$ ), the signal ( $\omega_s$ ), and the idler ( $\omega_i$ ). The sum of these three fields  $j = \{p, s, i\}$  is given by

$$\vec{E}(x, z, t) = \frac{\vec{u}_x}{2} \sum_{j=\{p,s,i\}} E_j(x, z) e^{i(k_j z - \omega_j t)} + c.c., \quad (2.54a)$$

$$k_j = \frac{n_j}{c} \omega_j, \quad j = \{p, s, i\} \quad (2.54b)$$

where  $\vec{u}_x$  is the polarization unit vector along the x-direction,  $k_j$  is the propagation constant,  $\omega_j$  is the angular frequency,  $n_j$  is the refractive index, and  $c$  is the speed of light. Each electric field  $E_j$  is decomposed into its spatial distribution  $F_j(x)$  and its amplitude  $A_j(z)$  such that  $E_j(x, z) = F_j(x)A_j(z)$ . Then these fields



from Eq. 2.54 and the polarization from Eq. 2.35 are substituted into the wave equation given by

$$\nabla^2 \vec{E} - \frac{1}{c^2} \frac{\partial^2 \vec{E}}{\partial t^2} = \mu_0 \frac{\partial^2 \vec{P}_L}{\partial t^2} + \mu_0 \frac{\partial^2 \vec{P}_{NL}}{\partial t^2}, \quad (2.55)$$

where  $\vec{P}_L$  and  $\vec{P}_{NL}$  are the linear and nonlinear parts of the polarization, respectively, which are found by substituting Eq. 2.54 into Eq. 2.35. It should be noted that the time dependence of the field components has been neglected meaning that we assume quasi-continuous-wave conditions. Integrating over the spatial mode profiles [42, 66], provides the following coupled mode equations for the evolution of the wave amplitudes  $A_j(z)$  inside the nonlinear medium

$$\frac{dA_p}{dz} = \frac{in_{NL}\omega_p}{c} \left[ \left( f_{pp}|A_p|^2 + 2 \sum_{j=\{p,s,i\}} f_{pj}|A_j|^2 \right) A_p + 2f_{psi}A_p^*A_sA_ie^{-i\Delta k_L z} \right], \quad (2.56a)$$

$$\frac{dA_s}{dz} = \frac{in_{NL}\omega_s}{c} \left[ \left( f_{ss}|A_s|^2 + 2 \sum_{j=\{p,p,i\}} f_{sj}|A_j|^2 \right) A_s + 2f_{spi}A_p^2A_i^*e^{i\Delta k_L z} \right], \quad (2.56b)$$

$$\frac{dA_i}{dz} = \frac{in_{NL}\omega_i}{c} \left[ \left( f_{ii}|A_i|^2 + 2 \sum_{j=\{p,p,s\}} f_{ij}|A_j|^2 \right) A_i + 2f_{ips}A_p^2A_s^*e^{i\Delta k_L z} \right], \quad (2.56c)$$

where  $\Delta k_L = 2k_p - k_s - k_i$  is the linear phase mismatch,  $n_{NL}$  is the nonlinear refractive index given in Section 2.4.1,  $f$  is the overlap integral between the spatial distribution of the fibre modes with the number of indices indicating the modes that should be considered. For simplicity, the overlap is assumed to be the same for all modes and represented by a constant  $f$ . This allows  $f$  to be factorised and the nonlinearity for mode  $j$  to be defined as

$$\gamma_j = \frac{n_{NL}\omega_j f}{c}. \quad (2.57)$$

Under the assumption that the pump amplitude is much stronger than the signal and idler  $|A_p| \gg |A_s|, |A_i|$  and that the pump is not depleted as a result of the amplification process  $|A_p(0)| \approx |A_p(z)|$ , Eq. 2.56a can be simplified to

$$\frac{dA_p}{dz} = 3i\gamma|A_p|^2 A_p, \quad \text{with solution} \quad A_p(z) = A_{p0}e^{3i\gamma P_0 z}, \quad (2.58)$$

where  $P_0 = |A_p(0)|^2$  is the incident pump power. The non-linear phase of  $3\gamma P_0 z$  is the self-phase modulation of the pump. This simplified expression for the pump amplitude and the strong pump approximation allow for Eq. 2.56b and 2.56c to be rewritten as

$$\frac{dA_s}{dz} = 2i\gamma [2P_0 A_s + A_{p0}^2 e^{i\theta z} A_i^*], \quad (2.59a)$$

$$\frac{dA_i}{dz} = 2i\gamma [2P_0 A_i + A_{p0}^2 e^{i\theta z} A_s^*], \quad (2.59b)$$

where  $\theta$  is nonlinear phase mismatch

$$\theta = 2(k_p + 3\gamma P_0) - k_s - k_i = \Delta k_L + 6\gamma P_0, \quad (2.60)$$

which only considers the SPM contribution to the total phase mismatch. Eq. 2.59 can be further simplified [42] by introducing an auxiliary field expression  $a_j(z) = A_j(z) \exp(-4i\gamma P_0 z)$  with  $j = \{s, i\}$ . The nonlinear phase shift in this expression accounts for the cross phase modulation produced by the pump on the signal and idler. This allows the coupled mode equations shown in Eq. 2.59 to be written as

$$\frac{da_s}{dz} = 2i\gamma A_{p0}^2 e^{i\Delta k z} a_i^*, \quad (2.61a)$$

$$\frac{da_i}{dz} = 2i\gamma A_{p0}^2 e^{i\Delta k z} a_s^*, \quad (2.61b)$$

where  $\Delta k$  is the total phase mismatch including the SPM of pump ( $2 \times 3\gamma P_0$ ) and the XPM on the signal and idler ( $-4\gamma P_0$  for each tone) given by

$$\Delta k = \theta - 8\gamma P_0 = \Delta k_L - 2\gamma P_0. \quad (2.62)$$

Eq. 2.62 shows that due to the difference in SPM and XPM there is an overall nonlinear phase mismatch which grows with increasing pump power. By considering the boundary conditions and the initial conditions such that the signal and idler enter at  $z = 0$ , and at  $t = 0$ ,  $a_i(0) = 0$ , and using the expression  $P_s(z) = |a_s(z)|^2$ , Eq. 2.61 can be solved to get the following relation for the signal power

$$P_s(z) = P_s(0) \left[ 1 + \left( \frac{\gamma P_0}{g} \right)^2 \sinh^2(gz) \right], \quad (2.63a)$$

$$g = \sqrt{(\gamma P_0)^2 - \left( \frac{\Delta k}{2} \right)^2}, \quad (2.63b)$$

where  $g$  is the parametric gain coefficient. Eq. 2.63 for the signal power at a distance  $z$  is quite insightful since it shows that the total phase mismatch  $\Delta k$  is harmful for the signal gain and it should be kept as close to 0 as possible. In other words the gain coefficient  $g$  must remain real to expect exponential gain. The signal gain after travelling a distance  $z = L$  in the nonlinear medium can be expressed as

$$G_s = \frac{P_s(L)}{P_s(0)} = 1 + \left( \frac{\gamma P_0}{g} \right)^2 \sinh^2(gL). \quad (2.64)$$

Eq. 2.64 can be explored under 2 limits. In the case where no special dispersion engineering has been done such that the total phase mismatch dominates  $\Delta k \gg \gamma P_0$ , the parametric gain coefficient becomes imaginary  $g = i|\Delta k/2|$  and the signal gain becomes

$$G_s \approx 1 + (\gamma P_0 L)^2 \left[ 1 - \frac{(\Delta k L)^2}{3} - \frac{2(\Delta k L)^4}{45} - \dots \right], \quad (2.65)$$

where a Taylor expansion of  $\sinh^2(gL)$  was used. This shows that the gain only scales quadratically with  $\gamma P_0 L$ .

In the other case where almost perfect matching is achieved such that  $\Delta k \ll \gamma P_0$ , the parametric gain coefficient is real,  $g = \gamma P_0$ . Here the signal gain can be expressed as

$$G_s = 1 + \sinh^2(\gamma P_0 L) \approx 1 + \frac{1}{4} e^{2\gamma P_0 L}, \quad (2.66)$$

which shows an exponential scaling with  $\gamma P_0 L$ . This result highlights the importance of ensuring that the phase mismatch is kept as low as possible in a  $\chi^{(3)}$  amplifiers to achieve gain that scales exponentially with TWPA length. However, achieving  $\Delta k \sim 0$  will only be possible over a limited band since for large detunings between the pump and signal, a residual linear phase mismatch  $\Delta k_L$  will remain due to the dispersion of the medium itself.

This analysis can be applied to JTWPAs and KI-TWPAs by considering the dispersion relation for a specific transmission line that is under investigation as well as the nonlinear constant  $\gamma$  for the nonlinearity in question. This dispersion relation will impact the linear phase mismatch  $\Delta k_L$ , while the type of nonlinearity will impact  $\gamma$ . The dispersion relation can be derived by cascading the ABCD transfer matrices (see Appendix B in [65]) of the transmission line unit cells which

are then used to calculate the  $S_{21}$  scattering matrix. The dispersion per unit length can then be extracted using  $k = -\text{unwrap}[\arg(S_{21})]/L$ .

It should be noted that this analysis only includes the fundamental harmonic of the pump and first idler that is generated. An analysis including higher order harmonics and mixing products can be found here [75, 94]. Additionally, a 3WM analysis of TWPAs can be found in [75, 105, 65].

This analysis will be applied specifically to a W-band KI-TWPA based on a ridge gap waveguide transmission line. More details on this can be found in Chapter 5.



## Chapter 3

# Cryogenic Measurement System

### 3.1 Introduction

A low device temperature is critical to the operation of a superconducting parametric amplifier. It is not sufficient to only cool down the amplifier to a temperature just below the superconducting critical temperature. Indeed, by considering the exponential scaling of the surface resistance with  $-T_c/T$  [57] that can be inferred from real part of the surface impedance (see Section 2.2.3), it is evident that operating temperature should be kept as low as possible. In practice, for this work the targeted operating temperature was around 1 K in an attempt to demonstrate that such an operating temperature was sufficiently low for superconducting devices with a critical temperature near 15 K, while achieving sufficient gain and noise level. In addition, the relatively high cooling and simplicity of  $^4\text{He}$  adsorption coolers, compared to much more expensive dilution refrigerators with base temperatures below 100 mK, makes this temperature more widely accessible in research and industrial environments where the described amplifiers could be employed. Nonetheless, cooling a device to 1 K temperatures and still being able to connect it to the outside world requires careful design of the body of the cryostat, temperature control systems, and the cryogenic cabling that connect to

the device under test (DUT).

This chapter aims to cover the approach to cryogenics from a user's perspective highlighting: basic design and material choices for 1 K capable cryostats; the procedures that should be followed during a routine cooldown; the operational principles of 1 K sorption coolers; the method by which radio/microwave frequency excitations are brought down from room temperature to a DUT; followed by measurements of one of these devices. It should be noted that the cryostat discussed in this chapter provides a generous cooling power budget at all cooling stages meaning that the 1 K base temperature can be reached and maintained for the full duration of a given measurement on a device while a number of parasitic heat loads are still acting on the DUT. It should be noted that the cooling power budget of this system could be increased by further through a number of changes such as the isolation of the 1 K cooling stage by including a radiation shield and fully gold plating the metals at each cold stage of the cryostat. However, this was not needed due to the cooling budget (see Fig. 3.1) being much higher than these parasitic heat loads. Therefore, the coldest stages of the cryostat were chosen to be less isolated to allow for a larger cooling volume and ease of access. This cooling system is fully custom and has been used for a number of previous projects prior to the current project. The fridge has been designed to be rugged, fast cooling and operated with relatively little intervention. Operation at lower temperatures such as 100 mK with single shot dilution coolers would require much more careful control of these parasitic heat sources to ensure that the cooling power and achieved hold time (ideally, hours between having to recycle) could be sufficient to test the parametric amplifiers explored in this project.

## 3.2 Cryostat Consideration

The three main sources of heat that a cryostat must mitigate are convection, radiation, and conduction. Convective heat loads are due to the exchange of



energy via the molecules that are present in the air, which are mitigated by hermetically sealing the cryostat and putting it under a vacuum. A system of a roughing pump and a turbo molecular pump can be used to reach a pressure of  $10^{-3}$  to  $10^{-5}$  mbar at room temperature, which is sufficient to begin the cool down process. In addition, it is important to ensure that the chosen materials within the vacuum chamber do not outgas strongly to ensure that a low enough vacuum can be maintained. Outgassing is a phenomena through which trapped gas or vapour is released into the chamber once a vacuum is present. Strong outgassants include many porous materials. Radiative heat is a result of black body radiation from materials at different temperatures, the method to mitigate this is to use radiation shields with low emissivity that protect subsequent cold stages from the stage before. This low emissivity can be achieved by gold plating parts in the cryostat as well as using reflective materials such a multi-layer insulation [106] composed of multiple layers of reflective polymers. Conductive heat loads are a result of heat transfer through solids that are in contact with one another as a result of their thermal conductivity. These conductive heat loads are mitigated by reducing the cross section of any parts that connect two separate temperature stages together and to use materials with a low thermal conductivity. This is specifically important in the physical construction of the cryostat, since the structure needs to be strong enough without using excessive material. Low thermal conductivity materials include stainless steel, and carbon fibre and various other composite materials, where most of these are used as thin wall tubes rather than solid rods. High conductivity materials include a number of metals such as copper, brass and aluminium, which are arranged in order of decreasing thermal conductivity.

In addition to the materials used for the structure of the cryostat, the materials of the wiring must be considered. Each thermometer and heater contributes to an overall heat load on the lowest stages of the cryostat. With this in mind, the minimum wire cross section should be used for any wiring that is connecting

### *3: CRYOGENIC MEASUREMENT SYSTEM*

parts at different temperature stages where sufficient thermal sinking should be employed to ensure that as much heat as possible is deposited on the highest temperature stages. Manganin which is name for an alloy composed of copper, manganese, and nickel is commonly used for inter temperature stage wiring due its low thermal conductivity and sufficiently high electrical conductivity. Wiring that is used for components at the same temperature stage can be standard copper.

Another consideration for material choices is the thermal contraction that occurs when the material is cooled to a cryogenic temperature. This is important when fasteners are used to secure parts to one another, which may be tightly secured at room temperature but may become loose at cryogenic temperatures. This can be detrimental if the part that loosens is the DUT, which would mean that the device may not have a sufficient thermal link to the cold stage. Usually the fasteners in cryostats are brass but sometimes stainless steel is used. It is important to note that brass shrinks more than stainless steel which means that a brass screw should be used with a stainless steel washer to ensure an extra tight hold. However, one should be careful since this differential thermal contraction can be too high and cause imprints on parts. One can safely use fasteners of the same material type to avoid such issues. In addition, when devices that are sensitive to magnetic fields are being tested in the cryostat it is important to ensure no materials with magnetic impurities are used since the can cause stray fields to be present in the cryostat and trapped by any superconducting materials as they transition to below the critical temperature. One should be careful when choosing stainless steel fasteners and parts since some grades of stainless steel have some magnetic impurities.

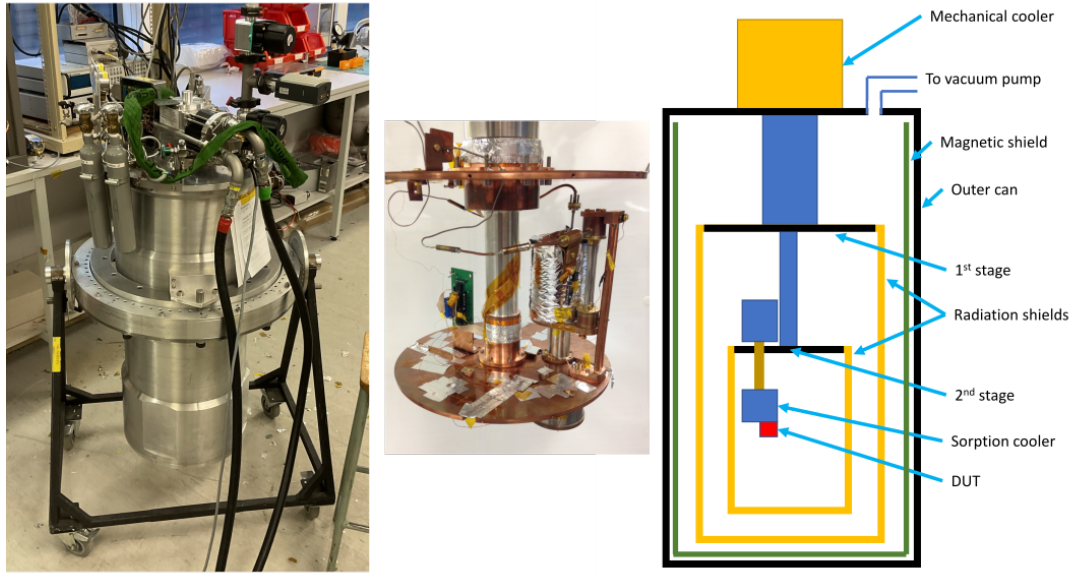


Figure 3.1: The left panel shows a photograph of a cryostat on a mobile frame. The middle panel shows the the 4 K stage of the cryostat with a 1 K sorption cooler and a heat switch mounted. The right panel shows a schematic drawing of the cryostat which includes the free standing  $\mu$  metal magnetic shield as well as the radiation shields that get secured to the 40 K and 4 K stages via screws.

### 3.2.1 Reaching Base Temperature

The cryostat shown in Fig. 3.1 operates using a Gifford-McMahon cold head<sup>1</sup>. This cold head was chosen due to the high cooling power for its size and price while being able to operate at any angle, which allows for more freedom with cryostat design, such as designing the cryostat with the cold head upside down. The main disadvantage of the GM cryo cooler is in the vibrations that are generated as it operates, which may result in additional noise in the cryogenic coaxial cables leading up to the DUT [108]. This effect should be characterised for the specific system used in this project to evaluate if the noise generated is significant with rectangular waveguide based systems.

The GM coldhead runs in a closed loop cycle with a  $^4\text{He}$  compressor which provides high pressure gas. This gas is exchanged via a two stage system (40

<sup>1</sup><https://www.shicryogenics.com/product/rdk-415d2-4k-cryocooler-series/>

### 3: CRYOGENIC MEASUREMENT SYSTEM

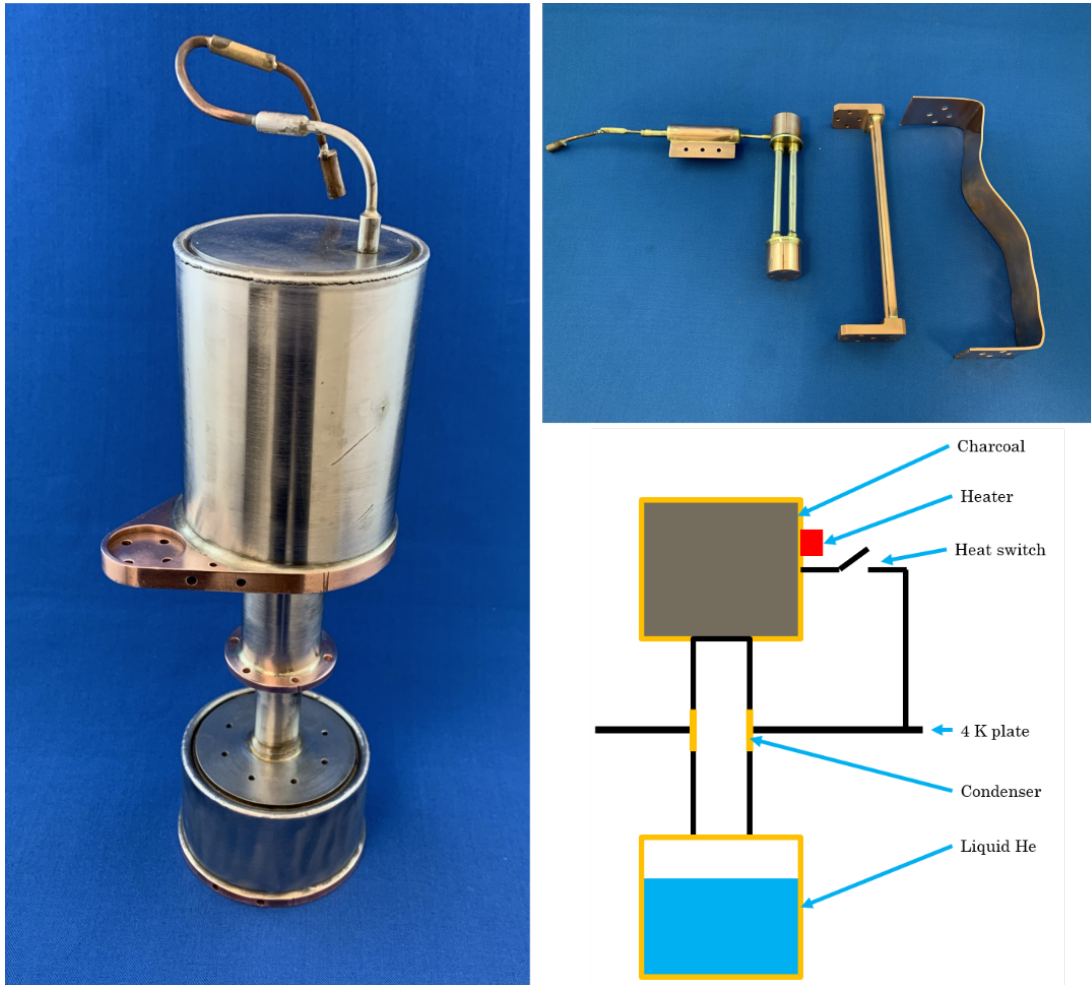


Figure 3.2: The left panel shows the 1 K helium-4 sorption cooler, which can also be seen mounted in the cryostat in Fig. 3.1. The upper right panel shows a picture with the convective heatswitch and copper brackets used to thermally connect the top of the switch to the 4 K plate as seen in Fig. 3.1. The lower right panel shows a schematic of the sorption cooler. The chamber which contains the charcoal is referred to as the cryopump while the chamber with liquid He is the evaporator pot. This 1 K system was developed by May *et al.* [107].

K and 4 K) with their own heat exchangers, and it is then return to the low pressure side of the cold head and taken back to compressor for re-pressurisation. The helium compressor is cooled by a water chiller which further dissipates the heat generated from the cooling process. This system allows a temperature as low as 3 K to be reached as shown by the heat load map in Fig. 3.3. During the process of cooling, the pressure inside the cryostat drops to as low as  $10^{-6}$  mbar

due to a process called cryo pumping, which traps remaining gasses on the cold surfaces on the inside of the cryostat.

Attaining temperatures lower than 4 K requires additional coolers mounted to the 2nd stage of the mechanical cooler [109], a schematic of a sorption cooler capable of 700 mK is shown in Fig. 3.2. A sorption cooler works by exploiting the vapour pressure curve of helium-4 or helium-3 shown in Fig. 3.4 as well as the ability of charcoal to adsorb helium gas at temperatures of around 4 K. At room temperature a sorption cooler is charged with around 80 bar of helium-4 or helium-3, which becomes approximately 1 bar at 4 K. At this temperature the charcoal absorbs nearly all the helium it has been charged with, so in order to get cooling the charcoal is heated to roughly 40 K which releases the helium gas. As the gas moved down the condenser it liquefies in the bottom chamber of the sorption cooler. Once all the helium has liquefied, the charcoal at the top of the cooler is cooled back down to 4 K which causes the charcoal to begin adsorbing helium once again. As a result of this, the helium vapour pressure in the lower chamber drops meaning that the temperature also drops depending on the pressure that is reached. The cooler will continue to run until the liquid has completely evaporated and is adsorbed onto the cryopump, at which point the cycle may be repeated. The base temperature that can be reached depends on the isotope of helium that is used, with helium-3 the base temperature can be as low as  $\sim 300$  mK while for helium-4 this is closer to  $\sim 700$  mK.

The temperature of the cryopump of the sorption is controlled via a convective heat switch that is connected to the 4 K stage. The heat switch works in a similar method to the sorption cooler except the desorbed helium is used to fill the stainless steel tubes with helium gas which cause convective currents to thermally connect the top and bottom of the switch. The use of such a heat switch meant that the sorption cooler could be operated entirely in a closed cycle using only heaters, hence without the need for cold moving parts, cold o-rings or external gas connections. The sustainable heat load of the 1 K system is shown

### 3: CRYOGENIC MEASUREMENT SYSTEM

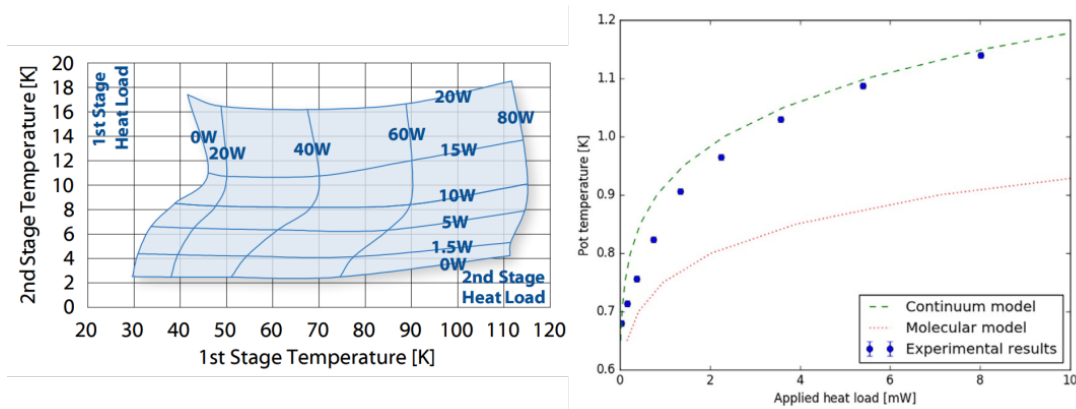


Figure 3.3: The left panel shows the heat load characteristics of the Sumitomo RDK-415D GM cryocooler (see footnote). The vertical lines represent heat loads on the 1st stage, while the horizontal line on the 2nd stage. The crossing points between these two lines shows the temperature of each stage with the set heat loads. The right panel shows the evaporation pot temperature for different heat loads of the 1 K helium-4 sorption cooler. The hold time for a heat load of 0.7 mW at a temperature of  $\sim 820$  mK was 22 hours [107]. The lines labelled the continuum and molecular model refer to the theoretical modelling of the expected pot temperature under different pressures and hence different flow regimes. These regimes are dictated by the Knudsen number  $K_n = l/L$  with  $l$  being the mean free path and  $L$  the characteristic length scale. At the lowest temperatures  $K_n$  is above the upper limit for the continuum regime while still below the minimum limit for the molecular flow regime i.e. in an intermediate regime in which the measured data falls (see [107] for full details).

in Fig. 3.3, where the hold time with an artificial heat load of  $\sim 1$  mW is roughly 22 hours. The heat load expected from the superconducting devices tested in this project is a result of using a pump tone up to -10 dBm in power which would correspond to around 0.1 mW of load. Radiative heat loads from the 4 K stage and radiation to the 1 K pot are expected to be orders of magnitude smaller than the radiative loading through the waveguide feeds connecting the DUT (see Section 3.2.2). The conductive heat load through the waveguide chain that includes thermal breaks (see Section 3.2.2) should be on the order of tens of  $\mu$ W. This means that the bottom of the 1 K fridge can be directly connected to a device without the need for separate radiation shield.

The temperature of the components is readout by two wire diode thermometers or four wire resistance temperature diodes (RTDs), where the four wire

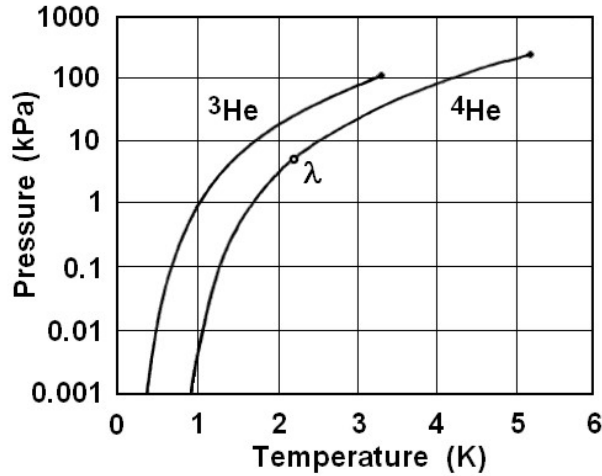


Figure 3.4: The saturated vapour pressure curves of helium-4 and helium 3. Showing the minimum temperature that can be reached by pumping on the saturated vapour above the liquid helium.

method avoids the resistance of the wires impacting the quality of the calibration. These temperature sensors (up to 4 diodes and 4 RTDs) could be readout by a readout controller system referred to as the SNAP unit, which could also control up to 8 heaters. This controller could also be programmed with PID commands and more complicated control procedures using XML scripting. In addition, a Lakeshore 372 AC resistance bridge was used for the readout of RTDs.

### 3.2.2 Cryogenic Device Testing

In order to test a device it needed to be connected to the outside world via some system of feeds and thermal breaks. In this case, the devices were designed to be tested with Ka band (26.5 to 40 GHz) rectangular waveguide. Conventionally, in rectangular waveguide systems thermal breaking is achieved by using a section of thin wall stainless steel waveguide to reduce the conductive heat loading between temperature stages. For this work, thermal breaks incorporating a hollow gap were used where the thermal break was held rigidly with pultruded carbon fibre tubes, which is shown in Fig. 3.5. In addition, the waveguide inputs on the cryostat had to be hermetic to ensure that the vacuum was not broken. This was



### 3: CRYOGENIC MEASUREMENT SYSTEM

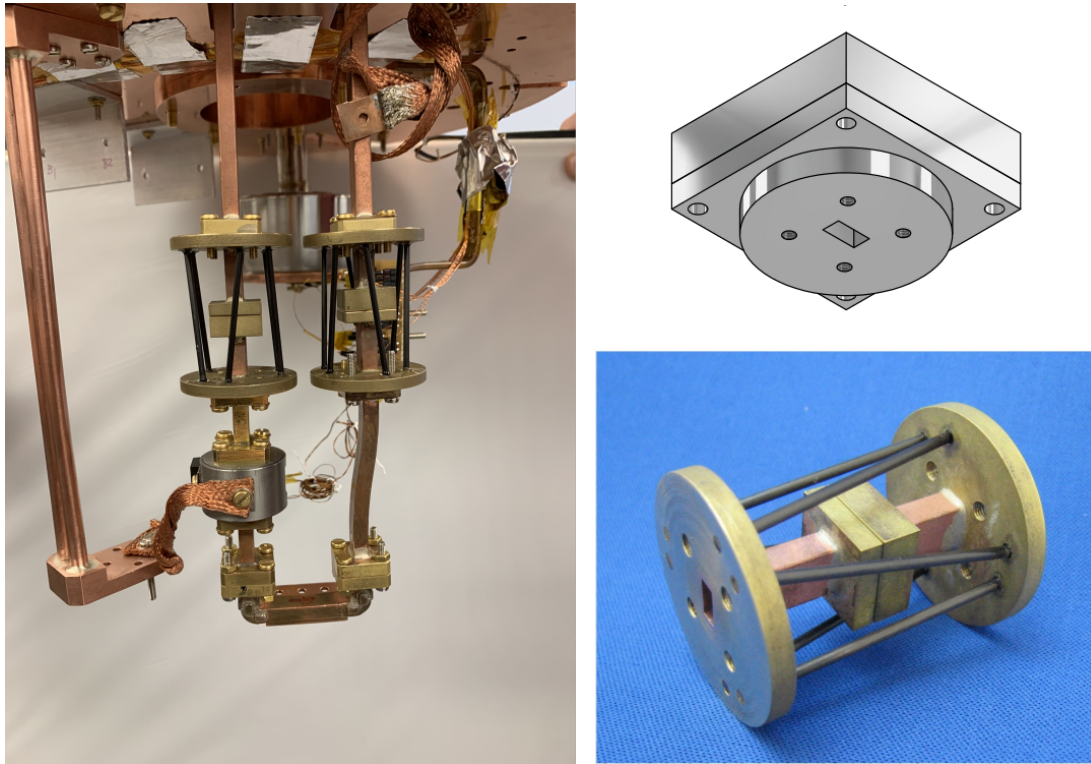


Figure 3.5: The left panel shows a niobium pillbox cavity mounted in the cryostat demonstrating the use of waveguide thermal breaks (see Section 3.3 for more information about the mounted device). The DUT in this case is directly connected to the 4 K stage via a copper braid but it can be connected to the 1 K sorption cooler behind it instead. The upper right panel shows a screenshot of an underside of a CAD model of a hermetic Ka band feedthrough that is used at the top of the cryostat (see right panel of Fig. 3.6 and right panel of Fig. 3.8 for a schematic drawing). The feedthrough is made of two parts between which a thin mylar film that is transparent to microwave radiation is compressed with an o-ring to create a vacuum seal. The lower right panel shows a close up of the Ka band thermal break that was developed by Melhuish *et al.* [110].

achieved by compressing a thin mylar film between two pieces of the feed with a o-ring to prevent vacuum leaks. The mylar film did let through some air particles but this effect could be reduced by using a thicker film. The use of these thermal breaks as opposed to sections of stainless steel waveguide significantly improved the losses of the whole waveguide chain. The loss from room temperature down to the device and back again was around 2 to 3 dB over the whole Ka band. Since the tested devices were superconducting, a magnetic shield was included in the



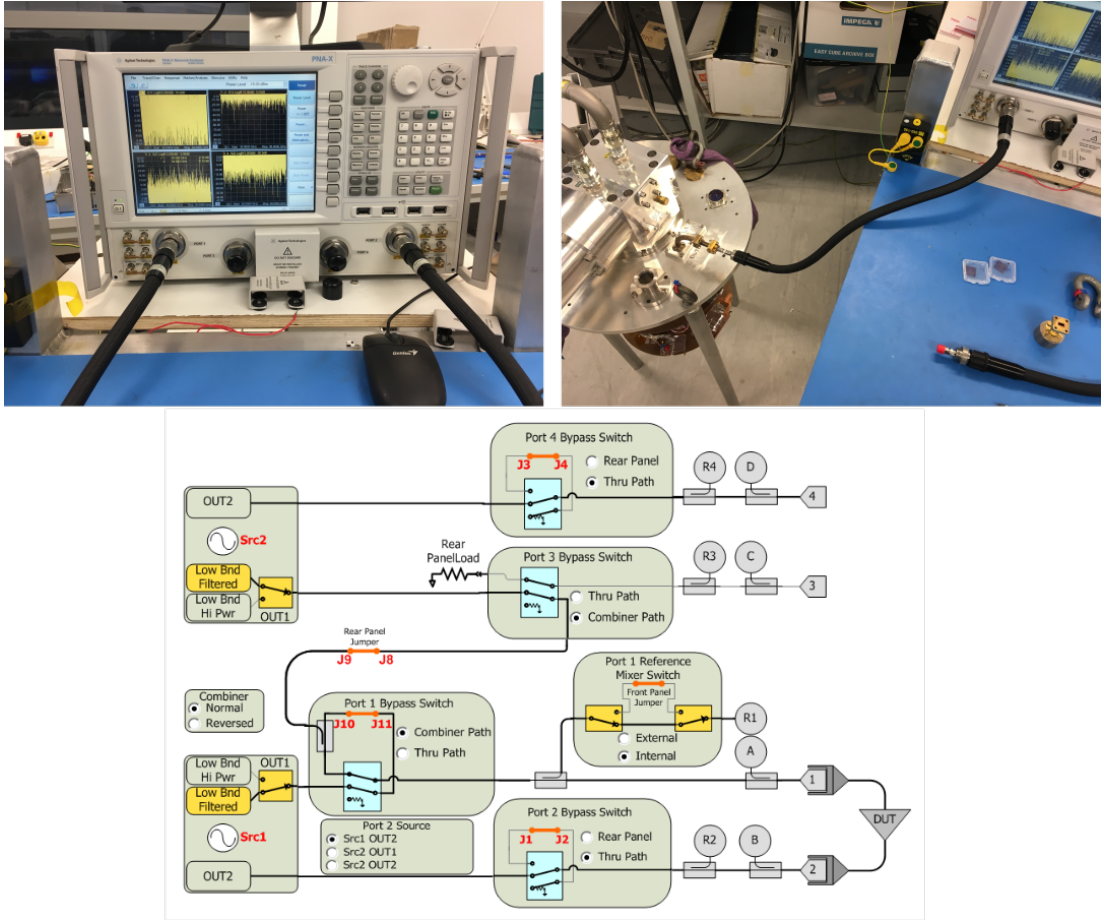


Figure 3.6: The left panel shows a photograph of the Keysight N5245A PNA-X which could operate in the range of 10 MHz to 50 GHz and had 2.4mm coaxial connections. The right panel shows one of the VNA coaxial lines connected to the rectangular waveguide hermetic feedthrough via a transition from 2.4 mm coaxial to Ka band waveguide. The lower panel shows the internal path configuration of the VNA. In the image it is configured for the routing of the outputs from the two internal synthesisers through a single port that is needed for mixing measurements.

cryostat, to reduce the stray fields that could be captured by the superconducting surfaces, which may cause unpredictable behaviour and additional loss. This shield was in the form of an open top  $\mu$ -metal can that was placed on the inside of vacuum can. This magnetic shield remained at room temperature since it was not in contact with any of the cold parts of the cryostat.

### 3.2.3 Microwave Testing Equipment

The devices that were fabricated in this project were tested with a Keysight N5245A vector network analyser, which is shown in Fig. 3.6. The VNA contains two internal synthesisers that could be used to test multiple devices connected at once or the internal routing of the VNA could be reconfigured electronically to allow for both synthesisers to route their outputs through a single port, which is shown by the layout in Fig. 3.6. This combined synthesiser configuration allowed for the signal and pump to be generated within the VNA, be combined internally and passed to the input of the cryostat. An alternative for two input measurements would be to use separate synthesisers that are combined externally. The VNA could output a maximum of 13 dBm through each synthesiser, however, the maximum power difference between the two synthesiser output could be a maximum of 30 dB due to a shared internal attenuator bank. The main advantage of using two external synthesisers is that the limit on the output power difference is avoided. However, since many two tone measurements require synchronised changes in output frequency (see Fig. 3.9) of the two synthesisers these would need to be centrally controlled.

A number of measurements were performed by programming the VNA via routines written in VBscript using the syntax that was provided by Keysight. These routines were instrumental in carrying out measurements that would be impractical to perform manually and would be prone to user error. Example of such measurements are shown in Fig. 3.9 which involve hundreds of S parameters sweeps at a number of powers or thousands of power spectra of two tone measurements at a given frequency spacing between the inputs with repetitions at different combinations of input powers. For the latter a routine was written that set frequency spacing between the two input tones and moved them with a constant spacing across the profile of the resonance, while at each frequency step a spectrum was recorded which could be used for analysis. This method was used

for the work in Section 3.3 and Section 4.4.2.

### 3.3 Circular Waveguide Resonator

The proceeding sections describe a circular waveguide resonator with an unexpected nonlinear behaviour. This work is included in this chapter since it was used to establish the cryogenic measurement techniques needed to measure nonlinear superconducting resonators. Specifically, it is demonstrated how to use the VNA to perform automated S-parameter sweeps at different powers as well as the two tone sweeps across resonance profiles with a constant frequency spacing to show mixing products and parametric gain.

This circular waveguide resonator was in the form of a niobium pillbox cavity. The goal of this project was to understand what the source of the nonlinear behaviour was and whether it could be used to attain parametric gain. It was shown that indeed, the cavity possessed nonlinear behaviour that manifested itself through resonance frequency changes with input power and the generation of a cascade of harmonics when two tones were inserted at the resonance frequency. The following section will only describe a brief overview of the project since it has been passed on to a different researcher who is continuing with the work. The initial part of the results were published in [32], while further work was carried on with the same device where the nonlinear properties and the gain were simulated [33].

#### 3.3.1 The Pillbox Cavity Resonator

The circular WG cavities were fabricated by milling a bulk niobium rod, the cavities are shown in Fig. 3.7. The associated covers that included a coupling aperture were fabricated from the same rod and were attached to the resonator body through mounting holes of a standard Ka band rectangular WG flange – shown in Fig. 3.5. Each aperture acts as a shunt inductance that allow for

### 3: CRYOGENIC MEASUREMENT SYSTEM

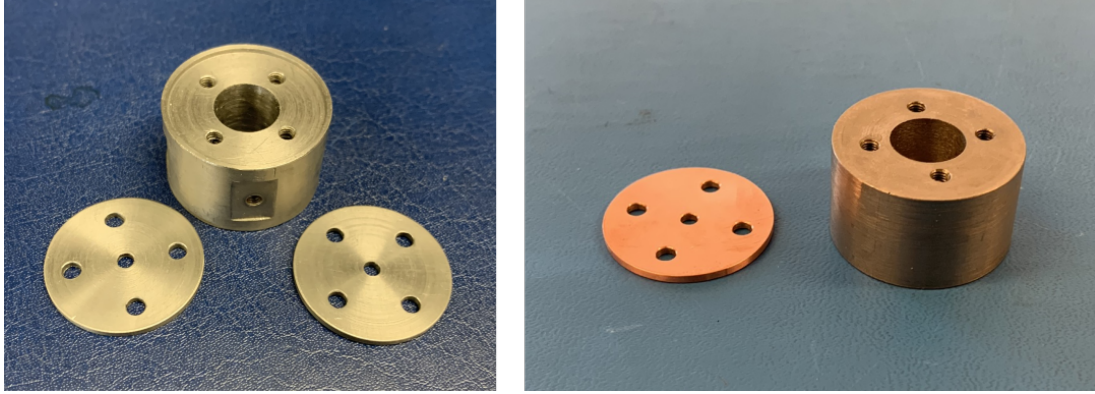


Figure 3.7: Circular WG cavities of inner diameter 11.9 mm and length 15.7 mm made from annealed niobium rod (99.9% purity). The cavities had multiple covers with circular apertures that were different in diameter and thickness in order to investigate different coupling regimes. After machining, the cavities were cleaned in sonicated chemical baths consisting of Decon 90 detergent, acetone and isopropyl alcohol. The left panel shows the two port cavity with two parts containing the aperture couplings next to it. These attached via screws passing through a rectangular waveguide feed as shown in the left panel of Fig. 3.5, while the right panel shows a single port cavity with a copper lid containing a coupling aperture.

standing waves to form between the two terminations, which is nearly equivalent to a capacitive gap coupled microstrip resonator [1]. Two variants of the circular WG cavities were fabricated, the first with one port exhibited a much larger loaded quality factor,  $Q_L$ , since this is the sum of the inverse of the internal quality factor of the cavity,  $Q_i$ , and the coupling apertures,  $Q_c$ , i.e.  $Q_L^{-1} = Q_i^{-1} + Q_c^{-1}$ . This single input cavity could be used in a combination with a circulator to extract useful parametric gain. A second cavity with two ports allowed for transmission measurements, which was the focus of this work. The internal and coupling quality factors can be determined from fitting to a resonance curve. The cavities were simulated in HFSS where the modes of the circular WG cavity resonances could be individually excited and identified.

The resonance frequency of a cavities were calculated analytically using the following expression

$$f_{nml} = \frac{c}{2\pi\sqrt{\epsilon_r}} \sqrt{k_c^2 + \left(\frac{l\pi}{d}\right)^2}, \quad (3.1)$$

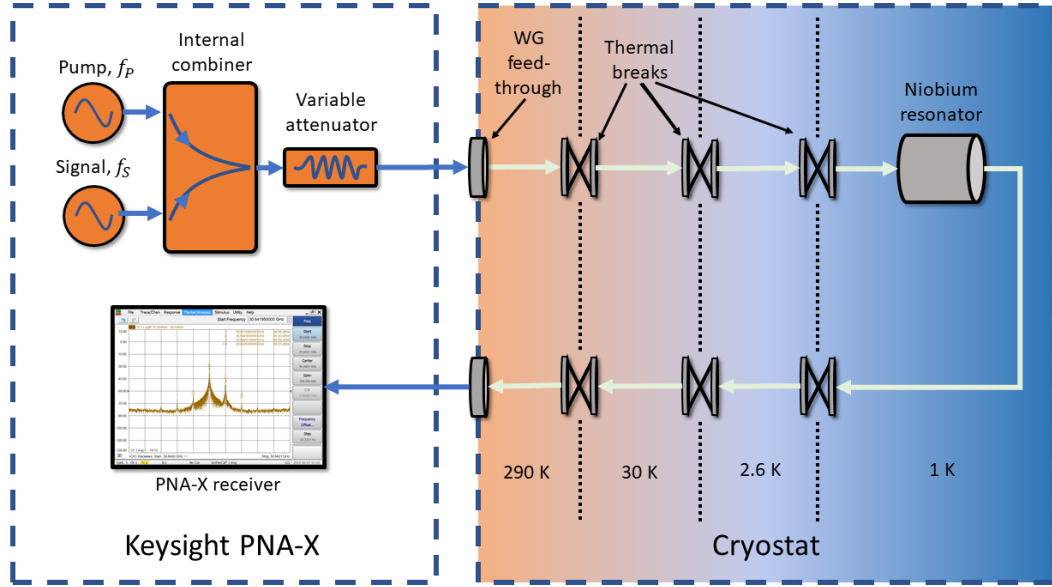


Figure 3.8: Schematic view of the signal flow from the generation of the two tones by separate sources within a Keysight N5245A PNA-X, through to the cryostat via Ka band copper rectangular waveguide and into the niobium resonator to be received at the internal receiver of the PNA-X. Due to the limitation of both tones being attenuated by a single attenuator bank, the maximum power difference between the tones was 30 dB. The IF bandwidth of the PNA-X was kept at 100 Hz for the measurements

where  $l$  is the resonant mode number,  $d$  is the length of the cavity, and  $k_c$  is the cut-off wavenumber for a given mode equal to  $p_{nm}/a$  for TM modes and  $p'_{nm}/a$  for TE modes. Here,  $p_{nm}$  and  $p'_{nm}$  represent the zeroes and extrema of Bessel functions of the 1st kind, respectively[1]. The radius is represented by  $a$ , and the integers  $n$  and  $m$  represent circumferential and radial field distribution variations. Eq. 3.1 shows that for a set of values of  $l$ , a longer cavity decreases the frequency separation between resonant modes, effectively pulling higher order resonances to a lower frequency.

### Measurements

The tested two-port circular waveguide cavity had a number of resonances within the Ka band. A  $TM_{110}$  resonance at 30.64 GHz was chosen due to it having the largest loaded quality factor of  $5 \times 10^3$  and the highest transmission value.

### 3: CRYOGENIC MEASUREMENT SYSTEM

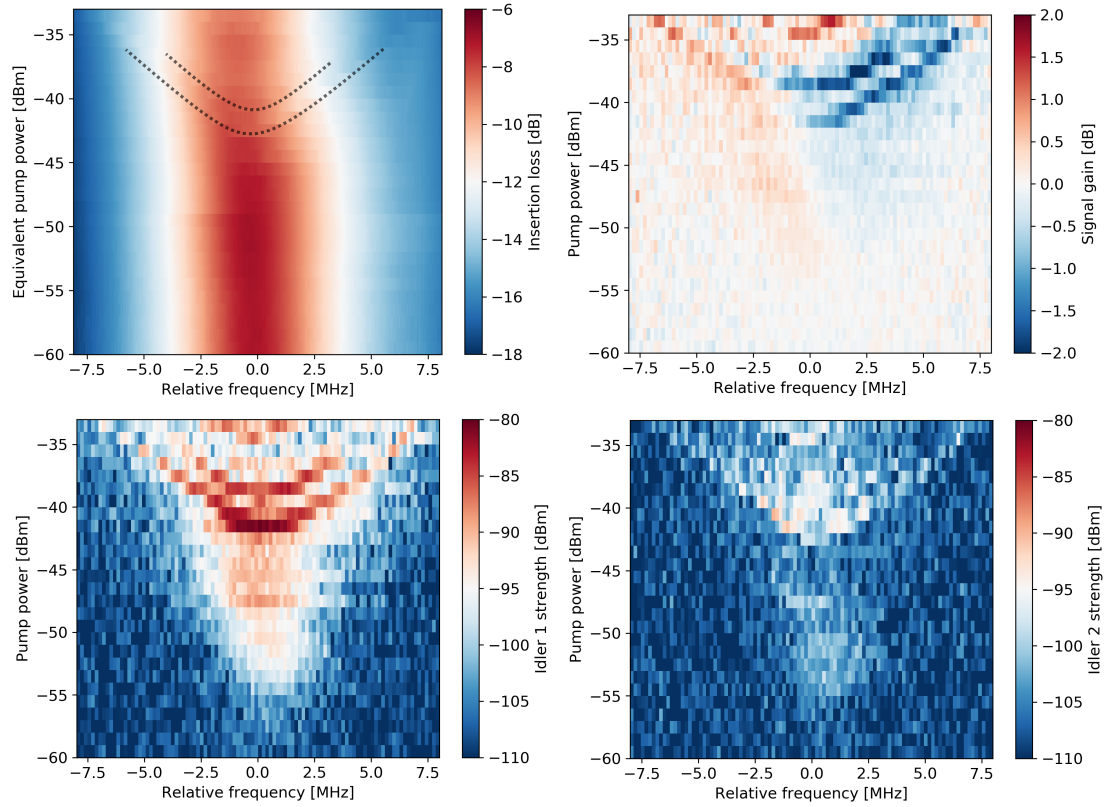


Figure 3.9: Investigation of a SC circular waveguide cavity  $TM_{110}$  resonance. The plots are centred at the resonance frequency of 30.64 GHz, which is referred to as the relative frequency here. *Top left:* Single tone transmission at various input power. Equivalent pump power (total power – signal power) is used for a more direct visual comparison with the gain data. Two dotted lines are included to draw attention to the positions of kinks in transmission. The waveguide feedline losses were not calibrated out. *Top right:* The gain in signal power relative to the transmission spectrum that is traced out by the pump tone. The signal was kept at a constant –60 dBm and 10 kHz below the pump tone as the two tones were swept through the profile of the resonance. *Bottom left:* The power of the idler at  $f_{i,1} = 2f_p - f_s$ . The receiver noise floor was at –110 dBm. *Bottom right:* The power of the idler at  $f_{i,2} = 2f_s - f_p$

Initially, single-tone transmission measurements were taken at a range of input powers corresponding to the sum of the signal and pump powers that were used in the subsequent two-tone tests. The resonances were identified by comparing predicted resonance frequencies from Eq. 3.1, as well as the field distribution in HFSS simulations of the cavity to match up to the measured data. However, above –45 dBm in pump power, a series of small kinks appeared in the transmission spectra, with up to four kinks being observed for a given input power as seen

by the top left panel of Fig. 3.9. The true nature of these kinks is not known, but it is hypothesised that they could be similar in nature to weak-link features that were observed by Abdo *et al.* [88] in stripline resonators. The weak links in the stripline resonator work were hypothesised to originate at the boundaries of the columnar structure of the NbN films that the resonators were based on. In the circular waveguide resonators no film depositions were performed so origin is likely to be different but the resulting kinks in transmission are very similar in appearance.

It should be noted that no magnetic shielding was used around the cavities. This may have allowed external fields to interact with the weak-link features or create vortex pinning sites that added additional RF losses to the resonator. Shifts in the resonance shape and position were observed when all other system parameters were kept constant. This had the effect of adding noise to the S-parameter measurements of the cavities and possibly obscuring any small shifts in resonance frequency due to non-linear inductances.

For the two-tone measurements, the VNA was set up such that the output of each source was a single-frequency CW signal. The sources of the VNA were power calibrated at the input of the cryostat and the receiver was calibrated with one of the VNA sources. During the test, the pump was kept above the signal in frequency at a constant spacing, and the tones were swept together over the profile of the resonance. The frequency spacing was set to be as small as possible while still being able to distinguish the two tones when received at the VNA. As discussed in Section 2.4.3 the expected gain is maximised when the detuning between signal and pump tones is as small as possible. To evaluate if any signal gain has occurred, the received power of the signal was referenced to a transmission spectrum that was traced out by the pump tone. Since the received signal power was measured simultaneously to that of the pump, using the inferred pump transmission rather than the single-tone transmission as the reference point helped to avoid the effect of a changing resonance shape, which

occurred due to the lack of magnetic shielding.

The signal gain and the generated idler strengths are shown in Fig. 3.9. The gain data shows that the signal experiences an increase in transmission of up to 2 dB positioned mostly on the jumps that are observed in the single-tone transmission data. Above the resonance frequency there are regions where the signal experiences parametric attenuation on the same jumps in transmission. These regions of signal gain/attenuation correspond with regions where the idlers at  $f_{i,1} = 2f_p - f_s$  and  $f_{i,2} = 2f_s - f_p$  are also strongly generated, which adds further evidence of 4WM occurring.

## Section Conclusion

It was demonstrated that parametric amplification was possible in bulk niobium circular waveguide cavities fabricated by simple milling techniques. An investigation of the insertion loss across a  $TM_{110}$  resonance at 30.64 GHz with changing input power did not show a shift in resonance frequency that would be characteristic of a strong non-linear inductance. The introduction of a CW pump tone in the presence of -60 dBm CW signal yielded signal gain relative to transmission of up to 2 dB. This gain was positioned on kinks in the transmission spectrum indicating that the nonlinear behaviour was strongest there.

It was later found that all nonlinear behaviour was a result of the contact between the lids that contained the irises and the body of the resonators. This was confirmed by cooling down the cavity with a copper iris instead of the ones made from Nb which showed no non linear behaviour at all. This meant that a type of nonlinear contact junction was created. It was found in further work by Gilles *et al.* [33] that the nonlinearity was well described by the Josephson equations, which allowed for the nonlinear behaviour to be simulated in Keysight's ADS with a method described in Section 4.2.3. In addition, the critical current of these contact junctions was measured by measuring the current through wires that were attached to the resonator via the iris screw holes, which was on the



order of a 1.5 mA. The measurements of the cavity were repeated at a lower temperature of 1 K which showed a gain value relative to transmission of around 5 dB. It might be possible that more gain could be extracted from this structure if the power of the signal was reduced further since high power of the signal in combination with the power of the pump may cause the amplifier to reach the compression point prematurely.

### 3.4 Design Of Modular Test Cryostat

One final piece of work that should be mentioned is a new test cryostat that was designed (Fig. 3.10 ) for measurements at different frequency bands through the use of a cartridge system (see Fig. 3.11). Unfortunately, not all the parts of this cryostat were fabricated in time by the end of this PhD project meaning that the cryostat could not be assembled or tested.

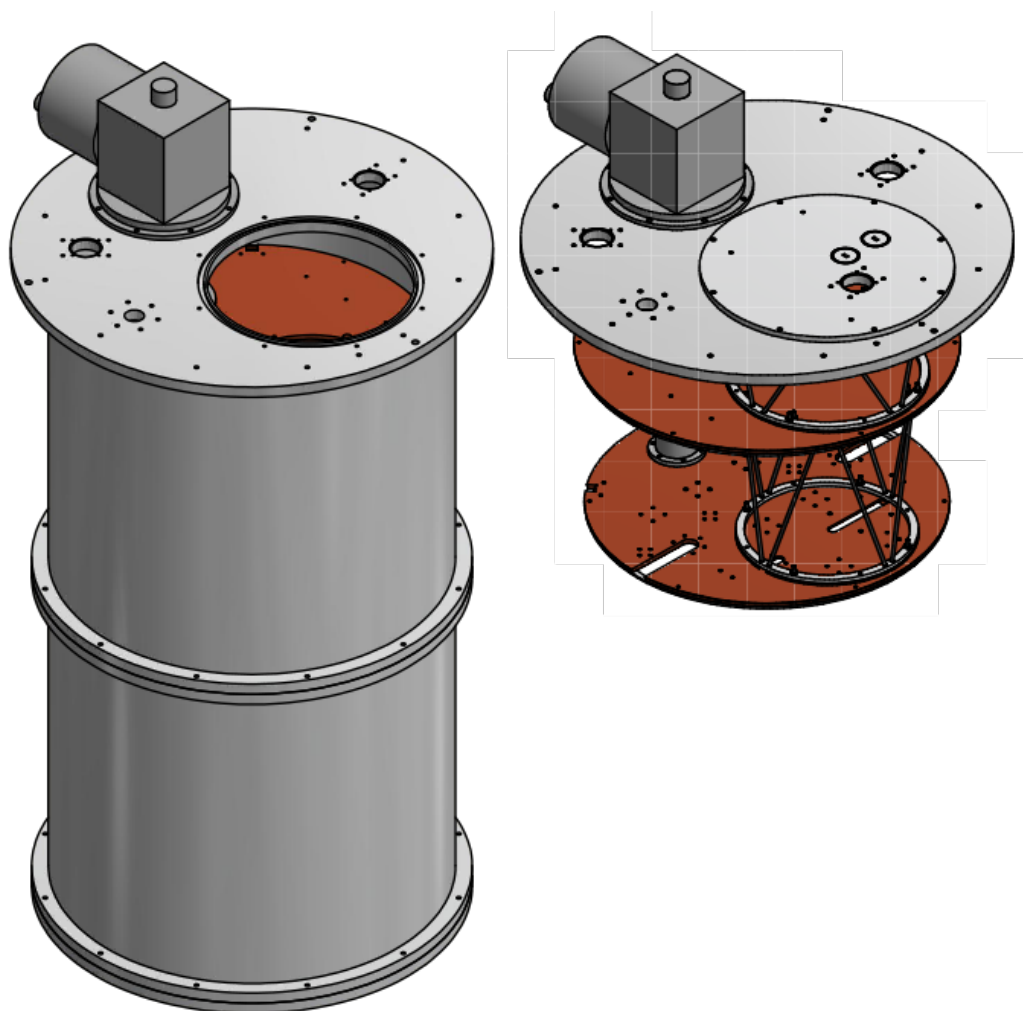


Figure 3.10: Images of the CAD model of a new modular test cryostat that can accept a cartridge which would contain the necessary rectangular waveguide feeds and the DUT at bottom. The right image shows the structure inside the cryostat as well as an inserted cartridge.

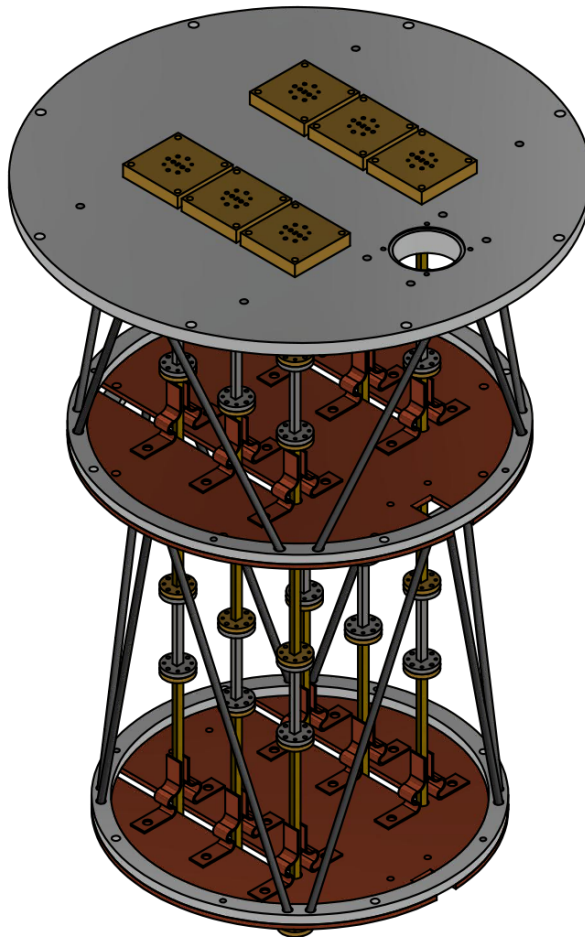


Figure 3.11: An image of the CAD model of a W band cartridge designed for the testing of multiple LNAs at the same time. The thermal breaking between cold stages was done with thin wall stainless steel waveguide pieces that are drawn in grey. There was space for a 55 pin hermetic DC connector for the connection of all the necessary DC biasing lines.



# Chapter 4

## Ka band Ridge Gap Waveguide KI RPA

### 4.1 Introduction

A resonator is the simplest test bed for the exploration and understanding of the nonlinear elements that can be embedded within. A nonlinear resonator is much more straightforward to engineer and realise than an electrically long, nonlinear-element loaded transmission line due to the overall shorter lengths involved. In addition to the applications of RPAs that require the amplification of a narrow-band signal like the readout of single qubits or in resonator-based axionic dark matter searches, the nonlinear resonators that these RPAs are based on are used in TWPA development. A nonlinear resonator must often be made in conjunction to the TWPA structure in order to characterise the properties of the nonlinear medium such as the nonlinear inductance fraction and the scaling current ( $\sim$  critical current).

As outlined in Section 3.3 an RPA is possible with a circular waveguide resonator provided that a nonlinear element can be introduced within the structure. However, circular waveguides are incompatible with wideband operation since

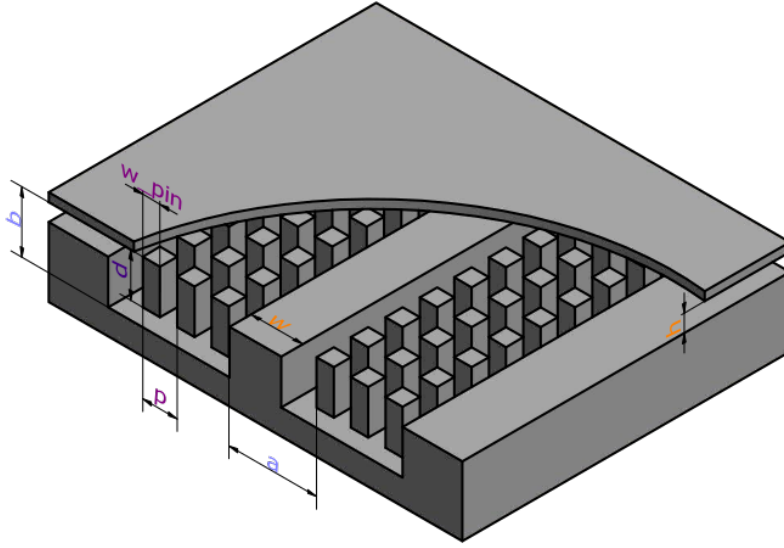


Figure 4.1: A RGWG model showing the central ridge of width  $w$  and height  $d$ , in a groove of width  $a$  and height  $b$  with 3 rows of pins either side of the ridge with width  $w_{\text{pin}}$ , height  $d$ , and period  $p$ . These dimensions are typically on a similar scale to the dimensions of rectangular waveguide at a similar frequency. The gap labelled  $h$  is exaggerated to demonstrate how the 2 parts of the structure are joined together.

they possess nonlinear dispersion meaning that total phase mismatch  $\Delta k$  (see Section 2.4.4) cannot be close to zero over a wide bandwidth. Phase matching would only be possible at specific set of conditions over a very narrow bandwidth. Therefore, alternative transmission line structures must be explored that possess linear dispersion, are readily scalable to high frequencies and can be engineered with a nonlinearity that dominates over the structure dynamics. In this case the nonlinearity in question is the kinetic inductance which is said to be dominant when the total structure inductance is predominantly made up of it.

One such structure is ridge gap waveguide (RGWG), shown in Fig. 4.1, which is able to support a quasi-TEM transmission mode in the region between a central ridge and top conductor separated by a small gap of size  $h$ . The ridge is protected by a meta-material referred to as a pin surface or a bed of nails which surrounds the ridge. This bed of nails performs two important functions: prevents the propagation of a global parallel plate mode that can exist between the top and

bottom surfaces of the box; and confines the fields of a propagating mode to the ridge [111, 112]. One of the key features of RGWG is that the propagating fields travel in a hollow space meaning that dielectric losses are absent. These dielectric losses become dominant in high frequency transmission lines where a large fraction of fields propagate in the dielectric volume. Another feature is the scalability of RGWG to hundreds of gigahertz as the structure can be scaled down in size without much increase in dissipation [113]. The bandwidth of RGWG is limited by the bandwidth over which the stopband of the bed of nails protecting the ridge can be engineered. This bandwidth can span multiple octaves when the gap is small relative to the length of nails  $h/d \ll 1$ .

RGWG can be used to engineer resonators that when coated with a thin layer of superconducting material can exhibit a nonlinear behaviour due to the kinetic inductance of the surfaces. The resulting nonlinear resonator can be used to realise an RPA, which exploits the current dependent kinetic inductance nonlinearity (see Section 2.3.2). In general, RGWG can be fabricated using conventional metal milling or silicon micro-machining techniques [113]. The extent to which the nonlinear inductance dominates over the total structure inductance is dictated by the kinetic inductance fraction,  $\alpha_k$ , which is dependent on the waveguide geometry and film properties. It is possible for  $\alpha_k$  to get close to unity when the SC coating is thin such that  $t \ll \lambda_L$ , and the hollow gap is small such that  $h < 1 \mu\text{m}$ , which can be achieved via the deposition of thin spacer along the outer perimeter of one of the involved bodies.

This chapter focuses on the design and realisation of a Ka band (26.5 to 40 GHz) RGWG resonator that is machined from high purity copper and coated in a multiplayer film structure (see Section 4.3.3 for more details) with the top NbTiN layer providing the kinetic inductance. Metal machining is explored due to the already established device manufacturing pipeline and expertise. NbTiN coating is chosen due to its high critical temperature lending itself to operation at 1 K with relatively low dissipation compared to a lower  $T_c$  films. Other factors

such as film uniformity and consistency of deposition have not been considered due to the disordered nature of the copper surface upon which the coating would be deposited. An additional factor in favour of NbTiN is the already established coating process on copper at the laboratory where the depositions are carried out. The nonlinear resonator is designed to operate in degenerate 4WM mode as a transmission amplifiers (see Fig. 2.9). This degenerate 4WM operation is the most straightforward to realise since it does not require any special impedance engineering and the two input tones can be brought down to the RPA through a single feedline.

Measurements of two coated resonators will be presented, one with a thick NbTiN coating and another with a top thin NbTiN coating. It will be shown that the thick film device agrees with the simulations in terms of the microwave design and does not show nonlinear behaviour due to the very large scaling current as expected. The tested thin film device will show nonlinear behaviour in the form of power dependent frequency shifts and the generation of mixing harmonics in the presence of two input tones.

### **4.1.1 Chapter Outline**

This chapter is split into three main parts: the microwave design and simulations; mechanical design and fabrication; followed by laboratory measurements. The first section will include design procedures for RGWG transmission lines and resonators with coupling to Ka band rectangular waveguide, followed by gain predictions using nonlinear circuit simulations that make use of equivalent circuit model of the KI RGWG RPA. The second section will cover the mechanical design of the resonator, the polishing of the copper surfaces in preparation for superconducting coating, followed by the procedures of the coating process via magnetron sputtering. The third section will cover the measurements of the resonator in the laboratory at room temperature, and at cryogenic temperatures



to extract the kinetic inductance fraction, nonlinear scaling current, and to show the presence of nonlinear mixing.

## 4.2 Design and Simulation

Multiple steps are involved in the design and simulation of a RGWG-based RPA. Namely, the design of RGWG transmission line that can operate over the desired bandwidth which then forms the foundation for the design of the RGWG resonator; the incorporation of the chosen superconducting coating including the estimate of the nonlinear scaling current; followed by the coupling to the chosen feedlines. The nonlinear resonator can then be represented by an equivalent circuit model to include the nonlinearity of the kinetic inductance. A circuit simulator that supports the harmonic balance simulation mode can be used to simulate resonance frequency shifts with power and the nonlinear parametric processes of interest. The nonlinear simulations can be used to explore the gain parameter space (discussed in Section 2.4.3) to find the optimum signal and pump parameters to extract the desired gain and bandwidth of the RPA.

### 4.2.1 Ridge Gap Waveguide

Ridge gap waveguide consists of the following elements: the textured pin surface (otherwise known as a bed of nails), and the continuous ridge that sits in the middle of the pin surface; and the lid to enclose the whole structure. In addition, if the ridge is absent then the groove that is left over makes a different transmission line referred to as groove gap waveguide (GGWG), this type of waveguide can be very useful in the transition region between rectangular waveguide and RGWG. Each of these elements require their own consideration and simulation. The simulations of the structure are performed using the eigenmode analysis method in HFSS, which show the set of possible propagating modes for a given set of boundary conditions.

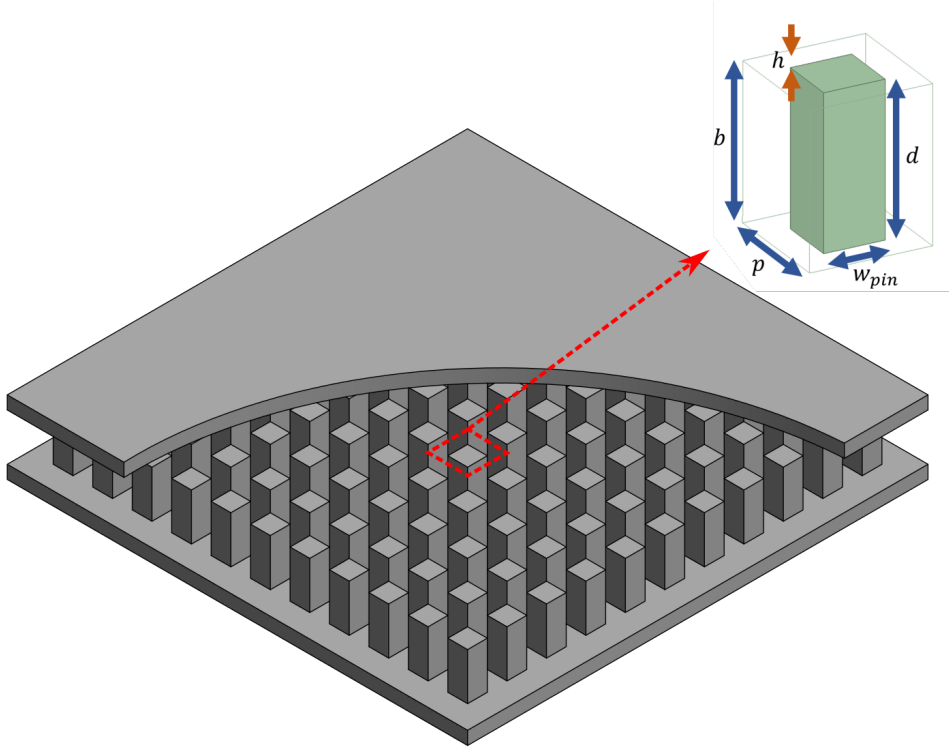


Figure 4.2: A model of a bed of nails array with a lid that is separated by a small gap  $h$ . The inset shows the repeating unit cell that is used to simulate the dispersion diagram of the full structure. Here,  $d$  is the nail length,  $w_{pin}$  is the nail width,  $h$  is the gap between the top of the nail and the PEC lid, and  $p$  is the nail period. In the simulation master and slave (coupled lattice) boundaries are set on the 2 pairs of horizontally opposing faces of the unit cell shown in the top right of the figure.

### The Bed Of Nails

The bed of nails is a meta material, meaning that it possesses properties that cannot exist naturally in nature. Without a perfect electrical conductor (PEC) lid, the bed of nails acts as a reactive surface. At a certain wavelengths it acts as a capacitive boundary, at others it acts as inductive boundary, which changes the phase of the reflected wave. This behaviour can be captured [114, 112] by representing the surface as an equivalent impedance in the form

$$Z_s = j\eta_0 \frac{1}{\epsilon_r} \tan(kd) \quad (4.1)$$

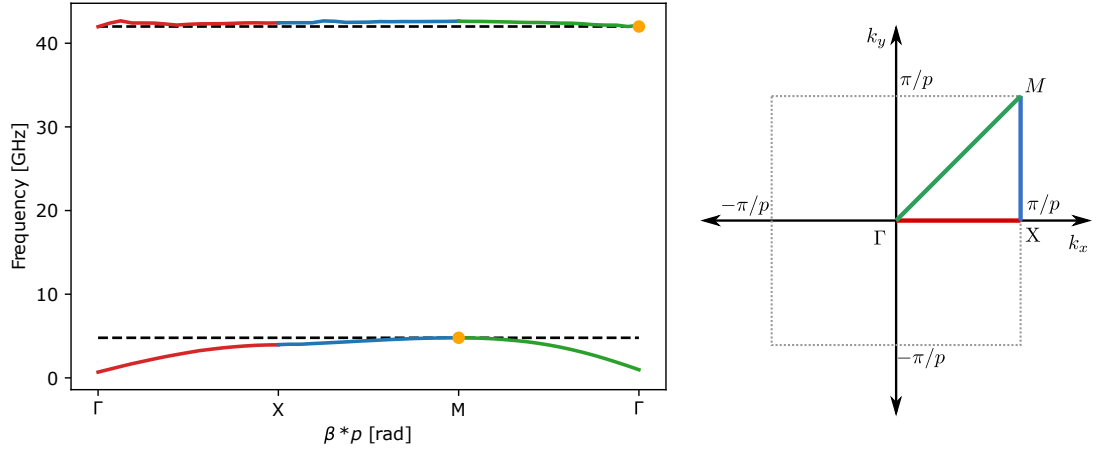


Figure 4.3: *Left:* The full dispersion diagram of a bed of nails periodic structure for the first 2 propagating modes, one below and one above the desired stopband of the structure. The black lines show the useable structure bandwidth that are positioned on the orange dots, which show the highest and lowest propagating frequency on the lower and upper modes, respectively. Note that the dispersion diagram is relatively flat due to the small gap that is used in this simulation. *Right:* The Brillouin zone showing the high symmetry points for a bed of nails cell of size  $p$ . The colours indicate the regions that cover the full dispersion diagram of the periodic structure. The dimensions of the simulated unit cell are:  $d = 3.55$  mm,  $h = 10$   $\mu$ m,  $w_{pin} = 1.5$  mm, and  $p = 1.5$ mm.

where  $\eta_0 = \mu_0 c$  is the impedance of free space,  $\epsilon_r$  is the dielectric constant of the medium in which the nails reside (equal to 1 for free space),  $k = 2\pi/\lambda$  is the wave number,  $d$  is the nail length,  $\lambda$  is the wavelength of the incident radiation. Eq. 4.1 can be analysed under three cases: (i)  $d \leq \lambda/4$  where  $Z_s$  is positive meaning that it acts as an inductance, (ii)  $\lambda/4 < d \leq \lambda/2$  where  $Z_s$  is negative and capacitive, and finally (iii)  $d = \lambda/4$  where  $Z_s \rightarrow \infty$  which represents a perfect magnetic conductor (PMC) boundary. This boundary means that tangential magnetic field to the surface are set to zero meaning no surface current can propagate. This means fields incident to this boundary will be reflected.

When this pin surface is covered by a PEC boundary separated by a small gap  $h$ , as shown in Fig 4.2, a wave can propagate through this gap. However, when this gap is smaller than a quarter of a wavelength then any incident waves will decay rapidly. This characteristic can be used constrain propagating radiation by opening up a channel between the nails that guides travelling waves (see

Fig. 4.5a). Furthermore, placing a continuous ridge in this channel will result in the structure shown in Fig. 4.1, which will constrain propagating radiation between the top of the ridge and the lid while preventing leakage to the sides due to the presence of the nails. The ridge and PEC surface above allow the propagation of the parallel plate mode which is quasi-TEM. The bed of nails is able to create this protecting stopband over a specific frequency band which is dependent on the dimensions of the nails. The bandwidth with a specific set of dimensions can be evaluated by plotting the full dispersion diagram by considering the Brillouin zone of the unit cell, which is shown in Fig. 4.3. This defines the fundamental propagation vectors across a unit cell which can be used to obtain the dispersion characteristics of the entire periodic structure. Since we want to investigate propagation in two directions along the lattice  $x$  and  $y$ , the propagation constant is defined as  $\beta = \mathbf{x}k_x + \mathbf{y}k_y$ , where  $k_x$  and  $k_y$  are the propagation constants along  $x$  and  $y$ , respectively. These directions follow the horizontals of the inset in Fig. 4.2. The high symmetry points of the Brillouin zone are given by

$$\Gamma = (k_x p = 0, k_y p = 0)$$

$$X = (k_x p = \pi, k_y p = 0)$$

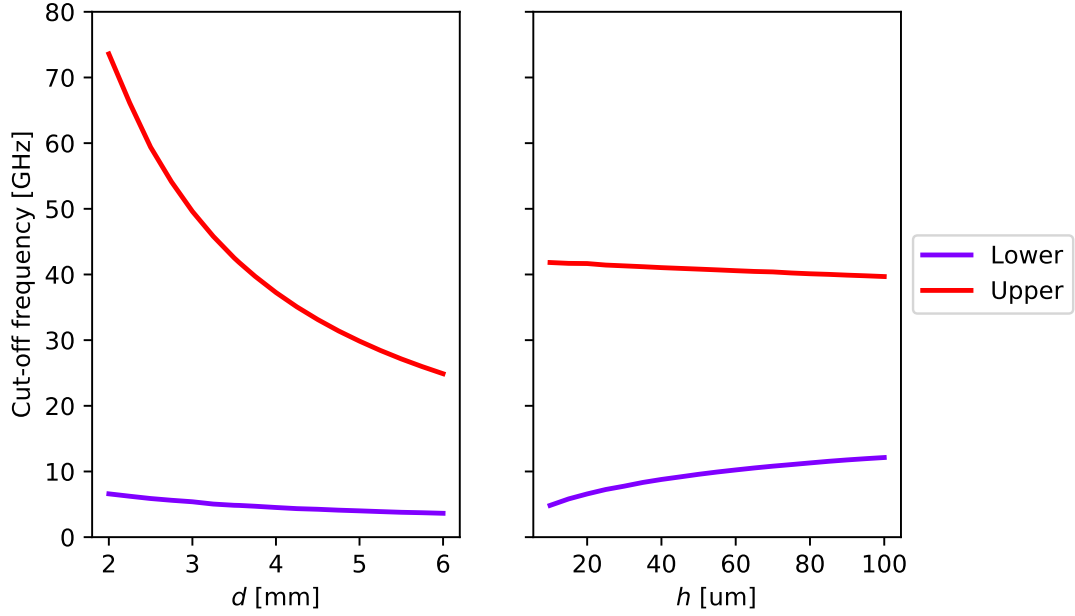
$$M = (k_x p = \pi, k_y p = \pi)$$

where  $p$  is the period of the lattice defined in Fig. 4.2.

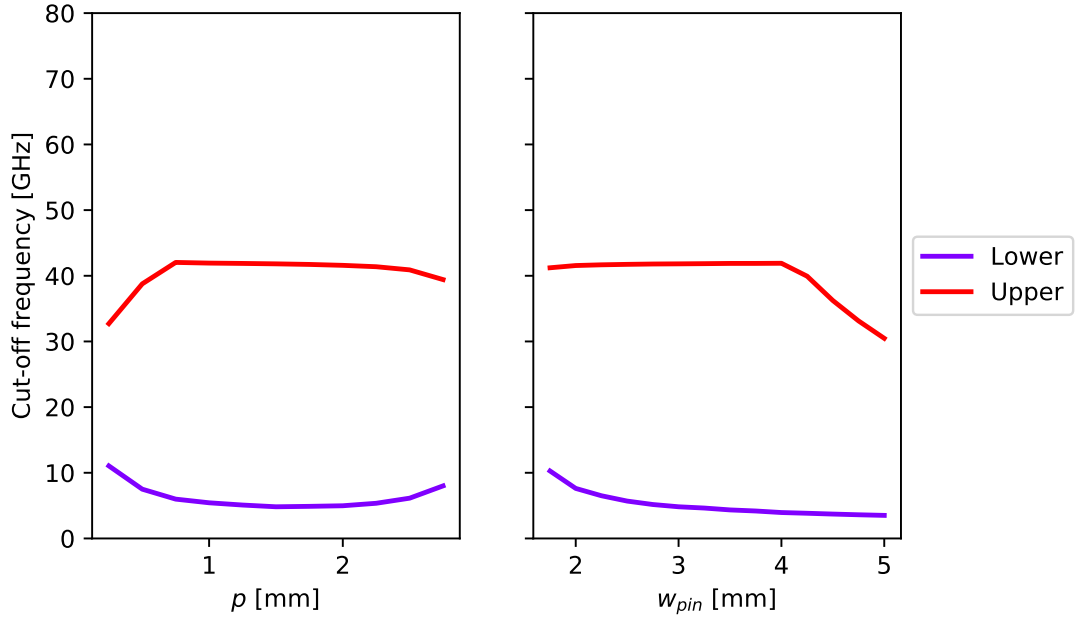
In the case of the unit cell shown in Fig. 4.2 the full dispersion diagram can be obtained in HFSS by setting the phase difference on the orthogonal master-slave boundary condition to two variables  $px$  and  $py$  and solving the first few possible eigenmodes. The full dispersion diagram is attained by three separate simulations that are stitched together. For each eigenmode (propagating mode) the first region of the dispersion diagram is found by simulating the region  $\Gamma$  to

$X$ . This is done by setting  $py = 0$  and sweeping over the  $px$  from 0 to  $\pi$ . The second region  $X$  to  $M$  is found by setting  $py = \pi$  and stepping  $px$  once again. For the final region of  $M$  to  $\Gamma$  setting the phase to a single variable for both sets of master-slave boundaries to  $ph$  and sweeping the variable between 0 to  $\pi$ . As shown by the orange circles in Fig. 4.3, the last zone ( $M$  to  $\Gamma$ ) of the dispersion diagram covers the highest and lowest frequency points at which propagation is possible for a specific mode. This result can be used to compute the structure bandwidth at a significantly reduced computing time by simulating the start and end of the  $M$  to  $\Gamma$  section of the dispersion diagram for each mode where  $ph = 0, \pi$ , instead of simulating the full dispersion diagram. These boundaries are plotted by considering the  $ph = \pi$  point of the mode below the stopband and the  $ph = 0$  for the first mode above the stopband, which gives the structure bandwidth for a particular set of dimensions.

It is important to engineer the bed of nails bandwidth such that it covers the whole of Ka band to ensure that any discrepancies between the simulated and fabricated resonators are accounted for. The resonance frequency can differ by as much as a few GHz for resonators with a thick film  $t \gg \lambda_L$  compared to one with a thin film  $t < \lambda_L$ . The bandwidth of the bed of nails surface was investigated as a function of the dimensions of the unit cell – the results are shown in Fig. 4.4. The bandwidth of the pin surface varies strongly with the nail length, however, this is constrained to be  $\sim b = 3.56$  mm, for taper-free compatibility with Ka band rectangular waveguide by matching the length of the short wall. The bandwidth also increases as the gap  $h$  decreases. As will be seen in section 4.3.3, the spacing between the outer rim of the resonator body and the lid is set by a spacer layer on the outer resonator perimeter, therefore the nails were chosen to be flush with the top face of the resonator, which ensured the smallest gap ( $\sim 10$   $\mu\text{m}$ ) and largest bandwidth. The nail width and period were chosen to be 1.5 and 3.0 mm, respectively, as a compromise between machining precisions and fabrication speed, which conveniently gives the best bandwidth. The completed design of the



(a) *Left:* Sweep of nail length with  $h = 10 \mu\text{m}$ . *Right:* Sweep of nail-to-lid gap with  $d = 3.56$  mm. Common parameters are  $p = 3$  mm and  $w_{pin} = 1.5$  mm.



(b) *Left:* Sweep of nail period with  $w_{pin} = 1.5$  mm. *Right:* Sweep of nail width with  $p = 1.5$  mm. Common parameters are  $d = 3.56$  mm and  $h = 10 \mu\text{m}$ .

Figure 4.4: The bandwidth of the bed of nails as a function the structure dimensions. The bandwidth is the stopband over which no modes propagate within an infinite array of nails and the PEC top. The final chosen nail dimensions were  $d = 3.55$  mm,  $h = 10 \mu\text{m}$ ,  $p = 3$  mm, and  $w_{pin} = 1.5$  mm.

bed of nails meta material allowed for the engineering of groove gap and ridge gap waveguides to progress.

### Groove Gap and Ridge Gap Waveguide

For compatibility with rectangular waveguide the groove of the groove gap waveguide was chosen to be the same width as the long wall of Ka band waveguide. The bandwidth of propagation of the GGWG mode was investigated in a similar method as the bed of nails, except propagation in only one direction was considered. The GGWG unit cell is shown in Fig. 4.5a and is composed of the groove and three nails on either side. Three were chosen to ensure that the fields of the groove mode did not interact with the edges of the cavity since the field decayed by a  $\sim 30$  dB per row of nails from the peak field in the centre of the groove, which is shown in Fig. 4.6. The dispersion diagram in Fig. 4.5 shows the dispersion of each eigenmode solution from the simulation and was calculated by dividing the phase difference set on the coupled lattice boundaries by the length of the cell in the direction of propagations. The phase was stepped between 0 and  $\pi$  which in effect set the dispersion value, at each value the eigenmode solutions were found. The dispersion diagram shows that the groove gap waveguide mode can propagate between  $\sim 22 - 40$  GHz which is the same as the rectangular waveguide mode.

Ridge gap waveguide can be constructed by placing a ridge in the middle of the groove of the previously simulated GGWG. The unit cell of the RGWG is shown in Fig. 4.7a. The width of the ridge does not affect the propagation of the RGWG mode, however, a wider ridge does decrease the impedance of the line meaning that for a given input power a larger surface current is stimulated. A ridge of 3.3 mm width was chosen since this minimised the coupling of the ridge mode to the adjacent nails. As shown by Fig. 4.7b, the RGWG mode can propagate over a very wide bandwidth covering the whole bed of nails stopband. The ridge and lid act as a parallel plate transmission line mode therefore such a bandwidth is

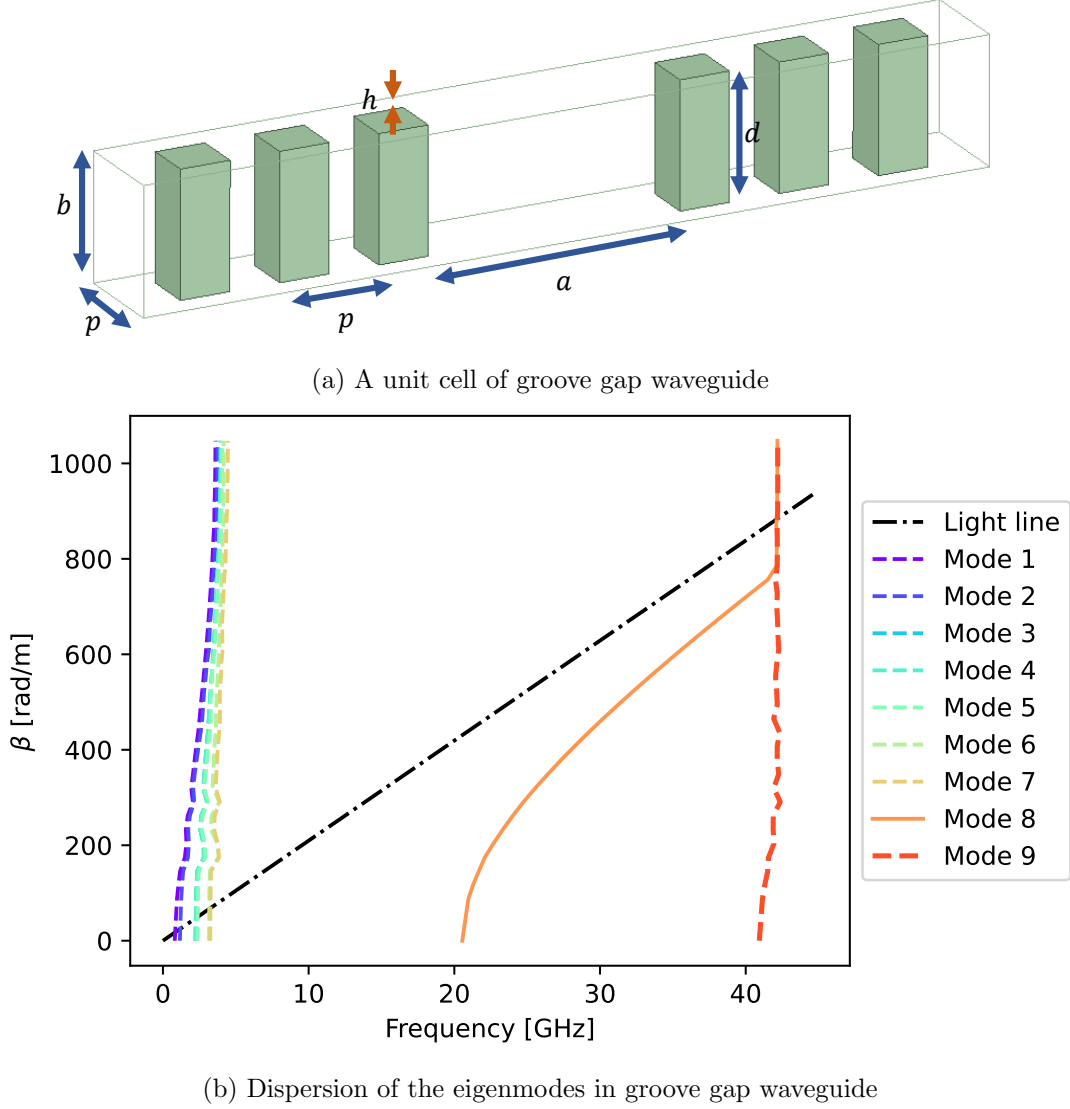


Figure 4.5: A diagram showing the unit cell used to simulate groove gap waveguide in HFSS and the resulting eigenmode dispersion diagram. The unit cell had a single set of lattice boundaries set on the faces along the direction of propagation of the confined wave (in/out of page). The width of the groove was set  $a = 7.11$  mm, matching the long wall of Ka band rectangular waveguide. The modes shown in the dispersion diagram are the solutions of an eigenmode simulation for a sweep of the phase difference between the lattice boundary faces. Modes below the light line ( $\beta = 2\pi f/c$ ) are allowed to propagate, which shows that mode 8 is the groove gap waveguide mode.



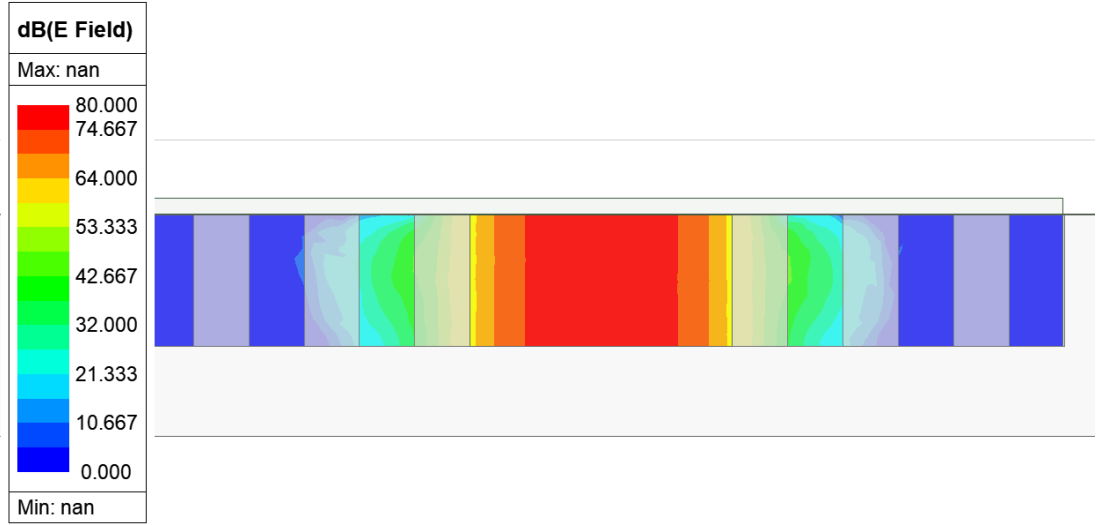


Figure 4.6: The magnitude of the complex electric field in a cross section of part of a GGWG. The field from the edge of the central groove decays by  $\sim 30$  dB per row of nails.

expected which does not have an inherent lower cut-off frequency, and an upper cut-off that is dictated by the propagation of higher order modes. The dispersion of this mode follows the light line which means it has linear dispersion. The nature of this dispersion means that RGWG is appropriate to be used in TWPAs, at least in regards to the wideband phase matching considerations. However, to any TWPA investigations it is important to engineer a RGWG resonator which can be operated as an RPA.

### 4.2.2 Ridge Gap Waveguide Resonator

There are various methods to engineer a resonator using RGWG. The type chosen here is a series resonator with two ports such that it could be measured in transmission. The ports are coupled to Ka band rectangular waveguide in order to be compatible with the cryogenic feeds presented in Chapter 3. A RGWG resonator in its simplest form is a short length of RGWG that is capacitively coupled to the input and output feedlines, as shown in Fig 4.8. Coupling this resonator directly to rectangular waveguide without any impedance matching or

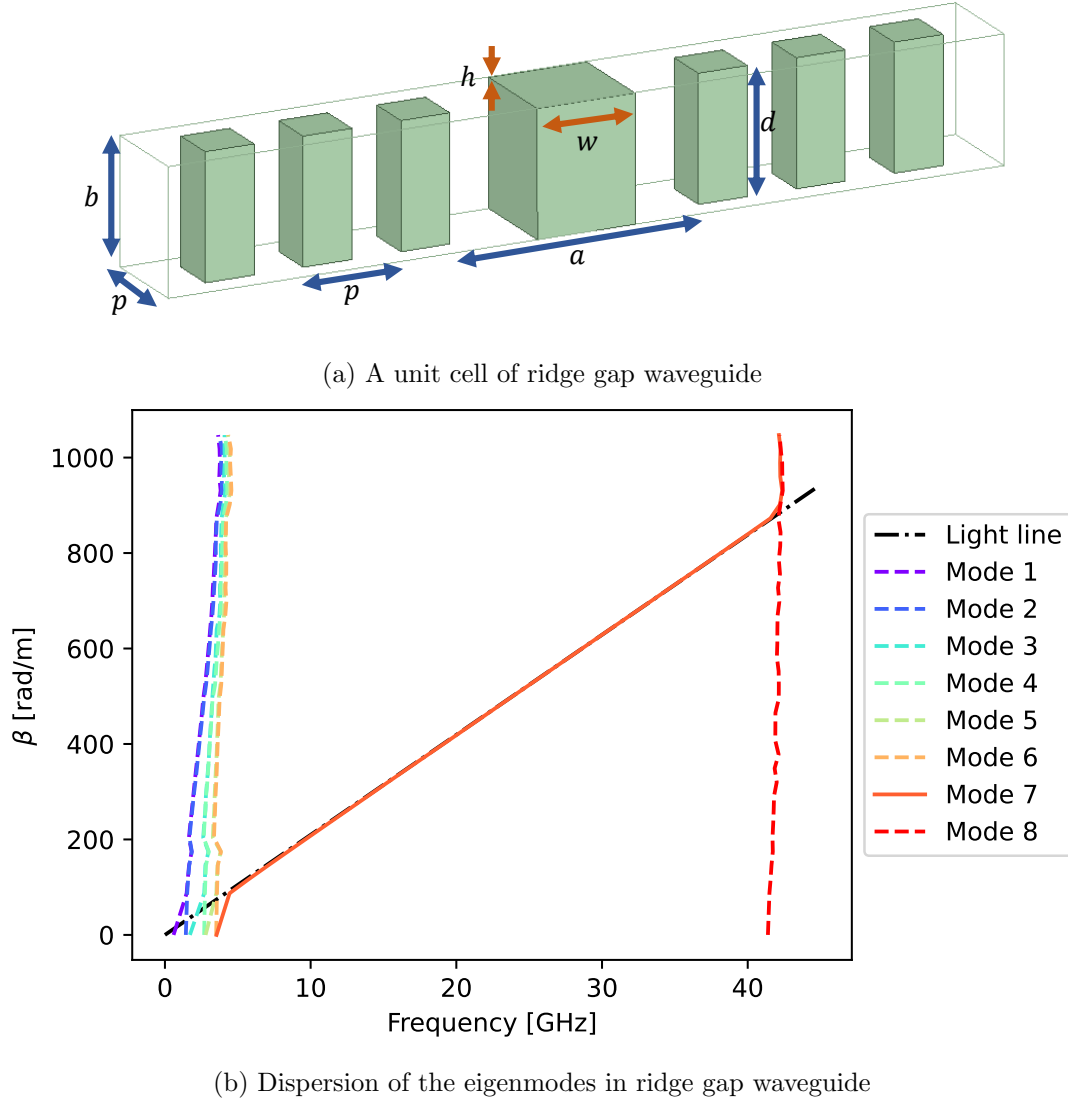


Figure 4.7: A diagram showing the unit cell used to simulate ridge gap waveguide in HFSS and the resulting eigenmode dispersion diagram.

coupling engineering results in a resonance with a linewidth  $\kappa \sim 150$  MHz, that translates to a quality of factor of  $\sim 250$  at 35 GHz. This broad resonance would mean a large operational bandwidth, however, the coupling quality factor,  $Q_c$ , determines the magnitude of the surface current that is induced at a given input power. A small  $Q_c$  reduces this induced current which means that a higher power is required to stimulate the nonlinear nature of the kinetic inductance due

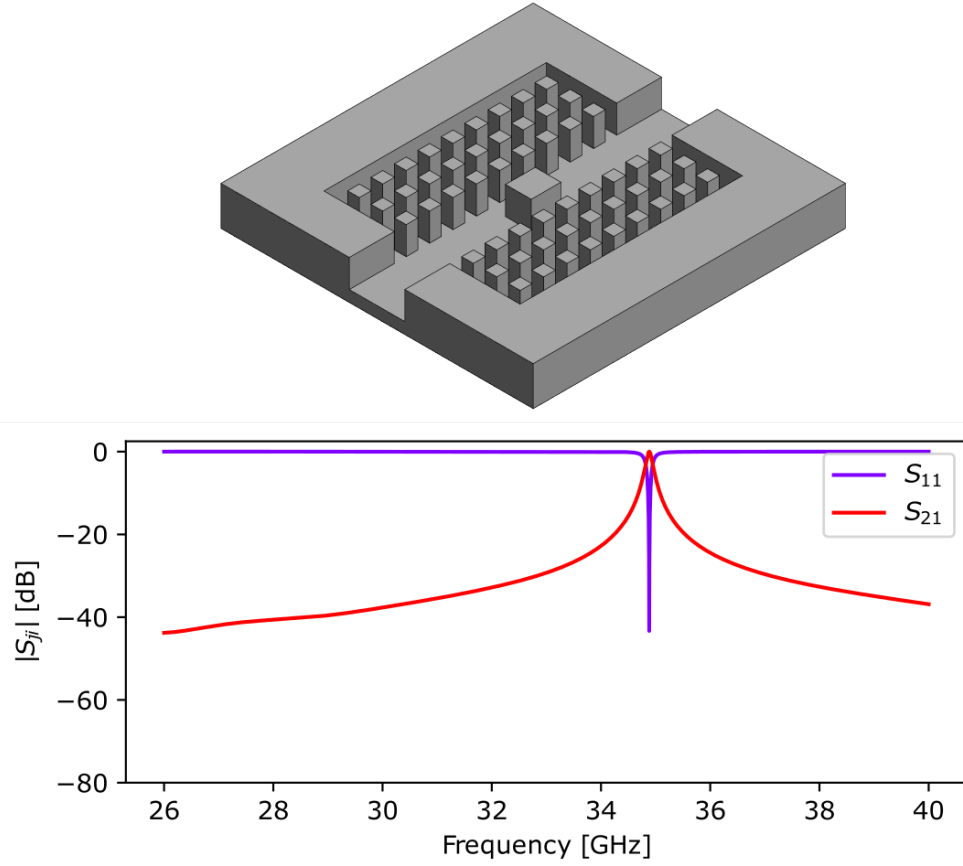


Figure 4.8: *Top*: a model of a ridge gap waveguide series resonator with a ridge of length 4.2 mm, width of 3.3 mm and height of 3.56 mm. The nail dimensions can be found in Fig. 4.4. The flat lid that sits on a  $h = 10 \mu\text{m}$  spacer is omitted to show the internal structure of the resonator. *Bottom*: the simulated S-parameter spectrum of the model with PEC boundaries showing a resonance at  $\sim 35$  GHz with  $Q \sim 300$ .

to the superconducting coating. If the coupling is too low then the necessary drive power could be much too large to be used in an amplifier chain where the subsequent amplifiers could become saturated or even damaged.

Two methods can be used to increase the quality factor of the ridge resonance: using an impedance taper to gradually step the impedance then engineering a RGWG resonator using capacitive gaps; or using an additional coupling resonator. The taper would need to step the impedance of rectangular waveguide (which has an average value of  $500 \Omega$  and  $377 \Omega$  at the top of the waveguide

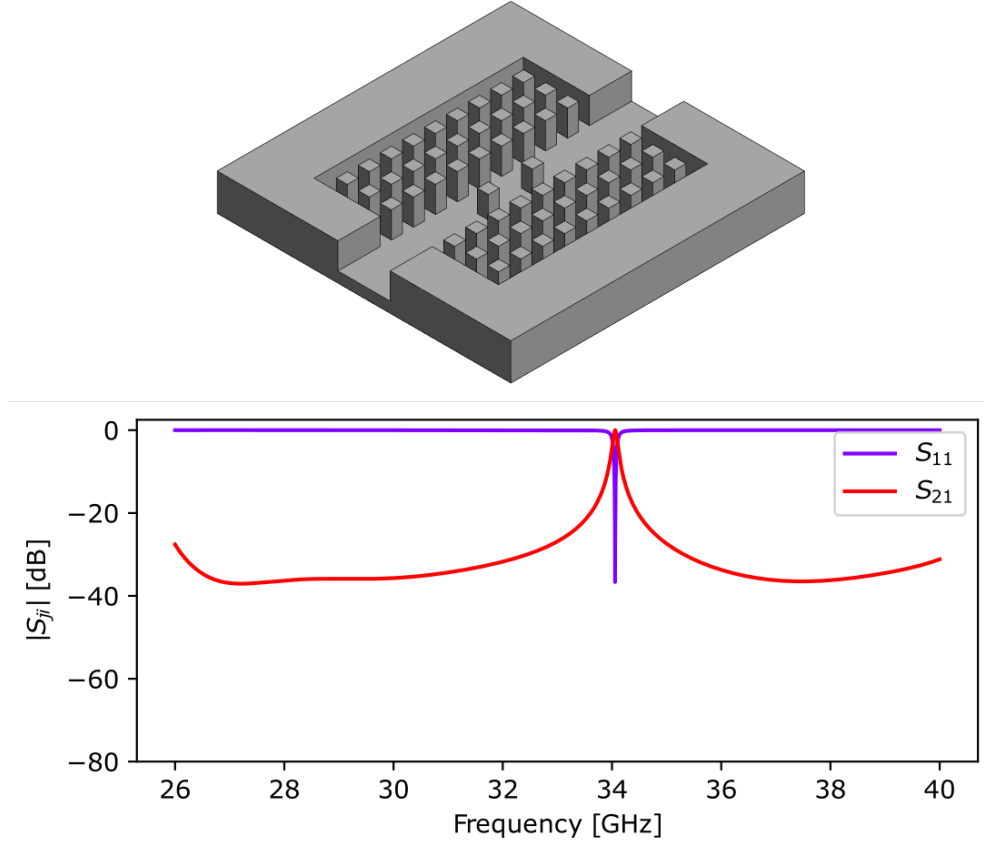


Figure 4.9: *Top*: a model of a groove gap series resonator formed between two pins that act as impedance boundaries. The two square pins have a centre-centre separation of 6.5 mm, a height of 3 mm and a width of 1.5 mm. The flat lid is omitted. *Bottom*: the simulated S-parameter spectrum of the model with PEC boundaries showing a resonance at  $\sim 34$  GHz with  $Q \sim 400$ .

band) to the impedance of the RGWG, which is of order of few  $\Omega$ . A Chebyshev, exponential [1] or Klopfenstein [115] taper would be able to accomplish this. However, such tapers require fine manufacturing tolerances and careful engineering to provide a smooth transition with minimal reflections. The second method is to use an additional coupling resonator at the input and output of the RGWG resonator to boost the quality factor of the ridge resonance. These coupling resonators effectively act as off-resonance bandpass filters relative to the resonance frequency of the RGWG resonator, isolating it further and increasing the quality factor. This method is not dissimilar to the engineering of GGWG

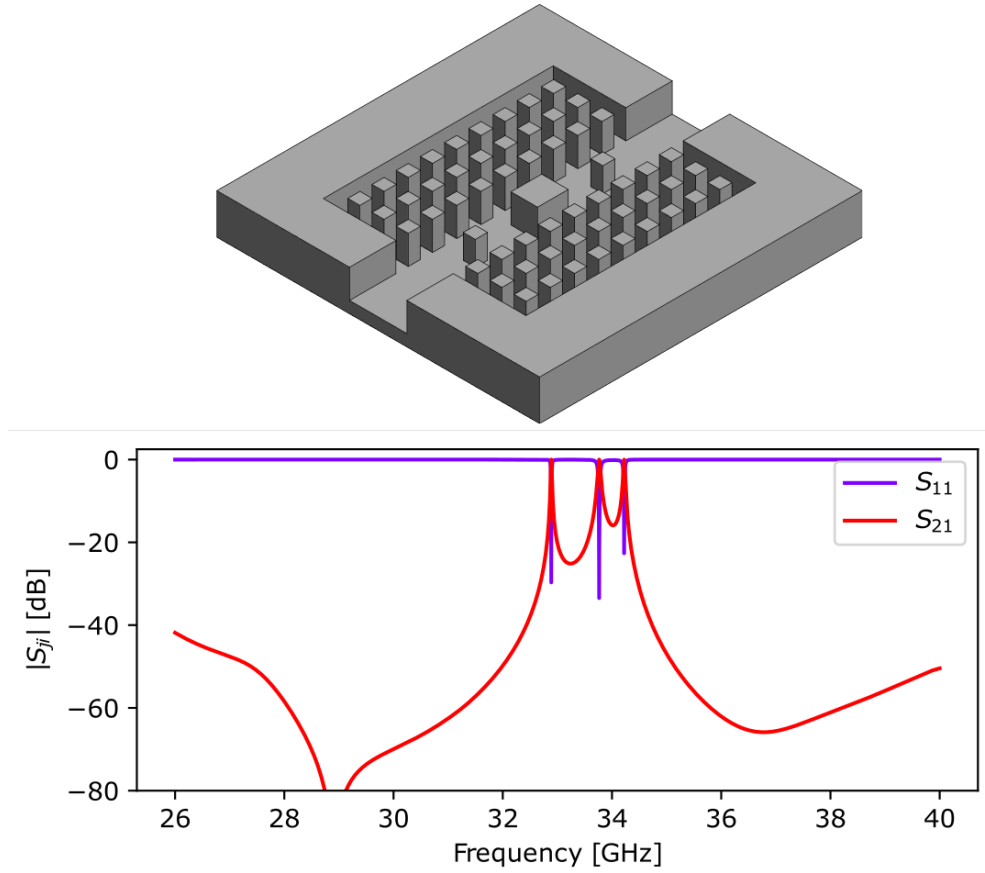


Figure 4.10: *Top*: a model of the three resonator structure combining GGWG and RGWG resonators. The two square pins have a centre-centre separation of 16.775 mm, a height of 3 mm and a width of 1.5 mm. The ridge is 4.2 mm long and 3.3 wide. *Bottom*: the simulated S-parameter spectrum of the model showing three resonances at  $\sim 32.9$ ,  $\sim 33.8$ , and  $\sim 34.2$  GHz with  $Q \sim 2000$ , 700, and 1100, respectively. The field distributions of these modes are shown in Fig. 4.11.

passband filters [116] that employ multiple resonators in series that are coupled via RGWG. This coupling resonator can be formed between two nails that are positioned in the middle of the groove of groove gap waveguide. These nails act as impedance boundaries and allow the formation of the resonator shown in Fig. 4.9. The resonance frequency is set by the centre-centre distance of the central pins, while the coupling is controlled by the dimensions of these pins – a taller and wider (in the longitudinal and/or transverse direction) pin will cause the coupling quality factor to increase. These two resonators can be combined in the

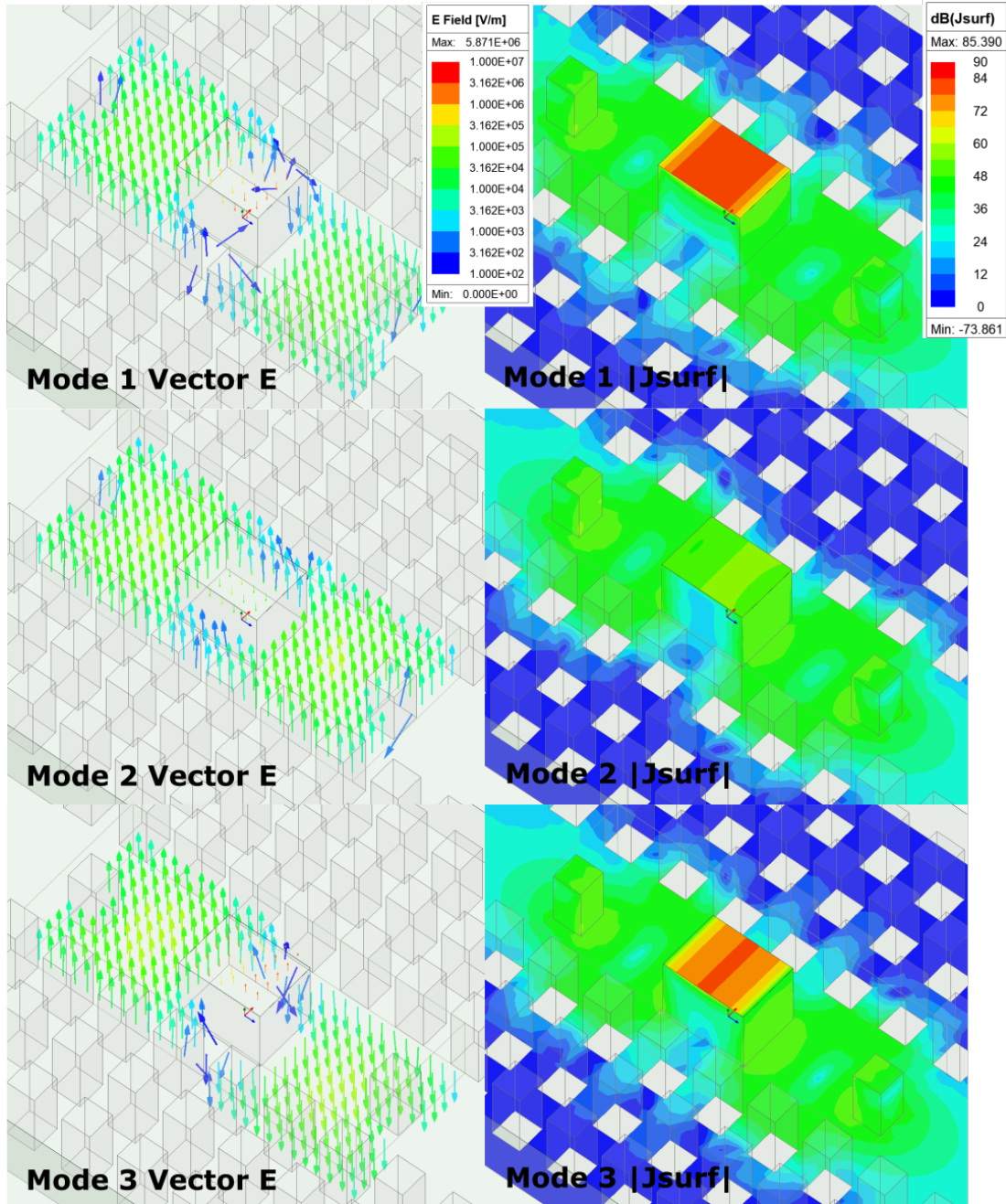


Figure 4.11: The electric field vector plots and magnitude of the complex surface current of the modes that exist in the three resonator device shown in Fig. 4.10. The surface current of mode 1 shows that this mode is dominated by the dimensions and surface dynamics of the ridge and the complementary area of the flat lid above it (the lid is made transparent to show fields within).

structure shown in Fig. 4.10, which is composed of a RGWG resonator in the middle and equal length GGWG resonators on either side of it.

This pin-coupled RGWG resonator allows for the quality factor of the ridge resonance to be tuned by changing the coupling resonator frequency and linewidth. The system is designed by choosing the length of the ridge that results in a resonance frequency at the desired frequency, then choosing a ridge to coupling pin spacing such GGWG resonance forms at a frequency near the ridge resonance, after which the coupling pin dimensions are tuned to increase the quality factor of the ridge resonance. In this work the resonator system is chosen with frequencies approximately in the middle of the Ka band, which is shown by the S-parameters in Fig. 4.10. Coupling three resonators in series will always result in three distinct resonance frequencies even if their individual resonance frequencies are identical since their mutual coupling must be taken into account. In a three series resonator system (just like in a 3 pole series filter) three distinct modes can exist that differ from one another in the phase of the fields in each pole. This can be demonstrated by the electric field vector plots in Fig. 4.11. The direction of the electric field vector arrows of the lowest frequency mode shows that the fields of the two GGWG resonators is in phase with the fields of the ridge mode on each respective side, Mode 2 shows the GGWG resonators in phase with one another while the fields of the ridge are fully in anti-phase. Mode 3 is similar to mode 1 except the GGWG resonators are now in anti-phase to the fields of each side of the ridge. Out of these 3 modes it is the first mode that is of most interest since it possess the strongest surface current distribution on the ridge region, being most similar to a pure RGWG resonator. This concentration of surface current means that the mode will respond strongly when the surface is coated with a thin superconducting layer which provides necessary nonlinear kinetic inductance.

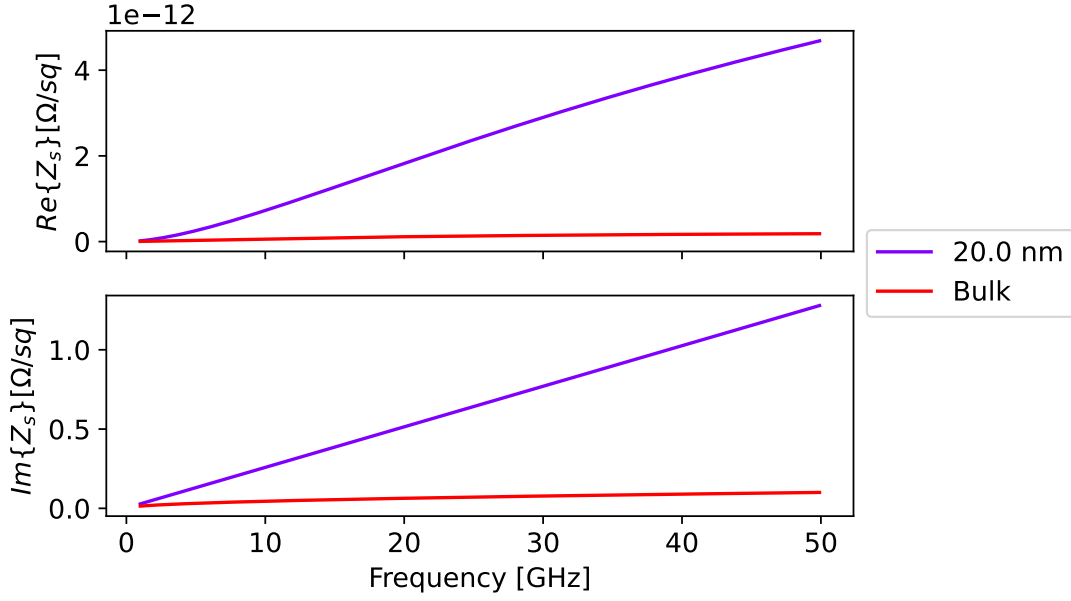


Figure 4.12: The calculated resistance and reactance of the surface impedance as a function of frequency of a 20 nm thick NbTiN coating and bulk NbTiN at 1 K. The parameters used in the calculation are [55]:  $\sigma_n = 0.55 \times 10^6$ ,  $T_c = 14.1$  K,  $\Delta_0/kT_c = 1.86$ ,  $\xi_0 = 170$  nm,  $l = 0.57$  nm. The London penetration depth with these parameters is calculated to be  $\lambda_L \approx 250$  nm.

### Superconducting Pin-Coupled RGWG Resonator

The linear contribution of the kinetic inductance ( $L_{k0}$  only, see Eq. 2.34) of the superconducting coating can be included in the HFSS simulation by setting a frequency dependent surface impedance on the inner surfaces of the resonator. The surface impedance of a superconductor was described in Section 2.2.3 and can be calculated using the Zimmermann conductivity (see Section 2.2.2). For this work NbTiN is chosen as the superconducting coating due to its high critical temperature (12 to 15 K range) lending itself to operation with low dissipation at 1 K, and its large London penetration depth (200 to 500  $\mu\text{m}$  range) which allows for a more significant kinetic inductance enhancement for a given thin film thickness (see Section 2.3.2 and Eq. 2.34). Two thicknesses of NbTiN were considered: a 20 nm film, which was chosen to maximise the kinetic inductance enhancement while still being able to achieve reasonable film thickness uniformity



with consideration to the metallic surface roughness (see Section 4.3.2); and a 1  $\mu\text{m}$  thick film which was chosen to act as a control and where the film effectively acted as bulk NbTiN from a kinetic inductance and critical current perspectives since the film thickness was much larger than the London penetration depth ( $\lambda_L \approx 250\text{ nm}$ ). The calculated surface impedance of bulk NbTiN and a 20 nm thick film is shown in Fig. 4.12. The bulk surface impedance was calculated using Eq. 2.23 while for the thin film this was calculated using 2.24.

The surface impedances presented in Fig. 4.12 were included in HFSS by importing the resistance and reactance as separate datasets for a given project file using the “Project Datasets” function. The datasets contained two columns, the first being the frequency and the second being the respective part of the impedance in units of  $\Omega/\square$ . The surface impedance was applied to a desired surface by applying an impedance boundary condition. In the boundary condition options the resistance and reactance fields were pointed to the relevant project dataset via the following command `pwl(“dataset name”,freq)`. The function `pwl()` carries out a piecewise linear interpolation of the provided data points against frequency, which uses a hard-coded global variable name “freq”.

Applying the relevant superconducting surface impedance boundary to the inner surfaces of the model allows for the inclusion of the dissipation due to BCS resistance and the resonance frequency shift due to the kinetic inductance. The dissipation does not include effects due to surface roughness or the proximity effect, which can cause regions with a reduced critical current and diminished critical temperature. For each resonance a comparison of the resonance frequency between the PEC and superconducting simulations can be used to calculate the kinetic inductance fraction. This fraction indicates which resonance will produce the strongest nonlinear effects due the kinetic inductance nonlinearity presented in Section 2.3.2. By considering the resonance frequency of two lumped element resonators, where one of these includes the contribution of the PEC structure only while the other includes an inductance contribution due to the linear kinetic

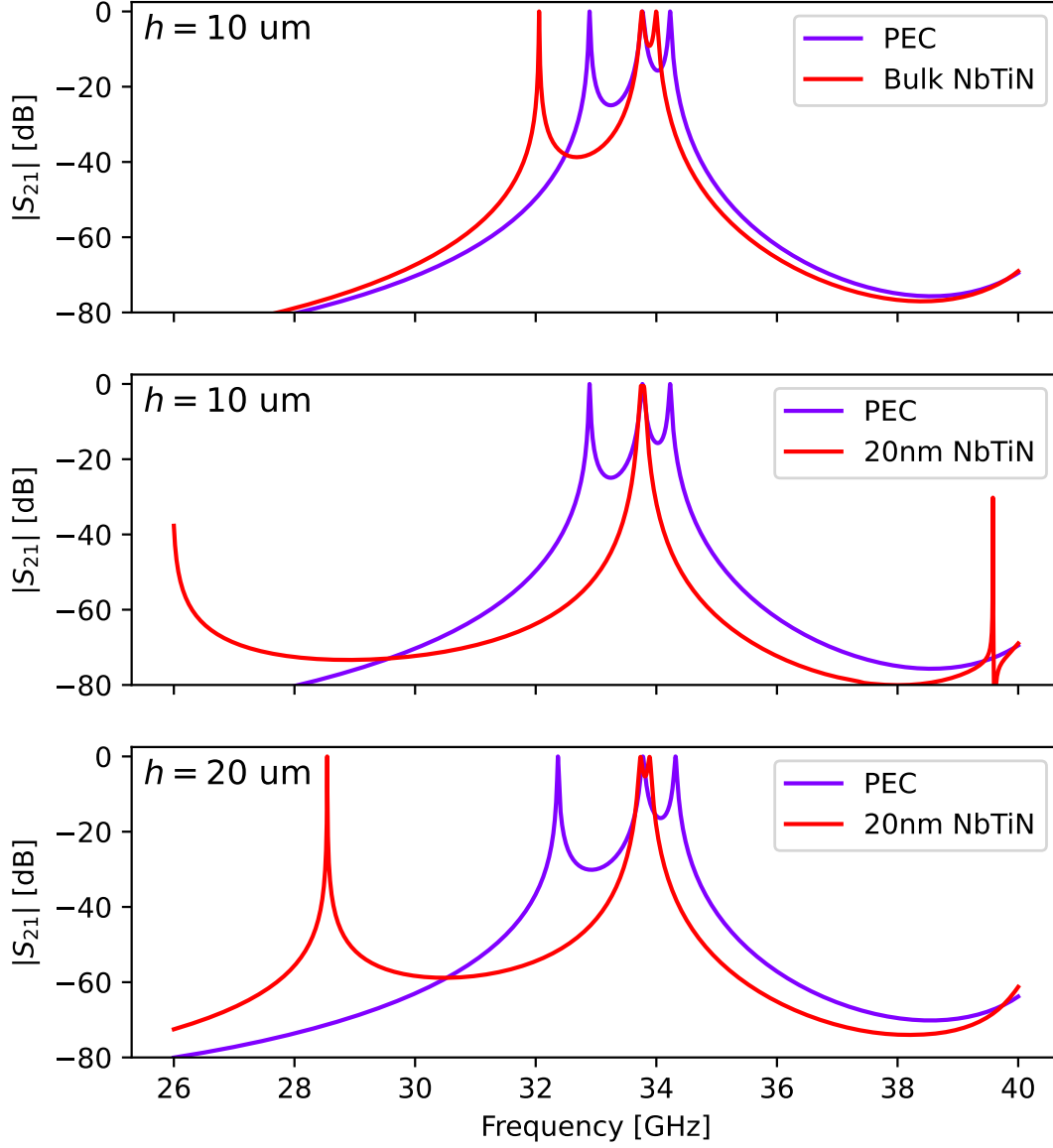


Figure 4.13: The simulated S-parameters of the pin-coupled RGWG resonator shown in Fig. 4.10 with two different NbTiN coatings: a coating of  $1 \mu\text{m}$ , which acts as bulk NbTiN, and a 20 nm thick NbTiN coating. For the latter case, an additional simulation is shown where the ridge-lid spacing has been increased to 20 nm which possesses a lower linear kinetic inductance fraction. The total quality factor,  $\omega_r/\kappa$ , of mode 1 is  $\sim 5,000$ , 43,000 and 13,000 moving from the upper to the lower plots. The other modes are have a Q of around 1,000. The KI fraction of each resonance is shown in Table 4.1.

Device	Resonance 1	Resonance 2	Resonance 3
10 $\mu\text{m}$ gap, bulk NbTiN	5.0%	<0.01%	1.3%
10 $\mu\text{m}$ gap, 20 nm NbTiN	37.6%	<0.1%	2.5%
20 $\mu\text{m}$ gap, 20 nm NbTiN	27.6%	<0.1%	2.5%

Table 4.1: The calculated linear kinetic inductance contribution of each resonance in the simulated superconducting pin-coupled RGWG resonator with two different coatings and ridge-lid spacings. The values were found by comparison to the equivalent PEC simulation.

inductance. The lumped element resonance frequency is given by  $f_r = 1/2\pi\sqrt{LC}$ , where  $L$  and  $C$  are the resonator inductance and capacitance, respectively. The superconducting resonator has an additional inductance such that  $L \rightarrow L_g + L_k$ , where  $L_g$  is the geometric inductance. These two resonance frequencies can be compared to find the linear kinetic inductance fraction,

$$\alpha_k = 1 - \left(1 - \frac{\Delta f}{f_{r,\text{PEC}}}\right)^2, \quad (4.2)$$

where  $\Delta f = f_{r,\text{PEC}} - f_{r,\text{SC}}$  is the resonance frequency difference between the PEC and the superconducting simulations.

The NbTiN surface impedances calculated in Fig. 4.12 were applied as impedance boundary conditions to all inner surfaces of the pin-coupled RGWG resonator shown in Fig. 4.10. The S-parameters from the simulations of the model with bulk NbTiN and a 20 nm thick coating of NbTiN are shown in Fig. 4.13. The plots in top and middle panel resulting from a simulation with ridge-lid spacing,  $h$  of 10  $\mu\text{m}$  show that the 20 nm NbTiN coating shifts the resonance due to mode 1 (see Fig. 4.11) to just outside the typical range of the Ka band. The Ka band waveguide lower cut-off is at  $\sim 22$  GHz, meaning that the resonance could be measured. However, the simulation in the middle panel of Fig. 4.13 shows that the resonance that is just below 26 GHz has a total quality factor of over  $100 \times 10^3$ , which would require a pristine coating with high purity, high

thickness uniformity, and low roughness ( $< 0.001$  Ra). Any additional loss due to impurities or film irregularity would severely hinder the transmission of such a resonance and would make it challenging to measure. This frequency shift can be reduced by lowering the inductance contribution of the superconducting coating which is done by increasing the geometric inductance contribution through increasing the ridge-lid gap to  $20\text{ }\mu\text{m}$ . This simulation with increased gap is shown in the bottom panel of Fig. 4.13, which indeed presents a reduced resonance frequency shift for mode 1 as well as a quality factor in the order of  $10 \times 10^3$ . Fig. 4.13 also shows that not only mode 1 experiences a resonance frequency shift as a result of the addition of the superconducting coating. Modes 2 and 3 show a small shift which allows for their linear kinetic inductance contribution to be calculated. These contributions are summarised in Tab. 4.1, which show that mode 2 with a null in surface current on the ridge has the smallest KI fraction, while mode 3 with what looked like a strong surface current in the ridge region has KI fraction that is an order magnitude smaller than mode 1. Indeed, mode 2 shift almost falls within the variation of resonance frequency under different solution and mesh conditions.

### **Kinetic Inductance Fraction**

The behaviour of mode 1 could be compared to a model where total mode inductance originates from the top surface of the ridge and equivalent area above it on the surface of the lid. This would be equivalent to a finite width parallel plate resonator where the total inductance per square is a sum of the geometric and kinetic components resulting in the following expression

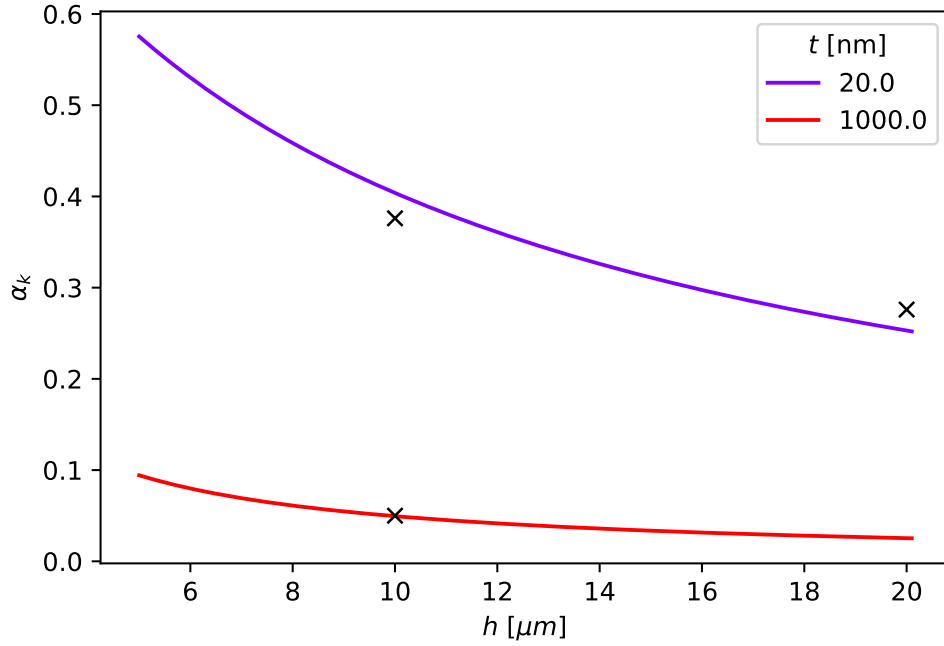


Figure 4.14: The linear kinetic inductance fraction as a function of ridge-lid separation  $h$  for a 20 nm NbTiN ( $\lambda_L = 250$  nm) film and a 1  $\mu\text{m}$  NbTiN coating. The thick coating produces the same result as bulk NbTiN. The black crosses are the kinetic inductance fraction values of mode 1 from Tab. 4.1.

$$L_{\text{tot}} = L_g + 2L_s, \quad (4.3a)$$

$$\text{where } L_g = \mu_0 h, \quad (4.3b)$$

$$\text{and } L_s = \mu_0 \lambda_L \coth \frac{t}{\lambda_L}, \quad (4.3c)$$

where the factor of 2 is included to account for the contribution of both superconducting surfaces. Here, the surface inductance,  $L_s$ , only includes the linear part i.e.  $I \ll I_c$  in Eq. 2.34. The NbTiN coatings investigated here have a penetration depth of 250 nm (calculated using Eq. 2.20), which gives the necessary scaling factor needed to calculate the linear kinetic inductance fraction given by

$$\alpha_k = \frac{2\lambda_L \coth t/\lambda_L}{h + 2\lambda_L \coth t/\lambda_L}. \quad (4.4)$$

The linear KI fraction from Eq. 4.4 is plotted in Fig. 4.14 for the two NbTiN coatings investigated. Also included in the figure are black crosses that show the kinetic inductance fraction of mode 1 from Tab. 4.1. These three crosses show that the values calculated using Eq. 4.4 are close to the ones found through via HFSS simulations followed by a calculation using Eq. 4.2. These data points can vary by a few percent depending on how close the solution frequency is set to the mode of interest, a multi solution frequency simulation could be performed to try to reduce this resonance frequency variation. The analytical model seems to be a good approximation of the inductance of mode 1.

It should be noted that the nonlinear kinetic inductance fraction may be different from its linear counterpart since the nonlinear KI fraction only includes the inductance of the film or trace that is stimulated by a current that approaches the critical current of that trace such that  $I \rightarrow I_c$ . Specifically, if one of the two participating surfaces is coated with a thick NbTiN film such that the critical current is very high and the other surface is coated with a thin film, then only the thin film KI is included in the nonlinear inductance contribution meaning that the nonlinear kinetic inductance fraction would be given by

$$\alpha_{k,NL} = \frac{\lambda_L \coth t/\lambda_L}{h + \lambda_L(1 + \coth t/\lambda_L)}, \quad (4.5)$$

where the total inductance is now a sum of the geometric, bulk kinetic and thin film kinetic inductances. This is an important consideration when considering the RGWG resonator where lower part is coated with a thick layer of NbTiN and only the flat lid has the thin film coating.

### Critical Current Estimates

In order to describe the expected performance of the RGWG RPA an estimate of the critical current of the superconducting coating is needed. The critical current sets the scale of the nonlinear behaviour of the resonator including the critical power near which parametric signal gain is maximum.

For the purpose of critical current analysis the superconducting coating on a the ridge can be considered to a be finite trace with the planar dimensions of the ridge. In the case of the flat lid, the equivalent area above the ridge is where the strong AC surface current is induced and therefore this can also be approximated as a strip of the dimensions of the ridge.

Most of the kinetic inductance parametric amplifiers discussed in Sections 2.4.3 and 2.4.4 employ narrow and thin film traces with widths  $w \leq \lambda_L^2/t$  (see note in Section 2.2.3) meaning that the current density within the film is nearly uniform. The critical current is of a similar order to the scaling current,  $I_*$ , which scales the kinetic inductance nonlinearity (see Section 2.3.2). At low temperatures for a trace with a uniform current density the scaling current can be estimated [37, 18, 64] using

$$I_* = wt\kappa_* \sqrt{\frac{N_0 \Delta^2}{\mu_0 \lambda_L^2}}, \quad (4.6)$$

where  $\kappa_*$  is constant of order 1 [117],  $N_0$  is the number density at the Fermi level and  $\Delta$  is the superconducting gap. In addition, an analysis has been performed on the critical current of these narrow films which includes the temperature dependence (valid for  $T \rightarrow T_c$ ) [118], this is refereed to as the Ginzburg-Landau pair-breaking current  $I_c^{GL}$  and is given by

$$I_c^{GL}(T) = \frac{2\Phi_0}{6\sqrt{3}\pi\mu_0\xi(0)} \left( \frac{w}{\lambda_\perp(0)} \right) (1 - T/T_c)^{3/2}, \quad (4.7)$$

where  $\mu_0$  is the permeability of free space,  $\Phi_0$  is the magnetic flux quantum and

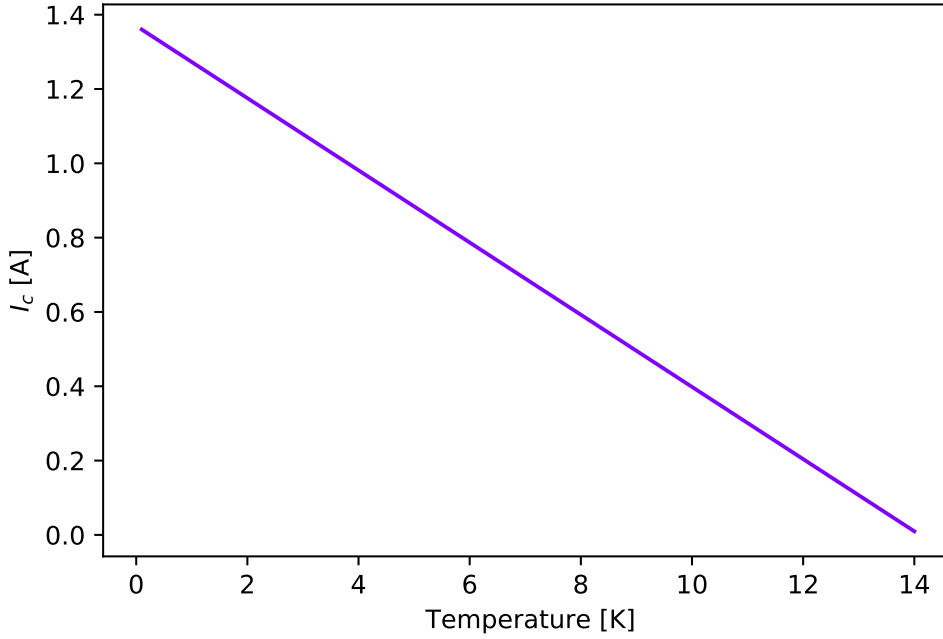


Figure 4.15: The theoretical critical current of a 3.3 mm wide and 20 nm thick NbTiN film against temperature. The following characteristics of NbTiN were used in the calculation  $T_c = 14.1$  K,  $\lambda_{\perp} = 3.13$   $\mu\text{m}$ ,  $\xi(0) = 8.4$  nm. The latter two were calculated using values from Hong *et al.* [55].

$\xi(0)$  is the low temperature Ginzburg-Landau (GL) coherence length. This GL coherence length can be calculated from the BCS coherence length,  $\xi_0$ , in dirty limit at zero temperature using the following relation [119]

$$\xi(0) \approx 0.855\sqrt{\xi_0 l}, \quad (4.8)$$

where  $l$  is the mean free path and  $\xi_0 = \hbar v_f / \Delta_0 \pi$ . Note that Eq. 4.7 has been rewritten in SI units compared to the CGS units used by Zolocheskii [118]. For completeness the conversion from CGS to SI was done by replacing any current with  $cI\sqrt{\mu_0/4\pi}$  and any charge, namely the elementary charge  $e$ , with  $q/\sqrt{4\pi\epsilon_0}$ . This resulted in the following conversion for the magnetic flux quantum  $\Phi_{0,\text{CGS}} = \sqrt{4\pi/\mu_0}\Phi_{0,\text{SI}}$ , due to their differing definitions in each unit system.

In the case of the superconducting RGWG resonators studied here the films



are much wider than the perpendicular penetration depth. The current accumulates at the edges of the film meaning that the current distribution is no longer constant and the critical current must take a different form since the critical current density of a given superconductor is constant. This wide film critical current has been studied [118] under various conditions where a number of upper bounds have been set for it. The formalism by Larkin and Onchinnikov [118] gives an estimate of this pair breaking current for pristine films with high crystal ordering, low roughness and perfect edges. However, such film quality may be challenging to achieve with depositions on a machined but polished metal surface. In these cases, polycrystalline films with a roughness of a similar order to the foundational layer, and edges that are dictated by the machining quality are achieved. The critical current of more realistic films can be much smaller than the pristine film values. However, it is instructive to calculate this upper bounds of the critical current to gauge its order of magnitude. The Larkin-Onchinnikov pair breaking current,  $I_c^{LO}$  for a wide film is given by

$$I_c^{LO}(T) = \frac{2\Phi_0}{6\sqrt{3}\pi^{1/2}\mu_0\xi(0)} \left( \frac{w}{\lambda_\perp(0)} \right)^{1/2} (1 - T/T_c), \quad (4.9)$$

which has again been rewritten from CGS to SI. Note, the difference in the scaling with film width and the temperature dependence compared to the narrow film pair-breaking current. From this point onwards, *only the LO critical current will be considered and the superscript “LO” will be dropped*. The perfect edge stipulation of Eq. 4.9 is important since  $I_c$  in a wide film is dependent on the pinning properties that arise at the edges of the trace. The critical current varies as  $1 - T/T_c$ , which means that both the operating temperature and the critical temperatures have a strong impact on the value of the critical current. A plot of Eq. 4.9 against temperature yields for the resonator coated with a 20 nm NbTiN film is shown in Fig. 4.15. At an operating temperature of 1 K the film critical current is around 1.3 A, which is particularly high and would require a strong

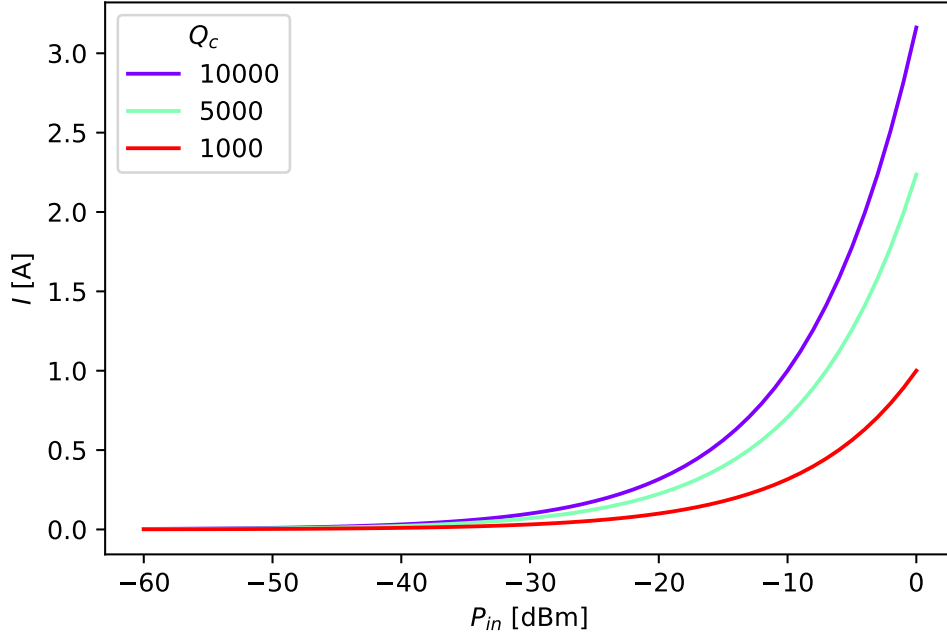


Figure 4.16: The expected circulating current in the resonator as a function of input power at different coupling quality factors. The impedance of the resonator was set to  $Z_0 = 2 \Omega$  for simplification purposes, since the impedances was calculated to be in the range of 1.2 to 2.6  $\Omega$  for all the variations with the bulk and 20 nm NbTiN coatings as well as the 10  $\mu\text{m}$  and 20  $\mu\text{m}$  ridge-lid spacings.

AC drive in order to induce such a current in a simple transmission line, where the AC current is given by  $I^2 = P_{in}/Z_0$

However, in a resonator the induced current,  $I$ , is a function of the resonators coupling quality factor,  $Q_c$ , which allows a significantly higher current to be achieved compared to a non-resonant structure. This current is given ([13] supplementary notes) by the following

$$I^2 = 2Q_c \frac{|1 - S_{11}|^2}{Z_0} P_{in}, \quad (4.10)$$

where  $Z_0$  is the impedance of the resonator,  $P_{in}$  is the power of the signal at input, and the  $|1 - S_{11}|^2 \approx 1$  term accounts for the transmission of the series resonator.

The induced circulating current needs to be estimated to evaluate whether it

is sufficient strong to stimulate the nonlinearity of the resonator, which is needed for parametric gain. The  $S_{11}$  at resonance and the resonator impedance can be extracted directly from the HFSS simulation. The total quality factor [1] is given by the following

$$\frac{1}{Q_t} = \frac{1}{Q_c} + \frac{1}{Q_i}, \quad (4.11)$$

where  $Q_c$  and  $Q_i$  are the coupling and internal quality factors of the structure. The  $Q_i$  is usually dominated by internal resonator losses such as the surface resistance, while  $Q_c$  is dictated by the impedance environment of the resonator. As shown by the strongly varying resonance width,  $\kappa$ , with different coupling schemes in the simulations presented in this section as well as the similarity of the  $Q_t$  between the PEC (where  $Q_i \rightarrow \infty$ ) and superconducting simulations, the total quality factor of the resonance can be assumed to be dominated by  $Q_c$ . Therefore,  $Q_c$  can be found by measuring  $Q_{\text{tot}}$  which is found via ratio of the resonance frequency to the full-width half-max (FWHM) of the resonance of interest in Fig. 4.13.

The resonator impedance can also be found using  $Z_0 = \sqrt{L/C}$ , where  $L$  and  $C$  are the total inductance and capacitance of the resonator, respectively. This is useful since a new simulation does not need to be carried out for every parameter change. The total resonator inductance is found by using Eq. 4.3, which is given in  $\text{H}/\square$ , and multiplying this by  $l/w$ , where  $l$  and  $w$  are the ridge length and width, respectively. The total capacitance is found using the expression for a parallel plate capacitor given by

$$C = \epsilon_0 \frac{wl}{h}. \quad (4.12)$$

These outlined parameters allow for the expected circulating current to be calculated at different input powers. This is plotted in Fig. 4.16 and shows that a  $Q_c$  of over  $10 \times 10^3$  may be needed to stimulate a strong enough circulating

current while still being below the maximum output power of the test equipment used in this project (see Chapter 3). Such a quality factor should be achievable if the device machining matches to the design specification and a film without significant impurities and low surface roughness is produced. A device temperature near 1 K is needed to ensure that the internal quality factor does not add significant dissipation and lower the total  $Q$ . This quality factor should provide a sufficient circulating current which can stimulate nonlinear behaviour and allow the superconducting RGWG resonator to operate as an RPA.

### 4.2.3 Nonlinear Circuit Simulations

The RGWG resonator described in this chapter shows promise as a high frequency resonant parametric amplifier. However, prior to any fabrication attempts it is imperative to predict the key performance metrics of this amplifier such as the critical pumping power (also referred to as the bifurcation power), as well as the achievable gain, the gain bandwidth, and the 1 dB compression point. As shown in the analysis of Section 2.4.3 the gain-bandwidth product of such an amplifier should be constant, and the 1 dB compression point would be dictated by the signal power at which the pump-driven resonance profile begins to shift.

The critical power, gain, and bandwidth can be extracted analytically using the analysis outlined in Section 2.4.3 with some additional development of the transmission matrix for the specific case of the series resonator presented in this chapter. An accurate model of the 1 dB compression point can also be developed by extending the number occupancy of the cavity (see Fig. 2.12) to include the effect of the signal power, which was successfully carried out in literature [86] and compared to measurements.

The work of this section presents a different approach that makes use of industry standard simulation software, Keysight ADS <sup>1</sup>, which is commonly used

---

<sup>1</sup><https://www.keysight.com/us/en/products/software/pathwave-design-software.html>

for transistor-based LNA design and the simulation of full feeding networks. This approach aims to simplify the design and simulation process to make the analysis of such resonant parametric amplifiers more accessible to a larger number of amplifier designers that may not be as familiar with the field of superconducting parametric amplifiers.

ADS has been used in the past [120] to analyse nonlinear Josephson circuits using a Verilog-A model of the Josephson junction. This analysis was compatible with time domain simulations only due to the use of a Verilog-A model which severely impacted the simulation speed (due to the necessary Fourier transforms to work in the frequency domain) and analysis complexity to extract the necessary circuit metrics. The methods presented here build the nonlinear circuits using components available in ADS, which allows the use of the full suite of simulation types such as Large Signal S-parameter (LSSP) mode, which allows the extraction of nonlinear S-parameters, as well as the Harmonic Balance (HB) mode, which allows multi-tone mixing simulations, tracking of mixing products culminating to the evaluation of the parametric processes taking place.

### **Equivalent Lumped Element Model**

The analysis presented in Section 4.2.2 shows that mode 1 of the superconducting resonator (see Fig. 4.11) has the strongest response to the added kinetic inductance and, therefore is a prime candidate for parametric gain. The dynamics of this mode are dominated by the ridge region of the resonator. This simplifies the modelling of this resonance and will be the focus of the proceeding analysis.

The first step in simulating superconducting RPAs in ADS is the construction of an equivalent circuit model of the resonator using linear and nonlinear components. The linear components consist of the equivalent lumped model elements, namely the geometric inductance and the parallel plate capacitance shown in Eq. 4.3c and 4.12, respectively. Note, that the inductance is given in units of  $\text{H}/\square$  meaning that this needs to be multiplied by  $l/w$  to get the total inductance. The

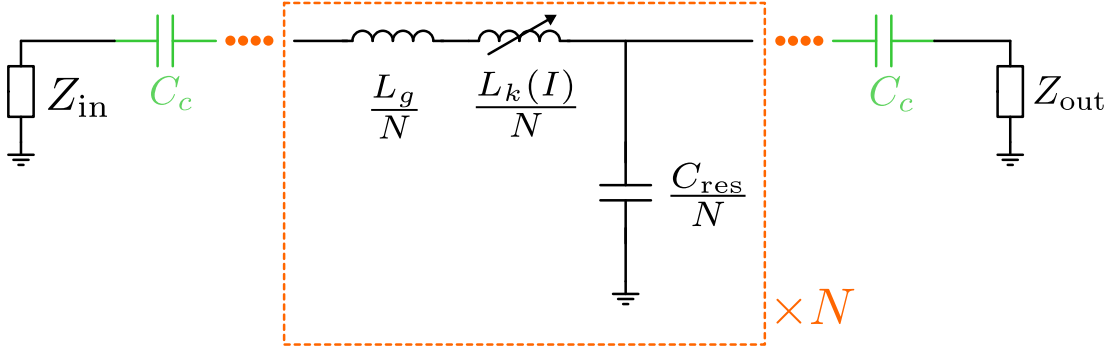


Figure 4.17: The equivalent circuit model of a series  $\lambda/2$  resonator coupled to input(output) port with impedance  $Z_{\text{in}}(Z_{\text{out}})$  via a coupling capacitance  $C_c$ . The total inductance and capacitance of the resonator is split up into an LC ladder that is  $N$  cells (orange box) long where  $N > 10$  per wavelength of the RGWG. The resonator is split into a geometric  $L_g$ , and kinetic  $L_k$  inductances as well as resonator capacitance  $C_{\text{res}}$ .

nonlinear part consists of a nonlinear inductor following the relation given by Eq. ??, which can be defined in ADS in a number of ways. One of these is to use the nonlinear inductor component which requires the definition of coefficients of a general inductance in the form  $L(I) = a + bI + cI^2 + \dots$ , where  $a, b, c$  are the nonlinear coefficients. Alternatively, the nonlinear inductance can be defined using a Symbolically Defined Device (SDD), which requires the definition of the voltage-current relationship of the inductor in the form

$$V = \frac{d}{dt} (L_k(I)I). \quad (4.13)$$

The SDD was chosen to represent the nonlinear inductor since it has additional functionality in generating noise, which may be useful in possible future developments involving RPA noise analyses. An equivalent lumped element representation of a lossless transmission line resonator can be in the form a series LC ladder, where the total inductance and capacitance of the ladder is equal to the values calculated using the parallel plate model presented previously. This lumped element representation is shown in Fig. 4.17 in which the resonator represented by  $N$  unit cells. Each unit cell contains a linear geometric and a nonlinear

kinetic inductor in series, as well as a capacitor to ground. The values of these elements are divided by the number of cells that are used in the mode, where at least 10 unit cells should be used per wavelength of transmission line. In this case, the  $\lambda/2$  resonator would require at least 5 unit cells. This distribution of the LC components means that the cut-off frequency of lumped element representation, which given by  $\omega_c = 2/\sqrt{L_{\text{cell}}C_{\text{cell}}}$ , above which the circuit acts a low pass filter significantly affecting transmission. Since this effect is an only due to the lumped element representation, the number of elements should be chosen such that cut off frequency is well above the maximum frequency of interest. The impedance of the input and output lines is set be the rectangular waveguide feeds which have an impedance  $Z_{\text{in}} = Z_{\text{out}} \approx 377\Omega$  at the top of the waveguide operational band. The resonator is coupled to these feedlines using a simplified capacitive coupling with capacitance  $C_c$ . The coupling capacitors can be used approximate the increased coupling Q that is achieved by including the coupling GGWG resonator at the input and output of the RGWG resonator.

### Power Dependent Frequency Shift

The resonance of interest is mode 1 of the superconducting pin-coupled RGWG resonator shown in bottom panel of Fig. 4.13. This resonance has a simulated linear resonance frequency of 28.542 GHz with a coupling  $\kappa = 2.2$  MHz, which results in a  $Q_{\text{tot}} \approx 12,000$ . This resonance profile in the linear regime was reproduced in the circuit simulation by tuning the coupling capacitors. A linear S-parameter simulation was used for this step due to the significant simulation speed advantage, the exact circuit for this simulation is shown in Fig. A.1.

The coupling capacitors shown in Fig. 4.17 were tuned to  $C_c = 1.41$  fF. This can be compared to the total resonator capacitance of  $C_{\text{res}} = 6.43$  pF and total inductance of  $L_{\text{tot}} = 44.85$  pH (of which 27% is the kinetic inductance). The small value of the coupling capacitance re-affirms that the resonance frequency shift due to the tuning of these coupling capacitors should be near negligible.

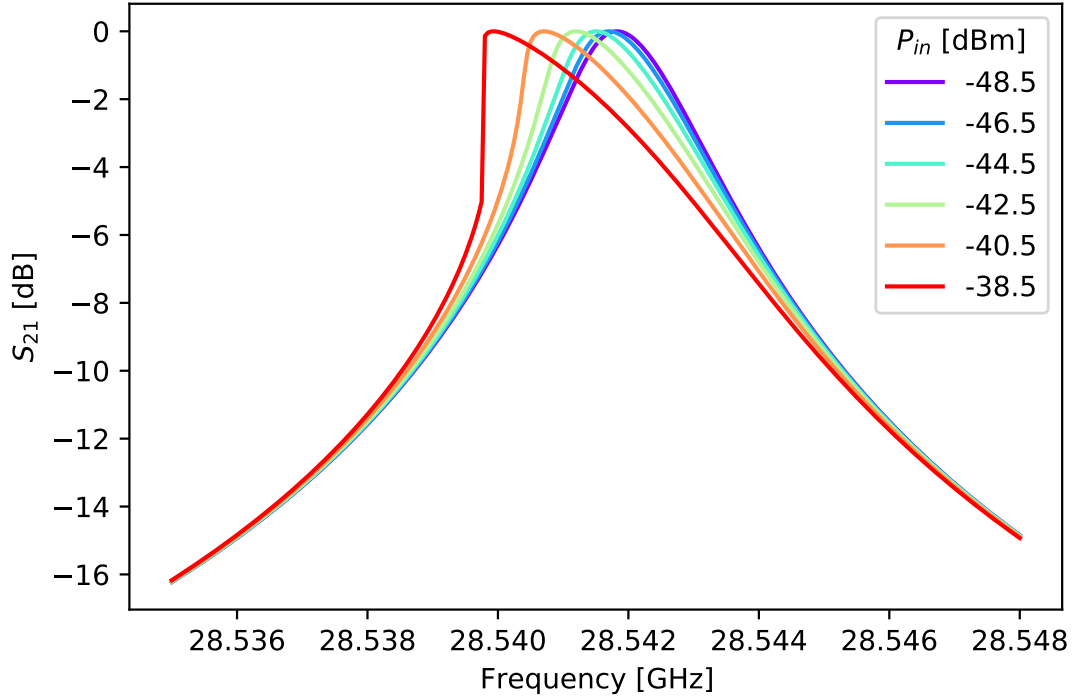


Figure 4.18: The simulated nonlinear insertion loss at a number of input powers leading up to the point where the resonator bifurcates. This point presents itself when the resonance profile bends to produce a near discontinuous jump in transmission, which is around  $-38.5$  dBm in this case. A scaling current of  $1.3$  A was set for this simulation.

The nonlinear S-parameters were found using the LSSP simulation mode in ADS (see Appendix A.1), where a scaling current of  $I_* = 1.3$  A was set (see Fig. 4.15). This circuit employed input and output ports with the ability of changing the input power. The simulated non-linear insertion loss at different input powers is shown in Fig. 4.18. These show a bending of the resonance as the input power approaches bifurcation. This bending is characteristic of a Duffing oscillator as it approaches critical drive [89] and follows the same trend as the mean photon occupancy inside a nonlinear resonator shown in Fig. 2.12. A parametric amplifier is usually operated below this point due to additional dissipation coming above it where the resonator dynamics become more complicated. The achievable parametric gain is maximised when the pump power is set to a value close to the bifurcation power, which in this case was found to be  $-38.5$  dBm.



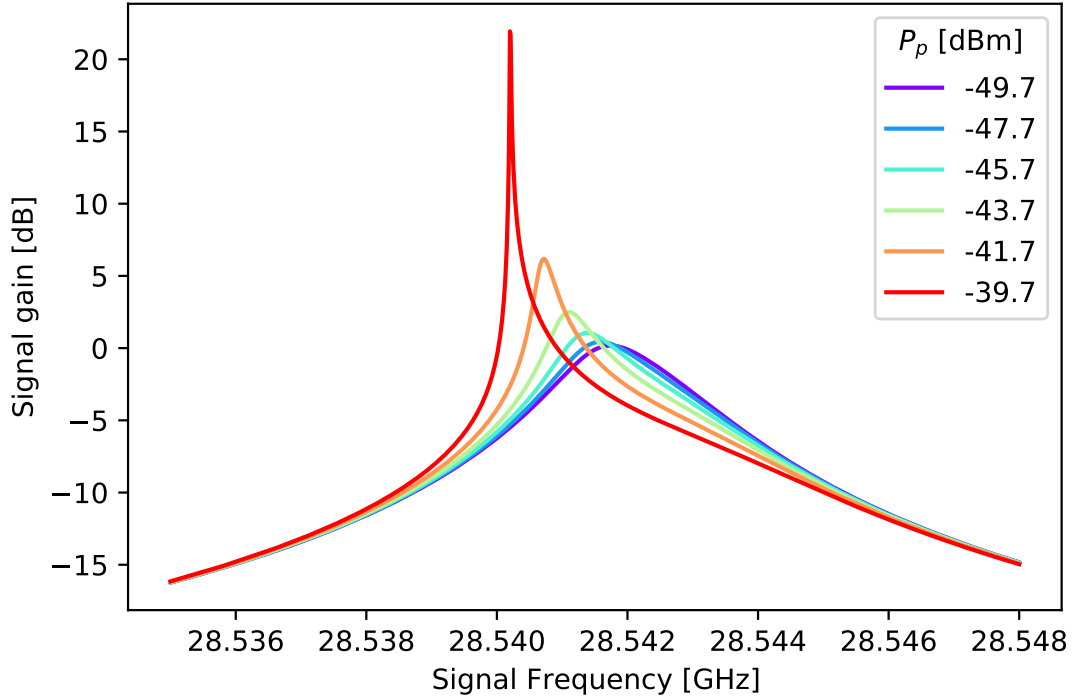


Figure 4.19: The parametric gain of a weak signal in the presence of a pump of different input power for a series pin-coupled RGWG resonator simulated with the HB simulation mode in ADS. The signal power is set to -110 dBm to ensure operation well below the compression point. A constant pump detuning of  $f_p - f_s = 10$  kHz is used. The scaling current was set to 1.3 A.

### Parametric Gain

The parametric signal gain can also be predicted by adding a second tone into the simulation and by employing the harmonic balance (HB) simulation mode in ADS. This mode also allows for specific generated harmonics to be tracked using a unique index (see Appendix A.1) meaning that evaluation of specific parametric processes is straightforward compared to other work [120, 94] where a transient analysis method is employed. The two input tones are inserted into the circuit described in Fig. 4.17 by using a multi-tone source in ADS (see Appendix A.1 for further details). As explained in Section 2.4.3 the parametric signal gain is maximised when pump is near the critical drive power (bifurcation power) with a zero signal to pump detuning. However, in order to reliably distinguish the

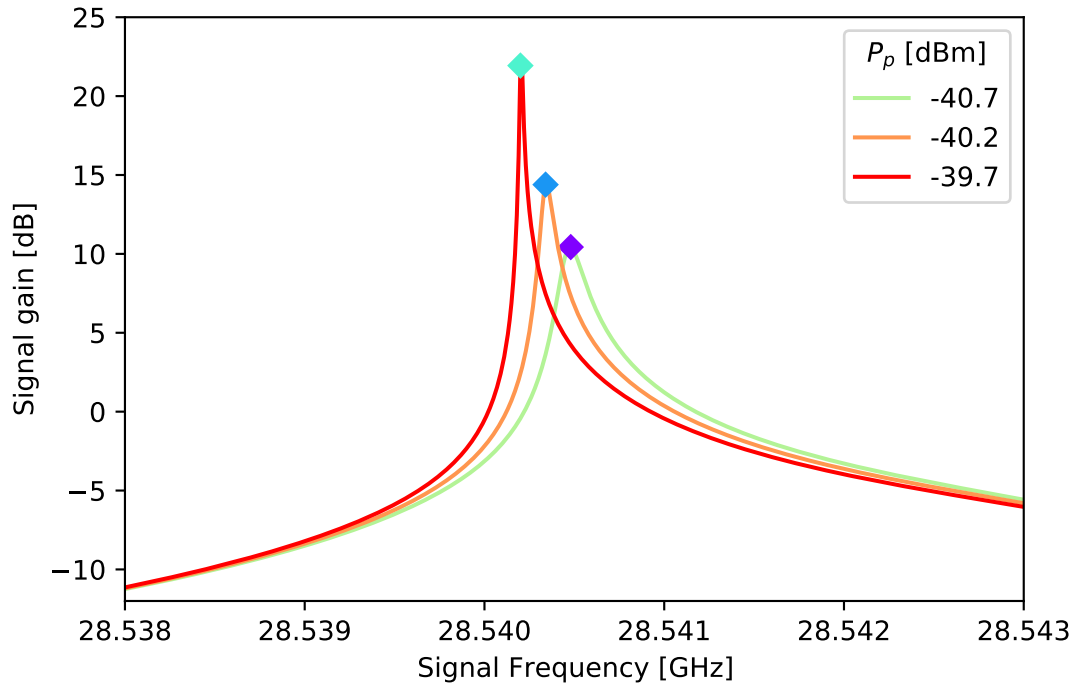
signal from the pump, this detuning is chosen to be 10 kHz. It is also important to consider the input power of the signal, which should be set to a sufficiently low value such that any possible gain compression effects could be safely ignored. To this effect, the signal power is set to -110 dBm to generate the initial gain curves, after which a more detailed analysis of the compression point can take place.

The simulated signal gain at different pump drives is shown in Fig. 4.19, which is in qualitative agreement with the analytical gain curves presented in Fig. 2.13. The analytic gain plots could be overlaid and potentially used for fitting to extract some additional amplifier metrics but this requires further development of the analytical expressions of the gain to include the transmission matrix of the series resonator. This expansion of the model is similar to the work carried out by by Anferov *et al.* [19] and Parker *et al.* [74]. The already calculated device RGWG RPA metrics can be used to calculate the Kerr coefficient  $K = -\frac{3}{8} \frac{\hbar \omega_0}{L_T I_*^2} \omega_0$  [74], which can be used to compute the dimensionless drive  $\xi = K \frac{1}{\hbar \omega \kappa^2} P_{in}$  [19].

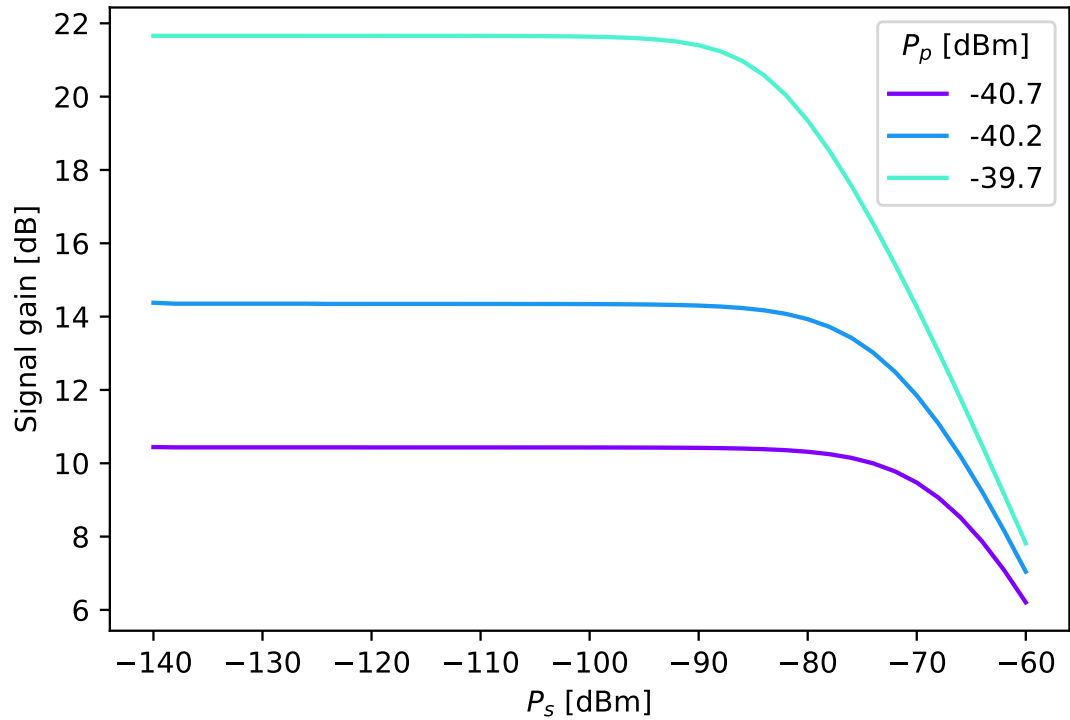
## Dynamic Range

In addition to the achievable gain it is necessary to know the dynamic range of the amplifier which is limited by the noise floor of the amplifier at the lowest point and the 1 dB compression point at the highest point. In an RPA, the 1 dB compression point occurs when the signal power is high enough such that it induces a Kerr shift to the resonance profile in addition to that of the pump tone. When this occurs, the pump and signal become detuned from the peak transmission (in the case of a series resonator) of the resonator and the gain begins to progressively decrease as the signal power increases. The dynamic range is evaluated when the pump is positioned at peak gain conditions for a given pump power and frequency. The circuit developed to extract the RPA gain can also be used to simulate the dynamic range (see Appendix A.1 for full details).

The dynamic range was simulated at three peak gain points as shown by Fig. 4.20. These curves show that the 1 dB compression point is between -90



(a) The simulated signal gain at three pump power near the peak value. The diamonds positioned on peak signal gain signify location at which points the dynamic range is evaluated.



(b) The dynamics range at three different gain settings.

Figure 4.20: The simulated signal gain for three different peak gain conditions and the dynamic range at each of these points.

to -60 dBm depending on how strongly the resonator is driven by the pump. The dynamic range can also be computed using analytic solutions developed by Planat *et al.* [86] of an expanded mean photon occupancy model that computes the value of  $\bar{n}$  with respect to the signal power in addition to that of the pump.

The simulated signal gain and compression point analysis provides the necessary parameter space for the measurements of the fabricated device.

### 4.3 Mechanical Design and Fabrication

The physical realisation of the RGWG resonator simulated in Section 4.2.2 was carried out in multiple stages. These were: the conception of a mechanical CAD model that included methods to assemble and align the two parts of the device; this model was use to create a set of technical drawings that contained the instructions for the machining workshop; the machining of the device in the workshop; the polishing/lapping of the flat surfaces in order to prepare the for thin film coating; and finally the coating of the devices via magnetron sputtering. The proceeding sections will cover these aspects of the device fabrication which will result with a set of resonators that are ready for measurement.

#### 4.3.1 Mechanical Design

The mechanical CAD model of the Ka band RGWG resonator was created in Autodesk Inventor <sup>2</sup> using the dimensions that were simulated in HFSS. This model, which is shown in Fig. 4.21, highlights some features of the design. The rectangular feeds shown are spaced such that they connect directly to the waveguides in the cryostat (see Chapter 3). These feeds lead to a E-plane mitered bends that make use of a miter distance from the radius of the bend  $d$  to waveguide short wall length  $b$  of  $d/b = 0.87$  [121]. This was chosen as a compromise between

---

<sup>2</sup><https://www.autodesk.com/products/inventor/>

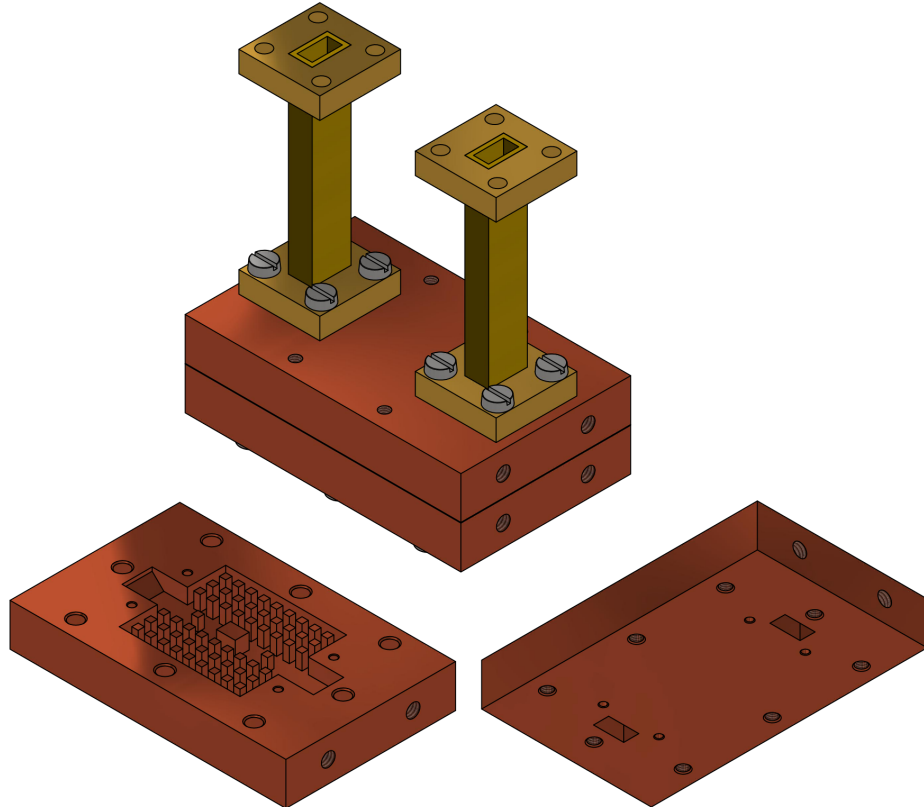


Figure 4.21: The mechanical model of the Ka band RGWG resonator. The top shows the full resonator assembly including rectangular waveguide feeds and fasteners. It should be noted that the fasteners are all brass to avoid stray magnetic fields due to impurities in some grades of stainless steel. The bottom left part is referred to as the resonator body while the bottom right is resonator lid. Both of these part show the inner features of the resonator. The resonator was designed such that the ridge and top of the nails were flush with the outer rim to allow these to be polished prior to thin film coating. The footprint of both resonator parts is 65x40x10 mm.

minimum  $S_{11}$  and total operational bandwidth, which allowed for the whole of the Ka band to be covered.

The unoccupied M3 and M4 threaded holes are for thermometry and thermal links for use inside the cryostat, respectively. The alignment of the two parts is achieved using 1.5mm dowel pins that make use of a transition fit on the resonator body meaning that the dowel pin is a tighter fit but can still be removed with a little force, while the resonator lid uses clearance holes that slide over the dowel pins with relative ease. Useful resources for dowel pin fitting can be found here

<sup>3</sup> <sup>4</sup>. The spacing between the mating surfaces of the two parts, referred to  $h$  as shown in Fig. 4.1, is achieved via a metallic film spacer such as standard aluminium foil or for a more specific spacing, this can be done via timed film deposition on the outer rim of the resonator body (see Section 4.3.3). The full set of technical drawings of the resonator can be found in Appendix A.2.

The body of the resonator was chosen to be made out of oxygen-free high-conductivity (OFHC) copper due to its high thermal conductivity at cryogenic temperatures, lack of magnetic impurities, and a high melting point. The thermal conductivity is particularly useful since it ensures that the whole resonator is at the same temperature during cooling cycles and when a particularly high input power is used when testing with the VNA. The lack of magnetic impurities means that the superconducting state is less likely to cause some stray flux to be trapped in its surface, causing additional dissipation. Finally, the high melting point is a necessity for the reactive magnetron sputtering of NbTiN which requires the surface to be at 650 °C. Other materials have been considered that have their own advantages. Aluminium is a superconductor below 1 K which means it could act as a magnetic shield if the device reaches a low enough temperature. However, the thermal conductivity of aluminium is much poorer; and the melting point is too low for the sputtering, which would cause surface deformation to occur once heated to the necessary temperature. Brass was avoided due the possibility of the zinc present within it being evaporated and poisoning the targets used in sputtering.

Five identical resonators were machined in order to be able to deposit different films at different thicknesses and to have back up devices in case some didn't work. One of the machined resonators is shown in Fig. 4.22. It can be seen in this image that there are machining marks present on all the surfaces. The overall root mean squared surface roughness can be assumed to in hundreds the of nanometres since

---

<sup>3</sup><http://www.pfeffer.ch/isotolerances.htm>

<sup>4</sup><https://amesweb.info/fits-tolerances/tolerance-calculator.aspx>

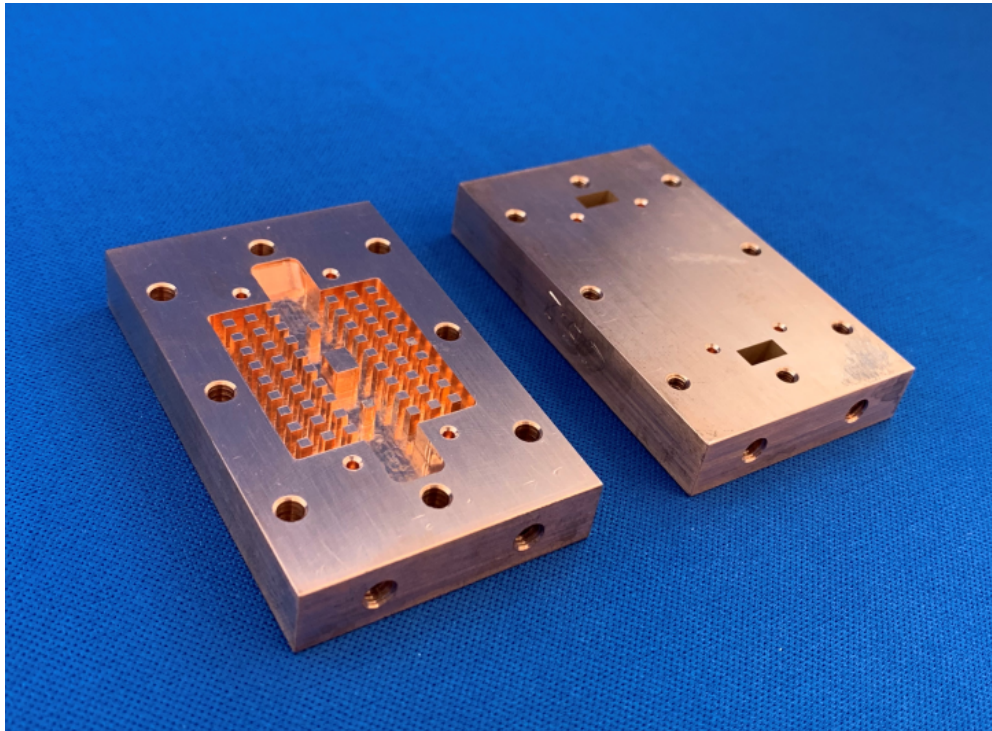


Figure 4.22: A photograph of one of five identical RGWG resonators that were machined from OFHC copper. Machining marks are visible along all of the surfaces.

the surface scatters the incident light upon it instead of showing a clear reflection. This surface roughness is problematic for thin film coating. A more quantitative analysis of the surface roughness can be achieved through measurement. A very small region can be measured using a technique called atomic force microscopy (AFM), which gives an estimate of the quality of the surface.

AFM [122] is a type of scanning probe microscopy that gathers information about a surface by running a fine tip probe across it. The AFM can be configured to measure the height distribution of small patch of a surface (usually a few tens of  $\mu\text{m}$  square). A simplified explanation of the principle of AFM surface displacement measurement is as follows. The probe is usually on a cantilever mechanism upon which a laser is directed at an angle followed by a photodetector measuring the intensity of the reflected light. When the tip contacts the surface it bends the cantilever and changes the intensity of the reflected light. This mechanism can be used to calibrate the probe position to multiple orders of

magnitude better precision than an optical system that is limited by the optical diffraction limit. By scanning the tip of the AFM over a surface in series of parallel lines an image of the surface topology can be built up.

A small square was measured in the middle of each machined resonator. The raw data exported from the AFM was analysed using open source software Gwyddion<sup>5</sup>. An example of this is presented in Fig. 4.23, which shows that the range in the data is of order of 2  $\mu\text{m}$ . The data set can be represented by single averaged value referred to as mean roughness (often denoted as Ra in units of micrometres by convention) which is given by the following equation

$$\text{Ra} = \frac{1}{L} \int_0^L |Z(x)| dx, \quad (4.14)$$

where L is the length of the line that is being evaluated (a single scan line) and  $Z(x)$  is the profile height function. This roughness was measured in the middle of each of the 5 resonators composed of 2 parts and the results ranged between 0.2 and 0.5 Ra.

As discussed in section 4.2.2 NbTiN coating thicknesses on the order of few 10s of nanometres are needed in order for a high kinetic inductance fraction to be reached. Irregularity in the film thickness can cause a multitude of issues: fluctuations in impedance due to varying surface inductance; extra dissipation due to regions where film is so thin that it has diminished critical temperature due to proximity effect; variation in critical current which can create regions where the critical current is surpassed and the current is carried by quasiparticles are experience a higher resistance. These effects all add dissipation which negatively impacts the resonance quality factor, on resonance transmission and any possible signal gain. Many of these issues can be alleviated by growing the superconducting films on a smoother surface. The machined surfaces can be polished by a technique referred to as lapping, which would significantly improve the flat mat-

---

<sup>5</sup><http://gwyddion.net/>



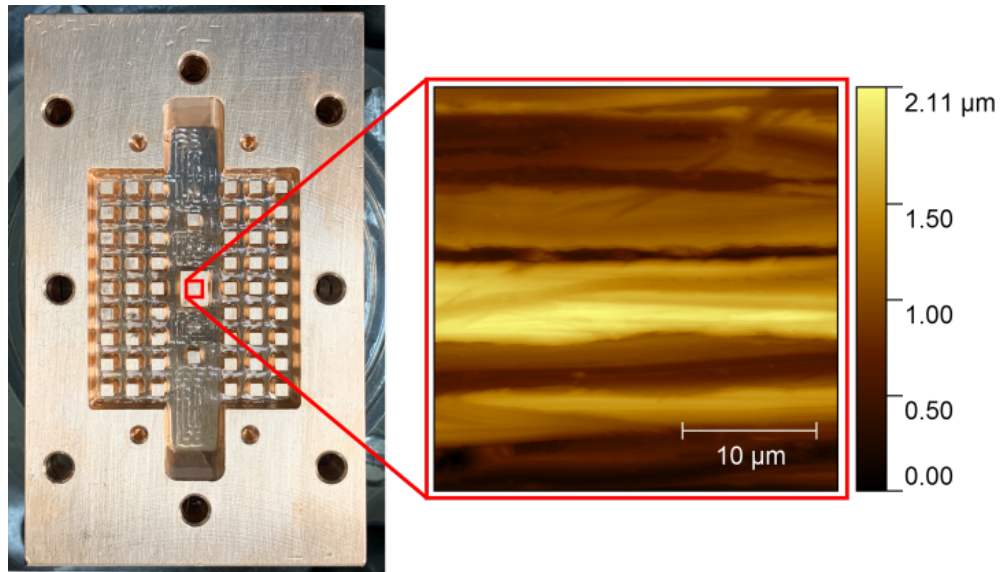


Figure 4.23: An AFM 3D profile of a 30 by 30  $\mu\text{m}$  square in the middle of the ridge of the RGWG resonator. The post-processing on the raw data included levelling using mean plane subtraction and alignment of row.

ing surfaces shown in 4.22. The surface of the ridge and the complementary flat region above the ridge on the lid are most crucial to the structure since the surface currents are most concentrated there and the dissipation due to film irregularities is highest.

### 4.3.2 Surface Polishing

#### Principles of Operation

Surface polishing/lapping is a processes in which two surfaces are rubbed together with an abrasive between them. The polishing of the copper surfaces of the resonators was achieved using a Logitech PM5 polishing and lapping system, the working principle of which is shown in Fig. 4.24. The polishing is achieved via an abrasive suspension which is drip onto an absorbent lapping pad that is affixed on a rotating lapping plate. The sample is attached to a lapping jig with the surface of interest face down. The sample is lowered onto the lapping pad under the weight of the piston loaded lapping jig, which itself can rotate freely. As the

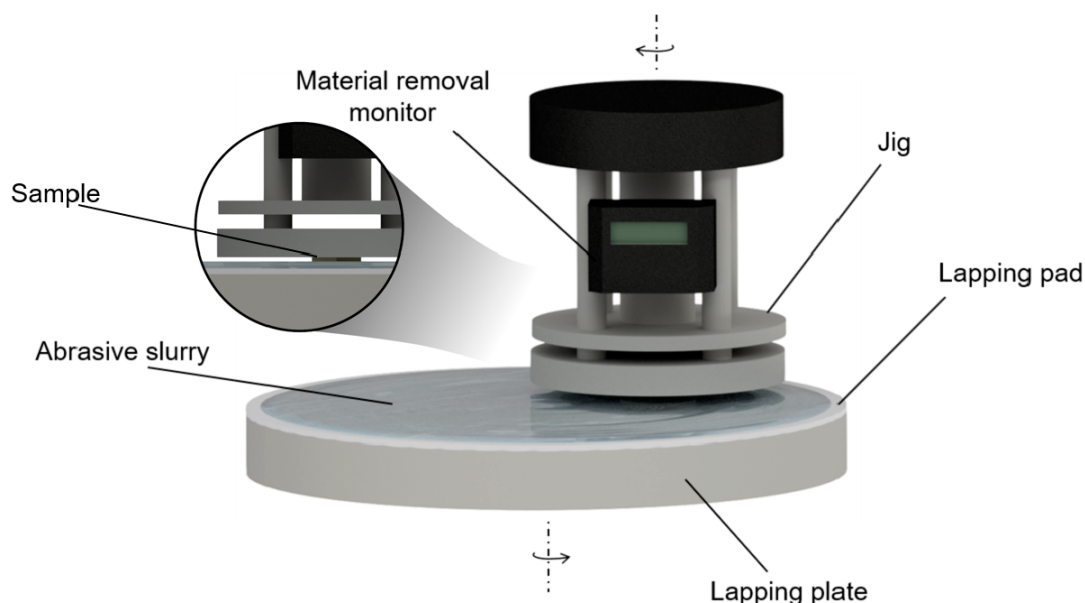


Figure 4.24: An illustration of the Logitech PM5 polishing and lapping system. An abrasive slurry is drip-fed onto the rotating lapping pad during the polishing process. The lapping jig to which the sample is affixed is held in place by a motorised arm that sweeps across the radius of the lapping plate. The lapping jig is allowed to freely rotate via the bearing on the jig arm and the contact with the lapping plate [123].

lapping plate and lapping jig rotate, the abrasive action of the slurry removes material from the sample's surface. This removal rate can be measured using a micro-resolution digital gauge which is attached to the lapping jig.

Typical abrasive slurries that are used in lapping include suspensions of alumina in water, synthetic diamond pastes, and colloidal silica (Col-K) suspensions. The size of the particulates in the suspension dictate the rate of material removal and the minimum achievable roughness of the polished surface. In order to achieve the necessary surface polish in the shortest time, the polishing is carried out in multiple stages of decreasing particulate size. The removal of material is achieved by two main surface mechanisms, these are shown in Fig. 4.25. The initial polishing steps involve abrasive polishing, where mechanical action of the large particulates works to smooth the sample surface. The final polishing step that achieves the smallest roughness (often on the nanometre scale) is conducted

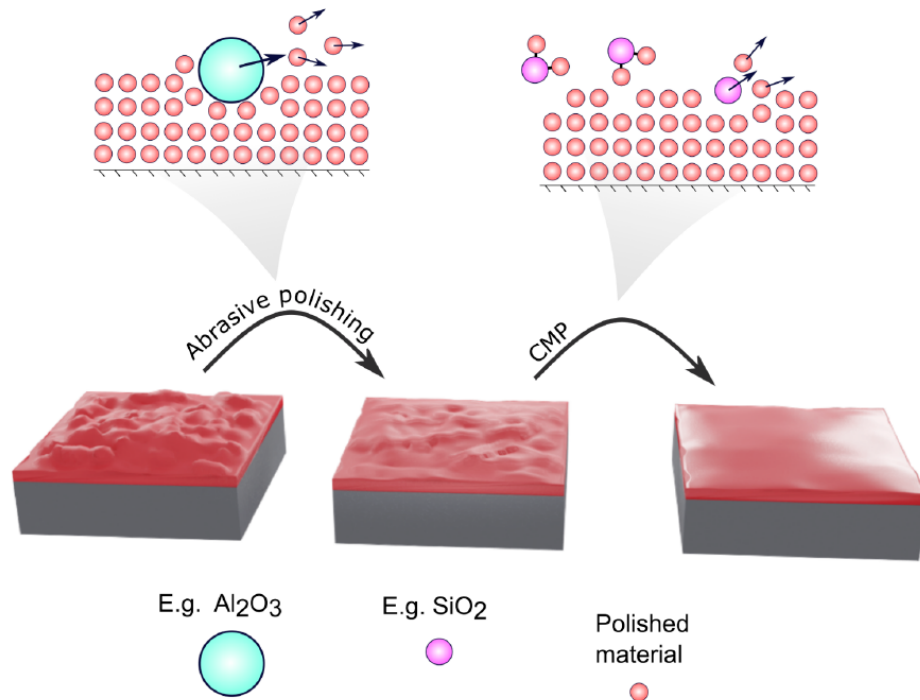


Figure 4.25: An illustration showing the two key mechanism in surface polishing. The first polishing stages are done via abrasive action using a slurry containing particulates such as alumina ( $\text{Al}_2\text{O}_3$ ) in multiple stages with particulates of decreasing size. The final polishing stage uses a suspension like colloidal silica ( $\text{SiO}_2$ ) via a CMP mechanism involving both mechanical polishing and chemical etching simultaneously [123].

via chemical-mechanical polishing (CMP), with the aforementioned colloidal silica suspensions. The CMP process includes a combination of mechanical action and chemical etching.

### The Process

The objective of the polishing was to reach a roughness of below at least  $\sim 0.01 \text{ Ra}$  on the inner mating surfaces of the resonators. This value was near the practical limit that could be achieved with this system for the machined copper surfaces without an extensive optimisation of the polishing process.

The most important element of the polishing was in the cleaning of the samples and the machine before and between each polishing steps. This was so to reduce

the impact of any foreign particulates and particulates from previous polishing steps on the final surface finish. Improper cleaning could result in scratches on the finished surface. The copper parts were first submersed in a solution of deionised (DI) water and detergent Decon 90 and placed in an ultrasonic bath for 15-20 minutes in order to dislodge and dissolve various oils and residues left over from the machining process. The sonication was repeated using acetone, isopropyl alcohol (IPA) and the DI water. The polishing machine was cleaned from the bottom up with a nylon brush, rinsed with DI water and dried with lint-free wipes. There were separate slurry tanks for each type of abrasive suspension to reduce contamination. The lapping plate used for the first steps were rinsed thoroughly and a new polishing pad was used for each polishing stage and each surface. The final polishing step with Col-K made use of a separate polyurethane lapping plate which required particularly thorough cleaning with a nylon brush and DI water. The perforated surface of that lapping plate could collect Col-K crystals which could scratch the surface of the sample being polished. The plate also needed to be conditioned using a weighted diamond conditioning block and DI water that was placed instead of the lapping jig. This conditioning cleaned the surface and flattened the plate.

The copper samples were affixed to the removable bottom plated of the piston of the lapping jig using wax adhesive. The wax was applied to the bottom plate when it was heated with a hot plate to a temperature where the wax runs freely. The sample was then pressed on the plate which secured it once the assembly has cooled. The sample would remain attached throughout all polishing steps.

A number of variations on the polishing process were tried with similar results. Initially a three step process was tested:

1. 9  $\mu\text{m}$  alumina and DI slurry, polishing pad, for 2 hours at 45 RPM
2. 3  $\mu\text{m}$  alumina and DI slurry, polishing pad, for 2 hours at 35 RPM
3. Pre-made Col-K solution, polyurethane plate, for 2 hours at 25 RPM

The rotation speeds of the lapping plate could be set where a higher rotation speed would increase the removal rate of material but a smaller speed would be improve the final finish for a specific step. A smaller rotation speed should be used for each subsequent polishing step for a better surface finish. The first step was used to ensure any global surface flatness was resolved in addition to smoothing out any big scratches on the surface.

Inspection of the surfaces visually can be a useful indication of surface quality. As a rule of thumb if one can see their own reflection on the surface then the surface roughness is at least a fraction of wavelength of visible light. The less red the surface looks the lower the roughness due to the shorter wavelengths of light being reflected instead of scattered by the surface.

As an alternative to the three step process it was found that a two step process could also achieve a very similar surface finish. This was the following:

1. 6  $\mu\text{m}$  alumina and DI slurry, polishing pad, for 2 hours at 45 RPM then 35 RPM for another hour
2. Pre-made Col-K solution, polyurethane plate, for 2 hours at 35 RPM then 25 RPM for another 1 hours

The progression of the copper surface is shown in Fig. 4.26 which demonstrates the appearance of a reflection as the surface gets smoother. The roughness was of the polished surfaced were measured again using AFM and showed that the roughness varied between 0.03 and 0.007 Ra. All surfaces apart from one were below 0.012 Ra. An example of the spectra is shown in Fig. 4.27.

The outlined methods are by no means the definitive instructions for polishing copper since no intermediate measurements were performed other than visual inspection. However, the comparison of the AFM roughness measurement before and after the polishing shows that the surface roughness has significantly improved.

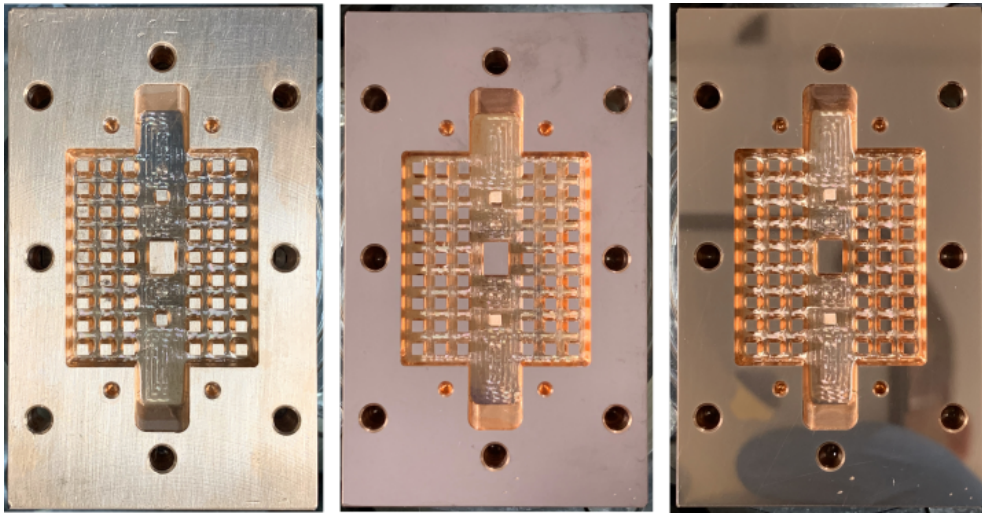


Figure 4.26: Photographs showing the progression of the polishing of the RGWG resonator using a two step process. From left to right: unpolished, post 6  $\mu\text{m}$  polish, post Col-K polish.

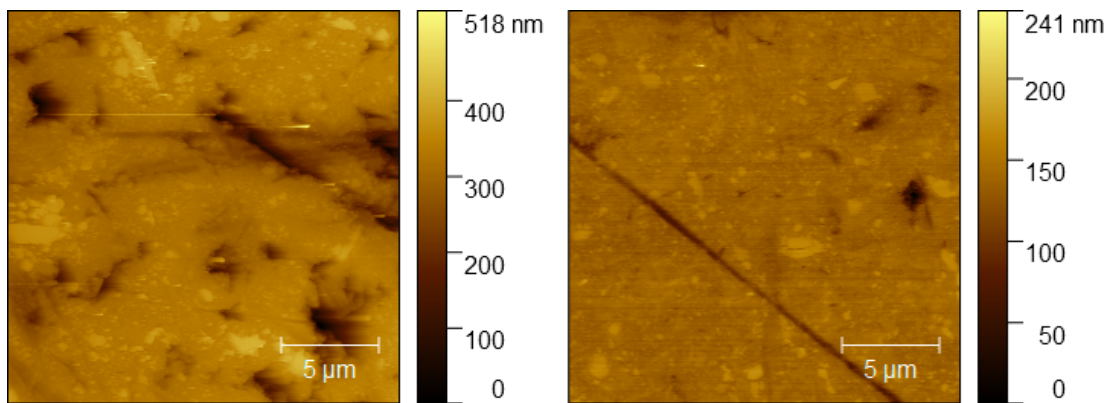


Figure 4.27: AFM images of the worst (left) and best (right) polished surface, where the surface roughnesses are 0.03 and 0.007 Ra, respectively.

One oversight in the design of the metal parts from a polishing perspective was including blind threaded holes on the polished faces, which were used for assembly. These threaded holes collected particulates and abrasive slurry at different polishing stages, which made cleaning these much more challenging and resulted in a poorer finish overall. The next iterations of such devices that require polishing should be designed with the number of holes and specifically blind threaded holes at a minimum. Instead, smooth through holes should be used where possible, with parts being secured with bolts with nuts.

### 4.3.3 Superconducting Coating

The quality of the superconducting coating is critical to the performance of the designed nonlinear resonator. The critical temperature determines the operating temperature at which acceptable dissipation is achieved due to the exponential scaling of the surface resistance. The quality of the crystalline structure, and thickness uniformity determine the critical current and linear kinetic inductance contribution from each surface. The ideal superconducting coating for high frequency parametric amplifiers is one with a high frequency superconducting gap (see Eq. 2.8), which ensures that the energy of the incident signal or pump does not break apart the Cooper pairs of the condensate and diminish the superconducting properties of the coating; a high critical temperature, which allows for operation between 1 to 4 K due to the exponentially scaling dissipation with temperature; and finally a large London penetration depth (or a low normal state conductivity as shown by Eq. 2.20), which provides a stronger enhancement of the kinetic inductance for a given film thickness (see Eq. 2.34). Currently, NbTiN [55] and NbN [124] are the most commonly used films for such applications, due to their high bandgaps ( $2\Delta_0$  at 1.2 and 1.5 THz, respectively), critical temperatures of around 15 K, and  $\lambda_L$  in the hundreds of nm range. NbTiN was chosen for this work specifically chosen to the already established deposition recipes in the facility where the coating procedures took place.

As discussed in Section 4.3.2 the flat copper resonator surfaces were prepared for the thin film coatings through a multi-step polishing process. The roughness of the foundational surface upon which the deposition takes place determines the roughness and thickness uniformity of any subsequently deposited layers. The design thickness of the thinnest NbTiN was 20 nm, which meant that a mean roughness of the copper surface that was less than this value was required. Depositing a thin superconducting layer directly on a normal metal can severely diminish or even prevent the superconductivity of the layer due to the proximity

effect [125]. This effect reduces the superconducting gap at the contact with normal conductor for a certain interface region that may span a few  $\mu\text{m}$  due to the mixing of Cooper pairs and normal electrons. This means that it would be likely that the NbTiN layer would not be superconducting at all in such a scenario. This can be prevented by separating the superconducting layer from the normal metal base using an insulating layer, which it self does not have a sea of delocalised electrons to interfere with the condensate of the superconductor. An insulating layer such as a AlN or  $\text{Al}_2\text{O}_3$  can be used to achieve this objective. The insulator choice should not have a strong impact of the characteristics of the superconducting layer due to the polycrystalline nature of the films that are grown. In the case where the substrate upon which the NbTiN layer is grown is highly ordered the substrate choice becomes a very important factor since film ordering is dependent on the lattice matching to the substrate. The minimum or optimal insulating layer thickness requires a separate investigation but is assumed that a few 10's of nanometers should provide sufficient isolation from the normal conductor.

In this work, an additional  $1\text{ }\mu\text{m}$  thick niobium layer was deposited on the raw copper surface prior to the deposition of the insulating layer. This was due to concerns that if any gaps in the insulating layer did occur during the deposition then the NbTiN layer would be in proximity to Nb rather than copper, which would have a less severe effect on the local superconducting properties. In addition, since the features of the device such as the pin surface are quite deep, attaining a uniform coating on the vertical faces is not possible with sputtering since continuous line of sight from the sputtering target is required. These vertical faces may receive a much thinner overall coating compared to the flat faces that are always exposed to the sputtered atoms. In hindsight, this may not be such an important concern judging from the visual inspection of the coated devices (as shown in Section 4.4.2) which do show a coating on even the deepest features. This may mean that a thicker insulating layer would be more beneficial



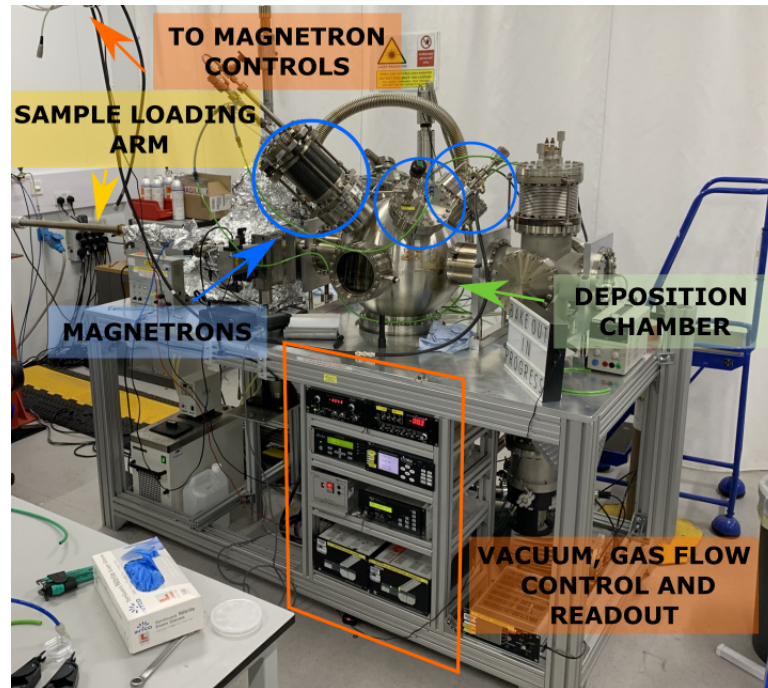


Figure 4.28: A labelled photograph of the magnetron sputtering system at STFC Daresbury. Shown is the ultra high vacuum deposition chamber, which contains a heated and rotating sample jig. A separate loading chamber is separated by a pneumatic gate valve, which separates the two chambers during a deposition. Both chambers have separate turbo molecular pumps that use scroll pumps for backing. Multiple gas supplies are connected to gas flow meters and controllers which are operated via a set of panels below the deposition chamber. Three water cooled magnetrons are connected to the deposition chamber, which are powered by a pulsed DC sources and controlled via a separate control panel.

in protecting the final thin coating.

### Deposition System Principles

The discussed depositions were performed using a magnetron sputtering system at STFC Daresbury laboratories <sup>6</sup>, which is shown in Fig 4.28. This is a common technique for the deposition of various metals, alloys, or ceramics onto any a variety of flat or stepped structures, where the most uniform coverage is achieved on the flat surfaces of the sample. Sputtering [126] is a process by which ions from a gaseous plasma are accelerated towards a source material called the “target”

<sup>6</sup><https://www.astec.stfc.ac.uk/Pages/Vacuum-Science-Group.aspx>

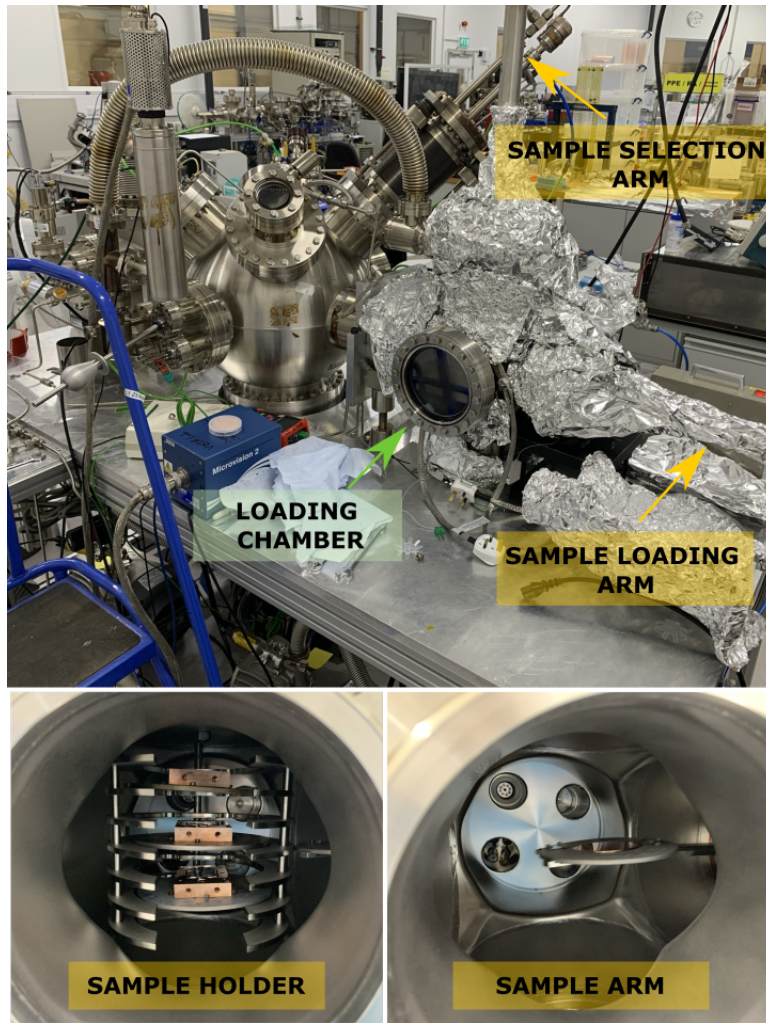


Figure 4.29: A labelled photograph of the loading chamber of the sputtering system. The chamber is opened by removing the chamber window after which vertical magnetic sample selection arm can be used to move the sample holder in order for a separate magnetic sample loading arm to move below a chosen sample plate. The plate is lowered onto the arm after which it can be moved into the deposition chamber.

(the material that is used to coat a sample), the secondary collisions of these ions with the target cause individual or clusters of neutral atoms to be ejected from the targets surface and travel in a straight line until colliding with another surface. Any sample in the way of this stream of ejected neutral atoms is covered in a thin coating of the target atoms. The thickness of the coating depends on the time the sample is exposed to this stream.

The chamber where this process occurs must be under an ultra high vacuum

(as low as  $1 \times 10^{-9}$  Torr base pressure) which has a threefold function: it ensures that the mean free path is large enough to allow sputtered atoms to reliably reach the sample; the plasma is able to be sustained and does not lose energy to air molecules in the system; and finally as few impurities as possible are trapped within the desired coating. This base pressure is reached by pumping down on the chamber while it is being heated (baked) for a number of days. The baking ensures as many adsorbed particles and molecules are evacuated from the system. The plasma is composed of ions of a highly pure noble gas such as argon (Ar) or krypton (Kr) due their inert nature, where using a Kr plasma has the effect of permitting a slightly faster deposition rate than the atomically lighter Ar. The plasma pressure is maintained by controlling the gas inlet rate and a variable outlet butterfly valve which leads to the vacuum pumps. The plasma is generated via the use a cathode that emits electrons and in the case of magnetron sputtering the electrons collide with the noble gas in a region close to the target's surface due the magnetron's generated magnetic field. The ionisation of the gas creates additional free electrons that further aid maintaining the plasma. The use of a magnetron compared to a diode arrangement means that the sputtering rate is higher due to the more localised plasma and higher collision rate as well as a reduced operating voltage of a few hundred volts compared to a few kV of a diode system.

Reactive sputtering can be achieved by introducing an additional reactive gas such as nitrogen ( $N_2$ ) or oxygen ( $O_2$ ) with the carrier noble gas. The additional gas can react with the atoms of the target to create a desired nitride or oxide coating. The flow rate ratio is critical to the stoichiometry of the resulting film.

The sputtering system used for this work is shown in Fig. 4.28, which shows the main deposition chamber, magnetrons, vacuum and gas flow controls, and the vacuum pump mounter from beneath the deposition chamber. Three magnetrons are shown which were mounted at roughly  $45^\circ$  angle to ensure uniform coating of a rotating sample. The magnetrons were connected to a DC power supply

which controlled the plasma. The targets that were available for use were Al, Nb, and NbTi which could be used to make the respective oxides or nitrides with reactive sputtering. The magnetron power supply was used in DC mode for metallic targets, but could be switched to pulsed DC mode for insulating films. The samples are loaded into the chamber via a sample loading chamber that is separated from the deposition chamber using a gate valve, which separates the two vacuums and allows for a better base pressure to be maintained in the main chamber while other samples stay in the also evacuated sample chamber, reducing the exposure of either chamber to the atmosphere.

Photographs of the sample loading chamber are shown in Fig. 4.29. These show how a sample can be selected once the chamber is closed using a system of magnetic arms. The vertical arm moves the sample holder vertically while the horizontal arm is able to “pick up” a chosen sample plate, which can then be moved to the deposition chamber onto a rotating deposition jig, which it self can be moved using pneumatic action to “collect” the sample plate from the magnetic arm. The height and weight of the copper samples was at the physical limit of what the sample carrying magnetic arm could support. The end of fingers of the horizontal magnetic arm had to be re-enforced to prevent significant drooping, which could have prevented the sample plate from clearing the deposition stage in the main chamber. In addition, the arm was mounted to the chamber using a flex joint which could be pushed down to provide some extra clearing. Once samples are loaded into the deposition chamber, the sample chamber is pumped and baked for a number of days before any sample can be moved into the deposition chamber. This ensure that a low enough vacuum is reached and as many adsorbed surfactants are evacuated from the chambers. The baking occurs via the use of heating elements wrapped around the sample chamber that are covered in foil to provide additional insulation. Once a sample is loaded into the deposition chamber, the chamber is pumped down for an additional day to reach the desired base pressure. In addition, the sample is baked and annealed using the heater in

the deposition chamber. The residual gasses in the deposition chamber could be monitored using a residual gas analyser which can show the relative pressure of the gasses being pumped out against their molecular weight. The predominant peaks were of  $H_2$ ,  $H_2O$ , and various hydrocarbons.

#### **Sample Preparation and Deposition Procedures**

The planned depositions included a number of devices with different NbTiN thicknesses and different spacer layers. The spacers layers were deposited on the outer rim of the body of the resonator as a trial to investigate whether the ridge to lid spacing could be controlled via the presence of this layer. During the spacer depositions the inner structure was covered by a stainless steel mask which was cut to shape by hand and placed on relevant part of the resonator. Other than the variations with spacer layers the planned devices included depositions on both faces of varying thickness of NbTiN. The first was a 1  $\mu m$  thick NbTiN coating directly on copper with the purpose of being used as a control to check that the linear properties of superconducting resonator agreed with theory. The other two resonators were chosen with a layer structure of 2  $\mu m$  Nb for the proximity effect consideration, then a 30 nm layer of AlN to act as the insulator, followed by either 50 nm NbTiN coating for one resonator and a 20 nm NbTiN coating for the other. Unfortunately, due to time constraints in the laboratory only the bulk film and 20 nm NbTiN film devices were finished. In addition, in the process of depositing the Nb spacer layers the target was used up and the first part of the multi-layer depositions had to be carried out using the NbTi instead of Nb. Note, that critical temperature of the NbTi is around 9 to 10 K and the deposition rate of NbTi was very similar to that of Nb. The use of NbTi instead of Nb as the base layer should not affect the properties of the top NbTiN layer due to the already disordered crystalline structure of the copper substrate.

The idea of using a Nb layer on the outer rim of the device to set the ridge to lid spacing proved to be a very time consuming part of the deposition process



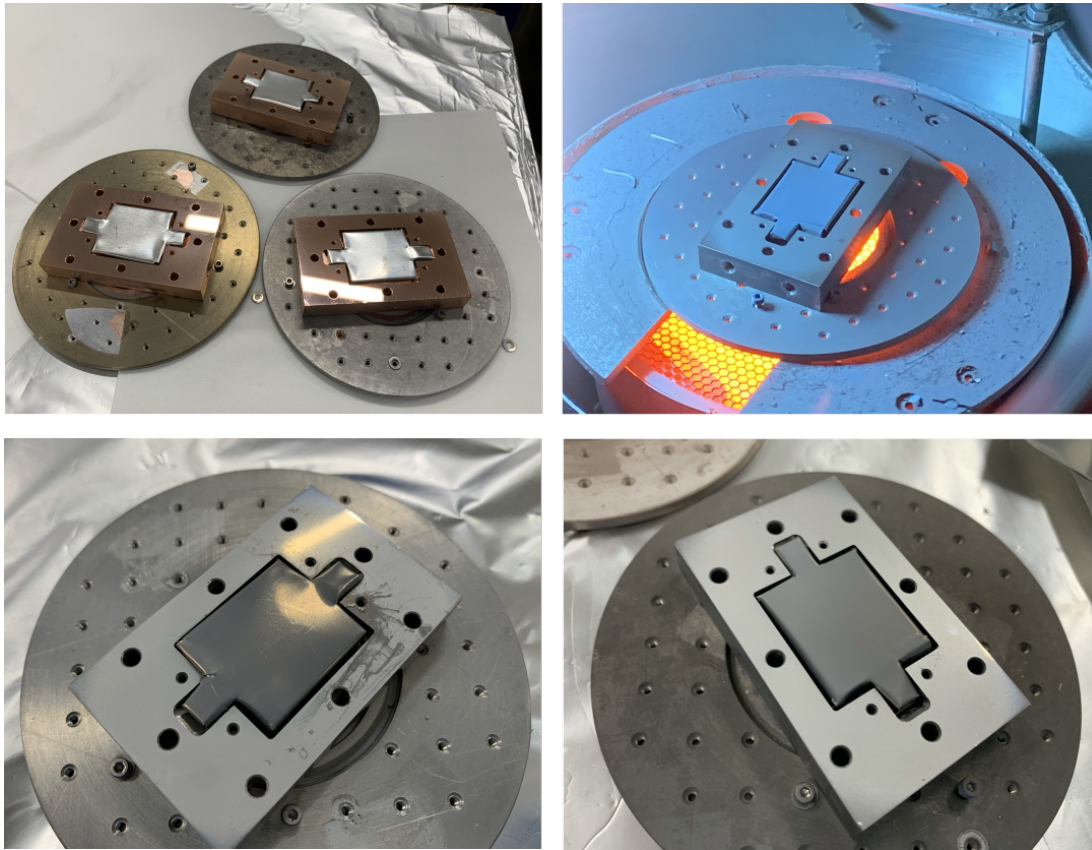


Figure 4.30: Photographs showing the deposition of the Nb spacer layers. The deposition rate of this was  $\sim 1\mu\text{m}/\text{hour}$ . The top left panel shows the three bodies on sample plates that had their internal structure masked off using stainless steel sheet masks that were cut and bent into place such that they were secured in place. Small pieces of sapphire substrate were also mounted on the sample plates to be used for film property characterisation. The top right panel shows the one of the bodies during the deposition as seen through a window with a shutter where the blue hue is the due to the krypton plasma. Bottom left shows the sputtering result on one of the bodies that was had some unintentional residue left over from the cleaning and drying process. Bottom right panel shows a coating with a visibly smoother finish, where the outer edges appear darker due to smoother Nb coating that resulted from a better polish on the edges of the body.

since the inner structure of the resonator needed to be masked off via the stainless steel mask as shown in Fig. 4.30. The fastest deposition rate of niobium in the sputtering system that could be safely and reliably achieved was on the order of  $\sim 1\mu\text{m}/\text{hour}$ . This meant that to deposit a spacer of  $20\mu\text{m}$  would require upwards of a 20 hours deposition time. This was unfeasible due to the requirement that

the sputtering system be supervised while a deposition is running. As a result, a spacer layer of 5  $\mu\text{m}$  was deposited where the majority of the rest of the desired 20  $\mu\text{m}$  ridge to lid spacing would be made a separate aluminium foil spacer. In addition to the particularly long coating time, the utilisation of the additional spacer layer step risked reducing the yield of successful devices. As shown by the lower left panel of Fig. 4.30, depositions on a surface that had some residue left over from the cleaning process (described below) allowed for uneven film growth meaning that large bumps formed on the surface. Such depositions may pose less risk if they were performed on a flat crystalline surface such as a silicon sample, which could be cleaned adequately more reliably. In addition, the roughness of the surface upon which the deposition takes place visibly influences the roughness of the resulting film as seen by the lower right panel of Fig. 4.30.

Prior to a deposition a sample must be thoroughly cleaned to remove as many surfactants and debris as possible. The samples were sonicated for 15 to 20 minutes while in a solution of acetone followed by a second sonication in de-ionised water. The samples were placed at a slant against the walls of the beaker such that debris from the blind holes of the parts would favourably be displaced. After the sonication, the samples were dried with a nitrogen gun to ensure all the remaining liquid was blown off. Particular care should be taken with any samples with crevices such as the blind holes of the resonators here to ensure that all liquid was blown out. Sometimes, some residue would be left on the surface, in which case the sample must be cleaned again since these residues can be detrimental to the quality of the coating on the surface as shown by the lower left panel of Fig. 4.30.

After cleaning the samples are placed on sample plates and prevented from moving by screws on all 4 sides of the device as shown by the upper left panel of Fig. 4.30. Prior to opening the sample loading chamber, the chamber is brought up to atmospheric pressure using a nitrogen atmosphere. This is achieved by pumping nitrogen gas into the sample chamber and ensuring that a positive

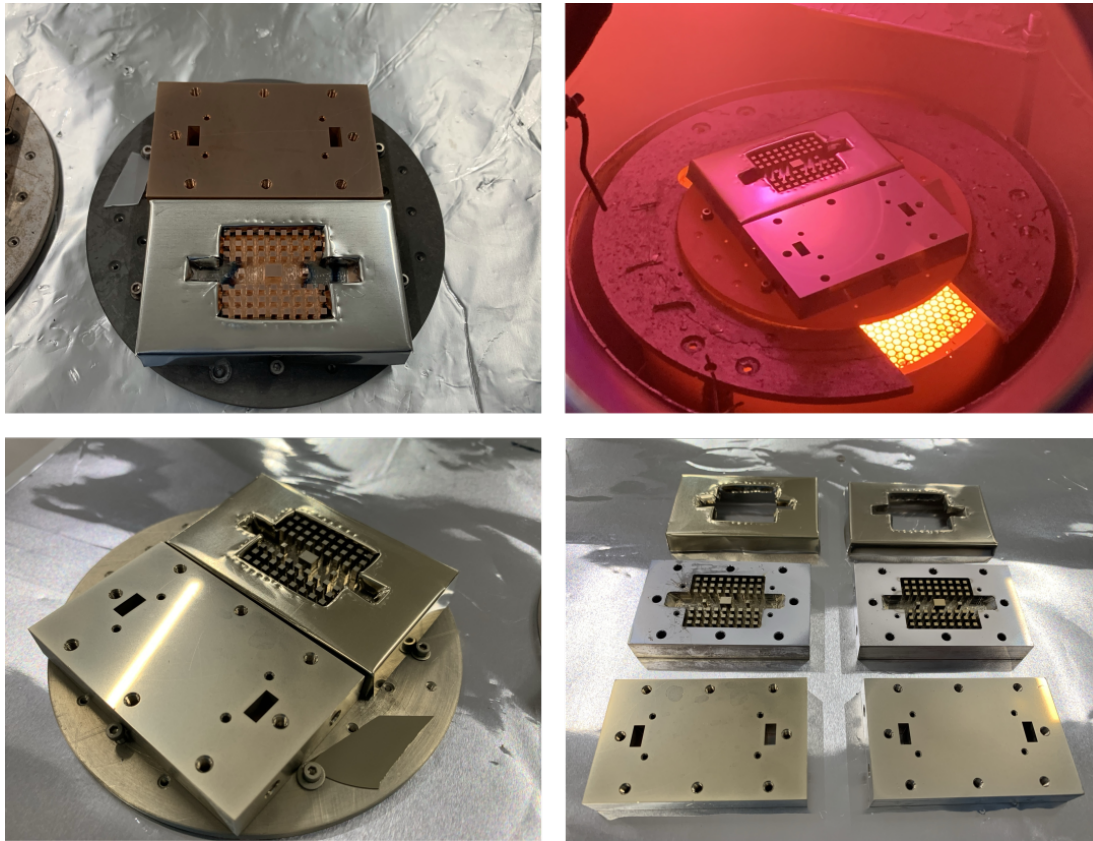


Figure 4.31: Photographs showing the deposition of the  $1\text{ }\mu\text{m}$  NbTiN layer on one device or a multi-layer film structure composed of  $2\text{ }\mu\text{m}$  NbTi layer,  $30\text{ nm}$  of AlN insulator and a  $20\text{ nm}$  coating of NbTiN. The deposition rate of AlN was  $\sim 90\text{ nm/hour}$ , while NbTiN had a rate of  $180\text{ nm/hour}$ . The top left panel shows the lid and body placed on a single deposition plate to deposit the same film(s) on both bodies simultaneously. The outer perimeter is masked off using a stainless steel mask to protect prevent the spacer layer from any further coating. The top right panel shows the deposition taking place where the pink hue is due to the Kr and  $\text{N}_2$  plasma. Bottom left two panels show the sputtering result on one of the the thick NbTiN layer and the multi-layers. The golden hue is characteristic of a NbTiN coating while the darker grey is the Nb coating.

pressure forms such as little of the air in the laboratory enters the chamber. This reduces the amount of impurities and surfactants that enter the sputtering system. The samples are then placed on the relevant shelves of the sample holder stack. After which, the sample chamber is closed back up with a new gasket and pumped down to base pressure while baking the chamber with the heating elements. This process can take 2 to 3 days to ensure the main deposition chamber



is not contaminated when the gate valve to the sample chamber is opened. After baking, the sample is chosen by a system of magnetically operated arms as shown in Fig. 4.29 and loaded into the deposition chamber. Once the sample is loaded into the deposition chamber, the sample plate is conductively heated via a current driven heating element connected to the rotating deposition stage. The sample is heated for a few hours to heat the surface up to temperature of 450 °C which is was established at the facility as the temperature which produces films with best surface adhesion and highest critical temperature in the case of superconducting films.

The settings used for the depositions were the ones that were established in the facility after a large number of trials and measurements. The Nb and NbTi depositions were performed with a Kr working pressure of 1.9 to 2.2. mTorr and DC sputtering with a power of 400 W and a plasma current of  $\sim 1$  A. The power supply is capable of higher power but the chosen power is at the limit of what the water cooling system can handle. A higher power deposition may be needed if the sample stage was not heated. The targets were also cleaned by the plasma with their shutters closed (to ensure that the sputtered impurities do not reach the sample's surface) for 15 to 30 minutes where a 30 minute cleaning would be used if a reactive plasma was ignited in prior use. The AlN depositions were performed with a Kr and N<sub>2</sub> plasma with relative pressure of 2 mTorr for Kr only, which then went up to 4.2 mTorr when N<sub>2</sub> was added. Pulsed DC operation was required since the targets surface becomes insulating, the pulses then sputter the insulating layer towards the sample. A 1.1  $\mu$ s duty cycle, 350 kHz pulse frequency and 200 W power with 1 A plasma current were used for this deposition. Similarly, the NbTiN deposition used the same settings as that of AlN except for a higher magnetron power of 300 W. Photographs of these depositions are shown in Fig. 4.31.

During these deposition shown in Fig. 4.30 and 4.31 there were pieces of sapphire secured next to the resonator parts which allowed for some film properties

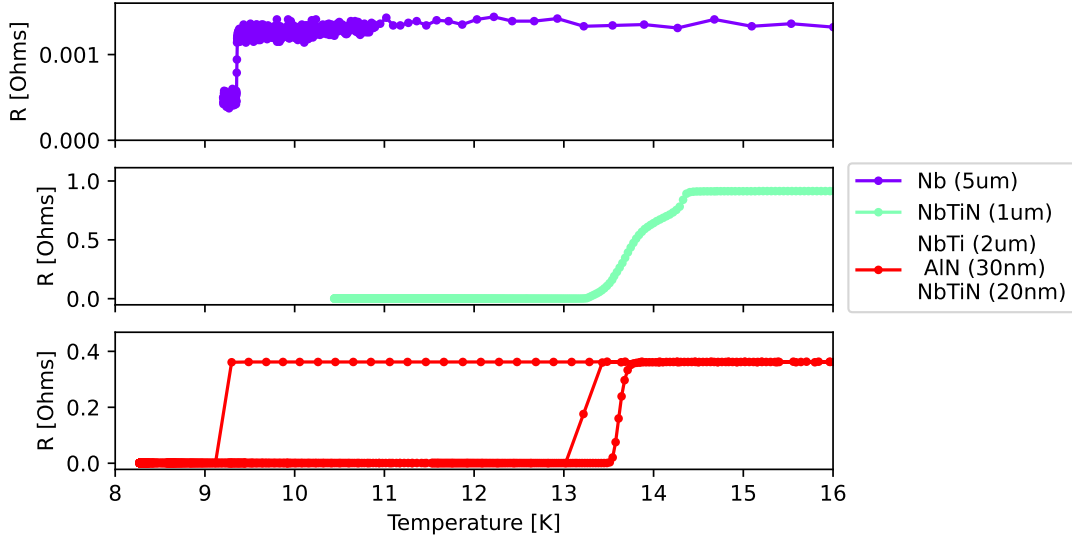


Figure 4.32: Cryogenic 4 point probe measurements that show the resistance against temperature of the films that were deposited on sapphire samples simultaneously to those shown in Fig. 4.30 and 4.31. In the multi-layer measurement 3 separate critical temperatures were present while cycling up and down in temperature.

to be measured. Specifically, measuring the resistance of the films with temperature can show the superconducting critical temperature. These measurements were carried out in a 4 point probe cartridge at STFC Daresbury laboratories. This method uses four probes that are assembled in a line and pressed down upon the surface of the sample. The two outer pins act as the current source and drain while the inner two pins are used to measure the voltage difference. The use of a four probe method compared to two probe method allows for the resistance of only the sample to be extracted. The results from these measurements are shown in Fig. 4.32. The Nb spacer layer had a typical critical temperature of 9.3 K, while the thick NbTiN layer had a critical temperature in 13.5 to 14.5 K range. Interestingly, the multi-layer sample showed three separate critical temperatures as the sample was cycled up and down in temperature. An explanation for this behaviour has not been understood in full but this may have been due to the pins of the 4 point probe piercing through the NbTiN layer during the temperature cycling. This may indicate that the thin NbTiN coating may not have the desired

higher critical temperature and may be much more lossy during measurement of the resonator.

The thickness of the deposited layers was inferred from previous rate tests performed in the facility. Direct measurements of the thickness were planned by using the stainless steel masks or the sapphire test substrates as the test subjects. The preference was to use the stainless steel samples which would likely provide a more equivalent representation of the film ordering that was present on the also metallic copper surface. The intention was to use a focussed ion beam (FIB) to mill a ridge in the single and multi-layer film structures and to measure the layer structure using an angled image using a scanning electron microscope (SEM). However, these machines were under maintenance for a significant number of time meaning that these measurements could not be performed. In addition, a ion beam etcher (IBE) with a part of the stainless steel sample being masked off, creating an edge that could be viewed under SEM. However, once again this machine had to undergo maintenance due to a malfunction during the procedure, which meant that this work could not be finished. One final alternative, could have made use of X-ray reflectometry (XRR), which would direct a beam of X-rays at the surface of the sample at different angles with the expectation that the X-rays would be reflected from the layer boundaries at different angles. Fitting the resulting reflected X-ray intensity vs incidence angle against a theoretical fit could provide estimates of the individual layer thickness. However, this data could not be taken and analysed by the end of this PhD project.

## 4.4 Resonator Measurements

As in Section 4.3.3 two polished resonators were coated in superconducting coatings. The first being coated with 1  $\mu\text{m}$  of NbTiN directly on the copper inner surfaces of the resonator, which will be referred to as the thick film device from here on. The second having a multi-layer coating of 2  $\mu\text{m}$  NbTi, 30 nm of AlN,

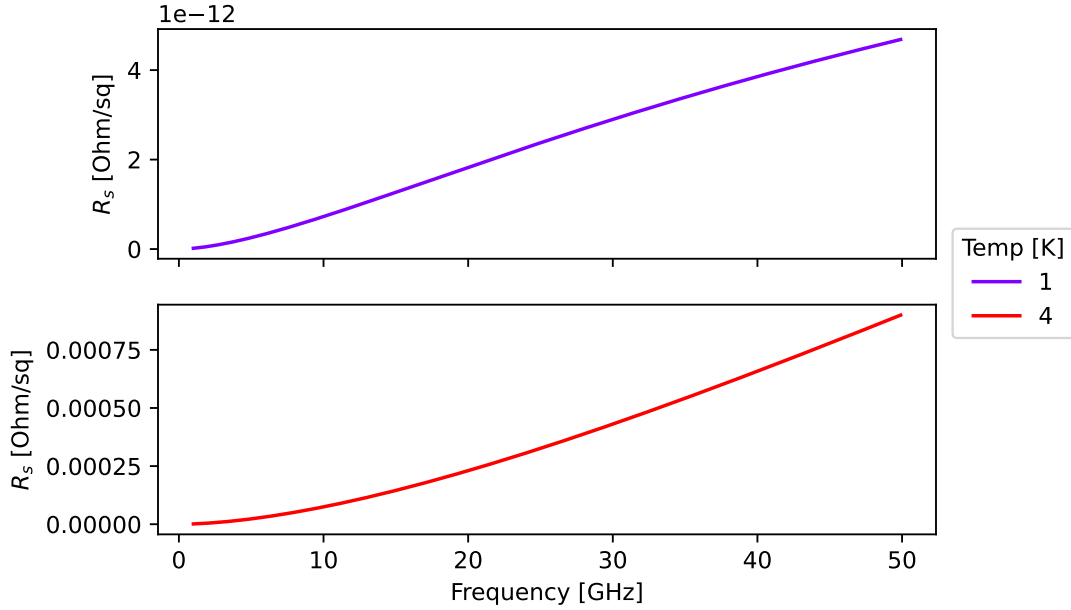


Figure 4.33: The surface resistance as a function of frequency for a 20 nm thick NbTiN film at 1 and 4 K. The material properties can be found by following the caption of Fig. 2.7.

followed by 20 nm of NbTiN, which will be referred to as the thin film device. Both of these resonators had spacer layer of 5  $\mu\text{m}$  Nb on the perimeter of the part containing the ridge and the nails as shown by Fig. 4.30. This meant without any additional foil spacers the resonators had a ridge to lid spacing,  $h$ , of 6  $\mu\text{m}$  and 5  $\mu\text{m}$ , for the thick film and thin film devices, respectively. The contribution of the AlN and NbTiN layers was excluded due to the uncertainties in the layer thickness that were calculated using previous rate tests.

The pin-coupled RGWG resonators of the proceeding analysis were measured in the cryostat that was described in Chapter 3. However, at the time that these measurements were being taken the magnitude of the difference in surface resistance when operating the device at 4 K vs 1 K was assumed to be less significant than it really was. More specifically, the large difference in surface resistance from 4 K to 1 K as shown by Fig. 4.33 (also see Fig. 2.2a for scaling relative to  $T_c$ ) was assumed to be significantly smaller. The difference in surface resistance is close to 8 to 9 order of magnitude assuming that all losses are predicted by the

Zimmermann conductivity. In actuality, this difference may be less severe when other dissipation channels are taken into account, such as the surface quality and crystalline nature of the coating. This trend of the surface resistance does show that a 1 K operating temperature is important. Simulations did show that a reasonable Q and transmission should still be possible. In addition, there have been studies to show that 4 K operation is fully feasible in KI parametric amplifiers [20], but in the early stages of testing a lower temperature is preferable until issues with the design of the device are ironed out. This was important since the the 1 K adsorption fridge that was in Chapter 3 had to be removed from the cryostat and replaced with an identical unit at a later time due to commitments of the research group to an external project which needed the 1 K system. By the time, the importance of the 1 K operating temperature was understood, the charging and commissioning of the fridge was not practically feasible by the time the project ended. These circumstances led to most the measurements in the proceeding section being carried out at 4 K. It will be shown that in addition to the larger than optimal operating temperature the thin films had a below than expected critical temperature which further exacerbated the issue. However, the resonators will be shown to present nonlinear behaviour and mixing between two tones even under these sub optimal operating conditions.

#### 4.4.1 Copper RGWG Resonator

Prior to cryogenic measurements, one of the uncoated but polished resonators was measured at room temperature with an aluminium foil spacer. This spacer was cut using a scalpel and a stencil in the shape of the outer perimeter of the lower part of the resonator. The prepared device is shown in Fig. 4.34. The measurements were performed using the VNA described in Chapter 3, where a calibration was performed with Ka band rectangular waveguide calibration kit. The measured S-parameters are shown in Fig. 4.35, these results are overlaid with

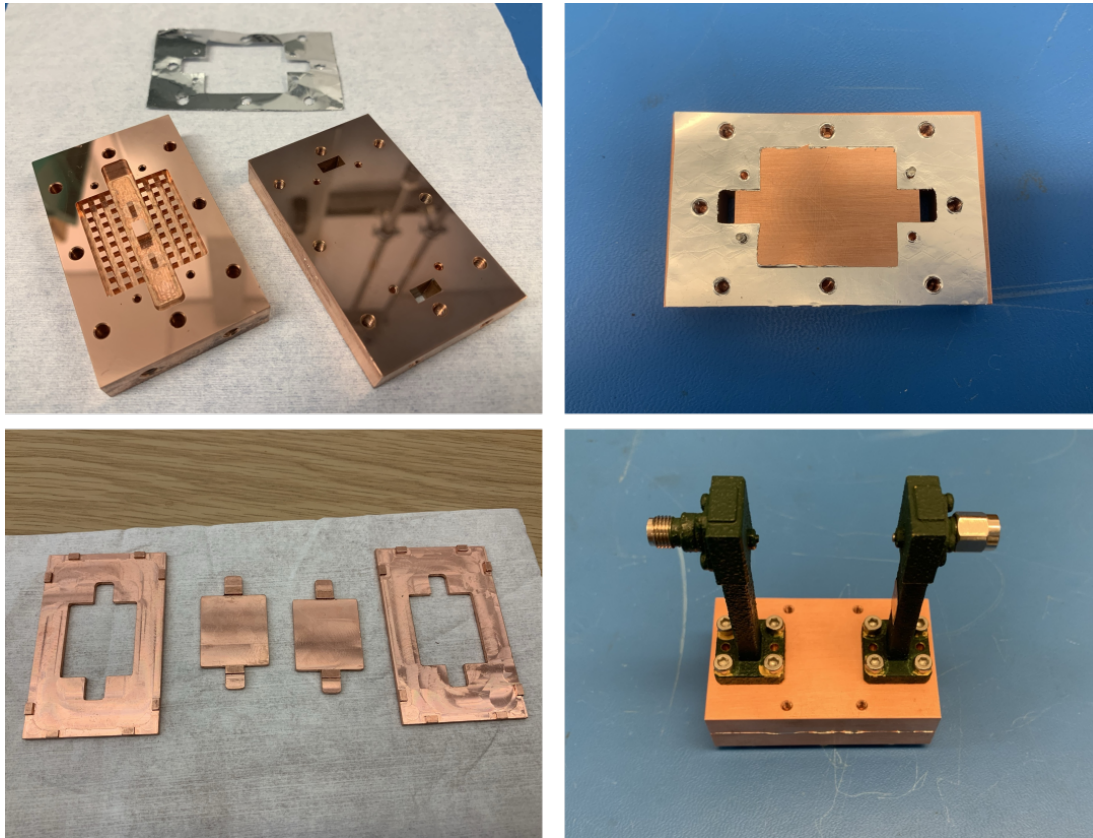


Figure 4.34: The preparation of a polished RGWG resonator for room temperature measurement with an aluminium foil spacer. The standard supermarket foil which was measured to have a micrometer screw gauge to have a consistent thickness of  $13\text{ }\mu\text{m}$  and was cut around a copper stencil that is shown in the lower left panel. The coaxial to rectangular waveguide transition were used to connect the resonator to the VNA.

an equivalent HFSS simulation. The results show one central resonance and two kinks in the transmission spectrum signifying the other two resonances. These resonances are very weak due to the loss of normal conducting copper. The location of the resonance and kinks are in line with the resonance frequencies of the PEC simulation shown in Fig. 4.10, the key difference in the two plots is the poorer transmission and quality factor that is expected from a normal conductor compared to a simulation with PEC. There is a slight disagreement in the position of the GGWG resonance (see Mode 2 in Fig 4.11) which indicates that the ridge to pin spacing is slightly different in the machined device compared to the specification. However judging by the frequency of the ridge resonance (Mode

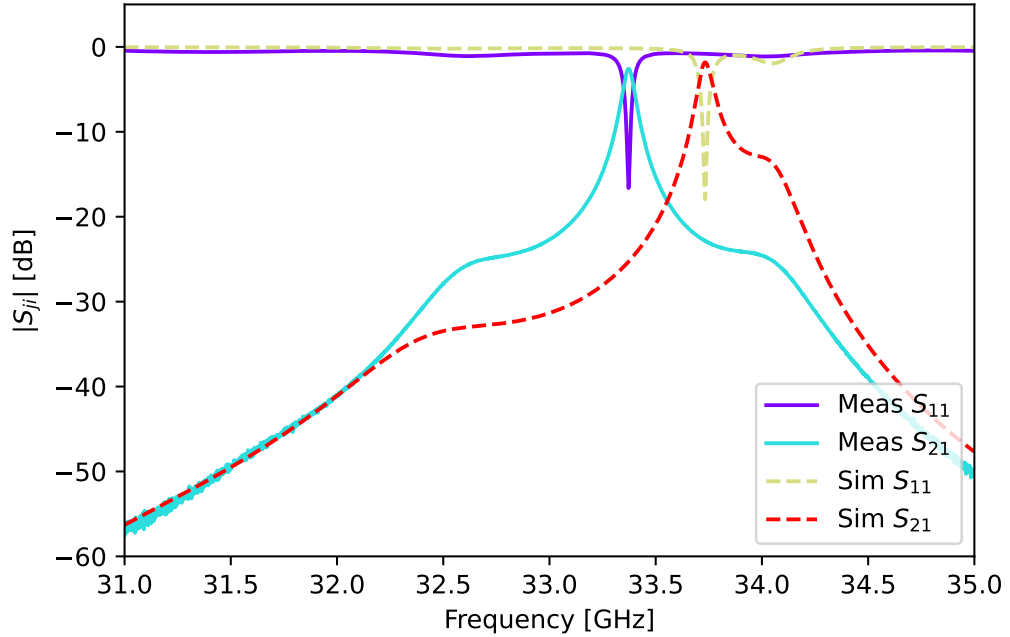


Figure 4.35: Comparison of the room temperature S-parameters of the polished copper resonator with a 13  $\mu\text{m}$  aluminium foil spacer to an equivalent HFSS simulation. The HFSS simulation used an imported CAD model that is shown in Appendix A.2 with the same 13  $\mu\text{m}$  spacer. The bandwidth shown covers all 3 structure resonances.

1), the length of the ridge is fairly close to specification. However,  $S_{21}$  of the ridge resonance from the measurements shows that the coupling pin is likely to be lower than designed since a taller pin should increase the coupling  $Q$ , which has the effect of lowering the transmission at room temperature.

## 4.4.2 Superconducting RGWG Resonators

### Thick NbTiN Coated RGWG Resonator

The next device to be measured was the resonator with a 1  $\mu\text{m}$  NbTiN coating on both the lid and body of the resonator. However, as shown in Fig. 4.30, significant build up occurred during the deposition of the spacer which impacted the desired spacing between the ridge and the lid. This resonator could be measured without an additional aluminium spacer since the kinetic inductance fraction of

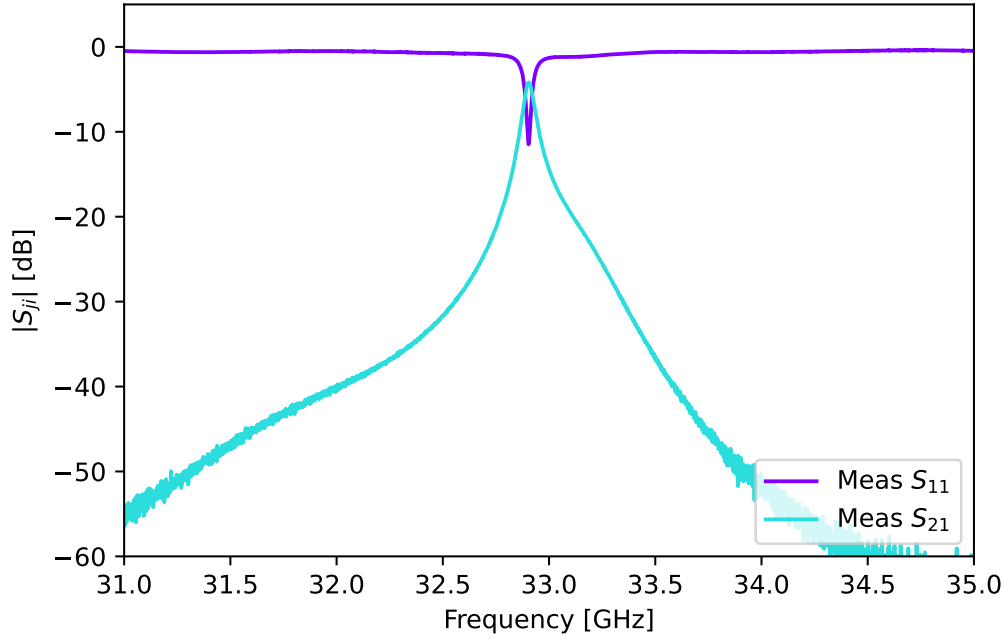


Figure 4.36: Room temperature measurement of 1  $\mu\text{m}$  NbTiN coated RGWG resonator with a design spacer layer of  $h = 6 \mu\text{m}$ . The spacer layer has some build up which is likely to affect the actual ridge to lid separation and the parallelism of the two surfaces.

the device should be low when at cryogenic temperatures and this should not shift the resonance of interest out of band. In addition, measurement without the foil spacer can provide insight to whether devices with these smaller ridge to lid spacings are feasible. At room temperature, due to the low conductivity of NbTiN, the measured S-parameter spectrum showed only the GGWG resonance which was at a frequency of 32.9 GHz as shown by Fig. 4.36. However, this resonance should've been closer to 34 GHz (see the GGWG resonance in Fig. 4.35). The build up on the spacer layer should not affect the frequency of this resonance to this extent since the groove gap waveguide mode results from a larger resonance volume in which a small change in vertical height should produce a negligible resonance frequency change. However, since the frequency of this resonance is lower than expected it must be that the height and position of the coupling pins in this resonator are slightly out of spec compared to the simulated dimensions.



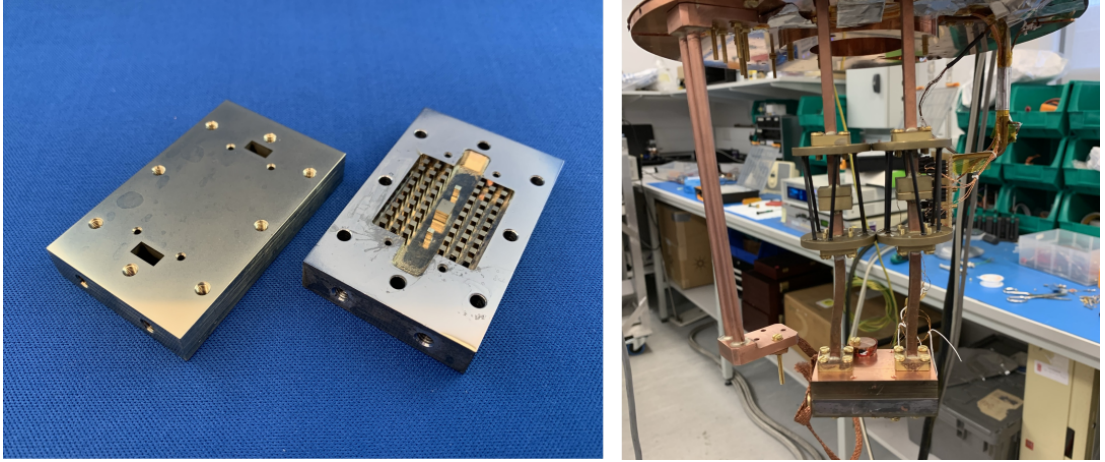


Figure 4.37: Photographs of the thick film device measurement in the cryostat at 4 K. Left panel shows the disassembled resonators while the right panel shows the resonator mounted to the rectangular waveguide feeds. The resonator was connected to the 4 K stage via a copper braid which provided a medium thermal link and allowed the temperature of the resonator to be changed with a single  $330\ \Omega$  heater. The feeds were thermally isolated at each temperature stage using thermal breaks that incorporate a hollow gap between waveguide flanges and are supported with carbon fibre tubes which have a low thermal conductivity (see Section 3.2.2))

This resonator was attached to the Ka band rectangular waveguide feeds in the cryostat as shown in Fig. 4.37. The resonator could be isolated from the 4 K stage using waveguide thermal breaks [110], which would allow a connection to the 1 K stage. However, since the 1 K stage was absent the resonator had a copper braid linking it back to the copper part which was attached to the 4 K stage. Thermally connecting the resonator in such a way limited the cooling power acting on it, which meant that a single  $330\ \Omega$  heater was sufficient to raising the temperature above  $T_c$ . The VNA was calibrated up the hermetic waveguide feedthroughs at room temperature using a Ka band rectangular waveguide calibration kit. However, this mean that the total loss of the waveguide chain from the DUT leading to room temperature was included in any measurements that were taken. The loss of each chain was between 1-2 dB. The cryogenic S-parameter of the resonator are shown in Fig. 4.38. The results are overlaid with the expected spectrum as simulated in HFSS using surface impedance boundaries that represent NbTiN

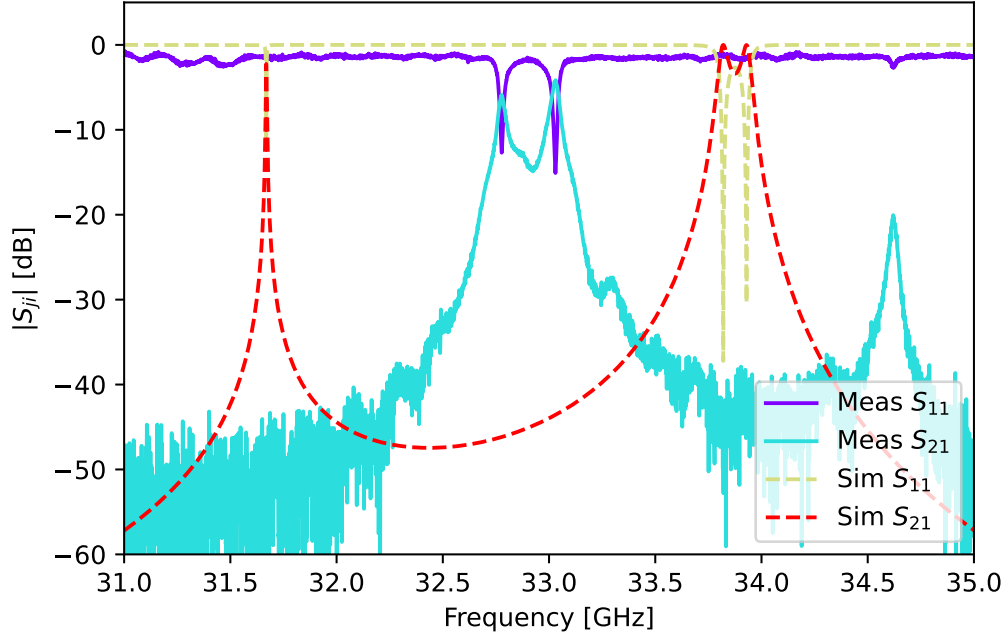


Figure 4.38: Cryogenic low power S-parameters at 4 K base temperature of the RGWG resonator shown in Fig. 4.37 with a 1  $\mu\text{m}$  coating of NbTiN on the inner surfaces. The spacing between the ridge and lid is set by the deposited Nb spacer layer on the outer area of the body of the resonator (the grey metallic finish), which resulted in a spacing of 6  $\mu\text{m}$ . Overlaid are the simulations performed in HFSS with surface impedance of NbTiN at 4 K, which was calculated using the Zimmermann conductivity (see Fig. 4.12).

at 4 K. The figure shows that as expected the GGWG resonance ( $\sim 33$  GHz in the measurements and  $\sim 33.8$  GHz in the simulation) that was seen in the room temperature measurements is lower than the simulated frequency of  $\sim 34$  GHz. A difference in coupling pin position and height from the design values are the most likely reason for the difference since these are the only dimensions that significantly affect this resonance. The frequency of resonance 1 and 3 (counting from lowest to highest frequency) are most sensitive to the ridge to lid spacing as well as the height of the coupling pins. It is likely one of the contributing factors for resonance 1 being higher in frequency in the measurement is increased ridge to lid spacing due to the build up on the spacer layer. This would lower the

linear kinetic inductance fraction and increase the resonance frequency. Another important observation is that the peak transmission and quality factor are lower for the measured resonances. This indicates that the surface losses are higher than the simulation with the Zimmermann conductivity predicts. This means that there are additional dissipation channels that contribute to the overall loss. These could be a result of a number of factors including the uneven coating with the superconducting film on places like the vertical faces, or losses due to breakages or discontinuities in the film. As shown in lower panel of Fig. 4.39 there was a mark on the top of the ridge which would likely impact the loss characteristics of the resonator.

A fix was attempted to remove the build up of material on the spacer which was thought to be impacting the frequency of the resonances. The goal of this procedure was the test if the discrepancy between simulation and measurement was at least partly due to the spacer layer. As shown by Fig 4.39, a rotary tool was used to remove the affected areas of the spacer. These affected areas should not have any AC current flowing across them so in theory this should not make the resonator behave worse. However, in the process of this fix some damage was caused to few of the outer nails of the pin surface where some had to be bent into position. The resonator with the attempted repair was cooled down once again in the cryostat and the resulting S-parameters are shown in Fig. 4.40. The figure shows that the transmission of the first two resonance has improved after the attempted repair, but the resonance frequencies remained unchanged. This may mean that the damage to the pins on one edges caused the lid to be propped up similarly to the issues that the build up on the spacer was causing. The resonator was examined once back at room temperature and some indents were present on the lid where the damaged nails were.

Investigating the resonance frequency of a resonator with kinetic inductance with temperature can be used to extract the critical temperature of the coating and the linear kinetic inductance fraction. As shown by [127] the fractional

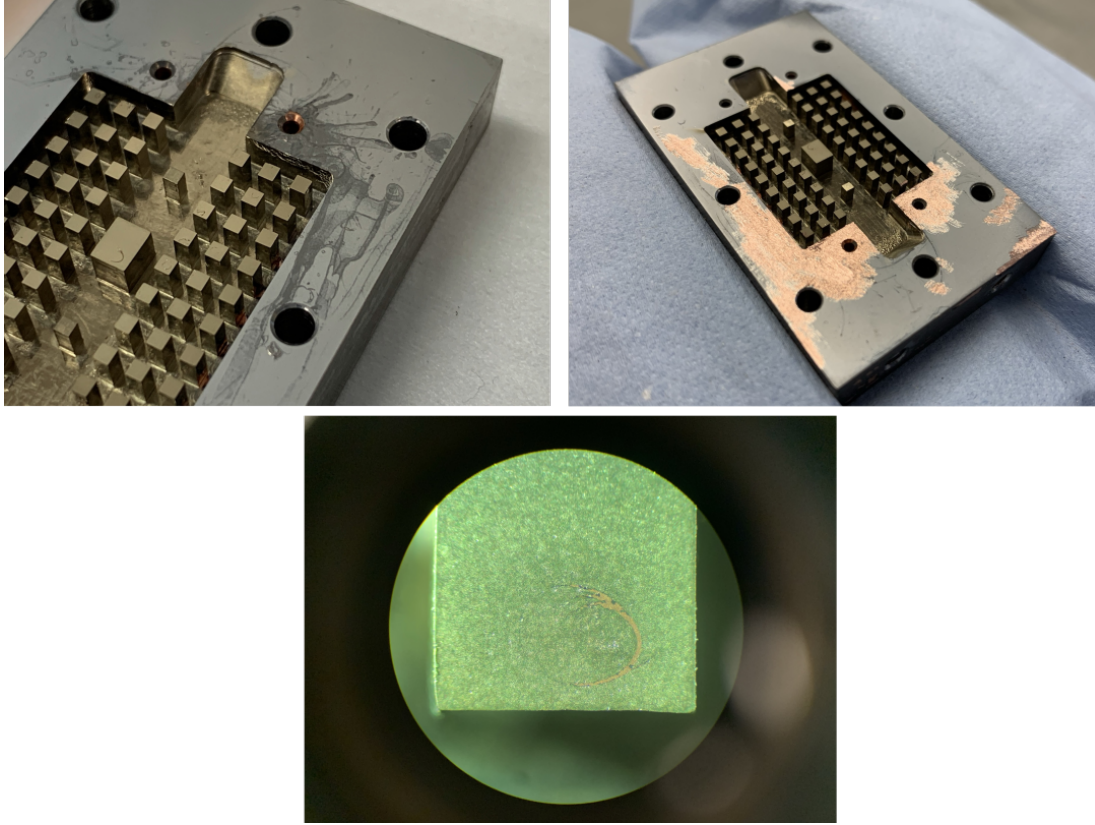


Figure 4.39: Left panel shows a close up of the build up on the spacer layer of the thick film device. The right panel shows the spacer after a rotary tool was used to remove the affected areas. In the process some nails at the edges of the device were damaged. The lower panel shows a microscope image of the surface of the ridge taken prior to the use of rotary tool, indicating that some coating is missing, which could have occurred during transport of the device.

frequency shift with temperature can be described by the following equation resulting from the two fluid model of a superconductor [128]

$$\frac{f(T) - f_0}{f_0} = \frac{-\alpha_{k,L}}{2 \left( 1 - \left( \frac{T}{T_c} \right)^4 \right)} + \frac{\alpha_{k,L}}{2} \quad (4.15)$$

where  $f(T)$  is the resonance frequency at a given temperature  $T \leq T_c$ ,  $f_0$  is the zero temperature resonance frequency, and  $\alpha_{k,L}$  is the linear kinetic inductance fraction. The linear kinetic inductance of the thick coating should scale with temperature for  $T \leq T_c$ , which should allow the desired parameters to be extracted

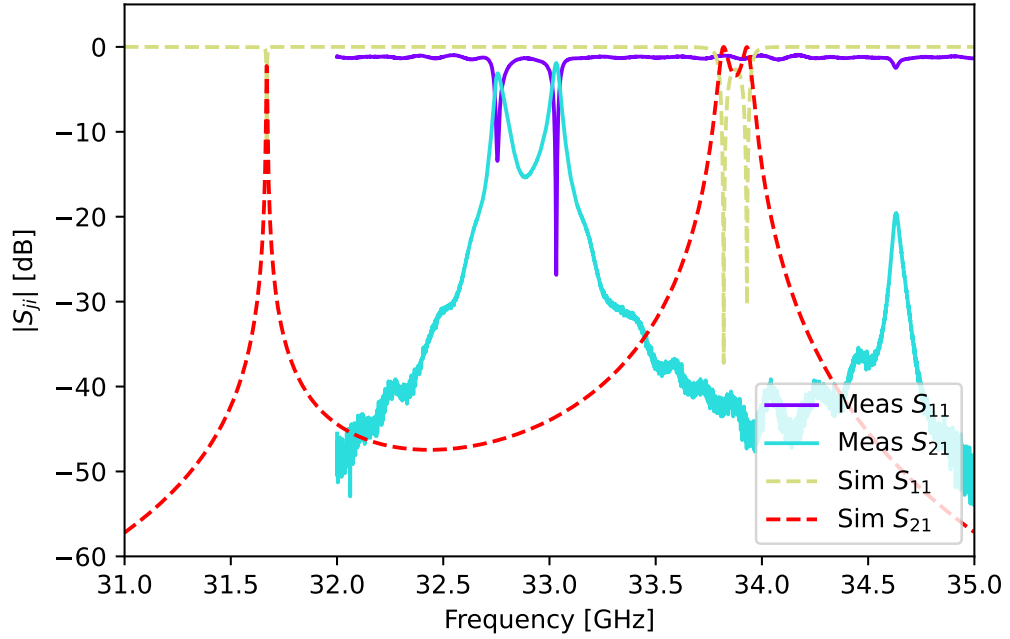


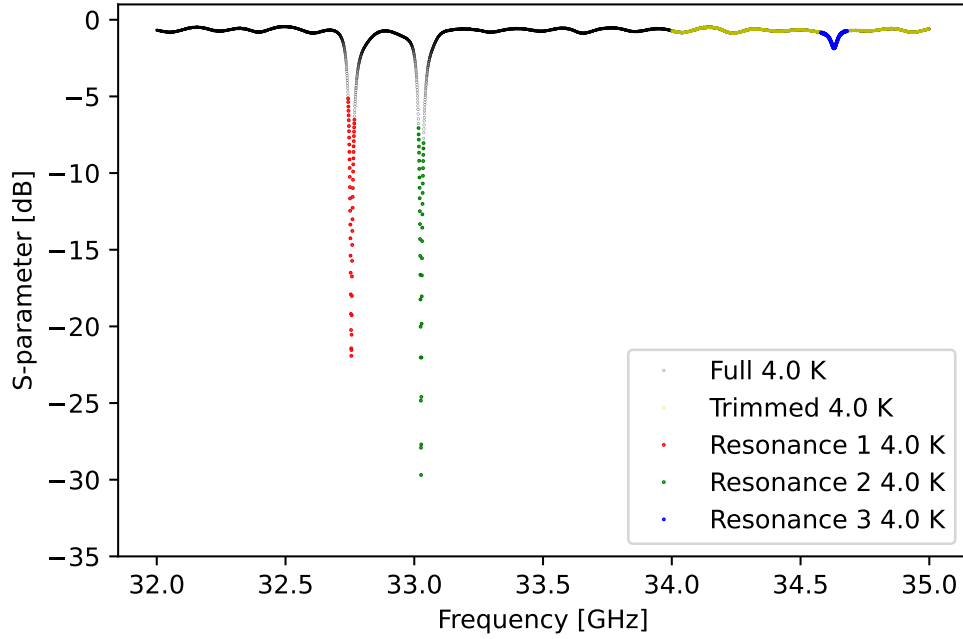
Figure 4.40: Cryogenic low power S-parameters at 4 K base temperature of the thick film RGWG resonator after a part of the deposited spacer layer was removed as shown in Fig. 4.39. The HFSS simulation is the same as in Fig. 4.38.

with a fit of Eq. 4.15.

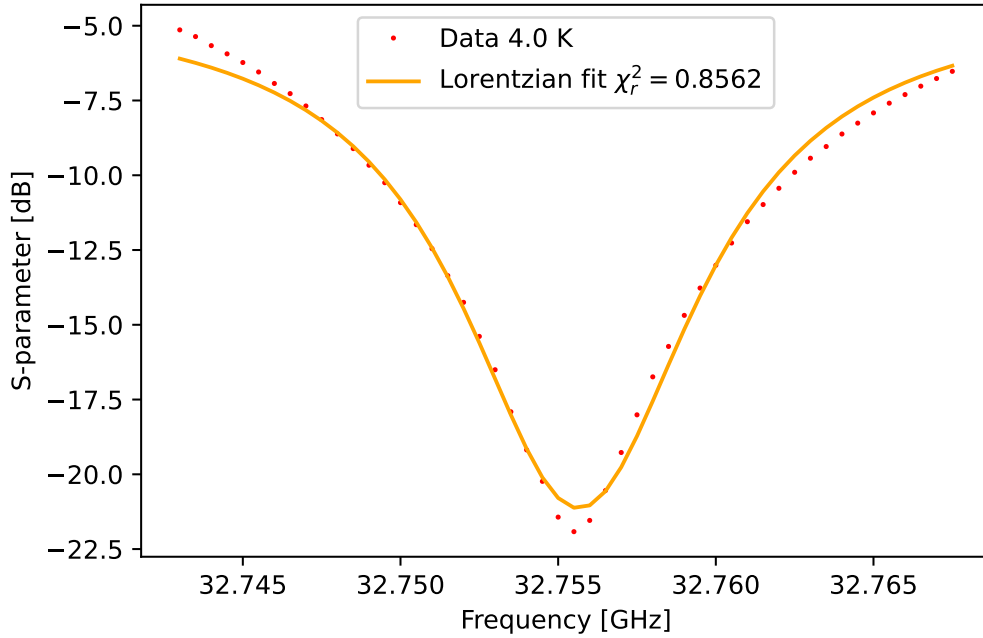
The data that was necessary for this fitting was collected by running a routine written for the VNA (see Section 3.2.3) which sent PID commands to the temperature control unit of the cryostat and saved an S-parameter spectrum after the desired device temperature was reached. An example of this routine in action for is shown by Fig. 4.41. Each detected resonance was fitted with a general Lorentzian function in the form

$$S_{11}(f) = S_0 + \frac{A\Delta f^2}{(f - f_0)^2 + \Delta f^2} \quad (4.16)$$

where  $S_0$  is a vertical offset to account to aid the fitting,  $A$  is the amplitude of the Lorentzian,  $f_0$  is the resonance frequency,  $\Delta f$  is the full-width half-max (FWHM), with an example fit shown in Fig. 4.41b. Following this, the data was

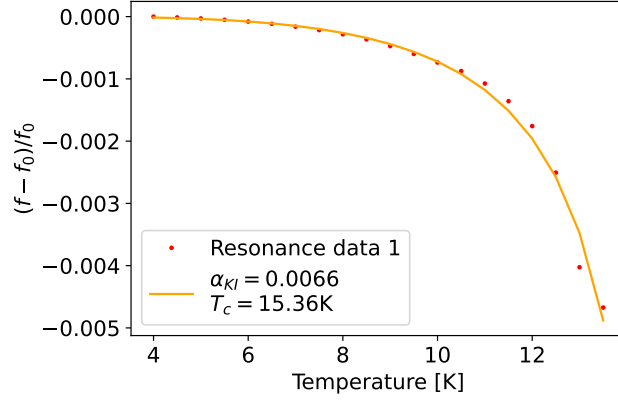


(a) An example of the resonance finding routine detecting three resonances

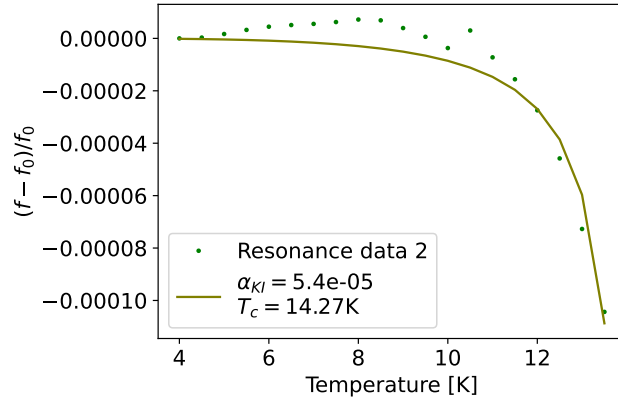


(b) An example Lorentzian fit on resonance 1

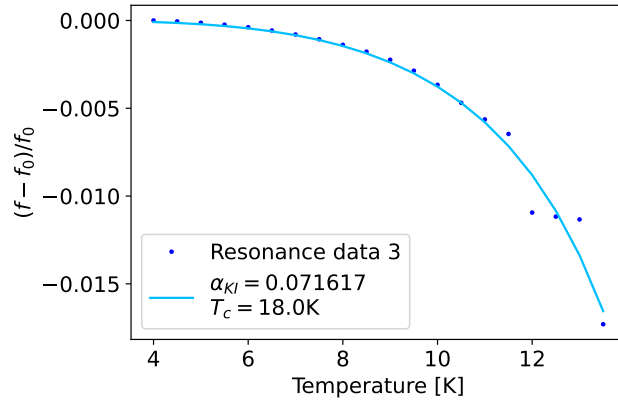
Figure 4.41: A demonstration of the resonance finding routine for a spectrum of three resonances. The final weaker resonance is found in a subset of the data that has been manually trimmed to ensure better detection at temperatures closer to  $T_c$  where this resonance gets even less shallow. Each resonance was fitted with a general Lorentzian function to extract the resonance frequency.



(a) Resonance 1



(b) Resonance 2



(c) Resonance 3

Figure 4.42: The fits of the fractional resonance shift with temperature of Eq. 4.15 of the three resonances present in the RGWG resonator with a  $1\text{ }\mu\text{m}$  coating of NbTiN. Note that resonance 3 disappear is very poorly detected near the critical temperature due the onset of higher dissipation.

analysed using an python routine which was written to automatically detect the frequency of the resonances, and fit a Lorentzian to the  $S_{11}$  of the resonance to extract the desired fit values. These resonance frequency extracted from the fits was then used to fit the temperature varying data to Eq. 4.15. The fits, which are shown in Fig. 4.42, revealed that resonance 3 experienced the largest frequency shift indicating that this has the largest linear kinetic inductance fraction of  $\sim 7\%$ , which is consistent with the shift that should be experienced by the ridge resonance for a structure with a ridge to lid spacing  $h = 6\mu\text{m}$  as shown by Fig. 4.14. This could mean that the ridge is significantly shorter than designed due to the much higher resonance frequency than expected. If this were the case then 1st and 3rd resonance in the simulation shown in Fig. 4.40 have swapped places (see mode 3 in Fig. 4.11), which would explain the lower than expected linear kinetic inductance fraction of the first resonance of the measurements. In addition, the resonance 1 and 2 data from Fig. 4.42 show a critical temperature that is similar to what was measured with the 4 point probe in Fig. 4.32. Note, that the data from resonance 3 becomes very uncertain due to the resonance being unable to be reliably detected for temperatures near to the expected  $T_c$ , which skews the extracted  $T_c$  from the fit. This analysis shows that resonance frequencies of the ridge resonance and on the other side of the GGWG resonance are likely to have swapped places compared to the simulation meaning that the device could be significantly out of specification. In addition, the extracted  $T_c$  is in the range expected for NbTiN.

### Thin NbTiN Coated RGWG Resonator

Compared to the thick film device, the thin film device with a 20 nm NbTiN coating should have a scaling current low enough to allow for its nonlinear properties to be probed. Specifically, this device was fabricated to demonstrate parametric signal gain. Prior to this the linear properties of the resonator were measured. This resonator required an additional aluminium foil spacer to ensure that the



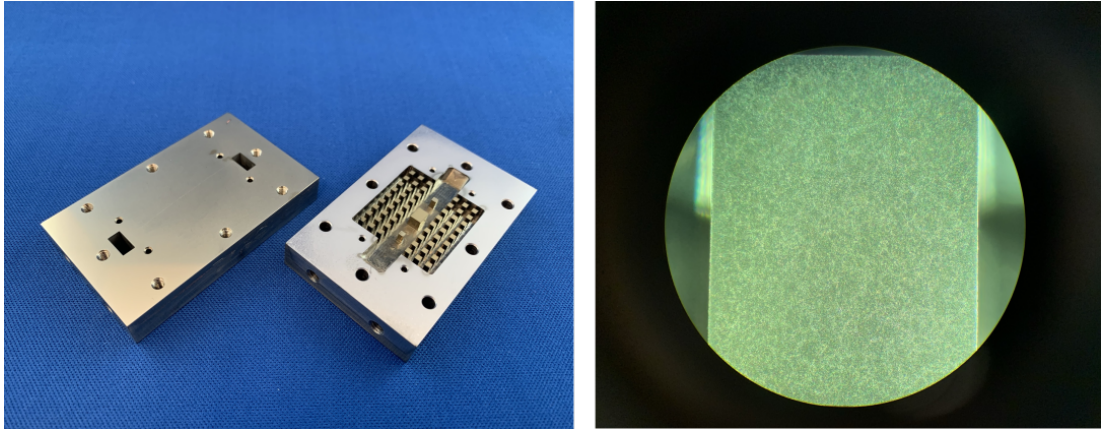


Figure 4.43: A photograph of the thin film device with a 20 nm NbTiN film, as well as a microscope image of the top of the ridge showing the quality of the surface. The ridge to gap spacing was set using a spacer deposition as well as an aluminium foil which produced a  $5 + 13 \mu\text{m}$  ridge to lid spacing.

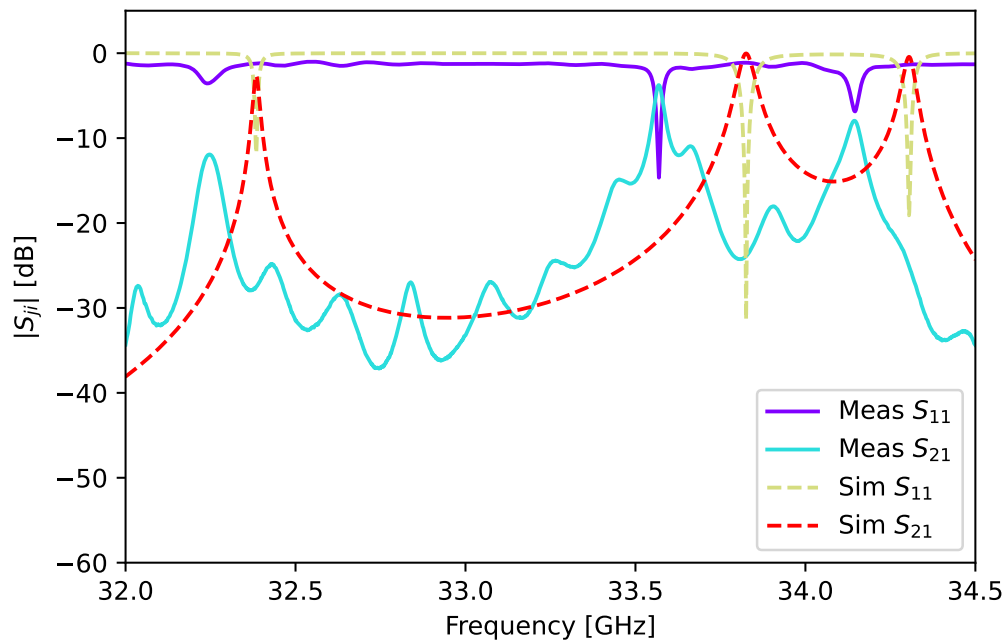


Figure 4.44: The measured and simulated S-parameters at 4 K of the thin film device with a total ridge to lid spacing of  $18 \mu\text{m}$ . The undulations in the measured insertion loss ( $S_{21}$ ) are likely due to a calibration issue. The resonance frequencies of the measured data should not be affected by the calibration.

ridge resonance was not shifted below the measurement band (see Fig. 4.13). This resulted in a ridge to lid spacing of 18  $\mu\text{m}$ . A room temperature measurement of the resonator showed the GGWG resonance at 33.435 GHz, which was closer to the simulated frequency of 33.8 GHz than the thick film device. This resonator, which is shown in Fig. 4.43, was cooled down using the same setup as shown in Fig. 4.37. The resulting S-parameters are shown in Fig. 4.44, which indicate a much better agreement between simulation and measurement in regards to the resonance frequencies of the modes. The losses in the measured data seem to be higher as indicated by the decreased transmission and lower quality factors. This could be due to the uncertainty in the critical temperature of the film that could possibly be as low 9 K as shown by Fig. 4.32. The dissipation increases as the temperature of the device approaches the critical temperature which manifests itself as a drop in transmission for the series resonance, which was observed to occur near 9 K in the measurements. It will be shown in Fig. 4.47 that indeed the critical temperature is likely to be even lower at around 6-7 K.

Characteristic of a nonlinear resonance is the bending of the resonance profile as shown by Fig. 4.18. However, this behaviour was not observed for this resonator even up to a drive power of 10 dBm. At this power the temperature of the device began to rise, which could be due to multiple factors. These include radiative heat load from the microwave excitation heating up the waveguide or significant surface resistance on sharp edges (with thinner coating) in the resonator, while the thermal link to the 3 K stage via the copper braid may be limiting the cooling power acting on the device. Instead the nonlinear behaviour of a resonance can be probed by inserting two, single frequency, closely spaced tones. A cascade of mixing products should appear at intervals of the spacing between the two input tones if the resonance is nonlinear. Two tones were inserted by configuring the VNA to use its two internal synthesisers and combiner to direct two tones through a single waveguide feed (see Section 3.2.3). Interestingly, only resonance 3 showed the appearance of mixing harmonics as shown by Fig.

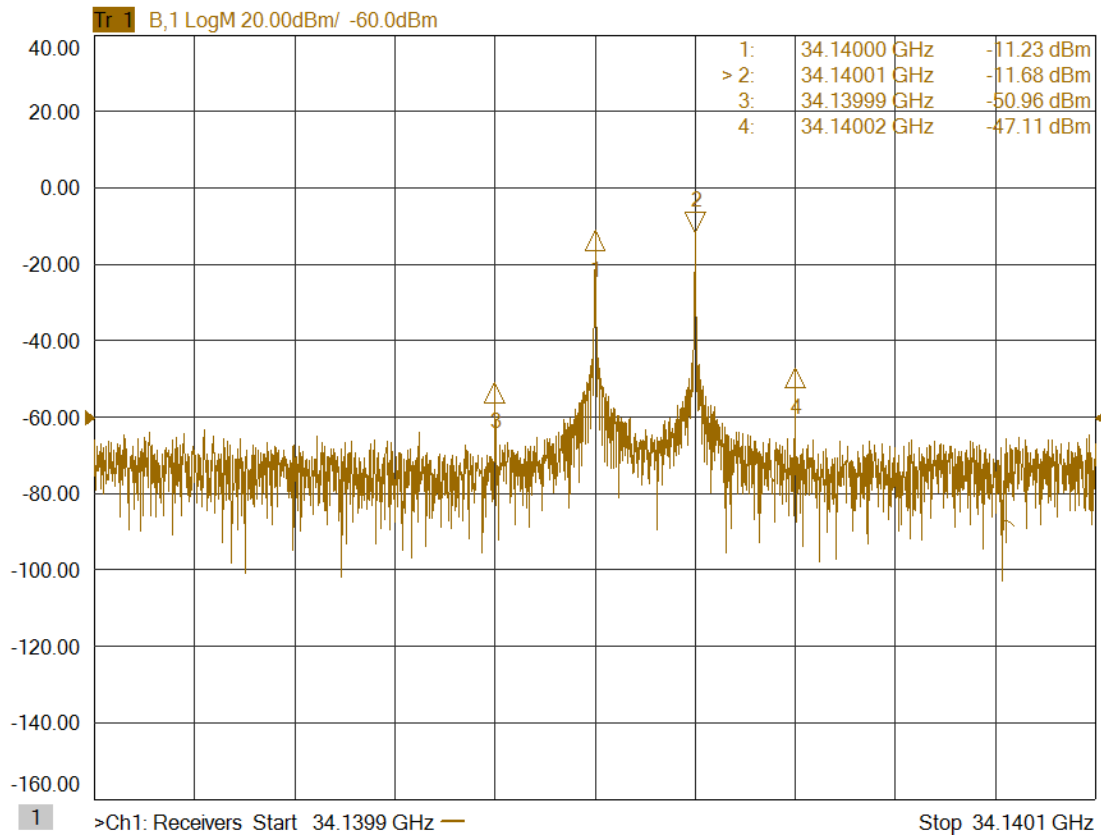


Figure 4.45: The received power spectrum when two tones at 0 dBm (measured at the output of the VNA cables) were inserted with a 10 kHz spacing in the middle of resonance 3 of the thin film device shown in Fig. 4.44.

4.45. It was expected that resonance 1 would show stronger nonlinear behaviour due to the surface current being strongest in the ridge region but no harmonic generation was observed. The reason behind this might be the reduced transmission of resonance 1, which prevented a strong enough surface current to build up which would stimulate the kinetic inductance nonlinearity. The weak harmonics indicated that parametric gain was unlikely to be possible in this device.

### Thick Film Body with Thin Film Lid

It was shown that the first resonance in the thick film device had a fairly good transmission and possessed some linear kinetic inductance but didn't show any nonlinear behaviour. It was hypothesised that combining the lower part of the

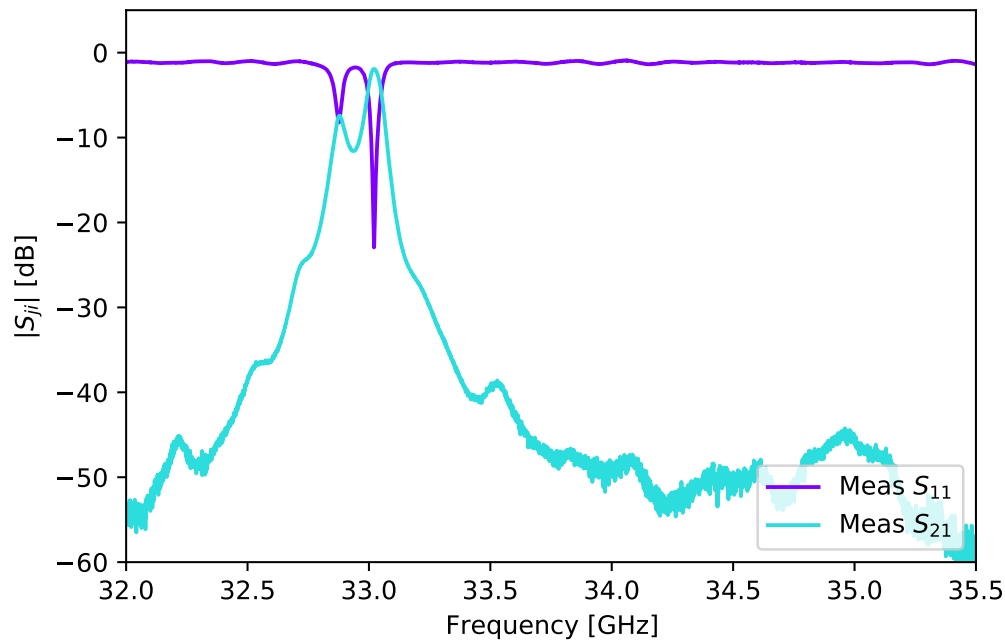


Figure 4.46: The measured S-parameters at 4 K of the RGWG resonator with the body of the thick film and the lid of the thin film device. The spacing was set by the deposited spacer layer only resulting in a ridge to lid spacing of 6  $\mu\text{m}$ . This can be compared to Fig. 4.40 since the same body and ridge to lid spacing was used.

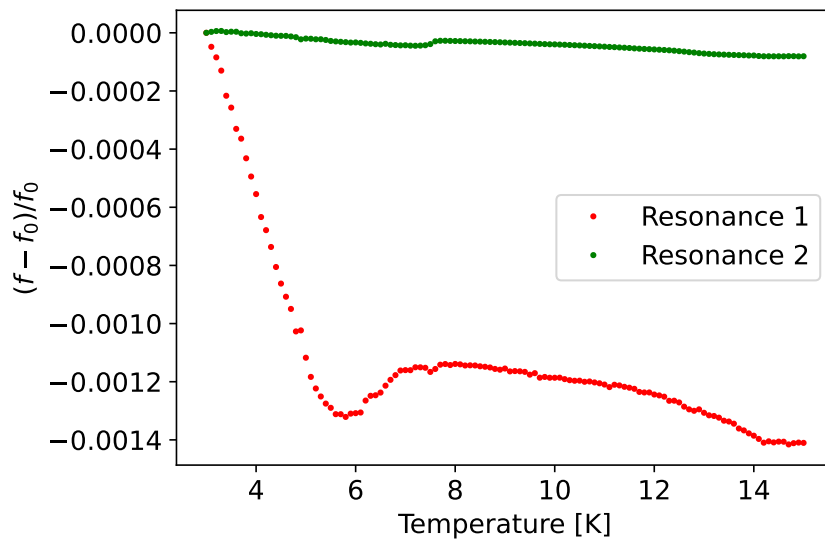


Figure 4.47: The fractional frequency shift as a function of temperature of the mixed resonator being composed of the thick film body and thin film lid. The two resonances refer to those shown in Fig. 4.46.

thick film device with the lid of thin film device could show stronger nonlinear behaviour than the thin film device due to the improved transmission. The higher levels of transmission would allow a higher current to build up which would bring the device closer to the scaling current where nonlinearity is stimulated. In order to maximise the nonlinear kinetic inductance fraction the resonator was cooled down without a spacer. The S-parameters of this device are shown in Fig. 4.46, which seems to have a similar spectrum to the bulk film device of Fig. 4.40, with main differences being lowest frequency resonance has a slightly lower transmission and the resonance near 35 GHz is not visible anymore. This reduced transmission would be consistent with a lower critical temperature of the thin film coating which would have much larger surface resistance than the thick film. A temperature sweep of the resonances was performed using the same method as for the thick film device which is shown in Fig. 4.47. This does indeed show that resonator is behaving as if there are two critical temperatures at  $\sim 6-7$  K and  $\sim 14$  K.

Measuring the S-parameter spectrum at different powers did not show the characteristic duffing oscillator bending for either resonance but did show a visible shift in resonance frequency of resonance 1. Inserting two tones at the centre of the resonance 1 showed the following power spectrum at the VNA's receiver 4.48. This spectrum shows that indeed resonance 1 is nonlinear and is showing mixing between the two strong input tones to generate a cascade of mixing product. This is a strong indication that the resonance is nonlinear but not nonlinear enough to show the characteristic resonance bending. In order to quantify the nonlinear properties it is important to extract the kinetic inductance scaling current,  $I_*$ , and the nonlinear kinetic inductance fraction,  $\alpha_{k,NL}$  (see Section 2.3.2). These quantities can be evaluated by measuring the resonance frequency shift against induced current inside the resonator. A relationship between the fractional resonance frequency shift and circulating current can be derived by using the equation for the resonance frequency of the LC resonator  $f_r = 1/2\pi(L_g + L_k(I))C$  and comparing

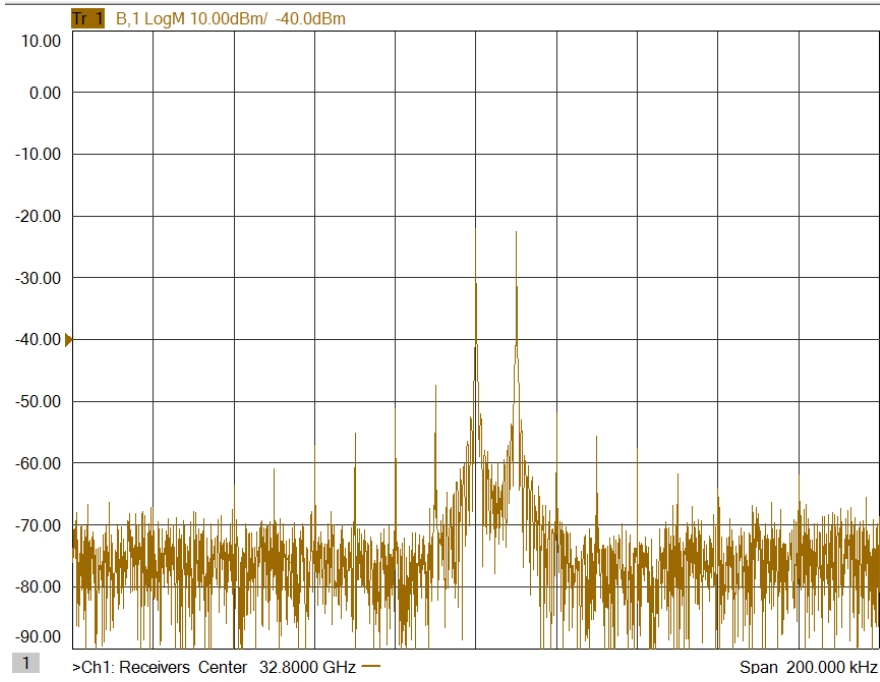


Figure 4.48: The received power spectrum when two tones at 0 dBm were inserted with a 10 kHz spacing in the middle of resonance 1 of the mixed film device. Visible is a cascade of evenly spaced harmonics indicating non linear behaviour.

this frequency at zero current and at a current  $I$ . Eq. 2.30 was substituted for  $L_k(I)$  to derive an equation for the fractional frequency difference followed by a Taylor expansion which resulted in the following

$$\frac{f - f_0}{f_0} \approx -\frac{\alpha_{k,NL}}{2} \left( \frac{I}{I_*} \right)^2. \quad (4.17)$$

Measuring the resonance frequency against input power of the VNA source can provide the necessary data needed to extract these nonlinear parameters in Eq. 4.17. The data was collected using a similar automated routine to the temperature sweep, except here it was the input power of the synthesiser in VNA that was changed and an S-parameter spectrum was taken. The temperature controller was set up to hold the resonator temperature slightly above the base temperature to account for any temperature rise that occurs at powers over 0 dBm which can induce a separate frequency shift. The data was then analysed

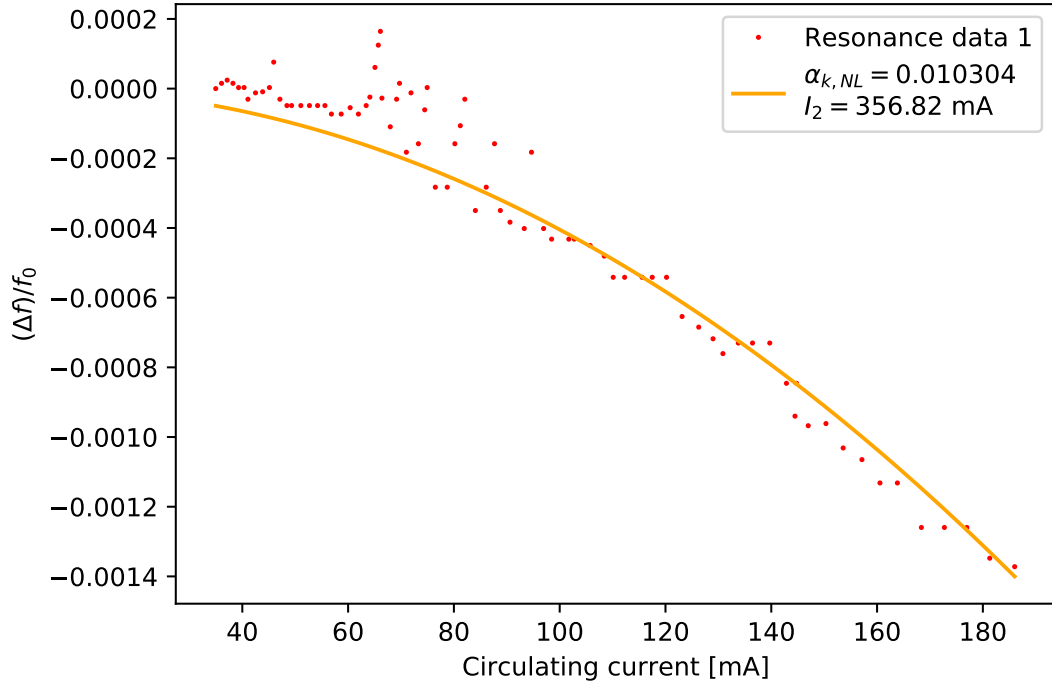


Figure 4.49: The fractional frequency shift against circulating current of resonance 1 of the mixed film device shown in Fig. 4.46. The input power which was measured at the input of the cryostat was converted to a circulating current using Eq. 4.10. This relied on the assumptions that the total  $Q$  measured as the  $-3$  dB point of the resonance was limited by the coupling  $Q$  such that  $Q_c \sim Q_t$ , which was measured to be  $\sim 1000$ . The impedance was calculated using Eq. 4.18 which was calculated to be near  $1 \Omega$ .  $I_2$  was used to signify the second order scaling current which is identical to  $I_*$ .

using a similar resonance finding routine as shown in Fig. 4.41, which prepared the data to be fitted to Eq. 4.17.

The induced current at the resonator surface in Eq. 4.17 can be calculated from the input power using Eq. 4.10 which requires estimates of the coupling quality factor  $Q_c$ , the minimum  $S_{11}$ , and the resonator impedance  $Z_0$ . In order to estimate the coupling quality factor it is necessary to assume that internal quality factor is significantly higher than  $Q_c$  such that the  $Q_t$ , which can be measured directly on the S-parameter spectrum, is limited by the  $Q_c$ . This assumption is likely to hold when the device temperature is lower since the internal  $Q$  varies with temperature. It is likely that  $Q_i$  is composed of temperature independent

and temperature dependent components, where the temperature dependency is a result of the real part of the conductivity given by the Mattis-Bardeen theory for dirty films or more generally by the Zimmermann theory (see Section 2.2.1 and 2.2.2). However, for this analysis  $Q_c \sim Q_t$  was used to estimate the order of magnitude of the scaling current. The resonator impedance was calculated using theoretical expression for the total inductance and capacitance to give

$$Z_0 = \sqrt{\frac{L_g + L_k}{C}} \quad (4.18)$$

where expressions for the geometric inductance  $L_g$ , kinetic inductance and resonator capacitance  $C_c$  can be found in Section 4.2.3. This expression for the impedance relies on an assumption that the resonator dynamics are described by the parallel plate model, which may not be the case since the resonance 1 of the measured device shown in Fig. 4.46 is like to be mode 3 of the simulated resonator (see Fig. 4.11) which is likely not dominated by the ridge lumped values. The impedance of this resonance may be higher than the estimated value, this uncertainty could be avoided if it were possible to measure the ridge resonance instead. The results of the power sweep analysis of resonance 1 are shown in Fig. 4.49. The nonlinear kinetic inductance fraction was estimated to be  $\sim 1\%$  with the scaling current at  $\sim 350$  mA. These values bare a significant amount of uncertainty as previously discussed so should be used as order of magnitude estimates. However, the estimates are on a similar order of magnitude to the theoretical values. The theoretical critical current that is shown by Fig. 4.15 is a factor of 3-4 different from the 4 K value of the 20 nm NbTiN layer while the kinetic inductance fraction of resonance 3 of a thin film device with a 10  $\mu\text{m}$  gap of Tab. 4.1 shows that the measured resonance should have a kinetic inductance fraction of a few percent. Note, the nonlinear kinetic inductance fraction of the measured device should be at around 50 % of the total linear kinetic inductance fraction as calculated with Eq. 4.5 using the design values of the resonator and



the coatings.

These extracted values of nonlinear kinetic inductance fraction and critical current show that such a superconductor coated metal RGWG resonator has potential to be used as the foundation for a resonant parametric amplifier. However, the measured kinetic inductance fraction is unlikely to generate more than a couple of dB of parametric signal gain judging from a comparison to the strength of the generated harmonics of the circular waveguide resonator that employed contact junctions (see Section 3.3). Instead, this analysis should be repeated at a lower temperature of 1 K which could boost the transmission and quality factor of the tested resonance. More importantly, a lower operating temperature may improve the transmission and quality factor of the ridge resonance allow it to be tested. This resonance should have a significantly higher kinetic inductance contribution and could provide measurable parametric gain. Testing the ridge resonance would provide more confidence in the extracted values of the  $\alpha_{k,NL}$  and  $I_*$ , which could be used in the ADS simulations discussed in Section 4.2.3 to simulate the nonlinear S-parameters and gain to confirm the validity of the theoretical description of the RPA.

## 4.5 Summary and Outlook

### 4.5.1 Summary

In summary, a type of high frequency transmission line structure, referred to as ridge gap waveguide, has been proposed to be used as the foundation for resonant superconducting amplifiers that exploit the nonlinearity of the kinetic inductance of thin films. It was shown that this structure can be designed to have a large nonlinear kinetic inductance and be engineered into a resonator with resonances within the Ka band (26.5 to 40 GHz). The high KI was achieved by employing a spacing as small 5  $\mu\text{m}$  between the resonant ridge and the lid above it via the

a deposition of a coating of Nb on the outer perimeter of the device. The bed of nails, which is the meta material that makes this structure possible, was described and simulated in Ansys HFSS. These simulations included two types of transmission lines that could be created with the the bed of nails, namely groove gap waveguide and ridge gap waveguide. The former was very similar to rectangular waveguide in its characteristics and allowed straightforward integration with rectangular waveguide feeds. The latter showed potential as a structure which could be engineered to have a large kinetic inductance fraction when coated with a thin layer of NbTiN. The resonator was designed and simulated in HFSS in which the superconducting nature of NbTiN was included using the surface impedance calculated via the Zimmermann conductivity. In addition, the nonlinear nature of the resonator and its possible parametric gain was simulated using an equivalent circuit model that was built in Keysight's ADS. In addition, it was shown that these simulations could be used to predict the compression point of such a resonant parametric amplifier.

The mechanical design of the copper resonator was outlined, which was followed by a description on how the metal surfaces should be prepared for thin film coating via a multi-step polishing process. The methods and procedures for the coating of the copper surfaces with a number of different superconducting and insulating films via a magnetron sputtering system were described. Room temperature and cryogenic measurements of the finished devices were presented which showed nonlinear behaviour of the resonator in the form of frequency shifting of the resonance frequencies with increasing input power and the generation of mixing harmonics when two strong input tones were presented at the input of the resonator. In addition, the critical temperature and linear kinetic inductance fraction were measured using the resonance frequency shift with temperature. The nonlinear kinetic inductance fraction and scaling current were extracted by examining the frequency shift with the power. This nonlinear behaviour was demonstrated even under a number non-optimal device conditions including a

higher than desired operating temperature of 4 K rather than 1 K due to the adsorption cooler having to be removed from the cryostat; a lower than expected critical temperature, which significantly increased the loss of the structure; and the use of a resonance with an inherently lower kinetic inductance fraction due to the resonance of interest appearing much weaker than designed likely due the fabricated device dimensions being out of specification.

## 4.5.2 Future Work

### Short-Term Design Improvements

The results of this chapter inspire confidence for further work to be carried out on the presented copper RGWG resonators. Further development is needed in order to realise a high quality device boasting a high kinetic inductance fraction and low loss, which could in theory produce over 20 dB of narrowband gain. Immediate further development should focus on the measurement of already fabricated devices to measure their precise physical dimensions as part of the troubleshooting to find out the reason behind the resonance frequencies of some resonators being significantly different from simulations. A more detailed study should be carried out on the superconducting coating on copper substrates, specifically the type and thickness of the isolating layer as well as the thickness and critical temperature analysis of the NbTiN layer or the use of other films like NbN that may have an even higher London penetration depth. Prior to any further coatings, the copper parts should be treated with chemical cleaning techniques in order to improve the surface quality of the surfaces that were not polished to improve the quality factor of the engineered resonances. The lower part of the resonator should be coated with a thick superconducting coating to avoid regions of diminished superconducting properties such as sharp edges or deep parts of structure. These thin regions pose the risk of increased dissipation and worse device performance. Instead the nonlinear film should be deposited on the flat surface of

the lid that is less prone to such issues. The use thick deposited spacer layers should be avoided due the difficulty in carrying these out successfully in terms of deposition time and the risk of losing devices that comes with this. Instead, separate foil spacers could be used with a thickness as low as 5  $\mu\text{m}$ . These considerations should allow for a much higher quality superconducting resonator to be realised. The specifications that should be targetted are the critical temperature that should be as high as possible to reduce the losses at 1 K; and a quality factor of at least 5000 on the ridge resonance with high transmission. This device should be characterised at 1 K and the resulting parametric gain should be compared to the simulations of the equivalent model in ADS.

### Future Iterations

Future iterations of the RGWG RPAs should avoid the use of coupling resonators to reach the desired quality factor due to the challenges in achieving the desired coupling quality factor for the ridge resonance. Especially, in cases when the detuning between the filtering groove gap waveguide resonances and the ridge resonances changes from device to device. Instead, wider band tapers from rectangular waveguide to RGWG such as Chebyshev, exponential or Klopfenstein [1] should be explored. These tapers would allow for a more conventional capacitively coupled resonator design, which would produce a resonance that would behave more predictably over the bandwidth of the taper. In addition, the next iteration of devices should be designed with a single port so that they could be operated in reflection mode with a circulator to avoid back leakage between ports. This method would also avoid having to overcome the losses of two separate transition at the input and output ports compared to just one transition in reflection.

In regards to device simulations, the HFSS quality factor analysis could be made more sophisticated by using tools such as pyEPR <sup>7</sup>, which would allow for the quality factor contributions of various joins and lossy interfaces to be

---

<sup>7</sup><https://github.com/zlatko-minev/pyEPR>

computed. This would also help determine the minimum number of rows of nails needed for the structure by evaluating contribution of the joins at the edges of the nail arrays. The ADS gain simulations could be expanded to incorporate the noise of such parametric amplifiers by estimating some possible noise models of superconducting coatings.

Alternative fabrication methods of the RGWG should be explored such as silicon micro-machining [113] which would remove the necessity of the insulating layer deposition and would significantly improve the quality of the deposited films due to the high ordering of the lattice structure of silicon substrates. Miniaturisation of the bed of nails and the resonator should be also explore which would simplify fabrication if micro-machining techniques were used. The smaller device could be contained with a metallic chip holder, which could secure it in place and house connections for waveguide flanges. Deposition techniques such as atomic layer deposition could be used to achieve a conformal coating on all parts of the structure. The higher quality films may allow for 4 K operation to be explored (inspired by KI-TWPA work by Malnou *et al.* [20]), which would open up more applications at this higher temperature.

Fabricating these structures on silicon would open the path to the use of lithography to realise slow wave structures such as IDCs [65] and the inclusion of DC bias lines, which would open up the path of 3WM operation. In such a 3WM amplifier the signal and pump tone could be inserted through separate ports on either side of the device with each having a type of bandpass structure to prevent leakage. This would automatically remove the need to filter out the pump tone after amplification which would mean that the pump tone would not saturate any subsequent amplifiers in the waveguide chain. However, in this scenario the pump would have to be brought down to the device via its own waveguide such as V band (40-75 GHz). Such 3WM RPAs are already being sold for chip based JPAs by Raytheon BBN <sup>8</sup>. These operate in 4WM when the signal and pump

---

<sup>8</sup><https://bbn-jpa.myshopify.com/>

#### *4: KA BAND RIDGE GAP WAVEGUIDE KI RPA*

enter through the same port and in 3WM mode through separate modes when a DC bias is include.

# Chapter 5

## W band Ridge Gap Waveguide KI TWPA

### 5.1 Introduction

The ultimate goal of this PhD project was to realise a wideband superconducting parametric amplifier operating at a higher frequency than achieved before. As discussed in Section 3.3 of Chapter 3 as well as in Chapter 4 narrowband parametric amplification was achieved within the Ka band (26 to 40 GHz) at  $\sim 30$  GHz in two types of superconducting resonant cavities employing two different types of nonlinearity.

The circular waveguide based Josephson RPAs that are discussed in Section 3.3 are incompatible with wideband parametric amplification due to the nonlinear dispersion of the TE/TM transmission modes inherent to circular waveguide. As detailed in Section 2.4.4, this incompatibility arises from the inability to maintain a phase matching condition over a wide band between the involved signal, pump and idler tones. However, the nonlinear contact junctions employed in this structure have potential to be used in conjunction with a mechanically tunable re-entrant cavity [129] which allows for the resonance frequency and in turn the

narrowband gain curve to be shifted. This tuneability is achieved by moving one of the walls of the cavity. Such a tunable device is the potential next step for the circular waveguide RPA (discussed in Section 3.3).

The ridge gap waveguide employed in the kinetic inductance RPAs that are discussed in Chapter 4 can support a quasi-TEM mode of transmission with linear dispersion, meaning that this structure is compatible with wideband parametric amplification. However, in order to achieve practical gain levels over a wide bandwidth the input tones must co-propagate within an electrically long transmission line. Such a structure is referred to as a travelling-wave parametric amplifier (TWPA). The physical length of such a device can be a decisive factor in whether fabrication is practical. Depending on the RGWG geometry and superconducting coating, the necessary electrical length can span into hundreds of wavelengths at the signal frequency. In RGWG with small conductor spacings that minimise the geometric inductance and thin superconducting coatings ( $t \ll \lambda_L$ ) that maximise the KI contribution, the KI fraction can reach over 90 % which significantly reduces the necessary electrical length to a sub-100  $\lambda$  range for gain levels that are over 10 to 15 dB.

At the Ka band a TWPA based on RGWG could be in 10 to 100 cm in length which would make the fabrication process quite complex due to the large parts involved. Whether this structure would be a metal milled where milling and surface polishing are challenging or silicon micromachined [113], where the large wafer size and aspect ratio affect the angle of side walls, which could cause issues with maintaining a constant impedance. However, designing RGWG TWPAs at higher frequency can be advantageous due to the reduced device size, which can simplify fabrication and allow for improved device quality. Additionally, the narrower ridge reduces the kinetic inductance scaling current,  $I_*$ , which in turn reduces the pump tone power necessary for amplification. At the W band (75 to 110 GHz) a TWPA that is under 10 cm in length could be realised. This device length could be reduced even further at frequencies of 100s GHz, however, at



these frequencies the additional complexity of feed chain (multipliers, additional wiring) must be considered. Therefore, due to the relative simplicity of a W band rectangular waveguide cryogenic feeding network that can incorporate cryogenic thermal breaks [110] this frequency band is chosen as the testing ground for superconducting RGWG TWPAs.

With these considerations in mind, this chapter provides the design methodology and tools needed to predict the performance of RGWG based KI TWPAs. The contents of this chapter should provide instructions for how such structures could be realised into working prototypes and pave the way for design of even higher frequency variants.

### 5.1.1 Motivation and Applications

Kinetic inductance travelling-wave parametric amplifiers (KI-TWPAs) promise high gain, large bandwidth and potential for quantum limited noise performance [12]. Currently, most KI-TWPAs [13, 61, 65] have been fabricated for sub-20 GHz and mK temperature operation. However, there is interest in extending this to higher frequency applications where quantum limited amplification is needed such as dark matter detection [130] and high frequency quantum computing [131]. At mm-wave energy scales these superconducting circuits are less sensitive to thermal background noise due to the higher photon energies involved. Hence, these paramps may achieve their low noise figures at temperatures of 1 K, which are accessible via higher heat lift fridges such as adsorption coolers. Recently, narrowband parametric amplification has been achieved at 95 GHz [19], while the highest reported frequency in a travelling wave design [18] has reached 30 GHz.

At mm-wave frequencies KI-TWPAs based on conventional transmission lines such as co-planar waveguides and microstrips face challenges in connecting their sub- $\mu\text{m}$  size traces to external feeding structures without suffering from large dielectric losses. A potential method to alleviate dielectric losses at frequencies over

100 GHz is to use more exotic transmission lines that incorporate a hollow gap between conducting surfaces instead of one filled with dielectric and can be coupled to waveguide feeds via low loss transitions. One such structure is the aforementioned ridge gap waveguide [111] which is readily scalable to frequencies of a few hundred GHz [113] and can support quasi-TEM mode of transmission over multiple octaves of bandwidth. Coating and patterning these RGWGs with a thin superconducting film such as NbTiN and maintaining a conductor separation in the micrometer to sub-micrometer range can help achieve kinetic inductance fractions in excess of 90%, which makes these transmission line structures potential KI-TWPAs candidates in mm-wave domain.

### 5.1.2 Chapter Outline

This chapter sets out the theoretical description and design pipeline of RGWGs and RGWG TWPAs at W band. Section 5.2 will cover the design and simulation of W band RGWG in HFSS including the bandwidth engineering of this structure and a discussion of the superconducting surface impedance simulations based on the Zimmermann conductivity (detailed description in Section 2.2.2). In addition this section will cover the scaling of the surface inductance and the kinetic inductance fraction with RGWG dimensions, as well as the nonlinear scaling with current. Section 5.3 will describe the design of a dispersion engineered TW RGWG with a focus on the periodically loaded transmission line and a discussion of the scaling current which dictates the scale of the nonlinear response. This section will show simulations of the equivalent circuit model to yield the nonlinear S-parameters and dispersion properties of this structure. The nonlinear simulations were performed using user-defined components in Keysight's ADS in the same way as in Chapter 4. In addition there will be a description of the method by which parametric signal gain is extracted using the dispersion engineered TW RGWG via harmonic balance simulation method in ADS. These

simulation results will be compared to the calculated gain curve from the solutions of the coupled mode equations (described in Section 2.4.4). Finally, Section 5.4 will provide a summary of the key results and outline the direction in which future high frequency RGWG research could take.

## 5.2 Ridge Gap Waveguide Design

The W band RGWG builds on the same principles that were developed for the Ka band RGWG which was engineered into an RPA (see Chapter 4). Many of the same structure elements are used including the bed of nails pin surface and a groove with dimensions tailored for integration with rectangular waveguide, with a central ridge within this groove for a quasi-TEM transmission mode.

A model of the W band RGWG is shown in Fig. 5.1, which includes a set of possible dimensions that allow for a straightforward integration with W band rectangular waveguide while having high nonlinear KI participation. Waveguide integration is achieved by matching dimensions  $a$  and  $b$  to that of rectangular waveguide. High KI participation is a result of choosing a gap of  $5\text{ }\mu\text{m}$ , which allows for a KI fraction of 60% but isn't so small as to make it challenging to maintain a constant spacing between the two RGWG parts via a spacer layer. The width of the ridge was chosen to allow for an introduction of impedance perturbations in the form of wider sections of the line without introducing higher order ridge modes. The lower cut-off of these modes scales inversely with the ridge width. The details behind these choices are discussed in proceeding sections of this chapter.

### 5.2.1 RGWG HFSS Simulations

RGWG design begins with the engineering of the pin surface which creates a stopband of the global parallel plate mode (see Section 4.2.1). The lower cut-off frequency of this stopband is governed by the length of the pins,  $d < \lambda/4$ , and

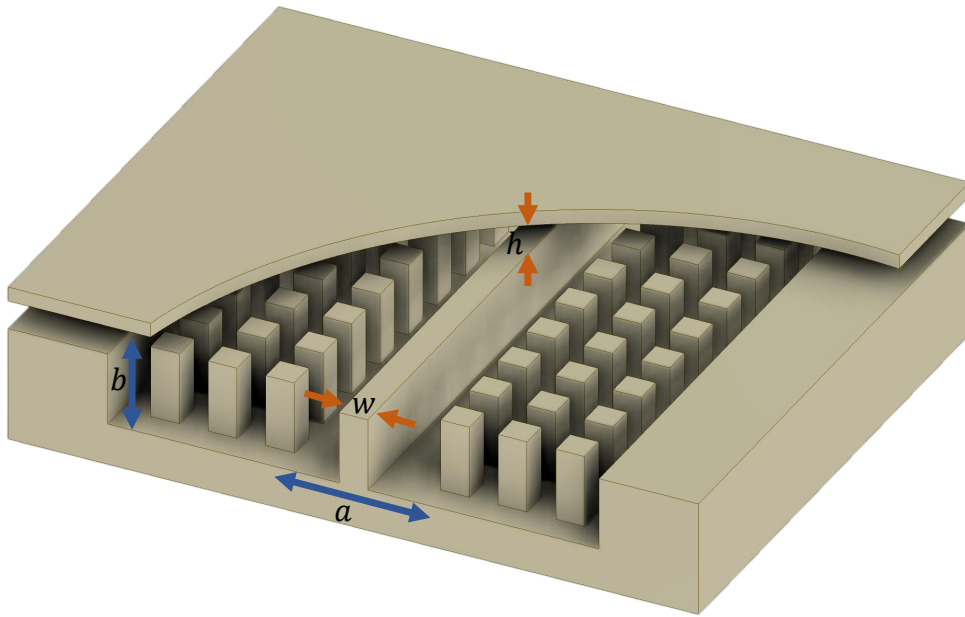


Figure 5.1: A RGWG model showing the central ridge of width  $w = 0.5$  mm in a groove of width  $a = 2.54$  mm and height  $b = 1.27$  mm, with 3 rows of pins with width of 0.5 mm and pin period of 1 mm. The pins and ridge are of the same height  $d$ . The gap labelled  $h$  is exaggerated to demonstrate how the 2 parts of the waveguide are joined together. In actuality, this gap is set to  $5\text{ }\mu\text{m}$  to provide a large kinetic inductance fraction.

the conductor spacing,  $h < \lambda/4$ . In the small conductor spacing regime  $h \ll d$ , this lower cut-off frequency varies rapidly with  $h$ . A small value of  $h$  leads to a lower cut-off frequency of the stopband of the bed of nails which can significantly extend the operational bandwidth. The upper cut-off is determined by the  $d + h$ , which means that this is dominated by  $d$  since  $d \gg h$ . A larger pin length leads to a reduction in the upper cut-off frequency. The value of  $d$  is chosen to be most compatible for integration with rectangular waveguide while  $h$  is chosen to be the same for the ridge and pin region due to fabrication considerations and should be as small as practically possible to maximise the kinetic inductance fraction.

Following the engineering of the pin surface, a wave guiding channel can be positioned between the pins. For a smooth transition from rectangular waveguide, the groove width can take the dimension of long side of rectangular waveguide,  $a$ , in addition this constrains  $d + h$  to the short side of rectangular waveguide,  $b$ . The upper cut-off of the single mode gap waveguide can be affected by the ridge

width, especially when  $w \rightarrow a$  and with the presence of a high KI coating, higher order gap waveguide modes begin to propagate. In the case of a ridge that is wider than  $\sim 700 \mu\text{m}$  the higher order ridge mode begin to propagate at  $\sim 110$  GHz.

As with the Ka band RGWG from Chapter 4 the main simulation tool for designing the bed of nails and ridge gap waveguide is HFSS. Three different structures were simulated in order to characterise the bandwidth of the allowed propagating modes in the W band RGWG and are shown in Fig. 5.2. The same method was used for the K-band RGWG design from Section 4.2.1. The pin surface unit cell shown in Fig. 5.2a was used to engineer the necessary stopband when this cell was expanded to be infinitely large via the use of 2 sets of master and slave (lattice) boundary conditions on horizontally opposing faces. The groove gap waveguide unit cell shown in Fig. 5.2b was used to show that a groove gap waveguide mode will propagate over the same bandwidth as the rectangular waveguide mode. A single pair of the lattice boundary conditions along the direction of signal propagation were used in this model. This groove gap waveguide region could be used in the intermediate transition from rectangular WG to RGWG. Finally, the RGWG unit cell shown in Fig. 5.2c was used to demonstrate that the desired ridge gap waveguide mode with linear dispersion will propagate over the whole bed of nails useful bandwidth.

In order to extract the allowed propagation modes and their dispersion properties an eigenmode analysis was performed on these structures. As with the Ka-band work in Chapter 4 the surface boundary conditions were set to perfect electrical conductors (PEC) instead of the superconducting surface impedance boundaries. These surface impedance boundaries, which vary with frequency, would give a more accurate representation of the structure bandwidth as a result of the inclusion of the reactance of the superconducting coating. However, the eigenmode simulation in HFSS does not support frequency dependent boundary conditions, only single-valued boundaries can be included. One could carry out

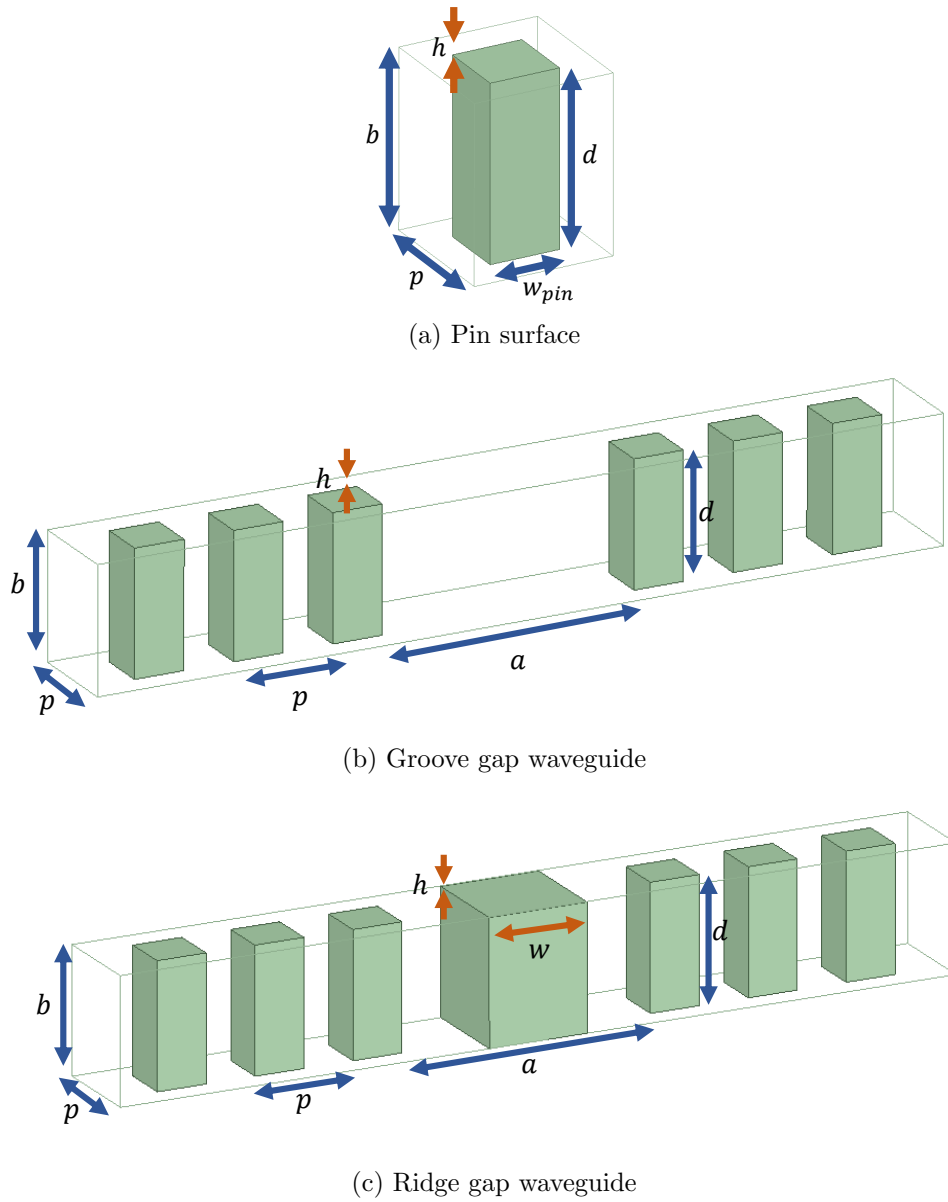


Figure 5.2: Unit cells used in the HFSS eigenmode analysis to identify allowed propagation modes. The unit cell used to simulate the pin surface employed master and slave (coupled lattice) boundaries on the 2 pairs of horizontally opposing faces. The unit cells of the groove gap and ridge gap waveguide unit cells had 1 set lattice boundaries on the faces along the direction of propagation of the confined wave (in/out of page). Here,  $d$ ,  $w_{\text{pin}}$ ,  $p$  are the pin length, width and period;  $h$  is the hollow gap between the top of the pin and the opposing conducting sheet;  $b$  is the separation between the two parallel surfaces of the structure and  $a$  is the width of the groove in groove gap waveguide.  $b$  and  $a$  correspond to the short and long wall of Ka band rectangular waveguide, respectively.

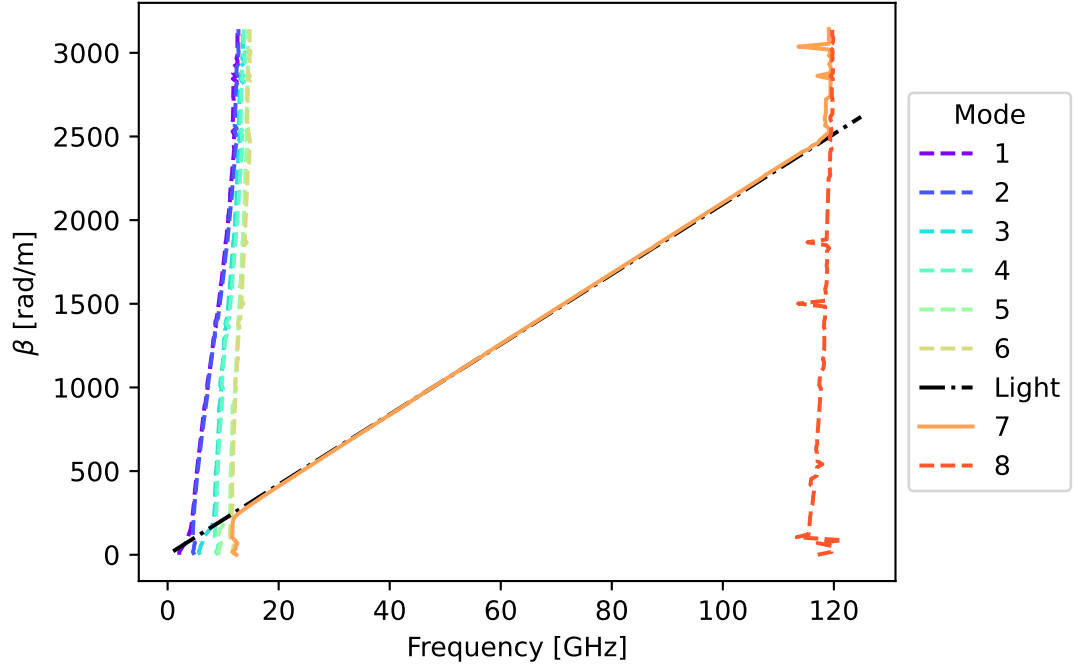


Figure 5.3: The dispersion of the first 8 propagation modes of the eigenmode simulation of RGWG in HFSS with PEC boundaries using the model from Fig. 5.2c. The structure dimensions are outlined in Fig. 5.1. Mode 7 is the quasi-TEM mode possessing near linear dispersion across a 20 to 115 GHz band. Therefore, the phase constant,  $\beta$ , can be used interchangeably with the angular wavenumber  $\beta \equiv k = 2\pi/\lambda$ .

separate simulations with single-valued surface impedance boundaries near the expected lower and upper cut-off frequencies in each structure. However, the PEC model provides a sufficiently accurate analysis of the RGWG structure and allows for nearly final design dimensions to be found, as shown by the mode dispersion plot in Fig. 5.3.

The structure bandwidth was confirmed in a driven modal simulation in Ansys HFSS which supports such frequency dependent boundaries. The frequency dependent surface impedance of the 30 nm NbTiN film is shown in Fig. 5.5 at 2 different temperatures and was found using the Zimmermann conductivity shown in Fig. 5.4. The surface impedance at 1 K was chosen for the simulation due to the greatly reduced surface resistance at this temperature. For this driven modal simulation, a model of a short section of a RGWG was investigated, which

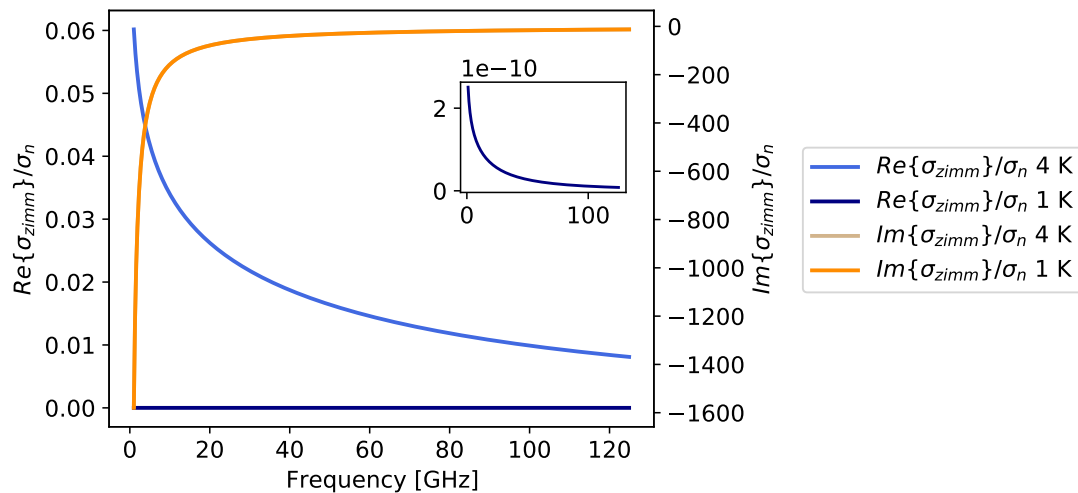


Figure 5.4: Real and imaginary components of the Zimmermann conductivity relative to the normal state conductivity of NbTiN at 4 and 1 K. The inset shows  $Re\{\sigma_{zimm}\}/\sigma_n$  at 1 K which varies on a much smaller scale. The parameters used for the calculation were adapted from [55, 132]:  $T_c = 15$  K,  $\Delta_0/k_b T_c = 1.86$ , BCS coherence length  $\xi_0 = 170$  nm, mean free path  $l = 0.57$  nm.

is shown in Fig. 5.6. The surface impedance boundaries are applied to all internal surfaces. By allowing the waveports to support additional modes, the single-mode bandwidth of the RGWG can be extracted by plotting the simulated S-parameters of all the modes. The results of this analysis are shown in Fig. 5.7 and indicate that the upper cut-off of the bandwidth predicted by the PEC simulation is very similar to that of the surface impedance driven modal analysis. The transmission of the RGWG mode remains near unity over the whole bandwidth of interest but other modes begin to propagate near the 115 GHz point, which may cause spurious resonances in a physical device. This analysis is also useful in finding the lower cut-off frequency of higher order RGWG modes on the ridge. This aspect should be considered when engineering impedance perturbations into the line via wider ridge sections. If the perturbed sections are too wide then the onset of higher order modes may cause interference and reduced transmission at the upper range of the desired operational band.



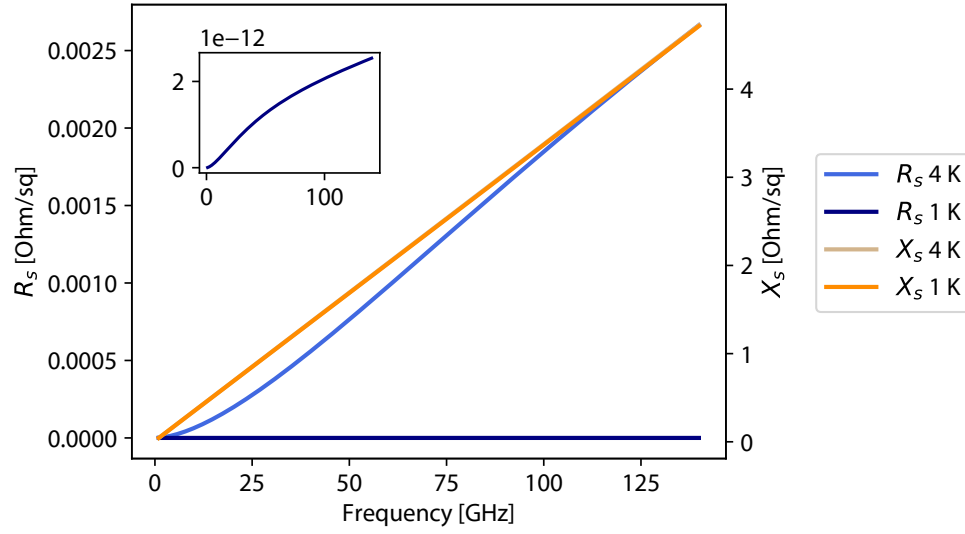


Figure 5.5: Surface impedance components of a 30nm NbTiN film with a typical normal state conductivity  $\sigma_n = 0.55 \times 10^6$  S m at 4 and 1 K. The inset shows the surface resistance at 1 K, which varies on a much smaller scale. The reactance curves at both temperatures are near identical showing that the reactance does not vary with temperature on this scale unlike the surface resistance. The common calculation parameters were identical to those used to produce Fig. 5.4.

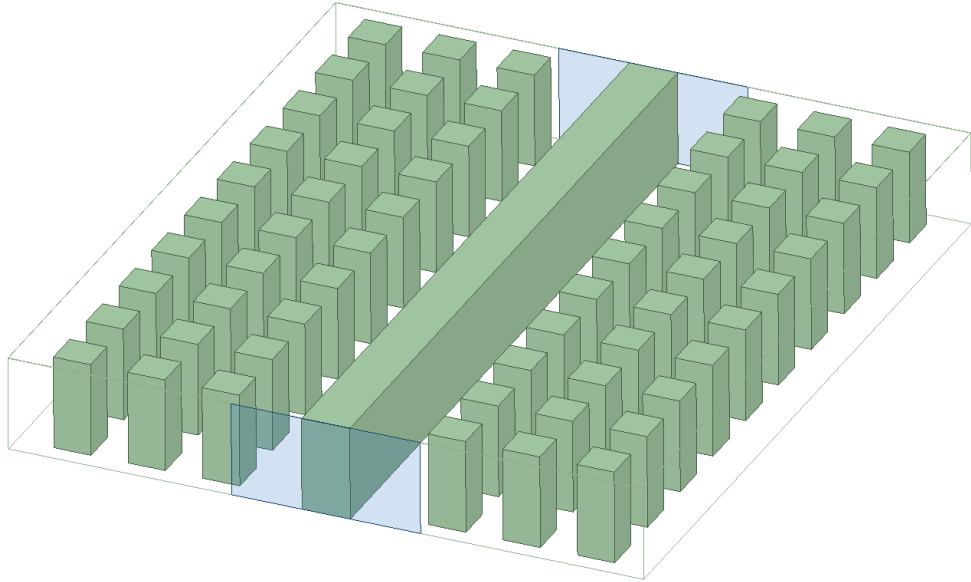


Figure 5.6: A model of a 10 mm long RGWG in HFSS used for a driven modal analysis with frequency dependent surface impedance boundaries. The light blue regions show the defined waveports of the structure. PEC boundaries are automatically applied to all outer surfaces. It was found that the impedance of the RGWG mode with  $w = 500$   $\mu\text{m}$  was approximately  $6 \Omega$ .

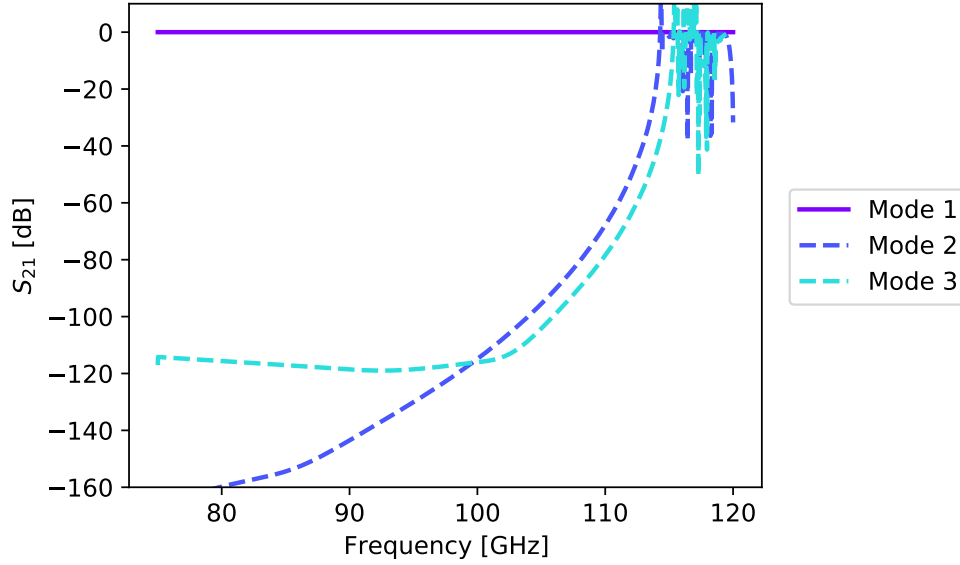


Figure 5.7: The transmission coefficient of the first 3 propagating modes in a simulation of the model in Fig. 5.6 with the surface impedance of a superconducting 30 nm NbTiN film from Fig. 5.5 applied to all inner surfaces. Mode 1 (solid line) is the TEM RGWG mode of interest while the other two modes (dashed lines) are the modes propagating in the groove and nail regions.

### 5.2.2 Kinetic Inductance Participation

A thin superconducting coating enhances the low current kinetic inductance and sets the scaling current of the line which dictates when structure nonlinearity is stimulated. Since the top of the ridge is easily accessible, the thin SC coating can be applied to this surface. A thin coating ( $t < \lambda_L$ ) on the textured surface deposited by a technique such as sputtering may cause current restrictions or discontinuities on sharp edges of the pins and ridges. These coating irregularities may give rise to undesired dissipative behaviour in regions of high current flow where the critical current may be surpassed locally. This may be alleviated by depositing a much thicker coating ( $t \gg \lambda_L$ ) on the textured surface or using a deposition technique such as atomic layer deposition, which can produce a thin conformal coating on all edges.

For this work, NbTiN coatings with a critical temperature  $T_c \sim 15$  K and resistivity in the range of  $200 \mu\Omega \text{ cm}$  are considered. This coating would allow

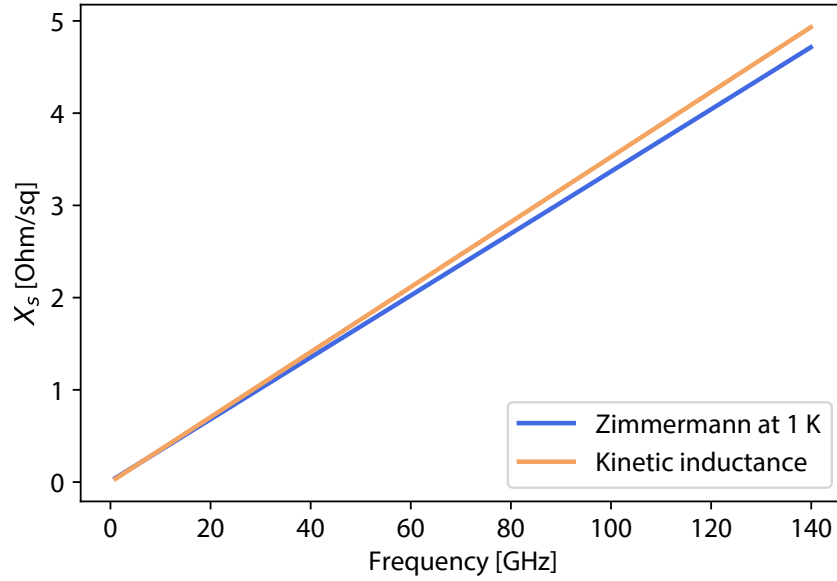


Figure 5.8: The surface reactance of 30 nm NbTiN film found via the Zimmermann conductivity from Fig. 5.5 against the surface reactance calculated using the kinetic inductance Eq. 2.34 with  $\lambda_L = 365$  nm.

paramp operation at  $\sim 1 - 4$  K with gain and noise figures comparable to equivalent transistor-based amplifiers [20]. At 1 K dissipation should be low due to the  $\exp(-T_c/T)$  scaling of the SC surface resistance [57].

The low current kinetic inductance,  $L_{k0}$ , introduced via the SC coating scales with the geometry and material of the film. The total kinetic inductance scales non-linearly with current as shown by Eq. ?? (see Section 2.3.2 for more details). For parametric processes to be explored it is first necessary to estimate the values of the low current KI and scaling current. The value of  $L_{k0}$  per square can be estimated using Eq. 4.3. This kinetic inductance can be used to calculate the surface reactance via  $X_s = \omega L_{k0}$ , which can be compared directly with the surface impedance calculated using the Zimmermann conductivity which does not vary strongly with temperature when  $T \ll T_c$ . A comparison between the two surface reactances is shown in Fig. 5.8, which shows that these agree to within a few percent.

To determine the extent to which the KI non-linearity dominates over the total inductance the KI fraction can be calculated using,  $\alpha = L_k/(L_g + L_k)$ , where  $L_g = \mu_0 h$  is the geometric inductance for a RGWG assuming it acts as a parallel plate transmission line separated by  $h$ . The scaling of  $\alpha$  against separation  $h$  at different film thicknesses  $t$  is shown in Figure 5.9. The kinetic inductance participation fraction is maximised for small  $h$  and  $t < \lambda_L$ , since  $L_g$  is reduced and  $L_k$  is maximised, respectively. However, a compromise must be made for fabrication purposes as outlined at the beginning of this chapter. A gap any smaller than  $5 \mu\text{m}$  becomes a challenge to maintain over multiple centimeters due to the necessary smoothness and parallelism of the RGWG surfaces. A short between the ridge and the lid would significantly impact structure transmission. The minimum film thickness requires consideration of the surface roughness of the RGWG and the ability to reliably grow the appropriate film, while also considering the critical current of the film.

### 5.2.3 Scaling Current Estimate

The scaling current is sensitive to a number of factors [118] including the substrate roughness and composition, film geometry, deposition conditions and operating temperature which means it can vary over orders of magnitude for a given SC material. Analytic solutions of the scaling current usually only set the upper bound for this value and have already been discussed in Section 4.2.2. The scaling current, which is of the order of the critical current,  $I_c$ , takes on different solutions based on the current distribution on the SC trace. For a thin film of thickness  $t \ll \lambda_L$  and width  $w \ll \lambda_\perp$ , where  $\lambda_\perp = \lambda_L^2/t$  is the perpendicular penetration depth, the current density can be assumed to be uniform across the film [133]. This low temperature scaling current can be estimated by Eq. 4.6 or more generally using Eq. 4.7. However, in the case where the trace is wider than the perpendicular penetration depth  $w \gg \lambda_\perp$ , the current distribution becomes

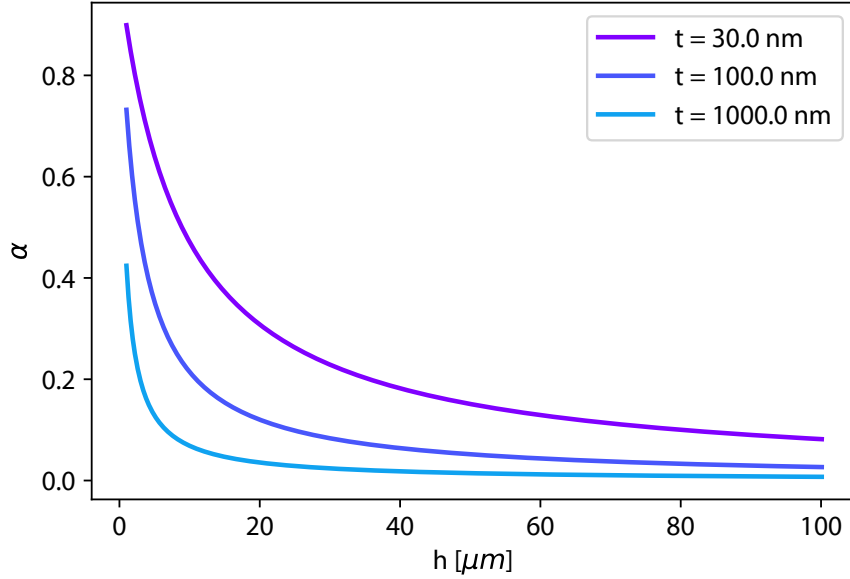


Figure 5.9: The kinetic inductance fraction scaling with the size of gap,  $h$ , at different film thickness. The thin film coating is present on both the top and bottom surfaces meaning that the kinetic inductance of both of these is included in the calculation. At the design values of  $t = 30$  nm and  $h = 5$  μm,  $\alpha_k \approx 0.64$ .

non-uniform and accumulates at the edges of the film [118]. In this work, the traces are of order 100 μm which means solutions of the wide film critical current should be explored. In this case the critical current is given by Eq. 4.9, which is shown in Fig. 5.10. This figure shows that for a 500 μm ridge the critical current at 1 K is  $\sim 400$  mA. It will be shown in Section 5.3.3 that the necessary AC current needed to stimulate significant parametric gain is  $\sim 10$  % of the scaling current. This means that around 40 mA of induced AC current would be required. The relationship between AC current and input power (in watts),  $P_{in}$ , given by

$$I^2 = \frac{|S_{21}|^2 P_{in}}{Z_0}, \quad (5.1)$$

where  $S_{21}$  is the transmission coefficient of the structure and  $Z_0$  is the impedance. This allows for the input power at a certain current to be estimated. For the 500 μm RGWG, which was simulated to have an impedance of  $\sim 6$  Ω, and assuming

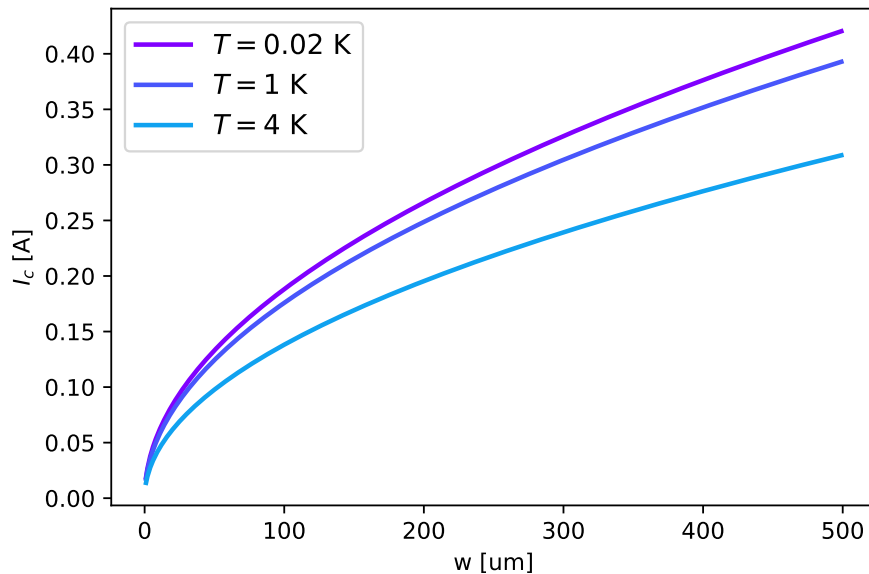


Figure 5.10: The critical current of a 30 nm thick NbTiN strip as a function of width,  $w$ , at 3 selected temperatures. Assumptions include pristine film edges and a width  $w > \lambda_{\perp}$ . The values used for this calculation were  $\lambda_L(0) = 365$  nm,  $\xi(0) = 9$  nm, and  $T_c = 15$  K. Three possible operating temperatures are shown with 1 K being a likely candidate for W band operation due the significantly better dissipation than at 4 K (see Fig. 5.5) and more accessible cooling capability than 20 mK.

that transmission is at unity, the necessary input power needed to achieve a 40 mA current is around 10 dBm. Such a drive power can be achieved using the VNA that was presented in Chapter 3. However, a 10 dBm drive power risks introducing a significant head load on the 1 K adsorption cooler if the thermal management is not adequate or there are resistive elements near the device. In addition, such an input power surpasses the rated input power of most cryogenic transistor based LNAs, which poses another issue in real world applications. However, as discussed previously it is challenging to achieve such a high quality film even in small devices. Therefore, for a large device the critical current would be much lower, possibly being lower by a factor of 10. Depending on the substrate used for the device, whether this is insulator-coated, machined then polished metal or micromachined silicon, growing an epitaxial film is very

challenging. Polycrystalline films are nearly always the likeliest result with edges that are far from being uniform. With this argument in mind, a 50 mA scaling current is selected for the proceeding analyses of the RGWG TWPA, assuming that such a scaling current would be realised on a metal machined structure.

This scaling current is likely to be larger of a film on a highly ordered silicon substrate that has been micro-machined. For such a case, alternative solutions to lower the drive power should be explored. One such solution could be to reduce the width of the ridge to  $\sim 50 \mu\text{m}$ , which would reduce the critical current to around 100 mA and increase the impedance to  $\sim 50 \Omega$ . This would mean that  $-10 \text{ dBm}$  of pump power would be needed to reach the condition for peak parametric gain. Another solution would involve a more significant redesign via a slow wave structure. Two such structures are suggested in Section 5.4 as a future direction for the development of these devices. Such structures would provide a significant reduction in the critical current magnitude and an increase in the gain achieved per length of TWPA.

In any chosen design, the most reliable method to extract the scaling current is via a direct measurement. This can be carried out via a kinetic inductance induced frequency shift measurement of a resonant cavity as function of ac or dc current. Such a method was employed for the Ka band RGWG resonator, which was discussed in Section 4.4.2.

### 5.3 Ridge Gap Waveguide TWPA

RGWG may be used as a foundation for a travelling wave parametric amplifier that can be scaled to frequencies over 100 GHz and possess low loss due to the hollow volume through which the signal propagates. A four wave mixing (4WM) variant of such a structure is most straightforward to realise since the pump tone propagates at a similar frequency to the signal and does not require a DC bias in order to operate. Therefore, a 4WM TWPA is selected as the theoretical testing

ground for the demonstration of the viability of a RGWG TWPA.

As a reminder of the operational principles, in the presence of a strong pump tone and weak signal a four photon mixing process can take place [75], referred to as degenerate 4WM. These tones are related by  $2\omega_p = \omega_s + \omega_i$ , where  $\omega_{p,s,i}$  are the frequencies of the pump, signal and idler tones, respectively.

For sufficient parametric gain the RGWG needs to be extended into an electrically long structure spanning hundreds of wavelengths. In addition, the phase relationship between the pump, signal and idler tones should be considered such that the linear dispersion difference is  $\Delta k_L = 2k_p - k_s - k_i = 0$ , where  $k_{p,s,i}$  are the propagation constants of the involved tones. The nonlinear SC line introduces a power dependent phase shift, which must be compensated for by introducing anomalous dispersion [13, 14, 61, 134] in order to achieve exponentially scaling gain with propagation length over a wide bandwidth. If this condition is not met, the gain will scale quadratically. Anomalous dispersion can be introduced into the transmission line in many ways, this is referred to as dispersion engineering.

### 5.3.1 Periodic Loading Structure

Various dispersion engineering schemes have been employed in TWPAs in literature such as periodic loading patterns [13, 61], periodic parallel resonators [60], and more complex structures like quasi-fractal interdigitated capacitors (IDC) [135] or fishbone IDC [95, 65, 18]. One of the simplest dispersion engineering schemes [61] involves the perturbation of the transmission line every  $\lambda_{per}/2$  such that stopbands are created at integer values of frequency  $f_{per}$  near which anomalous dispersion is introduced. By positioning the pump tone near one of these dispersion features, the nonlinear phase slippage caused by the pump self-modulation may be partially or even fully cancelled out.

One method to introduce anomalous dispersion in RGWG is by employing periodic widening of the ridge as shown in Fig. 5.11. The impedance of the



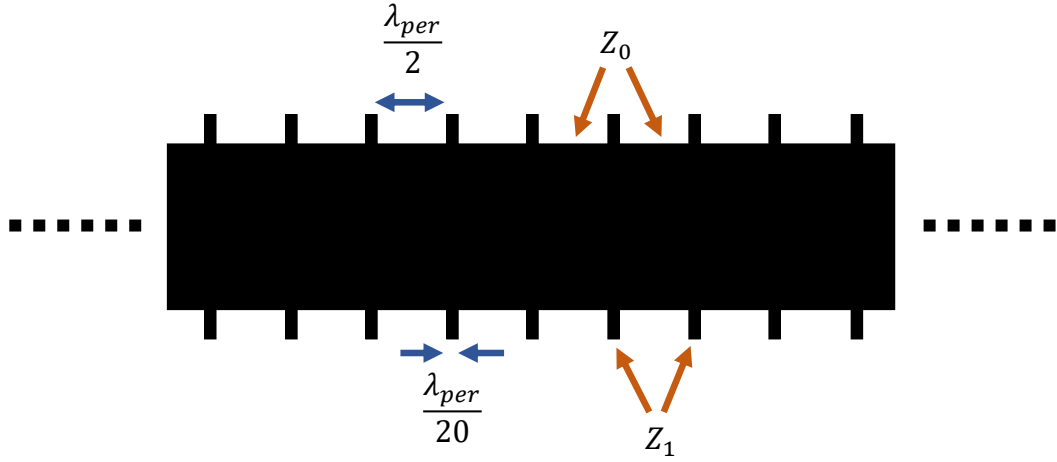


Figure 5.11: A schematic of a section of the ridge in a dispersion engineered RGWG using design principle from [61]. The physical width of the main line is  $500\text{ }\mu\text{m}$ , while the repeating perturbations are  $650\text{ }\mu\text{m}$  wide, and  $\lambda_{per}/20 = 25\text{ }\mu\text{m}$  long. The separation of loading midpoints is  $\lambda_{per}/2 = 250\text{ }\mu\text{m}$ .

loaded and unloaded sections is estimated using  $Z_0 = \sqrt{(L_g + gL_{k0})/C}$ , where  $C$  is the section capacitance and  $g = 2$  is a geometric factor accounting for the SC coating of both parallel surfaces of the RGWG. For comparison, these impedances were also extracted from the waveports of from the HFSS models of the unperturbed and perturbed sections, which showed an agreement within  $\sim 5\%$  of the analytic solutions. Therefore, the analytic solutions are sufficiently accurate for the proceeding analysis in addition to being easily calculated without the need for full 3D EM simulations.

The impedance of the perturbations was  $\sim 20\%$  lower than the main line, which introduced a weak dispersion feature near the  $f_{per}$  that becomes stronger as the number of repeating units is increased. As a result, a travelling wave structure spanning  $450\lambda_{per}$  was investigated as a compromise between total device length and total signal gain. Such an electrically long structure can be simulated directly in HFSS to show the stopband structure, however, this is extremely

computationally taxing. In addition, HFSS is unable to take into account the current dependence of the kinetic inductance nor does it support the harmonic balance simulation method needed to show the parametric processes taking place. HFSS is most useful for short sections of RGWG to understand the operational bandwidth, kinetic inductance scaling and structure impedance. For the analysis of the electrically long structure an alternative approach should be used. It was already shown that Keysight's ADS can be used to simulate resonant paramps in Section 4.2.3 and here this is extended to travelling wave paramps. It will be shown that ADS can be used to extract the non-linear S-parameters and the predicted parametric gain for TWPAs.

### 5.3.2 Nonlinear S-parameters

An equivalent circuit model of the nonlinear RGWG is described in Fig. 5.12. Similarly to the Ka band RGWG RPA in Section 4.2.3 the circuit takes into account the nonlinear inductance via a general symbolically defined device (SDD) component, which requires a voltage definition in the form  $V = -\frac{d}{dt}L_k(I)I$ . Resulting in the following voltage relationship for each nonlinear element

$$V = -L_{k0} \frac{d}{dt} \left( I + \frac{I^3}{I_*^2} \right). \quad (5.2)$$

Unlike the Ka band RPA which made use of a single nonlinear element, these W band RGWG equivalent circuit elements were used to form repeating unit cells that could be connected in series to make up a long transmission line. However, taking the lumped element values and scaling them to the appropriate length of transmission line sections meant that their cut-off frequency,  $\omega_c = 2/\sqrt{LC}$ , was approaching 100 GHz, which overlapped with the frequency of operation of the TWPA. This cut-off proximity can modify the impedance of the lumped-element transmission line even though such an effect would not be present in the full transmission line model. This limitation can be resolved by splitting the lumped

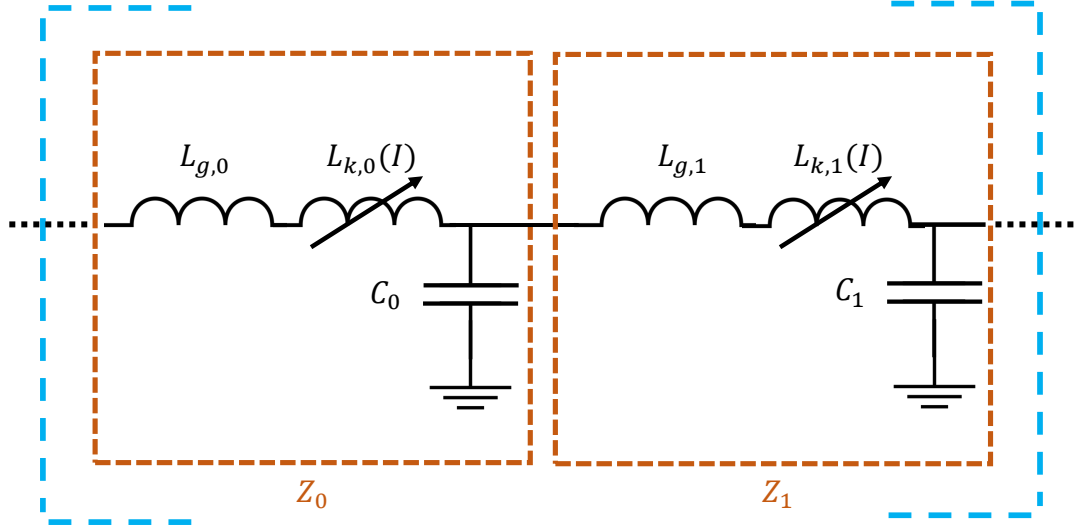


Figure 5.12: An equivalent circuit model of  $\lambda_{\text{per}}/2$  cell showing an unperturbed and perturbed section of the RGWG. The impedances of the main line and perturbed sections were chosen to be  $Z_0 \sim 6 \Omega$  and  $Z_1 \sim 4.75 \Omega$ , respectively. The kinetic inductance contribution of two surfaces coated with 30 nm of NbTiN ( $\lambda_L \sim 365 \text{ nm}$ ) was included in the impedance calculation. A conductor spacing of  $h = 5 \mu\text{m}$  was chosen, which resulted in  $\alpha \sim 60 \%$ . This impedance were confirmed in HFSS simulations. The corresponding equivalent circuit parameters were  $L_{m,0} \sim 12.5 \text{ nH m}^{-1}$ ,  $L_{g,0} \sim 9.5 \text{ nH m}^{-1}$ ,  $L_{k,0} \sim 22 \text{ nH m}^{-1}$ ,  $L_{k,1} \sim 17 \text{ nH m}^{-1}$ ,  $C_0 \sim 0.9 \text{ nF m}^{-1}$ ,  $C_1 \sim 1.1 \text{ nF m}^{-1}$ . The scaling current was chosen to be 50 mA as discussed in Section 5.2.3.

elements into a longer LC ladder with the same total inductance and capacitance, which pushed this artificial cut-off to a higher frequency. Usually, splitting the inductors and capacitors into 10 distributing components each in the LC ladder was sufficient to alleviate this issue. However, a single  $\lambda_{\text{per}}/2$  cell could contain upwards of 20 inductors and 20 capacitors, which would mean that the total number of on-screen components would quickly rise to a level where mistakes are difficult to spot and investigating different length circuits becomes cumbersome. This challenge can be overcome by nesting these unit cells within subcircuits. For example, an LC ladder of a single unit cell can be placed in a subcircuit with its own input and output which allows it to be nested into a further subcircuit with 10 unit cells and so on. In this way a long transmission line with a periodic

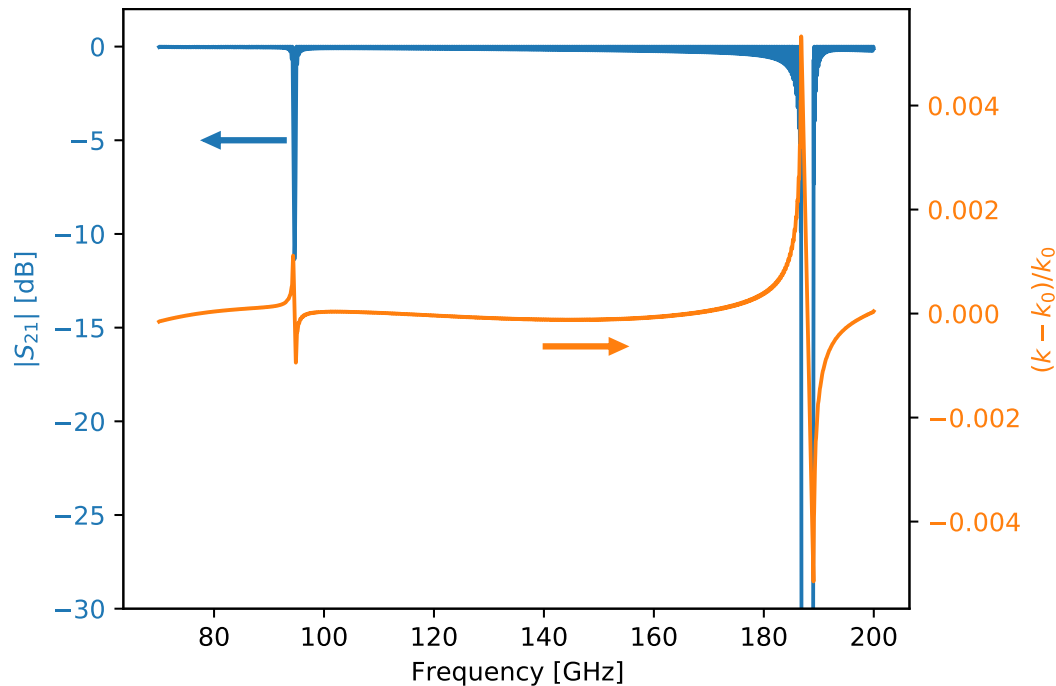


Figure 5.13: Transmission coefficient and effective dispersion from a simulation of 900  $\lambda/2$  dispersion engineered RGWG cells in ADS, corresponding to a physical propagation length of 25 cm. The first 2 stopbands at  $f_{per} \sim 95$  GHz and  $2f_{per} \sim 190$  GHz are shown. The second stopband would be outside of the single-mode bandwidth of the RGWG but appears in the lumped element representation since these transmission line effects are not accounted for in the equivalent circuit model. The unperturbed dispersion,  $k_0$ , was found by fitting a second order polynomial to the perturbed dispersion,  $k$ .

structure could be represented by few nested subcircuit components. This method allowed for a transmission line containing a total of  $N = 900$  cells each of length  $\lambda_{per}/2$  to be constructed. The input and output ports were set to be perfectly impedance matched to the transmission line by setting the port impedance to  $Z_0 = \sqrt{(L_{m,0} + L_{k0})/C_0}$ .

A large signal S-parameter (LSSP) simulation within ADS was used to generate the nonlinear S-parameters and dispersion properties as shown in Fig. 5.13 (see Appendix B.1 for further details). The dispersion of the perturbed transmission line was calculated via  $k = -\text{unwrap}[\arg(S_{21})]/L$ , where  $L$  is the device length. The relative strength of the dispersion introduced by the perturbations

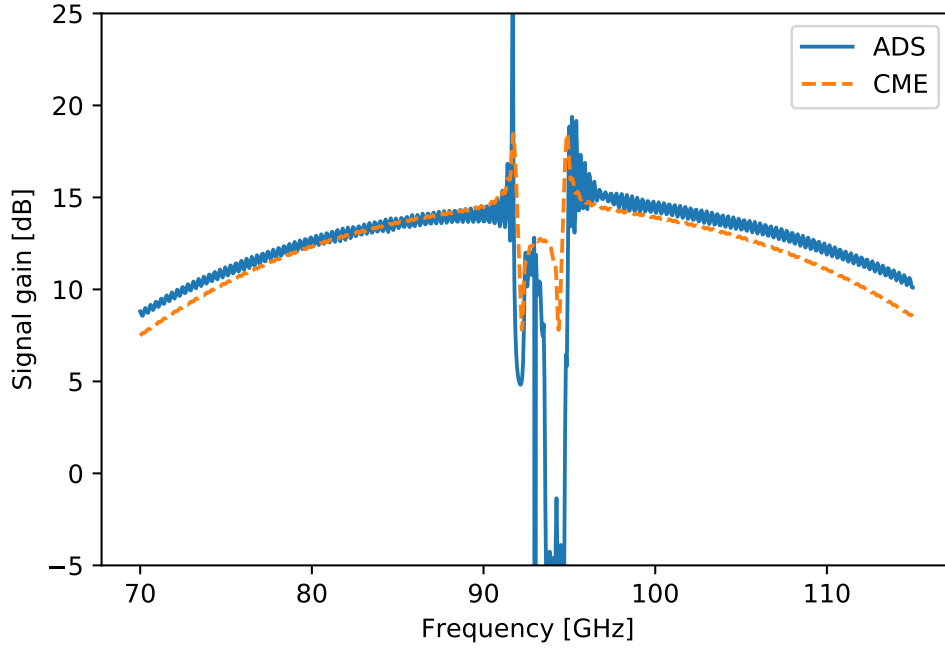


Figure 5.14: The simulated signal gain using the ADS method (solid) and solutions of the CMEs (dashed). The pump power in ADS was set to -9 dBm and was positioned at 93 GHz, while the signal was at -80 dBm to avoid significant depletion of the pump tone as a result of the mixing. The CME solution [92] uses the dispersion properties extracted from the 900 cell LSSP simulation to calculate the phase mismatch between the 3 involved tones. Here, the calculated CME gain that fits the ADS gain corresponds to a  $I/I_* \sim 0.075$  compared to  $I/I_* \sim 0.09$  in ADS.

can be visualised via the effective dispersion  $k_{\text{eff}} = (k - k_0)/k_0$ , which can be extracted by comparing this to the the dispersion of a unperturbed transmission line  $k_0$  with the same electrical length. Alternatively, since the dispersion of a TEM line should be linear,  $k_0$  could be estimated via a linear fitting over the perturbed data. This effective dispersion is shown in Fig. 5.13. It should be noted that the perturbed dispersion,  $k$ , is used for calculations of the phase matching between the 3 involved tones and the effective dispersion is used only as a visual aid for the relative strength of the anomalous dispersion.

### 5.3.3 TWPA gain

Similarly to the gain analysis in Section 4.2.3, the harmonic balance simulation mode was employed to analyse the generated mixing products due to the signal and pump at the input of device. The order of harmonics for each input tone was set to 10 in the harmonic balance simulation properties as a trade-off between simulation speed and simulation accuracy. The power of the signal was tracked by selecting the appropriate harmonic index at the signal frequency. The signal gain was evaluated by comparing the power in against the power out as found using a labelled probe on the end of the device. The input power of the pump was initially set to -20 dBm with the signal set to -80 dBm to ensure the pump tone did not significantly deplete as a result of the mixing. See Appendix B.1 for further details.

As discussed in Section 2.4.4, maximum signal gain is achieved when the 4WM total phase mismatch,  $\Delta k$ , is minimised [13, 92, 42]. This condition is given by,

$$\Delta k = \Delta k_L - \Delta \theta_{\text{NL}}, \quad (5.3)$$

with

$$\begin{aligned} \Delta k_L &= 2k_p - k_s - k_i, \\ \Delta \theta_{\text{NL}} &= \frac{k_p I_p^2}{2\alpha I_*^2}, \end{aligned}$$

where  $\Delta k_L$  is the linear phase mismatch,  $\Delta \theta_{\text{NL}}$  is the nonlinear phase shift, and  $I_p$  is the AC current due to the pump tone. The  $\Delta \theta_{\text{NL}}$  term is introduced due to the SPM and XPM, which is a phase shift that arises due to the strong pump modulating the phase velocity within the nonlinear transmission line (see Section 2.4.4). Eq. 5.3 shows that  $\Delta k$  is pump current dependent, which means that the optimal pump tone position near the dispersion feature is not the same for each drive power. In the ADS simulation this optimal point is found by initially

positioning the pump 1-2 GHz below the  $\sim 95$  GHz dispersion feature, which is shown in Fig. 5.13, after which the pump tone is moved closer to the dispersion feature while the power is increased incrementally until the signal gain reaches a maximum across the whole band of interest. It was found that for a scaling current of 50 mA the maximum gain was achieved for a pump power of -9 dBm, which corresponded to  $\sim 4.5$  mA of AC current and  $I/I_* \approx 0.09$ . Fig. 5.14 shows the simulated gain of the 25 cm RGWG TWPA with more than 10 dB of signal gain over the 75 to 110 GHz band. This gain figure could be improved by a number of techniques such as more careful engineering of the dispersion transmission line, by employing a slow-wave structure to extend the electrical length or by simply extending the length of the already presented structure. The slow-wave structure option is discussed in Section 5.4 as a prospect for future work.

The simulated gain in Fig. 5.14 can be compared to the gain extracted from analytic solutions of the coupled mode equations (CME) that describe the amplitudes of the propagating waves within the TWPA (see Section 2.4.4). The CME solutions are often used as a prediction of the signal gain profile in many published works on TWPAs and therefore could be used as a partial validation of the simulated gain curve from ADS. Here, the solutions to the CMEs made use of the dispersion data of the LSSP simulation rather than an analytical expression of the transmission line dispersion. This ensured that both gain calculation methods made use of identical dispersion properties which allowed for a more direct comparison between the two gain methods. The CME gain shown in Fig. 5.14 is generally in agreement with the gain profile generated by ADS. The main differences are: the gain at the upper and lower parts of the frequency range; the drop in gain near the dispersion feature; and the  $I/I_*$  ratio that generate the gain profiles. The required  $I/I_*$  ratio in the CME fitting ( $\sim 0.075$ ) is smaller than that found through ADS ( $\sim 0.09$ ). This is likely due to the low order CMEs not accounting for power flow towards the generation of higher order harmonics,

meaning that the required pump current to achieve the equivalent gain level is smaller. The CME solutions used only take into account the pump, signal and idler tones but do not consider higher order harmonics of these tones. The general shape of the CME gain changes as higher order harmonics are included, which could explain the difference with the ADS gain. These higher order CME solutions are more labour intensive to solve but have been shown [92, 94] to provide a more accurate gain description. However, even with the higher order harmonics taken into account another limitation of the CME method is that it does not take into account for the drop in transmission within the stopband that is generated by the dispersion engineering. This stopband can reduce the signal gain when the signal or idler tones fall into it, meaning that phase matching is lost in those instances. In comparison, this behaviour is fully captured by the ADS analysis method since the whole microwave network is simulated. One last difference is the drop in the gain near the dispersion feature. This difference is most likely are result of the differences in phase matching between the two methods. The expression for phase matching shown in Eq. 5.3 does not include contributions from higher order harmonics or 3WM mixing processes (see [65] for full phase matching equation) which could be a cause of the discrepancy between the two methods.

Plotting the phase mismatch of Eq. 5.3 can give quantitative confirmation whether the dispersion engineered transmission line provides sufficient anomalous dispersion to compensate for the self-phase modulation of the pump tone such that  $\Delta k \approx 0$ , which is the condition for exponentially scaling of the gain with TWPA length. Fig. 5.15 shows a plot of the linear phase mismatch  $\Delta k_L$  that includes the anomalous dispersion, and the pump self-modulation. The condition for phase matching is satisfied where the sum of these two contributions reaches zero. Ideally, the total phase mismatch should be as close to zero as possible over the whole band for maximum gain over the whole band of interest. It can be seen in Fig. 5.15 that the linear phase mismatch achieved through the



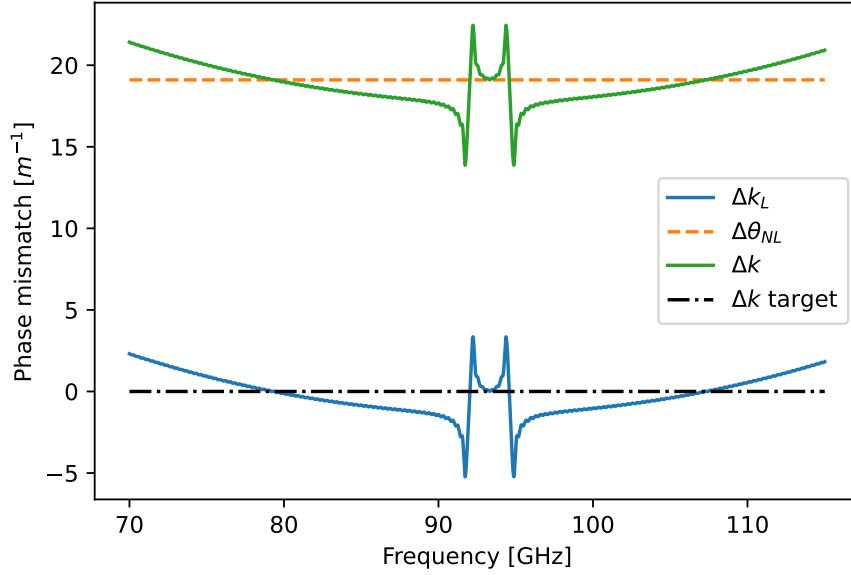


Figure 5.15: A plot showing the effect of dispersion engineering on the total phase mismatch  $\Delta k$ . The linear phase mismatch,  $\Delta k_L$ , represents the anomalous dispersion introduced via dispersion engineering and is calculated using the simulated dispersion of the  $450\lambda$  dispersion engineered RGWG. The pump is at the same frequency and power as in Fig. 5.14.  $\Delta\theta_{NL}$  shows the phase shift that needs to be compensated by the anomalous dispersion in order to achieve total phase matching,  $\Delta k \approx 0$  and exponentially scaling gain.

selected dispersion engineering scheme is not sufficient to compensate for the phase slippage due to the pump self-modulation. This can be compared to work by Klimovich [136] where such a plot is also produced (see Fig 2.9 in [136]) showing full compensation of the nonlinear phase shift. The uncompensated phase mismatch,  $\Delta k \neq 0$ , shows that more signal gain can be extracted from the existing TWPA structure if a stronger dispersion feature is employed. As seen in Fig. 5.13 the  $3\lambda/2$  dispersion feature at  $2f_{per}$  is significantly stronger than the one at  $f_{per}$ . Therefore, if the loading spacing shown in Fig. 5.11 is reduced by a factor of 2 such that the  $3\lambda/2$  dispersion feature lands within the W band, then this could be used to achieve  $\Delta k \approx 0$ , which could result in significantly larger gain figure of over 20 dB. Alternatively, the  $\lambda/2$  dispersion feature could be made stronger by increasing the impedance difference between the feed line

and perturbations, which could come at a cost of additional gain ripple due to stronger reflections. Numerous other considerations could be taken into account to increase the gain for a given length of such TWPAs (outlined in the Section 5.4) which could pave the way for RGWG TWPAs with much more practical device lengths that produce gain figures of over 20 dB.

## 5.4 Summary and Outlook

### 5.4.1 Summary

This work proposed a transmission line for high frequency KI-TWPAs in the form of RGWG. This structure is scaleable to frequencies of a few 100 GHz with feature sizes in the hundreds of  $\mu\text{m}$  range, meaning that it can be fabricated with high speed metal milling techniques or silicon micromachining and coated in a superconducting film. A NbTiN coating was chosen due to its high kinetic inductance and high critical temperature allowing for a highly nonlinear structure and operation at 1 K. It was shown via superconducting HFSS simulations that the RGWG transmission line can have over an octave of bandwidth for single mode quasi-TEM transmission, which would ultimately be limited by external factors such as the transition to the chosen feed transmission line. Dispersion engineering this RGWG with periodic perturbations to introduce anomalous dispersion showed that 4WM signal gain can be achieved over the whole of W band which is fully covered by this single-mode bandwidth of the TW-RGWG. The nonlinear S-parameters as well as the gain profile of this structure were simulated in Keysight's ADS via a equivalent lumped element representation of the TW RGWG. This simulation method which agreed with the first order CME solutions showed that parametric signal gain of over 10 dB was achieved over a 75–110 GHz range in TWPA that is 25 cm in length. It was discussed that higher gain figures could be achieved if a stronger dispersion feature was employed that fully compensated for

pump self-modulation such that the total phase mismatching condition,  $\Delta k \approx 0$ , would be satisfied.

### 5.4.2 First Prototype

The device described in this chapter shows promising results that present exciting challenges in the fabrication and measurement of such high frequency KI TWPAs. However, there are a number of challenges that are left to be addressed in the design stage that include: the design of low loss transitions to the input and output feedlines; the use of even smaller conductor spacing structure to increase the nonlinear kinetic inductance contribution; as well as exploration of slow wave structures to increase the gain per length which would allow a reduction of the overall device length and could significantly reduce the complexity of fabrication.

A low loss transition should be engineered between W band rectangular waveguide and the RGWG. In terms of fabrication complexity, removing the restriction of the  $a$  and  $b$  dimensions shown in Fig. 5.1 to match that of the feeding waveguide would allow more freedom with dimensions of the pin surface. Shorter pins would offer a bandwidth and fabrication advantage. The operational bandwidth of the current design (75 to 110 GHz) is at the top side of the bandwidth of the bed of nails (20 to 115 GHz), meaning that the bed of nails range of 20 to 75 GHz is effectively unused. Shifting the middle bed of nails bandwidth to the middle of W-band would mean that the nails could be shorter. These shorter nails would provide a fabrication advantage when using silicon micromachining since less silicon would need to be removed from the starting silicon wafer. Finally, a transition between WG and RGWG employing a Klopfenstein taper [115] could be engineered to step the impedance from  $500 \Omega$  of the rectangular waveguide (average over the band of rectangular waveguide) to the  $\sim 6 \Omega$  of the RGWG.

The nonlinear kinetic inductance contribution to the RGWG could be increased by setting the conductor spacing to a smaller value than  $h = 5 \mu\text{m}$ . The

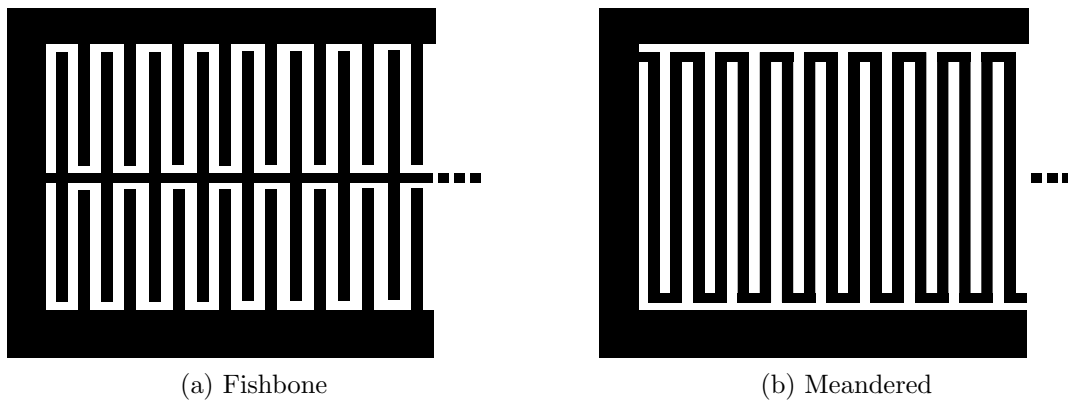


Figure 5.16: Examples of patterned traces that would reduce the phase velocity of a propagating tone within a transmission line. Metallised parts are shown in black. These patterns would be etched into the thin superconducting coating on a flat silicon chip of the silicon micromachined variant of the RGWG TWPA. Milling this structure in a metal machined variant would not achieve the desired effect on the reduced phase velocity due to the continuity of the superconducting coating. (a): a fishbone pattern that has increased capacitance due to the proximity of the trace fingers to those of the ground plane. (b): a meandered trace that would increase the inductance via the self inductance of the trace.

current value of  $h$  could already pose a challenge for devices in the tens of cm range but if a shorter device could be designed then a conductor spacing of  $h = 1\text{ }\mu\text{m}$  could be used to increase the kinetic inductance fraction from 60 % to over 90 %, which would increase the gain per length and could aid in significantly reducing the necessary TWPA length.

### 5.4.3 Future Work

Slow wave structures are a method to reduce the phase velocity of the travelling wave by increasing the capacitance or inductance of the transmission line. Such an approach could be realised in silicon micromachined RGWG by patterning the flat, untextured surface of the RGWG to increase the overall reactance. Two examples of such structures can be seen in Fig. 5.16 which shows a fishbone structure for increased capacitance and meandered trace for increased inductance. The fishbone pattern is preferred since it would reduce the phase velocity without affecting the nonlinear KI fraction, while the meander would lower this fraction due

its increased geometric inductance contribution. The patterning of the superconducting coating could be done on the flat lid only, for the reason of reducing the overall number of processing steps for the part containing the pin surface and the ridge. A further advantage of the fishbone structure is that the increased capacitance would reduce the characteristic impedance of the line and would allow for an even larger AC current to be induced for a given drive power. Additionally, the patterned trace through which the AC current flows is reduced, which means that the critical current would be reduced. As discussed in Section 5.2.3 a high quality film of a large width may have a scaling current that could present a challenge when providing the necessary AC drive through the pump tone without causing heating to the feeding components and the TWPA. A slow wave pattern with a trace width of  $\sim 10\text{ }\mu\text{m}$  would reduce the scaling current to the  $\sim 40\text{ mA}$  range, which would mean that  $\sim 4\text{ mA}$  of AC current would be needed to stimulate sufficient nonlinearity within the TWPA and provide parametric signal gain.

The outlined slow wave patterns shown in Fig. 5.16 could allow for dispersion engineering to be incorporated via sections with longer “bones” or longer meanders that would create steps in RGWG impedance. This change of pattern width is similar to the impedance changes achieved through steps in ridge width as shown in Fig. 5.11 with the difference being that the dispersion engineering would now be contained one physical piece of the device – the superconductor coated flat lid – which could aid with device yield and would allow the same pin surface to be used with different iterations of the dispersion engineered part. This may improve prototyping speed and could make the exploration of different dispersion engineering schemes more accessible.

The next step in the development of these RGWG TWPAs would be the testing of the outlined design ideas in a simpler device. A convenient test bed for the waveguide transitions, high KI structures, and slow wave patterning schemes could be a W band series resonator not dissimilar to the one described in Chapter 4. Such a resonator would be simpler to operate since no dispersion engineering

would be needed and would allow the measurement of critical paramp parameters such as the kinetic inductance fraction, the scaling current and the film critical temperature that could be used as input for the RGWG TWPA simulations in ADS.

# Appendix A

## Ka Band RGWG Resonator

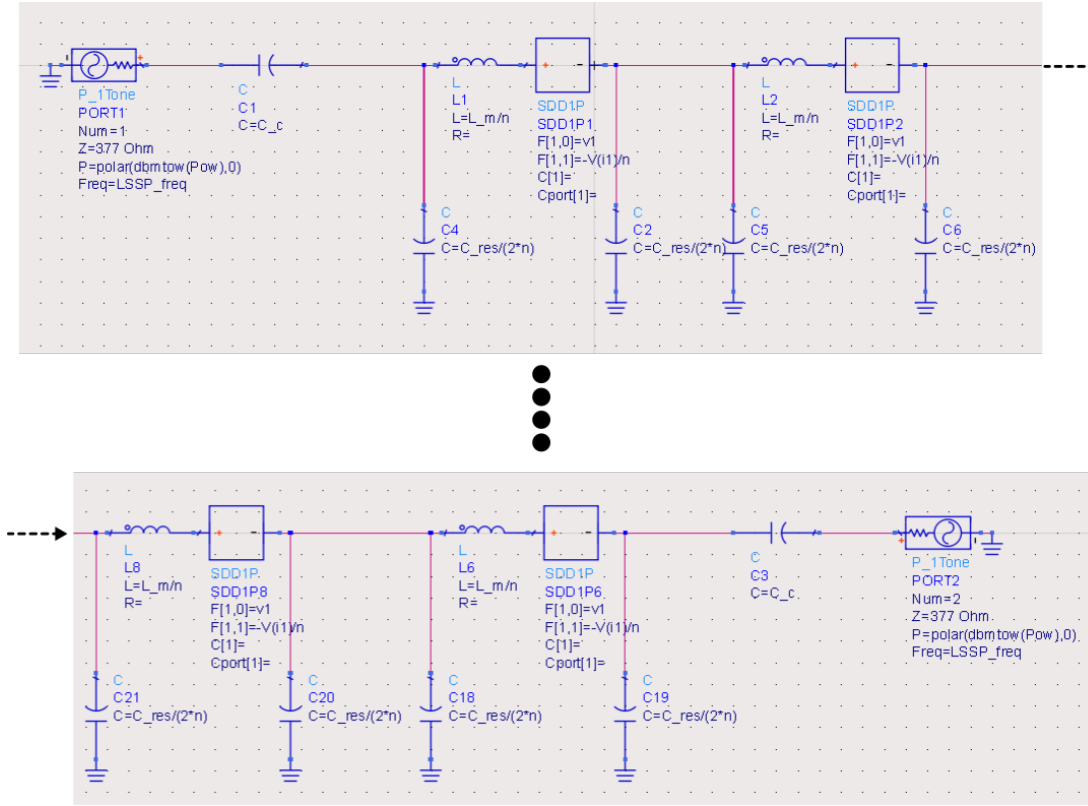
### A.1 ADS Simulation Circuits

This section aims to show details on the specific circuits used in Keysight ADS to simulate the Ka band RGWG resonator detailed in Section 4.2.3.

The full circuit used for the simulation of linear and nonlinear S-parameters is shown in Fig. A.1. The resonator is made up of 10 identical  $\pi$  LC cells. The  $\pi$  refers to the shape of the unit cell, where the cell capacitors are split into two with capacitance  $C_{\text{res}}/2n$  each. This splitting ensures that each unit cell is symmetrical and there are no differences at the input and output of the resonator. The input and output ports were the same for the S-parameter and the Large Signal S-parameter (LSSP) simulations since the power arguments were simply ignored by the S-parameter simulator, while for the Harmonic Balance (HB) simulation these were replaced by a multi-source port and a  $377\ \Omega$  termination.

The S-parameter simulation setup was carried out using the respective simulation card from the component palette, the parameters for include the start and end frequencies as well as the frequency step. The simulation setup for the LSSP simulation is shown in Fig. A.2, which was set up to sweep across the resonance profile using the LSSP frequency for a number of different input powers. This

## A: KA BAND RGWG RESONATOR

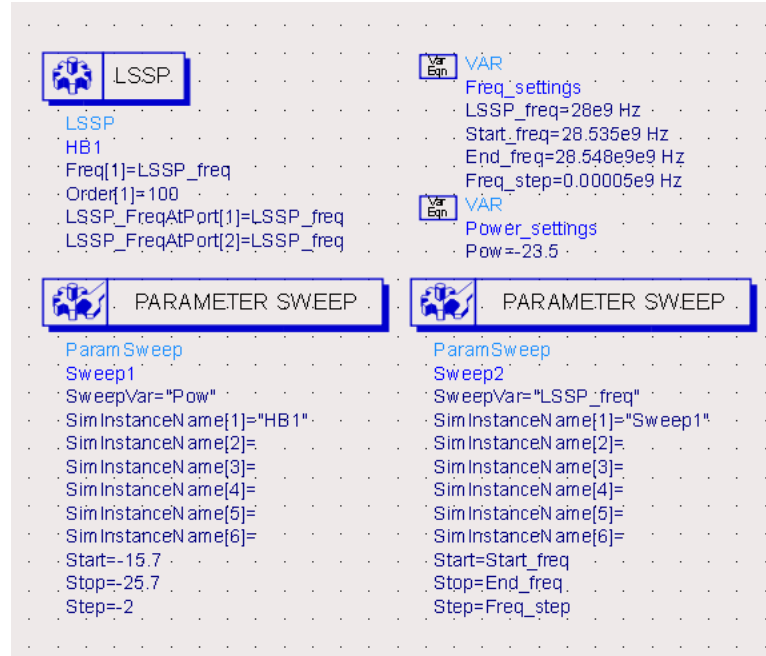


(a) A truncated set of screenshots showing the start and end of the circuit.

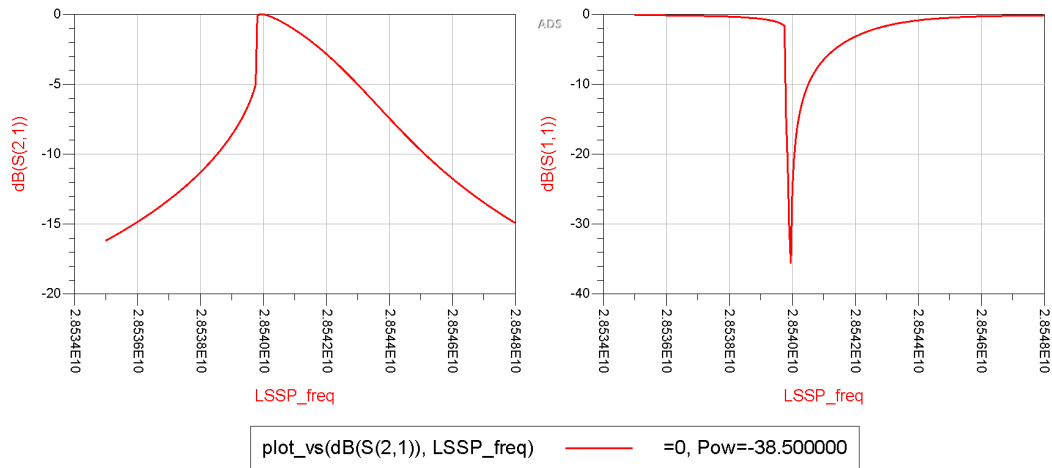
(b) The circuit parameters and equations used to calculate the lumped element values. The scaling current was set to 1.3 A as shown in Fig. 4.15.

Figure A.1: The equivalent circuits of the pin-coupled RGWG resonator used in the S-parameter, LSSP, and HB simulations. The HB simulation used a multi-tone source for input and 377 Ohm termination for the output.





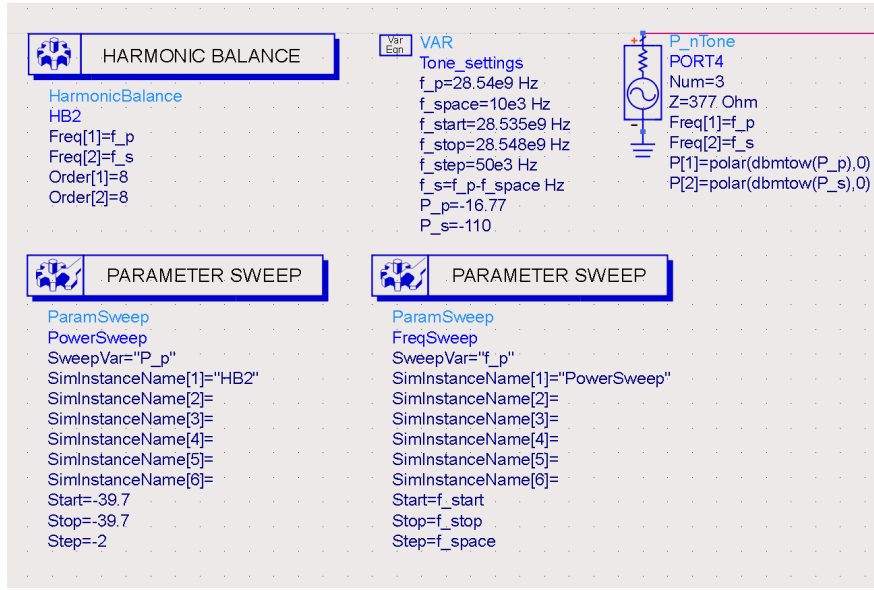
(a) Simulation setup used to sweep over the resonance profile at different input powers.



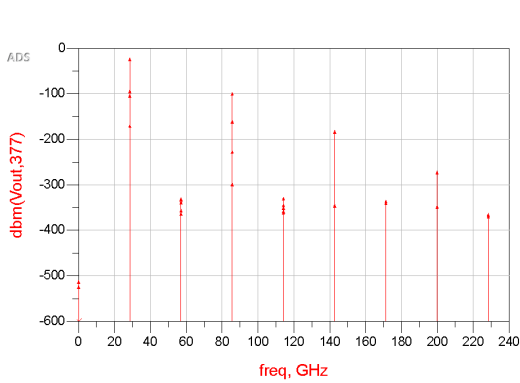
(b) Nonlinear  $S_{21}$  and  $S_{11}$  parameters at -38.5 dBm

Figure A.2: The LSSP simulation setup applied to the circuits shown in Fig. A.1 and example result screen.

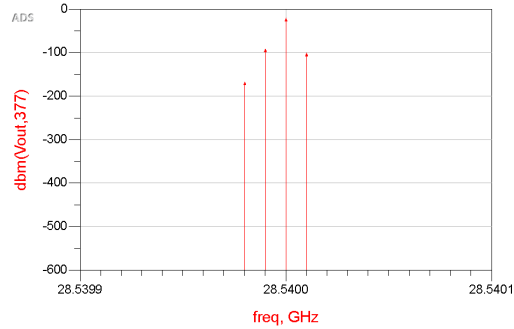
## A: KA BAND RGWG RESONATOR



(a) Simulation setup, the input tone frequency and power parameters as well as the multi-tone source component that replaces the single-tone source shown in Fig. A.1.



(b) The generated harmonic spectrum measured at the output of the resonator



(c) The harmonics that form within the resonance profile of interest showing the signal and pump in the middle as well as the two generated idlers.

Figure A.3: The HB simulation applied to the circuits shown in Fig. A.1 as well as the example output for at a single pump power and frequency.

required two separate parameters sweeps that were linked to one another. An example of the results scree of a single power LSSP sweep is shown in the lower panel of Fig. A.2. The order parameter in the LSSP simulation should be set to a value in the range of 50 to 200, where a higher order produces slightly more accurate values near the resonator bifurcation point with a slight simulation time penalty.

The HB simulation was carried using the simulation palettes shown in Fig. A.3. This HB component required parameters for the fundamental frequencies of the input tones as well as the order of harmonics to be calculate for each of these tones. In addition, any specific frequency corresponding to a harmonic of interest could be set. However, this was not needed in this simulation and did not affect the results when trialled. The frequency of the signal was set to be a function of the pump frequency with a constant offset of 10 kHz, which meant that only the pump frequency needed to be swept. Alternatively, the signal frequency could be swept instead if the pump frequency was made a function of the signal frequency. The swept variable sets the default plotting parameters in the ADS result screen. The lower panels of Fig. A.3 shows the generated harmonics at the output of the resonator specified by a terminal  $V_{out}$  set on a connecting wire right before the  $377\ \Omega$  termination.

Similarly to the LSSP simulation two parameter sweeps were needed to sweep over the resonance profile at different pump powers. Since the parametric gain is evaluated at the signal frequency only, it is needed to track the power of that output harmonic. This achieved using the  $Mix()$  function, which has a number of arguments equal to the number of fundamental frequencies set on the HB simulation setup component. The harmonic of interest can be identified by outputting a table of  $V_{out}$  in dBm as well as  $Mix(1)$  and  $Mix(2)$ , which is shown in the top panel of Fig. A.4. If more fundamental frequencies are set in the simulation then the  $Mix()$  functions for these should be viewed displayed in the table too. The evaluation of the signal gain requires the signal input power to be available at the results screen of ADS. This is done by adding this variable to the “Output” table in the properties of the HB simulation component. Note, the addition argument in  $dbm()$  is the reference impedance, which is required to get the correct signal power.

Finally, the setup for the compression point analysis is shown in Fig. A.5. This uses the HB simulation mode with a simplified sweep where only the signal

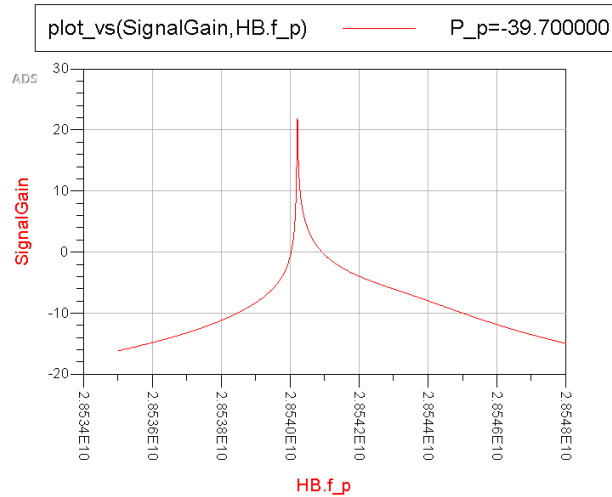
## A: KA BAND RGWG RESONATOR

freq	dBm(Vout,377)	Mix(1)	Mix(2)
0.000000 Hz	<invalid>	0	0
10.00000 kHz	-510.479892	1	-1
20.00000 kHz	-521.736956	2	-2
28.53998 GHz	-168.311970	-1	2
28.53999 GHz	-91.842643	0	1
28.54000 GHz	-21.480277	1	0
28.54001 GHz	-101.507570	2	-1
57.07997 GHz	-335.624231	-1	3
57.07998 GHz	-353.567677	0	2
57.07999 GHz	-329.381299	1	1
57.08000 GHz	-360.864587	2	0
57.08001 GHz	-328.717847	3	-1
85.61997 GHz	-296.116970	0	3
85.61998 GHz	-225.194814	1	2
85.61999 GHz	-158.426183	2	1
85.62000 GHz	-97.603130	3	0
114.1600 GHz	-327.824499	0	4
114.1600 GHz	-348.187061	1	3
114.1600 GHz	-355.466467	2	2
114.1600 GHz	-342.267987	3	1
114.1600 GHz	-358.814674	4	0
142.6999 GHz	-343.049495	0	5
142.7000 GHz	-180.965078	5	0
171.2399 GHz	-337.868451	0	6
171.2400 GHz	-334.140720	6	0
199.7799 GHz	-345.637090	0	7
199.7800 GHz	-270.242076	7	0
228.3199 GHz	-363.495496	0	8
228.3200 GHz	-367.368720	8	0

(a) The power of output harmonics and the corresponding index numbers needed for the *Mix()* function. The 5th row in the table is identified as the signal due to the matching power and frequency.

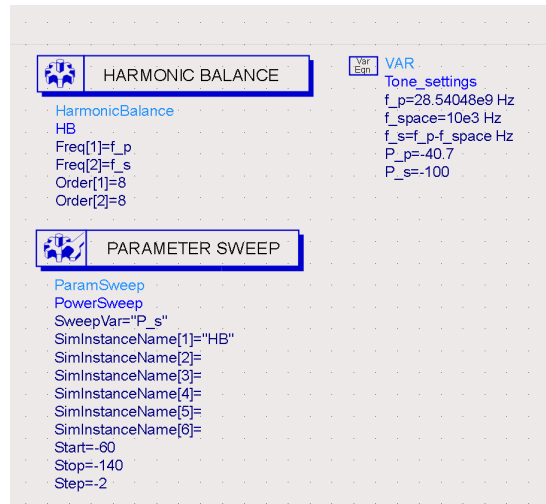
$$\text{Eqn } \text{VOUTtone} = \text{dBm}(\text{mix}(\text{Vout}, \{0, 1\}), 377)$$

$$\text{Eqn } \text{SignalGain} = \text{VOUTtone} - P_s$$



(b) The signal gain when the pump frequency is swept across the profile of the resonance and the equations used to calculate the gain.

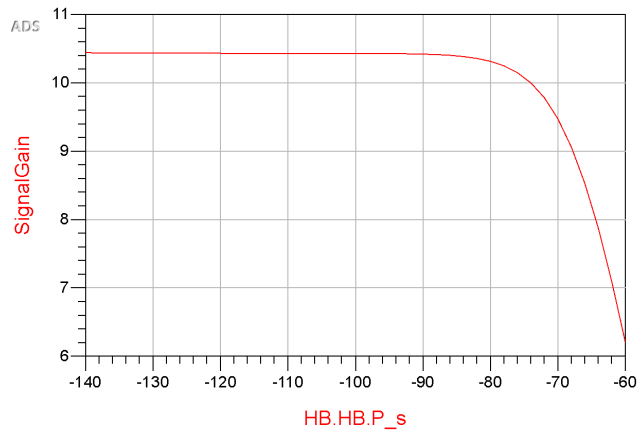
Figure A.4: A figure explaining the use of the *Mix()* function and an example gain curve that makes use of this to identify the signal tone.



(a) The simulation setup components for a compression point analysis

$$\text{Eqn} \text{ VOUTtone} = \text{dBm}(\text{mix}(\text{Vout}, \{0, 1\}), 377)$$

$$\text{Eqn} \text{ SignalGain} = \text{VOUTtone} - \text{HB.HB.P}_s$$



(b) An example of the dynamic range plot

Figure A.5: The amplifier compression point analysis using the HB simulation mode and a parameter sweep to sweep the signal input power. The parameters in the top panel are used to produce the dynamic range plot in the lower panel.

input power for a given pump power. The frequency positioning of the tones and the power of the pump is chosen to be on a specific peak gain curve.

## **A.2 Technical Drawings**

This section shows the set of technical drawings that were submitted to the Schuster machining workshop at the University of Manchester for the fabrication of Ka band ridge gap waveguide resonator. Note, that an additional 50  $\mu\text{m}$  of material was added to the upper face of part that contained the pin surface and the ridge to account for the approximate amount of material that was removed during the polishing process. The drawings are split between Fig. A.6, A.7, and A.8. The first figure shows the full assembly as well as the dimensions of the base with hole positioning and largest internal structures. The second figure shows the ridge and nail dimensions as well as underside of the same part. The third figure shows the dimensions of the lid which contains the rectangular waveguide feedthrough.

## A.2: TECHNICAL DRAWINGS

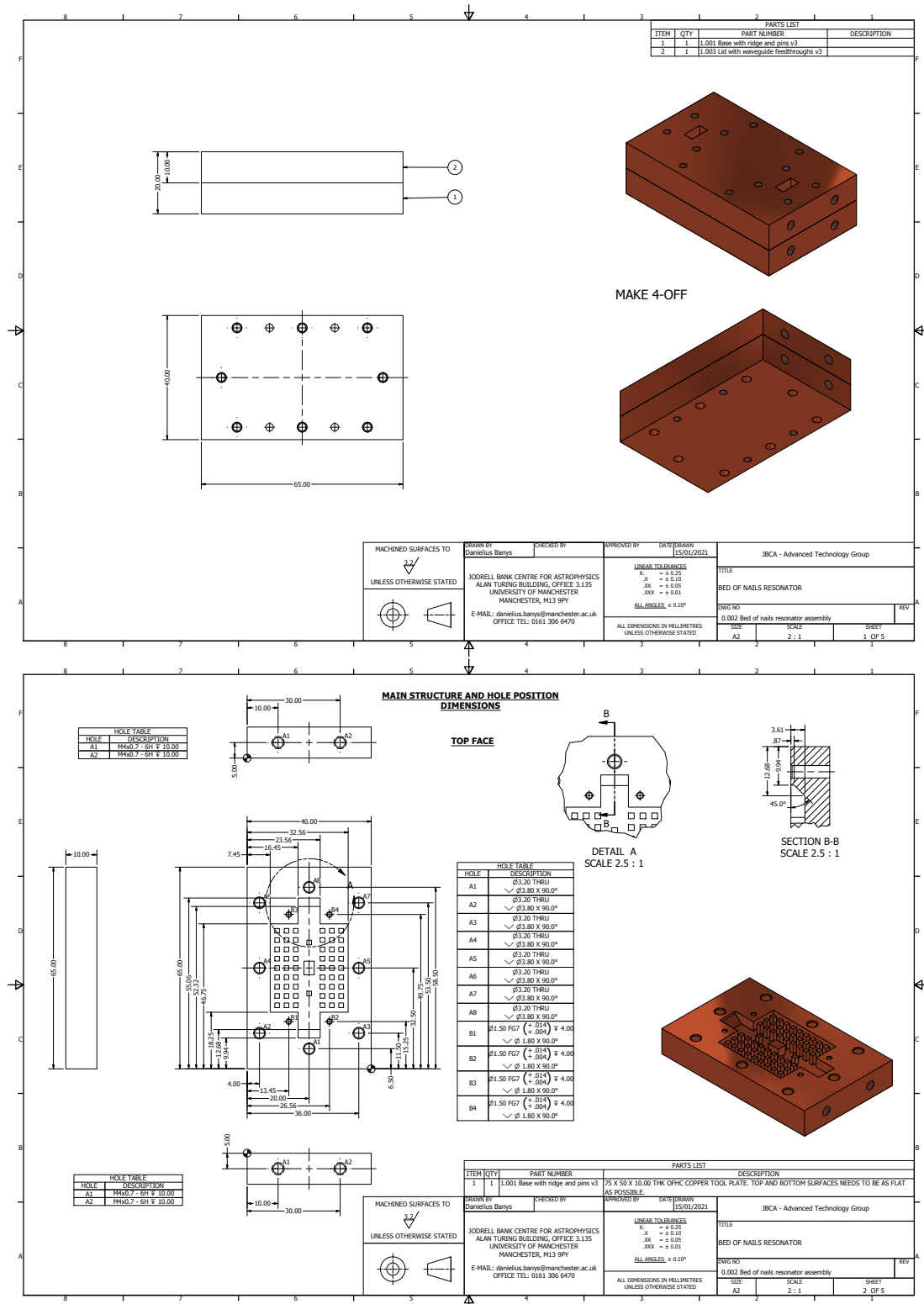


Figure A.6: Pages 1 and 2 of the technical drawings submitted for the manufacture of the Ka band pin-coupled RGWG resonator.

## A: KA BAND RGWG RESONATOR

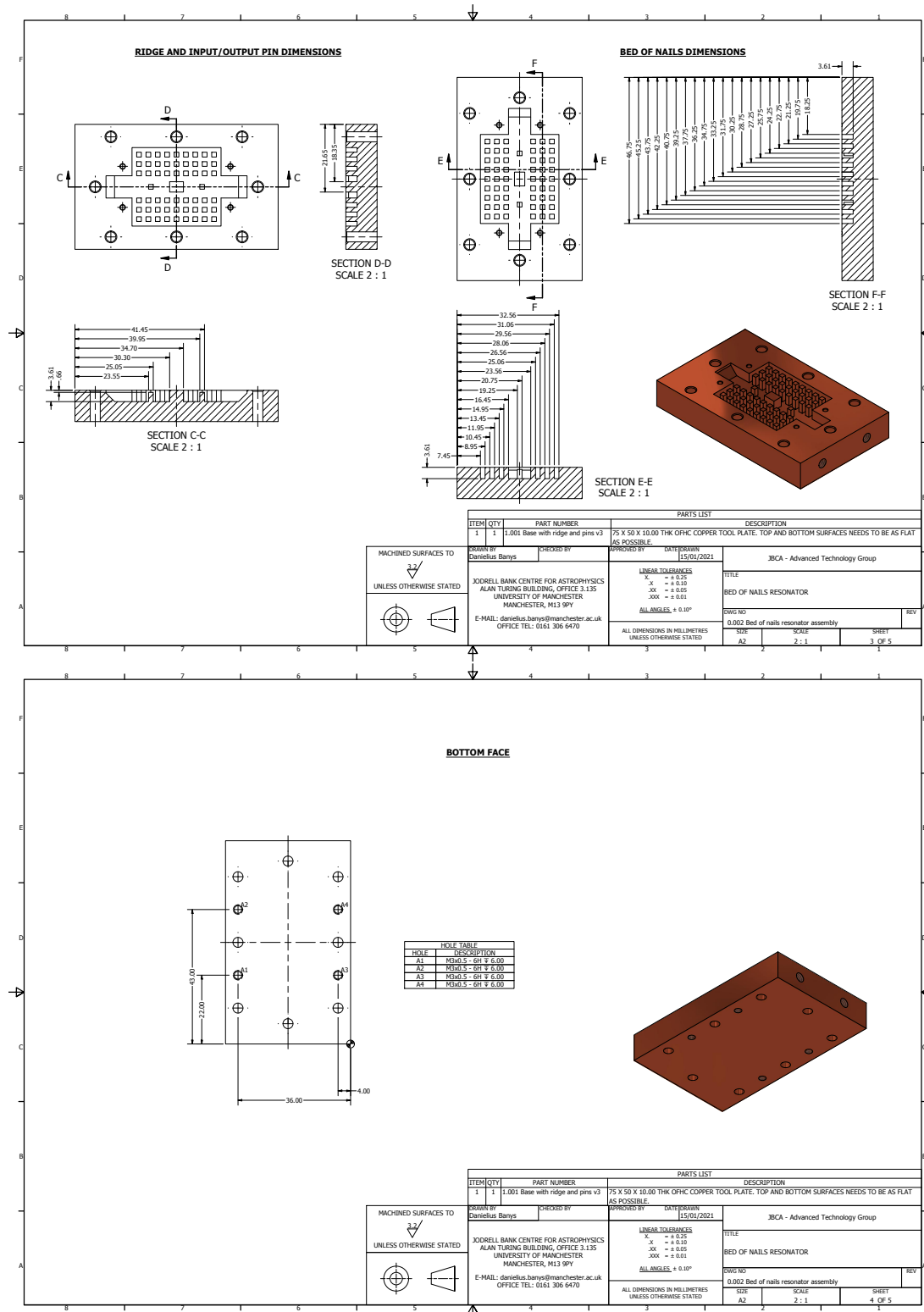


Figure A.7: Pages 3 and 4 of the technical drawings submitted for the manufacture of the Ka band pin-coupled RGWG resonator.



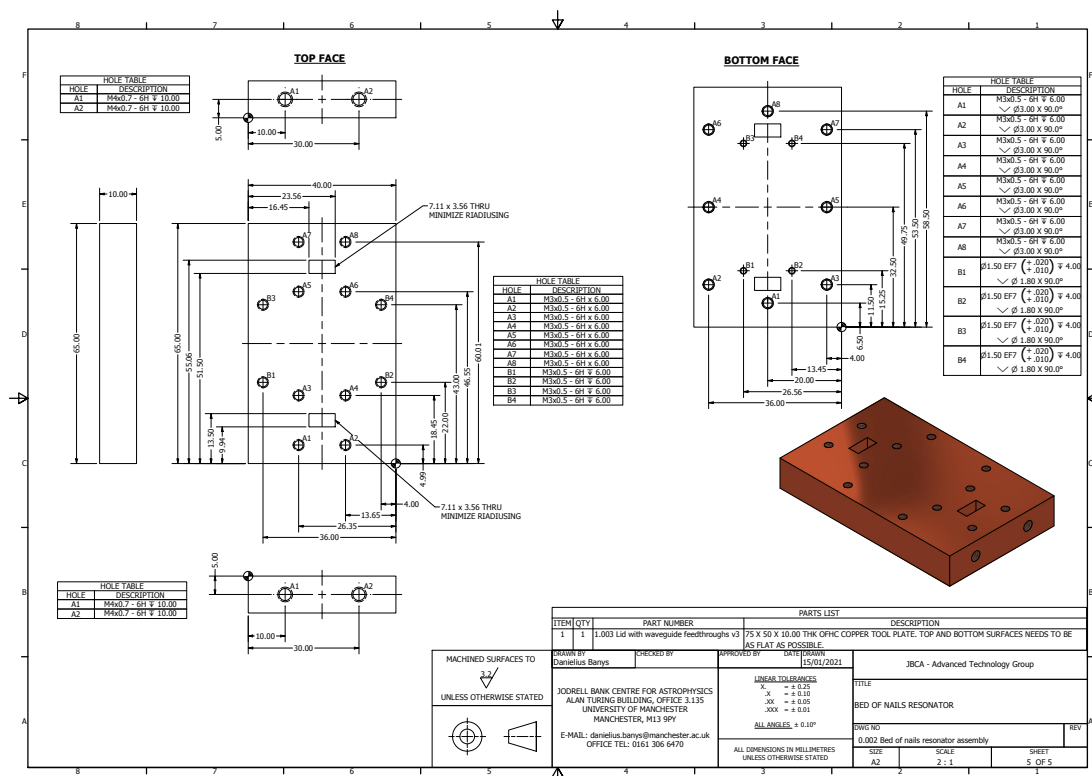


Figure A.8: Page 5 of the technical drawings submitted for the manufacture of the Ka band pin-coupled RGWG resonator.



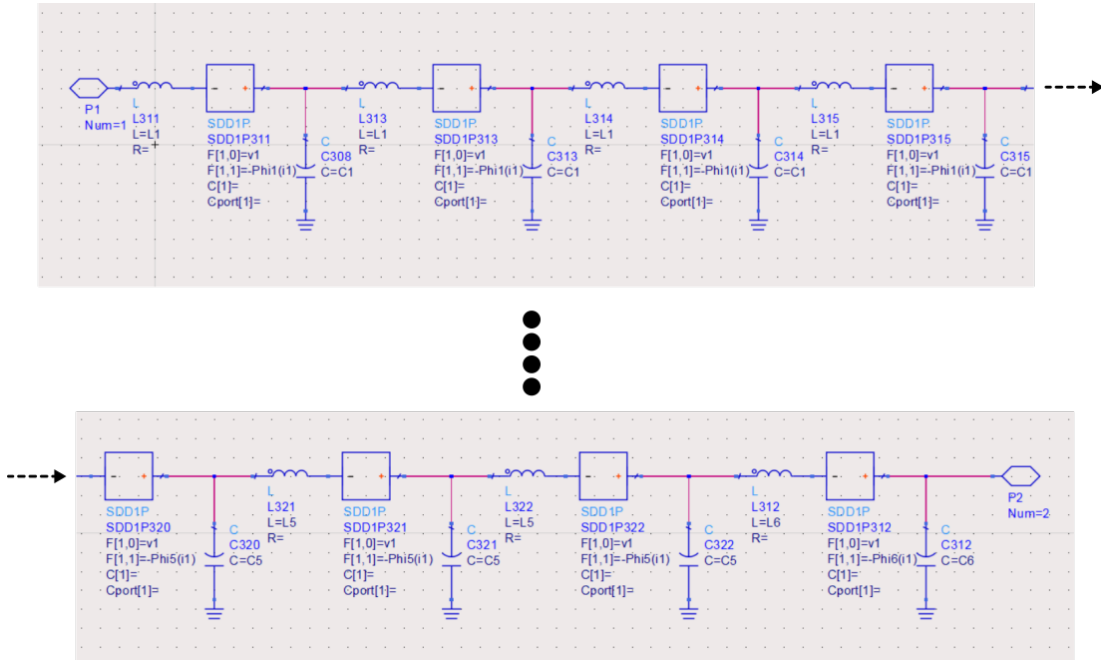
# Appendix B

## W Band KI RGWG TWPA

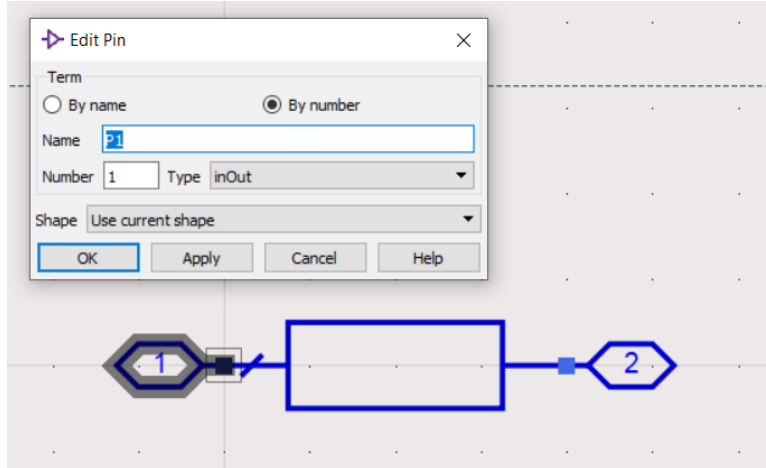
### B.1 ADS Simulation Circuit

This section aims to show the specific details on how the W band RGWG TWPA that was described in Chapter 5 was simulated in ADS to attain the structure S-parameters and the parametric gain.

The methods described here are very similar to those in Appendix A.1, which described a Ka band RGWG RPA rather than a TWPA. The key difference in the two approaches is the much larger number of LC components needed to describe the electrically long dispersion engineered RGWG. In this structure, the unloaded and loaded parts of the transmission line (see Fig. 5.2 and 5.12) are represented by their own LC ladder. One important consideration in the LC representation is to ensure that the LC cut-off frequency  $\omega_c = 2/\sqrt{LC}$  is sufficiently high such that it does not affect the guide wavelength of the travelling wave. This is done by splitting up the LC components such that there are at least 10 of each component per design wavelength. The final simulated structure was  $450\lambda$  in length which would mean that near 1350 lumped elements would be needed to describe the whole structure. The assembly of such a large number of components would prove practically challenging. In addition, the graphical interface of ADS has a



(a) A truncated set of screenshots showing the start and end of the circuit.



(b) A screenshot showing the definition of the symbol that contains the LC ladder for a single unit cell

Figure B.1: The procedure for nesting elements of an LC ladder into unit cells.

maximum number of components that it can display, and this number may be close to the elements needed. A work around to this issue and an improvement to the usability of the circuit came in the form of the use of subcircuits that could be used to host a set number of LC components. This subcircuit could be represented by a single symbol, which could then itself be placed in a subcircuit. This nesting

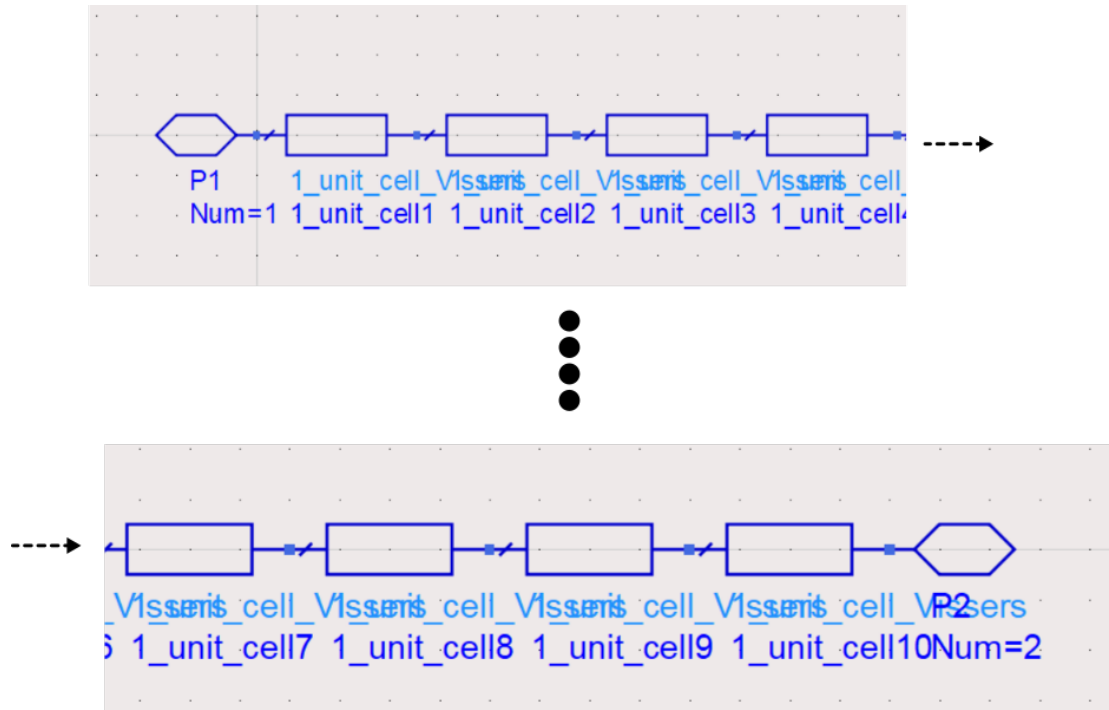
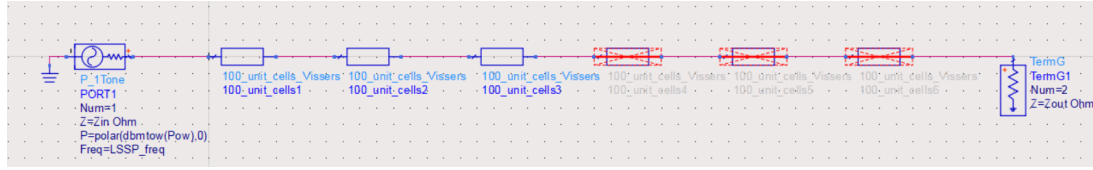


Figure B.2: A further nesting of cells into groups of 10 cells. A symbol is defined to represent 10 cells.

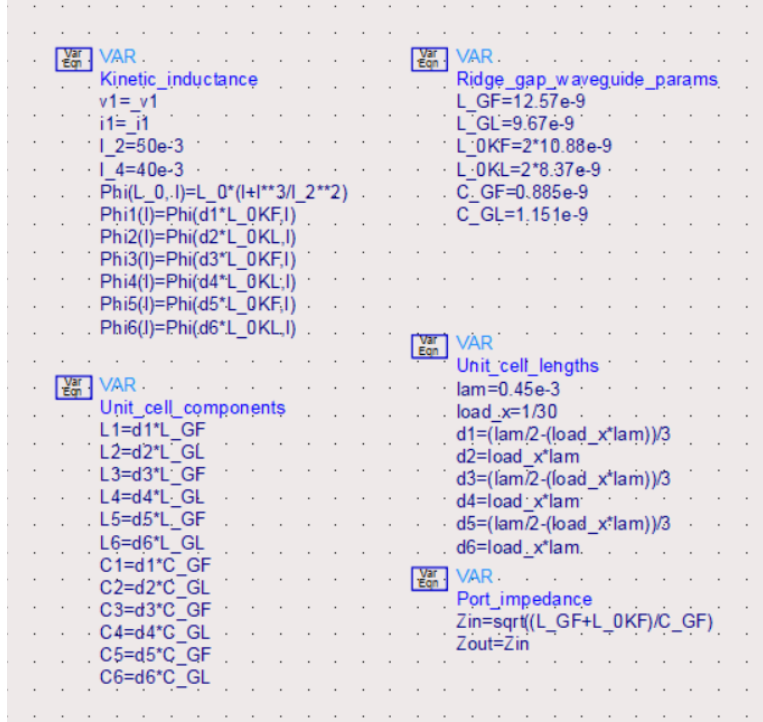
of components allowed for the whole  $450\lambda_{\text{per}}$  structure to be represented by only a few components. A single nested component is shown in Fig. B.1, which is used to build up a circuit of 10 nested components as shown in Fig. B.2, which are further nested to make up 100 cells that represent  $\lambda_{\text{per}}$  each.

The circuit used for simulating the S-parameters (linear and non-linear) is shown in Fig. B.3. It is demonstrated in the circuit how large sections of the transmission line can be deactivated and shorted to conveniently change the length of the simulated line. The impedance of the input and output ports was set to that of the unloaded section of the RGWG which is around  $6\Omega$ . The circuit parameters were defined at the top level of the circuit that is shown and these automatically linked to the defined elements within unit cells. One had to ensure that the same variable names were used in the unit cells as defined in the top level circuit.

The LSSP simulation parameters and result screen that was assembled is



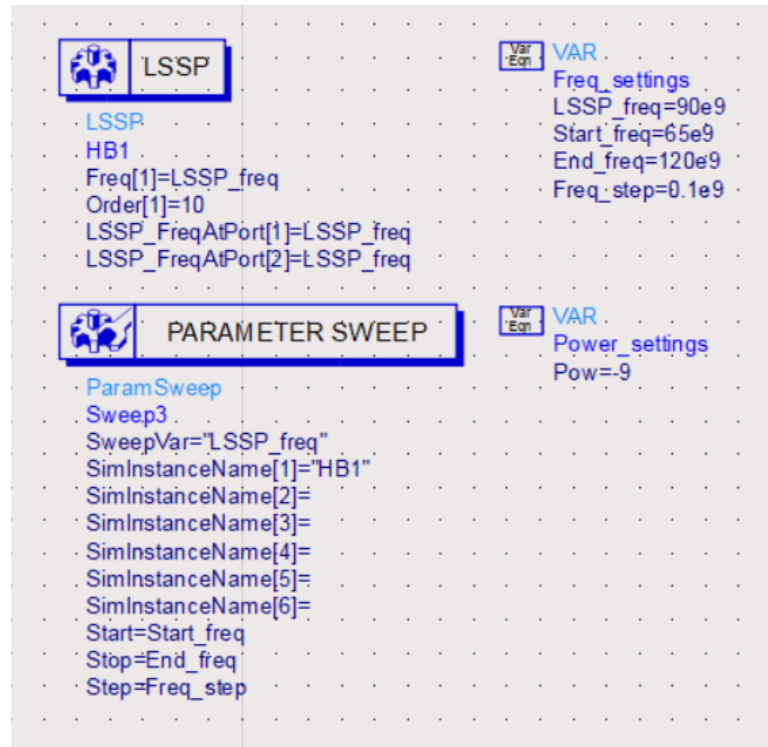
(a) The circuit as shown with elements that contain 100 unit cells each.



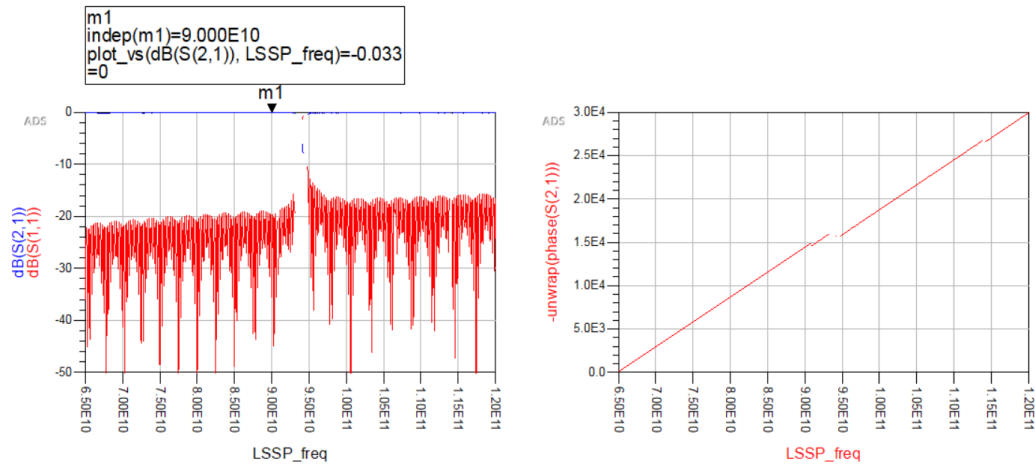
(b) The circuit parameters and the nonlinearity equations. Subscripts “GF”, “GL”, “KF”, “KL”, represent the geometric and kinetic components of the feed and loaded section of transmission line.

Figure B.3: The circuit used to simulate the  $450\lambda_{\text{per}}$  RGWG TWPA described in Section 5.3.

shown in Fig. B.4. It is important to note that unlike the LSSP simulation used for the RPA of Chapter 4 and Appendix A.1, this LSSP simulation was significantly more computationally taxing. This was due to the much larger number of components that needed to be solved and the large frequency range with a fairly small step that needed to be simulated. As the power of the drive was increased close to the power that produced maximum gain (around 10% of the scaling current), the simulation would stall and enter a power-stepping routine which would often succeed after a few attempts at that specific frequency



(a) The simulation setup used to carry out the LSSP simulations.



(b) Results screen of LSSP simulation at the drive power used to attain maximum gain. S-parameters on the left and unwrapped  $S_{21}$  phase on the right.

Figure B.4: The large signal s-parameter simulation setup that was used to simulate the linear and nonlinear S-parameters of the periodically loaded RGWG.

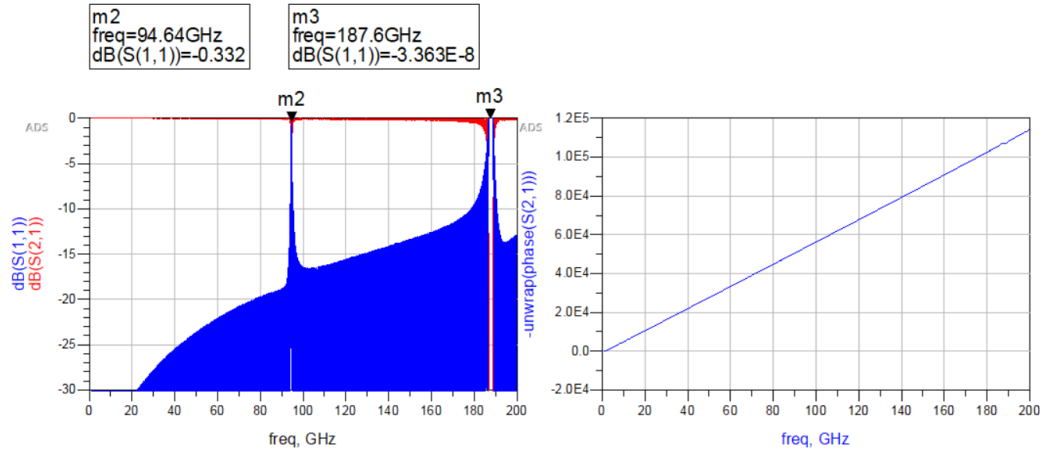
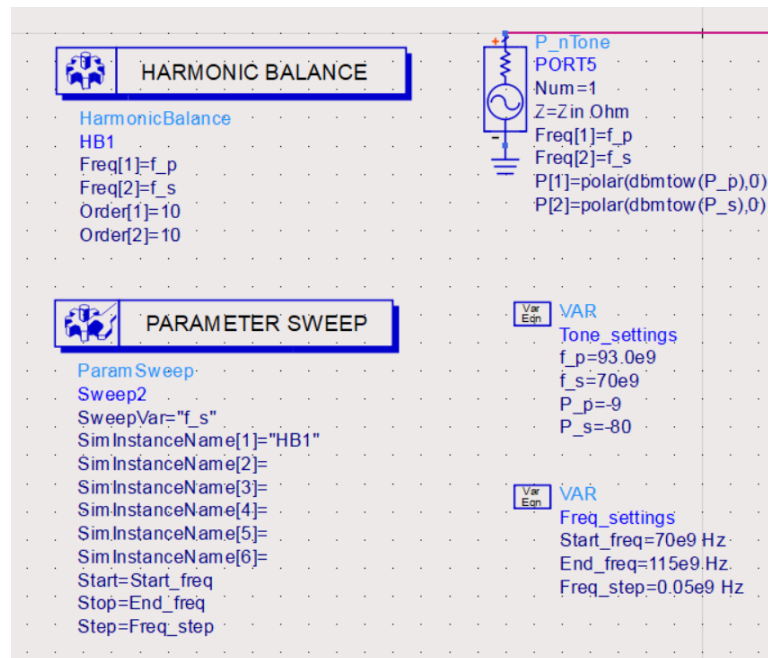


Figure B.5: The linear S-parameters that are simulated using the circuit shown in Fig. B.4.

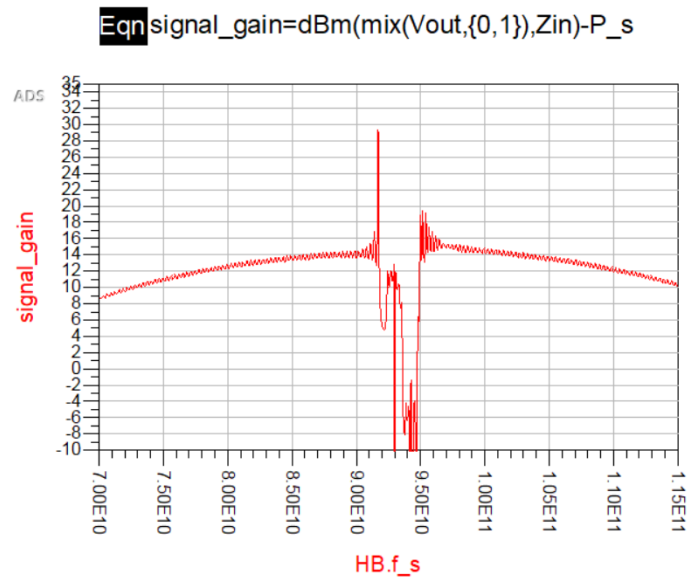
but would also fail at times. The LSSP simulation shown in Fig. B.4 took approximately 10 hours to complete and the results were not fully useable due to the solver skipping critical points near the resonance. In addition, the unwrapped  $S_{21}$  phase is shown in the same figure. It was found that the linear S-parameters provided an adequate description of the dispersion engineering since this did not require the nonlinear behaviour to manifest itself. Therefore, the linear S-parameters simulation was used from the component palette to simulate the same circuit that is shown B.4. The linear S-parameter simulator ignores the power dependency of the input ports. The results of this simulation are shown in Fig. B.5 including the unwrapped  $S_{21}$  which was used to show the relative dispersion of the dispersion engineered structure in Fig. 5.13 as well as in the calculation of the linear phase mismatch of Eq. 5.3.

Finally, the signal gain was simulated using the harmonic balance simulation mode and parameter sweep that is shown in Fig. B.6. The harmonic at the signal frequency was tracked using the Mix() function just as described in Appendix A.1. The relevant circuit parameters were parsed by setting the output variables in the harmonic balance component properties, which allowed for the signal gain to be





(a) The simulation setup and the multi-tone source used to carry out the HB simulations.



(b) The result output screen showing the TWPA gain.

Figure B.6: The harmonic balance simulation setup used to simulate the gain of the W-band RGWG TWPA.

evaluated. The dBm() function which shows the output at the probe point Vout (end of the circuit before the termination) had the reference impedance set to the port impedance to ensure the correct gain was shown. Otherwise the default reference impedance of  $50\Omega$  will be used.

# Bibliography

- [1] D. M. Pozar, *Microwave Engineering*. Chichester, England: John Wiley & Sons, 4 ed., Nov. 2011.
- [2] C.-C. Chiong, Y. Wang, K.-C. Chang, and H. Wang, “Low-noise amplifier for next-generation radio astronomy telescopes: Review of the state-of-the-art cryogenic lnas in the most challenging applications,” *IEEE Microwave Magazine*, vol. 23, no. 1, pp. 31–47, 2022.
- [3] V. Belitsky, M. Bylund, V. Desmaris, A. Ermakov, S.-E. Ferm, M. Fredrixon, S. Krause, I. Lapkin, D. Meledin, A. Pavolotsky, H. Rashid, S. Shafiee, M. Strandberg, E. Sundin, P. Y. Aghdam, R. Hesper, J. Barkhof, M. E. Bekema, J. Adema, R. de Haan, A. Koops, W. Boland, P. Yagoubov, G. Marconi, G. Siringo, E. Humphreys, G. H. Tan, R. Laing, L. Testi, T. Mroczkowski, W. Wild, K. S. Saini, and E. Bryerton, “ALMA band 5 receiver cartridge,” *Astronomy & Astrophysics*, vol. 611, p. A98, Mar. 2018.
- [4] H. Heffner, “The fundamental noise limit of linear amplifiers,” *Proceedings of the IRE*, vol. 50, no. 7, pp. 1604–1608, 1962.
- [5] C. M. Caves, “Quantum limits on noise in linear amplifiers,” *Phys. Rev. D*, vol. 26, pp. 1817–1839, Oct 1982.
- [6] A. A. Clerk, M. H. Devoret, S. M. Girvin, F. Marquardt, and R. J. Schoelkopf, “Introduction to quantum noise, measurement, and amplification,” *Reviews of Modern Physics*, vol. 82, pp. 1155–1208, Apr. 2010.

- [7] M. A. McCulloch, J. Grahn, S. J. Melhuish, P.-A. Nilsson, L. Piccirillo, J. Schlee, and N. Wadefalk, “Dependence of noise temperature on physical temperature for cryogenic low-noise amplifiers,” *Journal of Astronomical Telescopes, Instruments, and Systems*, vol. 3, p. 014003, Mar. 2017.
- [8] E. Cha, N. Wadefalk, G. Moschetti, A. Pourkabirian, J. Stenarson, and J. Grahn, “A 300- $\mu$ w cryogenic hemt lna for quantum computing,” in *2020 IEEE/MTT-S International Microwave Symposium (IMS)*, pp. 1299–1302, 2020.
- [9] D. Cuadrado-Calle, D. George, G. A. Fuller, K. Cleary, L. Samoska, P. Kangaslahti, J. W. Kooi, M. Soria, M. Varonen, R. Lai, and X. Mei, “Broad-band mmic lnas for alma band 2+3 with noise temperature below 28 k,” *IEEE Transactions on Microwave Theory and Techniques*, vol. 65, no. 5, pp. 1589–1597, 2017.
- [10] L. A. Samoska, “An overview of solid-state integrated circuit amplifiers in the submillimeter-wave and thz regime,” *IEEE Transactions on Terahertz Science and Technology*, vol. 1, no. 1, pp. 9–24, 2011.
- [11] M. A. Castellanos-Beltran, K. D. Irwin, G. C. Hilton, L. R. Vale, and K. W. Lehnert, “Amplification and squeezing of quantum noise with a tunable josephson metamaterial,” *Nature Physics*, vol. 4, pp. 929–931, Oct. 2008.
- [12] M. Esposito, A. Ranadive, L. Planat, and N. Roch, “Perspective on traveling wave microwave parametric amplifiers,” *Applied Physics Letters*, vol. 119, no. 12, p. 120501, 2021.
- [13] B. H. Eom, P. K. Day, H. G. LeDuc, and J. Zmuidzinas, “A wideband, low-noise superconducting amplifier with high dynamic range,” *Nature Physics*, vol. 8, no. 8, pp. 623–627, 2012.

- [14] C. Bockstiegel, J. Gao, M. R. Vissers, M. Sandberg, S. Chaudhuri, A. Sanders, L. R. Vale, K. D. Irwin, and D. P. Pappas, “Development of a broadband nbtin traveling wave parametric amplifier for mkid readout,” *Journal of Low Temperature Physics*, vol. 176, pp. 476–482, Aug 2014.
- [15] A. Bienfait, J. J. Pla, Y. Kubo, M. Stern, X. Zhou, C. C. Lo, C. D. Weis, T. Schenkel, M. L. W. Thewalt, D. Vion, D. Esteve, B. Julsgaard, K. Mølmer, J. J. L. Morton, and P. Bertet, “Reaching the quantum limit of sensitivity in electron spin resonance,” *Nature Nanotechnology*, vol. 11, pp. 253–257, Dec. 2015.
- [16] J. Stehlik, Y.-Y. Liu, C. M. Quintana, C. Eichler, T. R. Hartke, and J. R. Petta, “Fast charge sensing of a cavity-coupled double quantum dot using a josephson parametric amplifier,” *Phys. Rev. Applied*, vol. 4, p. 014018, Jul 2015.
- [17] P. Krantz, M. Kjaergaard, F. Yan, T. P. Orlando, S. Gustavsson, and W. D. Oliver, “A quantum engineer’s guide to superconducting qubits,” *Applied Physics Reviews*, vol. 6, no. 2, p. 021318, 2019.
- [18] S. Shu, N. Klimovich, B. H. Eom, A. D. Beyer, R. B. Thakur, H. G. Leduc, and P. K. Day, “Nonlinearity and wide-band parametric amplification in a (nb,ti)n microstrip transmission line,” *Phys. Rev. Research*, vol. 3, p. 023184, Jun 2021.
- [19] A. Anferov, A. Suleymanzade, A. Oriani, J. Simon, and D. I. Schuster, “Millimeter-wave four-wave mixing via kinetic inductance for quantum devices,” *Phys. Rev. Applied*, vol. 13, p. 024056, Feb 2020.
- [20] M. Malnou, J. Aumentado, M. R. Vissers, J. D. Wheeler, J. Hubmayr, J. N. Ullom, and J. Gao, “Performance of a kinetic-inductance traveling-wave parametric amplifier at 4 kelvin: Toward an alternative to semiconductor amplifiers,” 2021.

- [21] J. Aumentado, “Superconducting parametric amplifiers: The state of the art in josephson parametric amplifiers,” *IEEE Microwave Magazine*, vol. 21, no. 8, pp. 45–59, 2020.
- [22] J. Carpenter, D. Iono, L. Testi, N. Whyborn, A. Wootten, and N. Evans, “The alma development roadmap,” 2019.
- [23] D. Woody, “Alma band 3 amplifier study final report,” May 2013.
- [24] P. Yagoubov, T. Mroczkowski, V. Belitsky, D. Cuadrado-Calle, F. Cuttaia, G. A. Fuller, J.-D. Gallego, A. Gonzalez, K. Kaneko, P. Mena, R. Molina, R. Nesti, V. Tapia, F. Villa, M. Beltrán, F. Cavaliere, J. Ceru, G. E. Chesmore, K. Coughlin, C. D. Breuck, M. Fredrixon, D. George, H. Gibson, J. Golec, A. Josaitis, F. Kemper, M. Kotiranta, I. Lapkin, I. López-Fernández, G. Marconi, S. Mariotti, W. McGenn, J. McMahon, A. Murk, F. Pezzotta, N. Phillips, N. Reyes, S. Ricciardi, M. Sandri, M. Strandberg, L. Terenzi, L. Testi, B. Thomas, Y. Uzawa, D. Viganò, and N. Wadefalk, “Wideband 67-116 GHz receiver development for ALMA band 2,” *Astronomy & Astrophysics*, vol. 634, p. A46, Feb. 2020.
- [25] A. Caldwell, G. Dvali, B. Majorovits, A. Millar, G. Raffelt, J. Redondo, O. Reimann, F. Simon, and F. Steffen, “Dielectric haloscopes: A new way to detect axion dark matter,” *Phys. Rev. Lett.*, vol. 118, p. 091801, Mar 2017.
- [26] J. Jeong, S. Youn, S. Bae, J. Kim, T. Seong, J. E. Kim, and Y. K. Semertzidis, “Search for invisible axion dark matter with a multiple-cell haloscope,” *Phys. Rev. Lett.*, vol. 125, p. 221302, Nov 2020.
- [27] K. M. Backes, D. A. Palken, S. A. Kenany, B. M. Brubaker, S. B. Cahn, A. Droster, G. C. Hilton, S. Ghosh, H. Jackson, S. K. Lamoreaux, A. F. Leder, K. W. Lehnert, S. M. Lewis, M. Malnou, R. H. Maruyama, N. M.

- Rapidis, M. Simanovskaia, S. Singh, D. H. Speller, I. Urdinaran, L. R. Vale, E. C. van Assendelft, K. van Bibber, and H. Wang, “A quantum enhanced search for dark matter axions,” *Nature*, vol. 590, pp. 238–242, Feb. 2021.
- [28] K. Wurtz, B. M. Brubaker, Y. Jiang, E. P. Ruddy, D. A. Palken, and K. W. Lehnert, “A cavity entanglement and state swapping method to accelerate the search for axion dark matter,” 2021.
- [29] G. Che, S. Gordon, P. Day, C. Groppi, R. Jackson, H. Mani, P. Mauskopf, H. Surdi, G. Trichopoulos, and M. Underhill, “A superconducting phase shifter and traveling wave kinetic inductance parametric amplifier for w-band astronomy,” 2017.
- [30] R. B. Thakur, N. Klimovich, P. K. Day, E. Shirokoff, P. D. Mauskopf, F. Faramarzi, and P. S. Barry, “Superconducting on-chip fourier transform spectrometer,” *Journal of Low Temperature Physics*, vol. 200, pp. 342–352, June 2020.
- [31] F. B. Faramarzi, P. Mauskopf, S. Gordon, G. Che, P. Day, H. Mani, H. Surdi, S. Sypkens, P. Barry, E. Shirokoff, and R. B. Thakur, “An on-chip superconducting kinetic inductance fourier transform spectrometer for millimeter-wave astronomy,” *Journal of Low Temperature Physics*, vol. 199, pp. 867–874, Jan. 2020.
- [32] D. Banys, M. A. McCulloch, S. Azzoni, B. Cooper, A. J. May, S. J. Melhuish, L. Piccirillo, and J. Wenninger, “Parametric amplification at ka band via nonlinear dynamics in superconducting 3d cavities,” *Journal of Low Temperature Physics*, vol. 200, pp. 295–304, Mar. 2020.
- [33] V. Gilles, D. Banys, M. A. McCulloch, L. Piccirillo, and T. Sweetnam, “Parametric amplification via superconducting contacts in a ka band niobium pillbox cavity,” *Journal of Low Temperature Physics*, Dec. 2022.

## BIBLIOGRAPHY

- [34] D. Banys, M. A. McCulloch, T. Sweetnam, V. Gilles, and L. Piccirillo, “Millimetre wave kinetic inductance parametric amplification using ridge gap waveguide,” *Journal of Low Temperature Physics*, vol. 209, pp. 734–742, Sept. 2022.
- [35] T. Sweetnam, D. Banys, V. Gilles, M. A. McCulloch, and L. Piccirillo, “Simulating the behaviour of travelling wave superconducting parametric amplifiers using a commercial circuit simulator,” 2022.
- [36] M. Tinkham, *Introduction to Superconductivity: v. 1*. Dover Books on Physics, Mineola, NY: Dover Publications, 2 ed., June 2004.
- [37] J. Zmuidzinas, “Superconducting microresonators: Physics and applications,” *Annual Review of Condensed Matter Physics*, vol. 3, no. 1, pp. 169–214, 2012.
- [38] J. Gao, *The physics of superconducting microwave resonators*. California Institute of Technology, 2008.
- [39] D. P. L. Aude, *Modeling superconductors using surface impedance techniques*. PhD thesis, Massachusetts Institute of Technology, 2010.
- [40] D. C. Mattis and J. Bardeen, “Theory of the anomalous skin effect in normal and superconducting metals,” *Phys. Rev.*, vol. 111, pp. 412–417, Jul 1958.
- [41] W. Zimmermann, E. Brandt, M. Bauer, E. Seider, and L. Genzel, “Optical conductivity of bcs superconductors with arbitrary purity,” *Physica C: Superconductivity*, vol. 183, no. 1, pp. 99–104, 1991.
- [42] L. Planat, *Resonant and traveling-wave parametric amplification near the quantum limit*. Theses, Université Grenoble Alpes [2020-....], June 2020.
- [43] D. Van Delft and P. Kes, “The discovery of superconductivity,” *Physics Today*, vol. 63, no. 9, pp. 38–43, 2010.



- [44] W. Meissner and R. Ochsenfeld, “A new effect when superconductivity occurs,” *science*, vol. 21, no. 44, pp. 787–788, 1933.
- [45] A. M. Forrest, “Meissner and ochsenfeld revisited,” *European Journal of Physics*, vol. 4, pp. 117–120, apr 1983.
- [46] F. London, “Electrodynamics of macroscopic fields in supraconductors,” *Nature*, vol. 137, pp. 991–992, June 1936.
- [47] A. B. Pippard and W. L. Bragg, “An experimental and theoretical study of the relation between magnetic field and current in a superconductor,” *Proceedings of the Royal Society of London. Series A. Mathematical and Physical Sciences*, vol. 216, no. 1127, pp. 547–568, 1953.
- [48] J. Bardeen, L. N. Cooper, and J. R. Schrieffer, “Microscopic theory of superconductivity,” *Phys. Rev.*, vol. 106, pp. 162–164, Apr 1957.
- [49] L. D. Landau and V. L. Ginzburg, “On the theory of superconductivity,” *Zh. Eksp. Teor. Fiz.*, vol. 20, p. 1064, 1950.
- [50] L. P. Gor’kov, “Microscopic derivation of the ginzburg-landau equations in the theory of superconductivity,” *Sov. Phys. JETP*, vol. 9, no. 6, pp. 1364–1367, 1959.
- [51] J. Ward, F. Rice, G. Chattopadhyay, and J. Zmuidzinas, “Supermix: A flexible software library for high-frequency circuit simulation, including sis mixers and superconducting elements,” in *Proceedings, Tenth International Symposium on Space Terahertz Technology*, pp. 269–281, 1999.
- [52] R. E. Glover and M. Tinkham, “Conductivity of superconducting films for photon energies between 0.3 and  $40kT_c$ ,” *Phys. Rev.*, vol. 108, pp. 243–256, Oct 1957.

- [53] B. Mühlischlegel, “The thermodynamic functions of the superconductor,” *journal for physics*, vol. 155, no. 3, pp. 313–327, 1959.
- [54] D. Linden, T. Orlando, and W. Lyons, “Modified two-fluid model for superconductor surface impedance calculation,” *IEEE Transactions on Applied Superconductivity*, vol. 4, no. 3, pp. 136–142, 1994.
- [55] T. Hong, K. Choi, K. Ik Sim, T. Ha, B. Cheol Park, H. Yamamori, and J. Hoon Kim, “Terahertz electrodynamics and superconducting energy gap of nb<sub>1-x</sub>tin,” *Journal of Applied Physics*, vol. 114, no. 24, p. 243905, 2013.
- [56] V. Belitsky, C. Risacher, M. Pantaleev, and V. Vassilev, “Superconducting microstrip line model studies at millimetre and sub-millimetre waves,” *International Journal of Infrared and Millimeter Waves*, vol. 27, pp. 809–834, Jun 2006.
- [57] A. Gurevich, “Theory of RF superconductivity for resonant cavities,” *Superconductor Science and Technology*, vol. 30, p. 034004, jan 2017.
- [58] B. Josephson, “Possible new effects in superconductive tunnelling,” *Physics Letters*, vol. 1, no. 7, pp. 251–253, 1962.
- [59] B. Yurke, L. R. Corruccini, P. G. Kaminsky, L. W. Rupp, A. D. Smith, A. H. Silver, R. W. Simon, and E. A. Whittaker, “Observation of parametric amplification and deamplification in a josephson parametric amplifier,” *Phys. Rev. A*, vol. 39, pp. 2519–2533, Mar 1989.
- [60] C. Macklin, K. O’Brien, D. Hover, M. E. Schwartz, V. Bolkhovskiy, X. Zhang, W. D. Oliver, and I. Siddiqi, “A near-quantum-limited josephson traveling-wave parametric amplifier,” *Science*, vol. 350, no. 6258, pp. 307–310, 2015.
- [61] M. R. Vissers, R. P. Erickson, H.-S. Ku, L. Vale, X. Wu, G. C. Hilton, and D. P. Pappas, “Low-noise kinetic inductance traveling-wave amplifier using

- three-wave mixing,” *Applied Physics Letters*, vol. 108, no. 1, p. 012601, 2016.
- [62] J. Gao, M. R. Vissers, M. Sandberg, D. Li, H. M. Cho, C. Bockstiegel, B. A. Mazin, H. G. Leduc, S. Chaudhuri, D. P. Pappas, and K. D. Irwin, “Properties of TiN for detector and amplifier applications,” *Journal of Low Temperature Physics*, vol. 176, pp. 136–141, Feb. 2014.
- [63] A. Semenov, I. Devyatov, M. Westig, and T. Klapwijk, “Effect of microwaves on superconductors for kinetic inductance detection and parametric amplification,” *Phys. Rev. Applied*, vol. 13, p. 024079, Feb 2020.
- [64] A. Anthore, H. Pothier, and D. Esteve, “Density of states in a superconductor carrying a supercurrent,” *Physical Review Letters*, vol. 90, mar 2003.
- [65] M. Malnou, M. Vissers, J. Wheeler, J. Aumentado, J. Hubmayr, J. Ullom, and J. Gao, “Three-wave mixing kinetic inductance traveling-wave amplifier with near-quantum-limited noise performance,” *PRX Quantum*, vol. 2, p. 010302, Jan 2021.
- [66] G. Agrawal, ed., *Nonlinear Fiber Optics (Fifth Edition)*. Optics and Photonics, Boston: Academic Press, fifth edition ed., 2013.
- [67] X. Zhou, V. Schmitt, P. Bertet, D. Vion, W. Wustmann, V. Shumeiko, and D. Esteve, “High-gain weakly nonlinear flux-modulated josephson parametric amplifier using a SQUID array,” *Physical Review B*, vol. 89, jun 2014.
- [68] J. Grebel, A. Bienfait, E. Dumur, H.-S. Chang, M.-H. Chou, C. R. Conner, G. A. Pears, R. G. Povey, Y. P. Zhong, and A. N. Cleland, “Flux-pumped impedance-engineered broadband josephson parametric amplifier,” *Applied Physics Letters*, vol. 118, no. 14, p. 142601, 2021.

- [69] T. Yamamoto, K. Inomata, M. Watanabe, K. Matsuba, T. Miyazaki, W. D. Oliver, Y. Nakamura, and J. S. Tsai, “Flux-driven josephson parametric amplifier,” 2008.
- [70] N. E. Frattini, V. V. Sivak, A. Lingenfelter, S. Shankar, and M. H. Devoret, “Optimizing the nonlinearity and dissipation of a SNAIL parametric amplifier for dynamic range,” *Physical Review Applied*, vol. 10, nov 2018.
- [71] V. Sivak, N. Frattini, V. Joshi, A. Lingenfelter, S. Shankar, and M. Devoret, “Kerr-free three-wave mixing in superconducting quantum circuits,” *Physical Review Applied*, vol. 11, may 2019.
- [72] V. V. Sivak, S. Shankar, G. Liu, J. Aumentado, and M. H. Devoret, “Josephson array-mode parametric amplifier,” *Phys. Rev. Applied*, vol. 13, p. 024014, Feb 2020.
- [73] A. Miano, G. Liu, V. V. Sivak, N. E. Frattini, V. R. Joshi, W. Dai, L. Frunzio, and M. H. Devoret, “Frequency-tunable kerr-free three-wave mixing with a gradiometric SNAIL,” *Applied Physics Letters*, vol. 120, p. 184002, may 2022.
- [74] D. J. Parker, M. Savytskyi, W. Vine, A. Laucht, T. Duty, A. Morello, A. L. Grimsmo, and J. J. Pla, “Degenerate parametric amplification via three-wave mixing using kinetic inductance,” *Physical Review Applied*, vol. 17, mar 2022.
- [75] R. P. Erickson and D. P. Pappas, “Theory of multiwave mixing within the superconducting kinetic-inductance traveling-wave amplifier,” *Phys. Rev. B*, vol. 95, p. 104506, Mar 2017.
- [76] R. Movshovich, B. Yurke, P. G. Kaminsky, A. D. Smith, A. H. Silver, R. W. Simon, and M. V. Schneider, “Observation of zero-point noise squeezing via

- a josephson-parametric amplifier,” *Phys. Rev. Lett.*, vol. 65, pp. 1419–1422, Sep 1990.
- [77] C. Eichler, D. Bozyigit, C. Lang, M. Baur, L. Steffen, J. M. Fink, S. Filipp, and A. Wallraff, “Observation of two-mode squeezing in the microwave frequency domain,” *Phys. Rev. Lett.*, vol. 107, p. 113601, Sep 2011.
- [78] E. Segev, B. Abdo, O. Shtempluck, and E. Buks, “Novel self-sustained modulation in superconducting stripline resonators,” *Europhysics Letters (EPL)*, vol. 78, p. 57002, May 2007.
- [79] E. A. Tholén, A. Ergül, K. Stannigel, C. Hutter, and D. B. Haviland, “Parametric amplification with weak-link nonlinearity in superconducting microresonators,” *Physica Scripta*, vol. T137, p. 014019, Dec. 2009.
- [80] I. Siddiqi, R. Vijay, F. Pierre, C. M. Wilson, M. Metcalfe, C. Rigetti, L. Frunzio, and M. H. Devoret, “Rf-driven josephson bifurcation amplifier for quantum measurement,” *Phys. Rev. Lett.*, vol. 93, p. 207002, Nov 2004.
- [81] V. E. Manucharyan, E. Boaknin, M. Metcalfe, R. Vijay, I. Siddiqi, and M. Devoret, “Microwave bifurcation of a josephson junction: Embedding-circuit requirements,” *Phys. Rev. B*, vol. 76, p. 014524, Jul 2007.
- [82] M. A. Castellanos-Beltran and K. W. Lehnert, “Widely tunable parametric amplifier based on a superconducting quantum interference device array resonator,” *Applied Physics Letters*, vol. 91, p. 083509, Aug. 2007.
- [83] J. Y. Mutus, T. C. White, R. Barends, Y. Chen, Z. Chen, B. Chiaro, A. Dunsworth, E. Jeffrey, J. Kelly, A. Megrant, C. Neill, P. J. J. O’Malley, P. Roushan, D. Sank, A. Vainsencher, J. Wenner, K. M. Sundqvist, A. N. Cleland, and J. M. Martinis, “Strong environmental coupling in a josephson

- parametric amplifier,” *Applied Physics Letters*, vol. 104, p. 263513, June 2014.
- [84] T. Roy, S. Kundu, M. Chand, A. M. Vadiraj, A. Ranadive, N. Nehra, M. P. Patankar, J. Aumentado, A. A. Clerk, and R. Vijay, “Broadband parametric amplification with impedance engineering: Beyond the gain-bandwidth product,” *Applied Physics Letters*, vol. 107, p. 262601, Dec. 2015.
- [85] G. Liu, T.-C. Chien, X. Cao, O. Lanes, E. Alpern, D. Pekker, and M. Hatridge, “Josephson parametric converter saturation and higher order effects,” *Applied Physics Letters*, vol. 111, p. 202603, Nov. 2017.
- [86] L. Planat, R. Dassonneville, J. P. Martínez, F. Foroughi, O. Buisson, W. Hasch-Guichard, C. Naud, R. Vijay, K. Murch, and N. Roch, “Understanding the saturation power of josephson parametric amplifiers made from squid arrays,” *Phys. Rev. Applied*, vol. 11, p. 034014, Mar 2019.
- [87] N. Roch, E. Flurin, F. Nguyen, P. Morfin, P. Campagne-Ibarcq, M. H. Devoret, and B. Huard, “Widely tunable, nondegenerate three-wave mixing microwave device operating near the quantum limit,” *Phys. Rev. Lett.*, vol. 108, p. 147701, Apr 2012.
- [88] B. Abdo, E. Segev, O. Shtempluck, and E. Buks, “Intermodulation gain in nonlinear NbN superconducting microwave resonators,” *Applied Physics Letters*, vol. 88, p. 022508, Jan. 2006.
- [89] B. Yurke and E. Buks, “Performance of cavity-parametric amplifiers, employing kerr nonlinearities, in the presence of two-photon loss,” *Journal of Lightwave Technology*, vol. 24, pp. 5054–5066, dec 2006.
- [90] C. Eichler and A. Wallraff, “Controlling the dynamic range of a josephson parametric amplifier,” *EPJ Quantum Technology*, vol. 1, Jan. 2014.

- [91] S. Boutin, D. M. Toyli, A. V. Venkatramani, A. W. Eddins, I. Siddiqi, and A. Blais, “Effect of higher-order nonlinearities on amplification and squeezing in josephson parametric amplifiers,” *Phys. Rev. Applied*, vol. 8, p. 054030, Nov 2017.
- [92] S. Chaudhuri, J. Gao, and K. Irwin, “Simulation and analysis of superconducting traveling-wave parametric amplifiers,” 2014.
- [93] R. Erickson, M. Vissers, M. Sandberg, S. Jefferts, and D. Pappas, “Frequency comb generation in superconducting resonators,” *Physical Review Letters*, vol. 113, Oct. 2014.
- [94] T. Dixon, J. Dunstan, G. Long, J. Williams, P. Meeson, and C. Shelly, “Capturing complex behavior in josephson traveling-wave parametric amplifiers,” *Phys. Rev. Applied*, vol. 14, p. 034058, Sep 2020.
- [95] S. Chaudhuri, D. Li, K. D. Irwin, C. Bockstiegel, J. Hubmayr, J. N. Ullom, M. R. Vissers, and J. Gao, “Broadband parametric amplifiers based on nonlinear kinetic inductance artificial transmission lines,” *Applied Physics Letters*, vol. 110, no. 15, p. 152601, 2017.
- [96] L. Planat, A. Ranadive, R. Dassonneville, J. Puertas Martínez, S. Léger, C. Naud, O. Buisson, W. Hasch-Guichard, D. M. Basko, and N. Roch, “Photonic-crystal josephson traveling-wave parametric amplifier,” *Phys. Rev. X*, vol. 10, p. 021021, Apr 2020.
- [97] T. C. White, J. Y. Mutus, I.-C. Hoi, R. Barends, B. Campbell, Y. Chen, Z. Chen, B. Chiaro, A. Dunsworth, E. Jeffrey, J. Kelly, A. Megrant, C. Neill, P. J. J. O’Malley, P. Roushan, D. Sank, A. Vainsencher, J. Wenner, S. Chaudhuri, J. Gao, and J. M. Martinis, “Traveling wave parametric amplifier with josephson junctions using minimal resonator phase matching,” *Applied Physics Letters*, vol. 106, no. 24, p. 242601, 2015.

- [98] K. O'Brien, C. Macklin, I. Siddiqi, and X. Zhang, "Resonant phase matching of josephson junction traveling wave parametric amplifiers," *Phys. Rev. Lett.*, vol. 113, p. 157001, Oct 2014.
- [99] N. E. Frattini, U. Vool, S. Shankar, A. Narla, K. M. Sliwa, and M. H. Devoret, "3-wave mixing josephson dipole element," *Applied Physics Letters*, vol. 110, p. 222603, May 2017.
- [100] A. Ranadive, M. Esposito, L. Planat, E. Bonet, C. Naud, O. Buisson, W. Guichard, and N. Roch, "Kerr reversal in josephson meta-material and traveling wave parametric amplification," *Nature Communications*, vol. 13, apr 2022.
- [101] C. Kow, V. Podolskiy, and A. Kamal, "Self phase-matched broadband amplification with a left-handed josephson transmission line," 2022.
- [102] K. Peng, M. Naghiloo, J. Wang, G. D. Cunningham, Y. Ye, and K. P. O'Brien, "Floquet-mode traveling-wave parametric amplifiers," *PRX Quantum*, vol. 3, apr 2022.
- [103] A. B. Zorin, M. Khabipov, J. Dietel, and R. Dolata, "Traveling-wave parametric amplifier based on three-wave mixing in a josephson metamaterial," 2017.
- [104] J. Hansryd, P. A. Andrekson, M. Westlund, J. Li, and P. O. Hedekvist, "Fiber-based optical parametric amplifiers and their applications," *IEEE Journal of Selected Topics in Quantum Electronics*, vol. 8, pp. 506–520, May 2002.
- [105] A. Zorin, "Flux-driven josephson traveling-wave parametric amplifier," *Physical Review Applied*, vol. 12, Oct. 2019.
- [106] M. Finckenor and D. Dooling, "Multilayer insulation material guidelines," tech. rep., 1999.



- [107] A. J. May, G. Coppi, V. Haynes, S. Melhuish, L. Piccirillo, T. Sarmento, and S. Teale, “A highly effective superfluid film breaker for high heat-lift 1 k sorption coolers,” *Cryogenics*, vol. 102, pp. 45–49, Sept. 2019.
- [108] R. Kalra, A. Laucht, J. P. Dehollain, D. Bar, S. Freer, S. Simmons, J. T. Muhonen, and A. Morello, “Vibration-induced electrical noise in a cryogen-free dilution refrigerator: Characterization, mitigation, and impact on qubit coherence,” *Review of Scientific Instruments*, vol. 87, p. 073905, July 2016.
- [109] L. Piccirillo, G. Coppi, and A. May, *Miniature Sorption Coolers Theory and Applications*. Applied Industrial Physics, United States: CRC Press, 1st ed., Feb. 2018.
- [110] S. J. Melhuish, M. A. McCulloch, L. Piccirillo, and C. Stott, “A high-performance wave guide cryogenic thermal break,” *Review of Scientific Instruments*, vol. 87, no. 10, p. 104706, 2016.
- [111] P.-S. Kildal, A. Zaman, E. Rajo-Iglesias, E. Alfonso, and A. Valero-Nogueira, “Design and experimental verification of ridge gap waveguide in bed of nails for parallel-plate mode suppression,” *IET Microwaves, Antennas & Propagation*, vol. 5, pp. 262–270(8), February 2011.
- [112] A. Polemi, S. Maci, and P.-S. Kildal, “Dispersion characteristics of a metamaterial-based parallel-plate ridge gap waveguide realized by bed of nails,” *IEEE Transactions on Antennas and Propagation*, vol. 59, pp. 904–913, Mar. 2011.
- [113] S. Rahiminejad, A. Zaman, E. Pucci, H. Raza, V. Vassilev, S. Haasl, P. Lundgren, P.-S. Kildal, and P. Enoksson, “Micromachined ridge gap waveguide and resonator for millimeter-wave applications,” *Sensors and Actuators A: Physical*, vol. 186, pp. 264–269, 2012. Selected Papers presented at Eurosensors XXV.

## BIBLIOGRAPHY

- [114] M. G. Silveirinha, C. A. Fernandes, and J. R. Costa, “Electromagnetic characterization of textured surfaces formed by metallic pins,” *IEEE Transactions on Antennas and Propagation*, vol. 56, no. 2, pp. 405–415, 2008.
- [115] R. W. Klopfenstein, “A transmission line taper of improved design,” *Proceedings of the IRE*, vol. 44, no. 1, pp. 31–35, 1956.
- [116] E. A. Alós, A. U. Zaman, and P.-S. Kildal, “Ka-band gap waveguide coupled-resonator filter for radio link diplexer application,” *IEEE Transactions on Components, Packaging and Manufacturing Technology*, vol. 3, no. 5, pp. 870–879, 2013.
- [117] S. Zhao, S. Withington, D. J. Goldie, and C. N. Thomas, “Nonlinear properties of supercurrent-carrying single- and multi-layer thin-film superconductors,” *Journal of Low Temperature Physics*, vol. 199, pp. 34–44, Apr 2020.
- [118] I. V. Zolochetskii, “Resistive states in wide superconducting films induced by dc and ac currents (review article),” *Low Temperature Physics*, vol. 40, no. 10, pp. 867–892, 2014.
- [119] L. Yu, N. Newman, and J. Rowell, “Measurement of the coherence length of sputtered nb/sub 0.62/ti/sub 0.38/n thin films,” *IEEE Transactions on Applied Superconductivity*, vol. 12, no. 2, pp. 1795–1798, 2002.
- [120] T. Zhang, C. Pegrum, J. Du, and Y. J. Guo, “Simulation and measurement of a ka-band HTS MMIC josephson junction mixer,” *Superconductor Science and Technology*, vol. 30, p. 015008, nov 2016.
- [121] F. Alessandri, M. Mongiardo, and R. Sorrentino, “Rigorous mode matching analysis of mitred e-plane bends in rectangular waveguide,” *IEEE Microwave and Guided Wave Letters*, vol. 4, no. 12, pp. 408–410, 1994.

- [122] P. Eaton and P. West, *Atomic Force Microscopy*. Oxford University Press, Mar. 2010.
- [123] W. Griggs, *Disorder-and strain-mediated magnetic phase modifications in FeRh thin films*. PhD thesis, University of Manchester, 2021.
- [124] M. Beck, M. Klammer, S. Lang, P. Leiderer, V. V. Kabanov, G. N. Gol'tsman, and J. Demsar, “Energy-gap dynamics of superconducting NbN thin films studied by time-resolved terahertz spectroscopy,” *Physical Review Letters*, vol. 107, oct 2011.
- [125] W. L. McMillan, “Tunneling model of the superconducting proximity effect,” *Phys. Rev.*, vol. 175, pp. 537–542, Nov 1968.
- [126] S. Swann, “Magnetron sputtering,” *Physics in Technology*, vol. 19, pp. 67–75, mar 1988.
- [127] E. T. Holland, Y. J. Rosen, N. Materise, N. Woollett, T. Voisin, Y. M. Wang, S. G. Torres, J. Mireles, G. Carosi, and J. L. DuBois, “High-kinetic inductance additive manufactured superconducting microwave cavity,” *Applied Physics Letters*, vol. 111, p. 202602, Nov. 2017.
- [128] J. P. Turneaure, J. Halbritter, and H. A. Schwettman, “The surface impedance of superconductors and normal conductors: The mattis-bardeen theory,” *Journal of Superconductivity*, vol. 4, pp. 341–355, Oct. 1991.
- [129] N. C. Carvalho, Y. Fan, and M. E. Tobar, “Piezoelectric tunable microwave superconducting cavity,” *Review of Scientific Instruments*, vol. 87, p. 094702, Sept. 2016.
- [130] S. Beurthey, N. Böhmer, P. Brun, A. Caldwell, L. Chevalier, C. Diaconu, G. Dvali, P. Freire, E. Garutti, C. Gooch, A. Hambarzumjan, S. Heyminck, F. Hubaut, J. Jochum, P. Karst, S. Khan, D. Kittlinger, S. Knirck,

- M. Kramer, C. Krieger, T. Lasserre, C. Lee, X. Li, A. Lindner, B. Majorovits, M. Matysek, S. Martens, E. Öz, P. Pataguppi, P. Pralavorio, G. Raffelt, J. Redondo, O. Reimann, A. Ringwald, N. Roch, K. Saikawa, J. Schaffran, A. Schmidt, J. Schütte-Engel, A. Sedlak, F. Steffen, L. Shtembari, C. Strandhagen, D. Strom, and G. Wieching, “Madmax status report,” 2020.
- [131] F. Faramarzi, P. Day, J. Glasby, S. Sypkens, M. Colangelo, R. Chamberlin, M. Mirhosseini, K. Schmidt, K. K. Berggren, and P. Mauskopf, “Initial design of a w-band superconducting kinetic inductance qubit,” *IEEE Transactions on Applied Superconductivity*, vol. 31, p. 1–5, Aug 2021.
- [132] E. F. C. Driessen, P. C. J. J. Coumou, R. R. Tromp, P. J. de Visser, and T. M. Klapwijk, “Strongly disordered tin and nbtin *s*-wave superconductors probed by microwave electrodynamics,” *Phys. Rev. Lett.*, vol. 109, p. 107003, Sep 2012.
- [133] J. Pearl, “Current distribution in superconducting films carrying quantized fluxoids,” *Applied Physics Letters*, vol. 5, no. 4, pp. 65–66, 1964.
- [134] W. Shan, Y. Sekimoto, and T. Noguchi, “Parametric amplification in a superconducting microstrip transmission line,” *IEEE Transactions on Applied Superconductivity*, vol. 26, no. 6, pp. 1–9, 2016.
- [135] A. A. Adamyan, S. E. de Graaf, S. E. Kubatkin, and A. V. Danilov, “Superconducting microwave parametric amplifier based on a quasi-fractal slow propagation line,” *Journal of Applied Physics*, vol. 119, no. 8, p. 083901, 2016.
- [136] N. S. Klimovich, *Traveling Wave Parametric Amplifiers and Other Nonlinear Kinetic Inductance Devices*. PhD thesis, 2022.

*The End*